ISSN 1880-8468

Technical Report of
International Development Engineering
国際開発工学報告

TRIDE-2012-02 February 14, 2012

Abstracts of Master Theses
Presented in February 2012

Department of International Development Engineering,
Graduate School of Science and Engineering,
Tokyo Institute of Technology
http://www.ide.titech.ac.jp/TR

Preface

Master theses of Department of International Development Engineering, Tokyo Institute of Technology were presented successfully on July 29, 2011 and February 14, 2012. This technical report consists of the abstracts of those theses.

Technical Report of International Development Engineering
TRIDE-2012-02

Table of Contents

Consumer Incentives for Purchasing Wooden Houses: Focusing on Potential Demand for Domestic Wood Utilization

Student Number: 09M18031 Name: Akihisa KURIYAMA Supervisor: Naoya ABE

国産木材の利用拡大可能性の観点からみた木造住宅購入者の購入動機に関する研究

栗山　昭久

本研究では、日本国内の成熟した人工林の利用が叫ばれる中、住宅市場における国産材利用拡大に向けて住宅購入者に国産木材に関する購入とその動機に関するアンケート調査を行った。同調査によるデータを分析した結果、国産木材の利用の是非は、住宅購入者の意識よりも施行者による判断や推奨が大きく影響していることが明らかになった。同時に、国産材の利用拡大に向けて、施行者が安定的かつ容易に使用できる供給体制の確立が必要であるという提言を示した。

1. Introduction

The decrease in forest area has been one of the most serious global issues in terms of climate change and biodiversity. In tropical areas, the decrease is very apparent, as shown in Fig. 1. On the other hand, the amount of Japanese trees, especially those in planted forests, has been rapidly increasing due to mass forest plantation during the post World War II era (Fig. 2).

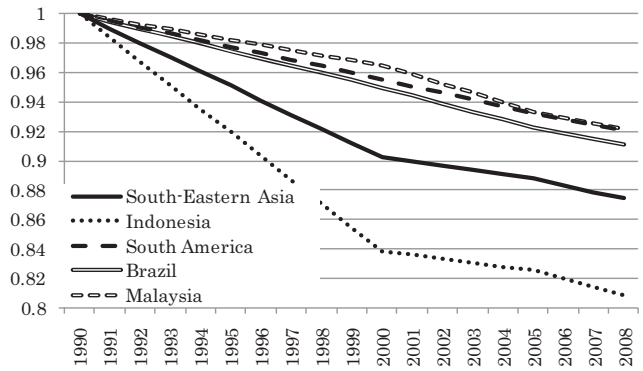

Fig. 1. Decreasing Rainforest (Source: FAOSTAT)

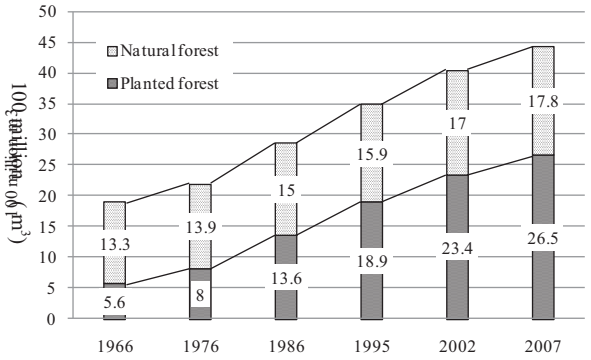

Fig. 2. Increasing planted forests in Japan (Source: Ref 6)

Forestry is important to Japan. First, Japan has to create carbon sinks for 13 million tons of CO2 because of the ratification of the Kyoto Protocol. In order to create these carbon sinks, it is necessary to conduct proper forest management and tidy forestry, which results in proper revenues for forest owners and associated wood product suppliers. Second, forestry contributes to local economies because the forest cluster is usually wide and is a large industry in terms of employment. In fact, forestry in European countries has a great impact on the local economy. For example, in 1996, the Swedish forestry cluster accounted for 33% of the Swedish industrial investments, 26% of all industrial employees, and 20% of Sweden's total exports (Svensén, 1999). In addition, the German forest cluster employed 1.3 million people in 2008, which is twice the number employed by the car industry (Kurisu, 2008).

In view of these facts, the Japanese government has launched several policies aimed at expanding the utilization of domestic wood (hereinafter referred to as DW), such as the Forestry Revitalization Project in 2009. These policies have "supply push" aspects, as shown in Fig. 3 ($S_0 \rightarrow S_1$). However, "supply push" policies lower the market price of DW, resulting in possible negative effects on wood producers. Thus, the demand curve, which shifts forward and to the right ($D_0 \rightarrow D_1$), is essential for keeping the market price high and ensuring the growth of the DW market.

A few studies, including that by Miyamoto (2009), have researched consumer demand for DW. These studies, however, are limited to local production and consumption of DW.

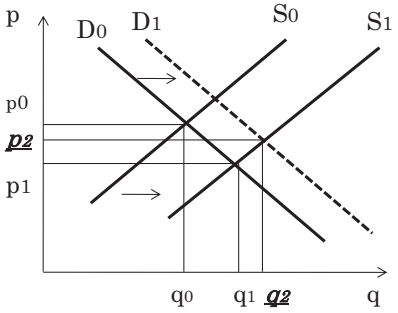

Fig. 3. Supply and Demand curves of domestic wood

2. Objectives

In this study, we focus on the Japanese housing market as a source of demand for DW because this market consumed 42% of DW in 2008. In order to investigate demand in the housing market, we created a main questionnaire for house buyers for Objective1 and Objective2, and added a complementary questionnaire for house builders for Objective2.

Objective 1: To identify the factors which affect purchaser's willingness and actual usage of DW (Section 4.1 and 4.2)

Objective 2: To investigate in building prices, focusing on usage of DW (Section 4.3 and 4.4)

The target respondents of this survey comprised two groups. The first group was in the Tokyo Metropolitan area, where land price is the highest in Japan. This price level may affect consumer behavior. The other group was in the Hokuriku area (Fukui, Toyama, Ishikawa, Niigata, and Nagano prefectures, collectively, in this study), where the average housing size is large. The process of area selection was based on the assumption that as compared to the people in Tokyo, the people in the Hokuriku area have a higher incentive to care about their houses. This is because the people in the Hokuriku tend to use more wood for house construction. A summary of comparison between both areas is shown in Table 1.

Table 1. Comparison between Tokyo and Hokuriku areas

	Tokyo	Hokuriku
Housing area per person (m^2/per)	64	113–147
Half life period of wooden house (Year)	29	35–44
Population density in 2005 (person/km^2)	5,721	162–281
Number of newly built wooden houses in 2009	36,792	30,011

In order to summarize builders' perspectives on DW as construction materials, we sent a complementary questionnaire to housing builders because house buyers always purchase houses through housing builders. The target of the complementary questionnaire was builders who deal with DW in the Tokyo area.

3. Survey methods

3.1 Questionnaire

For the main questionnaire, we adopted a web-based survey approach, for the following three reasons. First, even though the respondents could not be selected randomly, the bias could be low because house buyers are mainly in their 30s and 40s, implying that they are probably familiar with the Internet. Second, access to personal information on who actually purchased a wooden house is nowadays restricted by local municipalities; therefore, it was almost impossible to access this data. Third, the web-based questionnaire has the advantage of distribution in several areas.

3.2 Model definition and estimation

3.2.1 Descriptions of Objectives 1

A consumer's decision to choose DW is assumed to be based upon his/her utility maximizing nature in response to characteristics such as area to live, age, income, etc. In order to consider the likely uncertainties around consumers' decision-making processes, owing to unobserved alternatives, unobserved individual attributes, and measurement errors (Manski 1977), a random utility model is used to determine the factors that influence the probability of consumers choosing DW. Thus, the utility model for choosing DW is represented as

$$U_i = X_i\beta + \varepsilon, \qquad \text{(Eq. 1)}$$

where U is the utility of a consumer using DW or not using DW, X_i denotes the observed factors, β denotes model coefficients, and ε denotes the unobserved factors.

The empirical models used in the study are specified as

$$\begin{aligned} WILL = {} & \beta_1 AREA + \beta_2 AGE + \beta_3 PR + \beta_4 OPINION \\ & + \beta_5 INFMAG + \beta_6 INFSALES + \beta_7 INFFRIEND + \beta_0 \end{aligned} \qquad \text{(eq.2)}$$

$$\begin{aligned} USAGE = {} & \beta_1 INCOME + \beta_2 PR + \beta_3 CHILD + \beta_4 PARENTS \\ & + \beta_5 RECOM + \beta_0 \end{aligned} \qquad \text{(eq.3)}$$

$$\begin{aligned} USAGE = {} & \beta_1 PR + \beta_2 RECOM + \beta_3 LSHARE \\ & + \beta_4 DESGIN + \beta_0 \end{aligned} \qquad \text{(eq.4)}$$

The description of variables is listed in Table 3.

Since the response variables for Eqs. 2, 3, and 4 were binary, binominal logistic regression analysis was applied to estimate the model parameters. Logistic regression is based on the cumulative logistic probability function, and estimates the probability of an action, given a set of categorical characteristics (Pindyck and Rubinfeld, 1981). In binary logistic regression, the probabilities for each outcome are specified as

$$P(Y_i = 1) = P_i = \frac{e^{X_i\beta}}{1 + e^{X_i\beta}} \qquad P(Y_i = 0) = 1 - P_i = \frac{1}{1 + e^{X_i\beta}} \qquad \text{(eq.5)}$$

The likelihood function for the model is (Greene, 1993)

$$L = \prod_{i=1}^{n} P_i^{y_i} (i - P_i)^{(1-y_i)} \qquad \text{(eq.6)}$$

where P_i is the probability of consumer i choosing DW. Maximum likelihood estimation procedures are employed to estimate the value of model parameters.

3.2.2 Description of Objective 2

We predicted building price using multiple linear regression analysis estimated by OLS (Ordinal Least Squares). The empirical models used in the study are specified as

$$\begin{aligned} BPIRICE = {} & \beta_1 INCOME + \beta_2 USAGE + \beta_3 LSHARE \\ & + \beta_4 DESGIN + \beta_5 OPINION + \beta_0 \end{aligned} \qquad \text{(eq.7)}$$

The description of variables is listed in Table 3.

The software that we ran for these analyses was Stata/SE 10.0 for Windows.

4. Results

Of the 585 questionnaires that were sent to the two groups through the web-based approach, there were 421 respondents: 206 from the Tokyo area and 208 from the Hokuriku area. The response rate was high because we used monitoring data offered by a survey company. A summary of the data is shown in Table 3.

Log-likelihood ratios of all the models were significant. None of the independent variables were highly correlated with others, and the absolute values of the correlation coefficients are lower than 0.33.

4.1. Consumer demand and incentive to use DW

In this section, we analyze willingness to use DW for housing structures. The results of the model are presented in Table 4. OPINION and PR of structure materials are positively significant. This implies that a consumer who ascribes importance to taking care of his/her house tends to prefer DW and their preferences were not determined by information sources.

Table 3. Description of variables

Dependent Variables		Mean | SD | Sample, (Tokyo, Hokuriku)
WILL[+]	Dummy variable: "1" if consumer wanted to use DW, "0" otherwise	See Table 4.
USAGE[+]	Dummy variable: "1" if consumer eventually used DW, "0" otherwise	See Tables 5 and 6.
BPRICE	Only building price, not including land price (10,000 Yen)	2627, 2472 1424, 984 166 194

Independent Variables		Mean	SD (Tokyo, Hokuriku)	Sample
AREA	Dummy variable: "1" if a consumer lives in the Hokuriku area, "0" in the Tokyo Area	-	-	205, 207
AGE	Consumer age	44.5, 40.1	8.3, 7.8	205, 207
PR	Dummy variable: "1" if a consumer is aware of DW, "0" otherwise	0.04, 0.05	-	206, 208
OPINION	Dummy variable: "1" if a consumer could reflect more than half of his/her opinions, "0" otherwise	0.62, 0.89	-	206, 208
INFMAG	Dummy variable: "1" if information from housing magazine or books was crucial in determining the house, "0" otherwise	0.13, 0.11	-	206, 208
INFSALES	Dummy variable: "1" if information from housing salesman was crucial to determining the house, "0" otherwise	0.32, 0.34	-	206, 208
INFFRIEND	Dummy variable: "1" if information from salesman was crucial to determining the house, "0" otherwise	0.13, 0.16	-	206, 208
INCOME	Consumer Income (10,000 Yen)	1048, 706	474, 350	194, 195
CHILD	Dummy variable: "1" if a consumer has a child/children, "0" otherwise	0.74, 0,75	-	205, 207
PARENT	Dummy variable: "1" if a consumer lives with his/her parents, "0" otherwise	0.10, 0.22	-	205, 207
RECOM	Dummy variable: "1" if a consumer was recommended the use of DW by builders, "0" otherwise	0.13, 0.11	-	80, 96
LSHARE	Dummy variable: "1" if a consumer ordered his/her house from a large share builder, "0" otherwise	0.23, 0.24	-	206, 208
DESIGN	Dummy variable: "1" if a consumer ordered his/her house from a design office builder, "0" otherwise	0.12, 0.13	-	206, 208

[+] We asked WILL and CHOICE for structure materials in respondents' houses.

Table 4. Binary logit estimates for willingness to use DW[++]

WILL (# of Res)	**Structure** (No: 237 Yes:176)		
	Coef	Marginal effects	SE
AGE	0.01	0.002	0.01
AREA	0.07	0.018	0.22
OPINION	**0.89** ***	0.2	0.27
PR	**1.08** **	0.26	0.51
INFMAG	-0.46	-0.11	0.33
INFSALES	0.33	0.08	0.22
INFFRIEND	0.27	0.07	0.29
Constant	**-1.52** **		0.61
LR chi2(6)	22.5***	Pseudo R2	0.04

Table 5. Binary logit estimates for eventual usage of DW in Structure 1[++]

USAGE (# of Res)	**Tokyo** (No: 47,Yes: 21)			**Hokuriku** (No: 55,Yes: 26)		
	Coef	Marginal effects	SE	Coef	Marginal effects	SE
INCOME	**1.1 x10^{-3}** *	0.2 x10^{-3}	0.6 x10^{-3}	0.6 x10^{-3}	0.1 x10^{-3}	0.7 x10^{-3}
PR	0.92	0.21	1.01	**2.00** **	0.46	0.94
CHILD	-0.14	-0.03	0.71	0.49	0.10	0.64
PARENTS	1.25	0.29	0.88	0.51	0.11	0.61
RECOM	**2.90** ***	0.62	0.90	**2.88** ***	0.60	1.15
Constant	**-2.64** ***		0.95	**-2.07** ***		0.83
LR chi2(5)	18.1***			13.6**		
Pseudo R2	0.22			0.13		

Table 6. Binary logit estimates for eventual usage of DW in Structure 2[++]

USAGE (# of Res)	**Tokyo** (No: 51,Yes: 22)			**Hokuriku** (No: 57,Yes: 28)		
	Coef	Marginal effects	SE	Coef	Marginal effects	SE
RECOM	**2.78** ***	0.60	0.92	**2.84** ***	0.59	1.13
LSHARE	**2.00** ***	0.44	0.70	0.28	0.06	0.63
DESGIN	**1.62** *	0.37	0.85	1.00	0.24	0.68
Constant	**-2.08** ***		0.48	**-1.16** ***		0.33
LR chi2(3)	22.6***			11.33**		
Pseudo R2	0.25			0.11		

4.2. Crucial factors of practical usage of DW

We analyze actual usage of DW for the persons who have willingness to use DW. The results of the models are presented in Tables 5. INCOME in the Tokyo is significant at the 10% level, but not in the Hokuriku. This may be because, as shown in Table 6, purchasers in the Tokyo had to order their houses to Large Share Builders or Design Offices, which in turn increases the total building price. As a result, the consumer cannot afford to consider a house in this area. Another important result is that RECOM is highly significant and influential for the practical usage of DW at the 1% significance level for both areas. This indicates that if the consumers were persuaded by builders to utilize DW, the probability of using DW would have been increased by around 60%.

4.3. Building price of using DW

As Table 7 shows, building price variations depend on consumers' choices. Although the utilization of DW increases the price in the Tokyo to 2.2 million Yen for the structure, the significance of the coefficient is low. In the Hokuriku area, the additional price of using DW for

[++] * Significant at the 10% level ** Significant at the 5% level *** Significant at the 1% level

structure was higher than that in the Tokyo, which was 3.3 million Yen. This implies that usage of DW in the Hokuriku area costs higher than that in the Tokyo due to its housing area, however, total buildings price in the Tokyo was higher than that in the Hokuriku.

Table 7. Estimated building price in the Tokyo, estimated by ordinary least squares (OLS)

BPRICE (# of Res)	**Tokyo** (No: 129, Yes: 18)			**Hokuriku** (No: 150, Yes: 24)		
	Coef	P > t	SE	Coef	P > t	SE
INCOME	**0.55**	**0.019**	0.23	**0.82**	**0**	0.20
USAGE	220	0.489	317	**332**	**0.095**	198
OPINON	**609**	**0.012**	240	**569**	**0.017**	236
LSHARE	**1,128**	**0**	255	363	0.036	172
DESGIN	-351	0.311	345	352	0.085	203
Constant	**1,362**	**0**	254	**1,145**	**0**	268
F		12.52***				8.74***
Adj R-squared		0.28				0.18

Though it was cleared that using DW was expensive, the maximum price difference between DW and imported wood is, in fact, less than 50 (10,000) Yen, which is calculated by the equation below:

Price Difference = (DW price(Yen/m^2) – Imported Price(Yen/m^2)) * Floor area per house (m^2) = 363,600,

where DW price is 18,182 Yen/m^2 and imported wood price is 15,152 Yen/m^2 (Forest Agency, 2011), and Floor per house is 120m^2 on average. Thus, it is assumed that a dominant part of the additional cost of using DW does not come from material price, but from additional design fees or procurement fees.

4.4. Important factors of wood supply

In order to investigate in the price gap, which is mentioned in section 4.3, we consider the complementary questionnaire received from 10 builders by fax. The most relevant question in this questionnaire was regarding the essential factors of construction materials that builders use. Table 8 shows that the important factors of materials are assured quality and procurement rather than price. Table 9 shows the three most frequent answers for the reasons of using DW. The results indicate that DW has a higher value because of its texture and social aspects.

Table 8. Factors that builders consider for construction materials

Assured quality	9	Killen dry wood	4
Assured procurement	5	JAS certification	4
Low price	3	(unit: persons)	

Table 9. Reasons why builders use DW (unit: persons)

Added value as texture	8	Suitable for Japanese	
Added value as CSR	5	humid climate	5

5. Conclusion and Discussion

In this study, we investigated consumers' incentives for using domestic wood and the crucial factors in the practical usage of DW. From the results indicated in 4.1, we observed that public relation activities for DW were effective in raising awareness of the utilization of DW. However, conversely, the results of 4.2 indicated that public relation activities were not effective for the practical utilization of DW in the Tokyo; instead, probability of choice in the Tokyo area was affected by the consumer's income. This is because contracts with large shared builders and design offices were effective. These results indicate that monetary factors were important in the Tokyo area. In the Hokuriku, on the other hand, the probability was not affected by consumer income. This implies that people with lower incomes in the Tokyo have a lower likelihood of using DW even if they are motivated to use it. The most crucial factor in the utilization of DW was the recommendation of DW by a builder. Thus, in order to promote the use of DW, an appeal to builders would be much more effective than a direct appeal to consumers. From 4.3, we estimated the marginal increase of building price when a consumer used DW. If consumers used DW, the additional fee would have been over 2 million yen. The increased price would not come from the material price itself, but from the additional design and procurement costs of DW. This may be because the use of DW has not been standardized for both builders and consumers.

Consequently, as indicated by 4.2, the key stakeholder in expanding the utilization of DW was not the end-user, that is, the housing buyers, but the semi-end user, that is, the housing builder. Furthermore, from 4.4, we can see that the important factor in the builders' choice of wood material was not price, which many logging producers claim, but assured quality and procurement of wood. Nowadays, the construction periods of houses are being shortened by incentives to cut construction costs, such as labor. Thus, builders prefer to use those materials that they can be used anytime and for any part of the house.

In light of these findings, we suggest higher utilization of domestic wood. First, it is important to make domestic wood an assured commodity in terms of quality and quantity. This leads housing builders to use DW without troublesome procedures or extra fees. Second, an usage of DW should be standardized in order to reduce additional design cost, especially in the Tokyo. As a result, according to the evidence from this study, builders can persuade house buyers to use DW, and consumers are likely to respond to this recommendation.

6. References

1. Miyamoto et al. 2009, Why Isn't Local Wood Used as Much as It Should be for Consumers' Needs?: Analysis of a Questionnaire on Housing in Akita Prefecture, Journal of the Japanese Forest Economic Society, 55(1) 56-64 (In Japanese).

2. Svensén, M (1999), The Swedish Forest Industry Cluster—What is It?, Swedish Forest Industries Federation.

3. Kurisu, Y (2008), The Challenge of Japanese Forest and Forestry—Minutes of ―High Level Seminar with Japanese Forest Cooperatives," ―Exchange meeting with German Forester," The Norinchukin Bank (In Japanese).

4. Manski, C (1977), The Structure of Random Utility Models, Theory and Decision 8 (3), 229–254.

5. Pindyck, RS and Rubinfeld, DL (1981), Econometric Models and Economic Forecasts, 2nd. McGraw-Hill, New York, 630pp.

6. Forest Agency (2011) Annual Report on Forest and Forestry in Japan, Ministry of Agriculture, Forestry and Fisheries, Japan.

STUDY OF PARKING SYSTEM IN ULAANBAATAR CITY

Student Number: 09M51614 Name: Erdenee ENKHBAT Supervisor: Shinya HANAOKA

ウランバートル市内の駐車場システムの検討
エルデネー エンフバト

Abstract: The parking issue is the important component of Transportation System. At present, Parking is inadequate in Ulaanbaatar city in Mongolia. The Thesis evaluates parking problems in Ulaanbaatar and provides approach to strengthen it. Learning about characteristic of parking system and studying from experience, in this study, The Parking Behavior, Parking Occupancy, Parking Requirement, Parking Generation Rate, Parking Demand and Parking Conceptual Design are mentioned. The gap between parking supply and demand in the current is estimated and then its cause and the solution to reduce it are discussed.

1. Introduction

Mongolia is being in development process. In recent years, economic development quickly brings about development of many other fields. The numbers of vehicle increases while the infrastructure as road, parking …has not caught yet. The vehicles often park illegal on and off-street because of insufficient parking. This situation expects research about parking system to improve it.

The Ulaanbaatar city's main problems and concerns on the current traffic situation are increasing traffic congestion, decreasing level of safety and amenity of road transportation, low awareness of road users, lack of traffic management capacity and deficient road transportation infrastructure.

Currently, parking supply does not meet parking demand. Road traffic has constantly increased along with population growth and increase in vehicle numbers. During the period 2001 to 2009, traffic volume in the city center doubled. In 2009, number of registered vehicles in the city was only about 92700 which are still low, but it is increased by 10.7% between 2001 and 2009. According to a recent statistic released by the Ministry of Road, Transport, Construction and Urban Development, Mongolia, total on and off-street parking areas increased to 210,800 square meter in 2008 whereas it was 189,800 square meter in 2000.

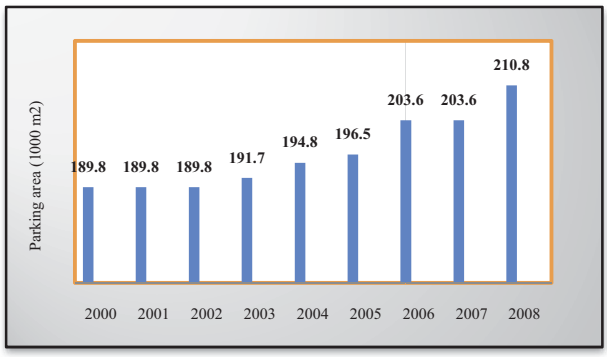

Figure-1 Statistic data of parking area

This is a very unsatisfactory result considering the growth in population and number of vehicles in the city. On the other hand, this is a result of parking expansion on the street, i.e. parking areas along the main roads.

The Municipality of Ulaanbaatar is currently managing about 112 parking lots (with a total area of nearly 21 hectares) only to meet more than 6 thousands car. Out of these mentioned parking areas above, the majority of 80% are on street parking areas, and remaining 20 % are off-street parking areas. Number of illegal parkers has increased in recent years.

The purpose of the Thesis willing to take is strengthening effectiveness of parking in Ulaanbaatar city. Due to the above-mentioned points, the major objectives of this study for parking are:

1. To understand the characteristic of Parker, questions that are provided are When, Where, Why do people park?
2. To identify existing demand for parking space of off-street parking area
3. To set up proper parking establishment to reduce parking problems

2. Parking Behavior Study

The interview survey and observation survey was conducted along Peace avenue at Central Business District in core areas are Office building parking area (OBPA), Shopping building parking area(SBPA), and Office and Shopping building parking area (O&SBPA) to answer these questions.

- Interview People has vehicle parked around survey area by ask directly
- Counting number of entering and existing vehicles was conducted at parking lots. Technique is when a vehicle enters or exists, a line will be marked in form that was prepared and total will be recorded every 2 hours.

2.1 Discussion

➢ *Purpose of parking:* Most of drivers used parking for going to work, business engagements and for shopping and marketing as the percentage for such purposes were 28%, 25% and 27%.

Table-1 Respondent Trip Purpose

Purpose	OBPA	SBPA	O&SBPA	Total no. of vehicles	Percent
	No. of vehicles				
Going to work	**19**	**6**	**17**	**42**	28
Business engagement	**25**	**4**	**9**	**38**	25
Shopping	**2**	**27**	**12**	**41**	27
School	**-**	**3**	**4**	**7**	5
Goods delivery	**3**	**8**	**6**	**17**	12
Others	**1**	**2**	**2**	**5**	3
TOTAL	50	50	50	150	100

➢ *Priority choosing:* Almost drivers interviewed want to park near destination.

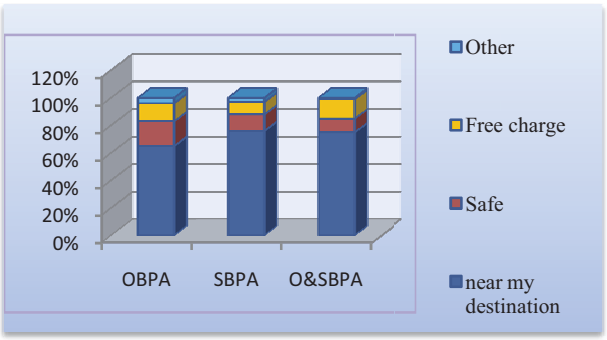

Figure-2 Priority choosing when park vehicles

According to response, almost people (71%) want to park near destination.

➢ *Parking duration:* The duration of parking differs by the purposes of parking of selected areas.

Table-2 Parking Duration by Purpose

Duration of parking	Work	Business engagement	Shop	School	Goods delivery	Other
Less than 30 min.	-	**3** 7.9%	**2** 4.9%	**2** 28.6 %	**4** 23.5%	-
31 min. to 1 hr.	**3** 7.1%	**4** 10.5%	**15** 36.6%	**5** 71.4 %	**12** 70.6%	**3** 60%
1 hr. to 3 hr.	**15** 35.7%	**11** 28.9%	**24** 58.5%	-	**1** 5.9%	**2** 40%
3 hr. to 5 hr.	**7** 16.6%	**18** 47.4%	-	-	-	-
5 hr. to 8 hr.	**14** 33.3%	**2** 5.3%	-	-	-	-
8 hr. onward	**3** 7.1%	-	-	-	-	-
Total	**42** 100%	**38** 100%	**41** 100%	**7** 100%	**17** 100%	**5** 100%

If the purposes are related to business matters, the duration of parking tends to be longer than in the case of shopping and delivering of goods.

➢ *The distance from Parking space to the destination:* About 80% of the drivers interviewed walk between 100 m to 300 m to their destination. It can be concluded that these drivers are willing to walk the distance 300 m radius from the parking area.

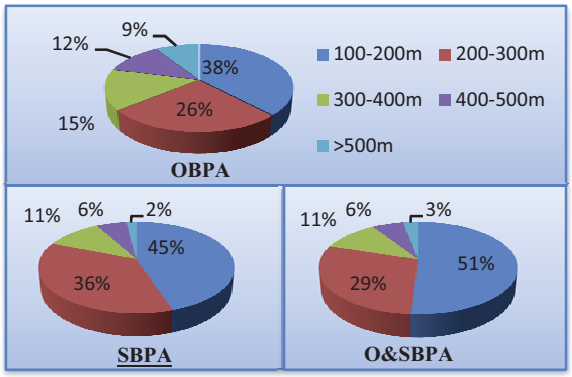

Figure-2 The distance from parking space to the destination.

So, Government should consider to the distance from parking to their service are when has plan to construct public parking. If distance is so far, people do not want to use it.

2.2 Occupancy study

Occupancy is important aspect of parking because it helps us to understand the dynamic of how parking demand fluctuates throughout the day. Motorists, in general, perceive on-street and off-street spaces with occupancies greater than 85% to be at capacity, depending on the overall capacity of the parking area. Parking is perceived as being full when the 85% occupancy is reached.

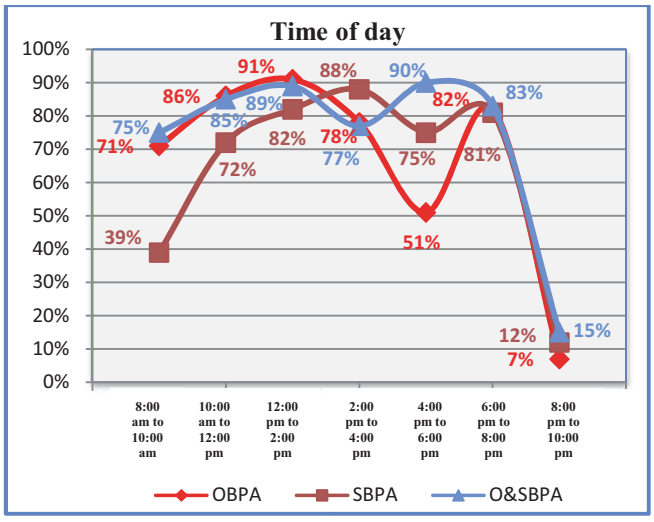

Figure-3 Parking Land Use Type Comparison

Figure-4 shows graphically overall daytime (noon to 2:00pm) and nighttime (4:00p.m to 6:00p.m) peak occupancy for selected areas. The occupancy for the remainder of the evening went down. Levels of occupancy are less than 91% of selected areas when see the result, but demand was very high in parking lots as observation on site. It is available to increase up to 100% in the case of level of service for parking, parking pavement marking and its information system. It means

efficiency of parking is raised. Occupancy is an important point to consider regarding the parking supply and demand

3. Parking demand analysis

The demand for parking is related to the type and level of activity, the mobility of the community, and the cultural attractiveness of the region. Parking demand is defined as the number of spaces that should be that should be provided to serve a particular land use.

3.1 Parking generation rate

Parking generation rates used to calculate parking demand for each building in the study area. These ratios are assigned according to the type of use present in the buildings. Parking generation rate was calculated from parking requirement and gross floor area by land use type. According to experience, regard to buildings have small area, the best way is use public parking. In fact of Ulaanbaatar, many building and new urban are required that have to have parking but they still contravene it, do not construct parking. So it is required to apply standards for parking requirements for existing and new buildings.

Parking requirements standard is in place in developed and as well as in developing countries, however, compliance and implementation of these standards differ due to economics, population density and other factors that exist in these cities. I have studied parking requirements of Asian cities and several cities of USA and Australia, in which all buildings are required to provide parking in order to obtain an appropriate parking generation rate for Ulaanbaatar city. After made comparison of key data (urban density, number of car ownership, GDP, and public transportation condition) above mentioned cities especially Asian cities, then parking generation rate was selected.
The parking requirements are based on gross floor area.

Table-3 Recommended parking generation rate by land use

Land Use	Parking generation rate (Stalls per 100 S.M of GFA)
Dwelling: single-family detached & duplex	1 .0 (per unit)
Dwelling: multi-family	2 .0 (per unit)
Banks and Financial Institutions	0.8
Automotive sales, service and repair business	0.5
Medical, Dental and Optical Clinics	0.6
Restaurants, cafes, bars, taverns and night clubs	0.3
Motels, hotels, bed and breakfast establishments	1.0 (each lodging room)
Business and Professional Offices	1.2
Retail stores and Service uses	1.1
Libraries, art galleries and museums	0.2
Schools – Elementary and Junior high schools	1 .0 (each classroom)
Schools – Vocational and college	1.0 (each ten students)
Churches	1.0 (each five seats)

Sources: Viet Nam National Standards TCVN 4601: 1988 'Office building standard', TCVN 4391: 2009, Government of the Philippines. The national building code and its implementing rules and regulations. Presidential Decree No. 1096 (1977 revised 2004).

3.2 Parking demand estimation

This analysis aims to demonstrate the balance of the existing parking demand/supply using the selected areas. Parking demand is estimated on the basis of person-trips or vehicle-trips; it is generally converted to a ratio of spaces per unit of land use, so that the generation rate can be converted to standards of parking requirements.

In order to calculate the Parking demand, it is needed to have the total floor area data. During the site study, total gross floor area of each building of selected study areas was defined.
Then, the parking generation rate was applied to total floor area to get parking demand.

$$PDid = TFAi \times PDRi \quad \ldots\ldots\ldots\ldots (1)$$

Where:

PDid: Parking demand by land use type i in zone d
TFAid: Total floor area by land use type i in zone (m^2)
PDRi: Parking generating rate by land use type I ($space/100m^{2)}$

After calculating, the result is as follows:

Table-4. Balance between Existing Supply and Demand

Land use type	Parking generating rate (100 m^2GFA)	Total floor area (m^2)	Required spaces Demand	Existing parking supply	Differences (Supply vs. Demand)	
					Space	(%)
OBPA	1.2	**12880**	**155**	**73**	**82**	**-53**
SBPA	1.1	**16720**	**184**	**107**	**77**	**-42**
O&SBPA	1.1	**17412**	**192**	**94**	**98**	**-51**

Table-4 indicates that parking spaces for the sample areas are not sufficient, more specifically demand level almost doubles its supply level.
After analysis, the assumption of parking area for each types of parking as follows:

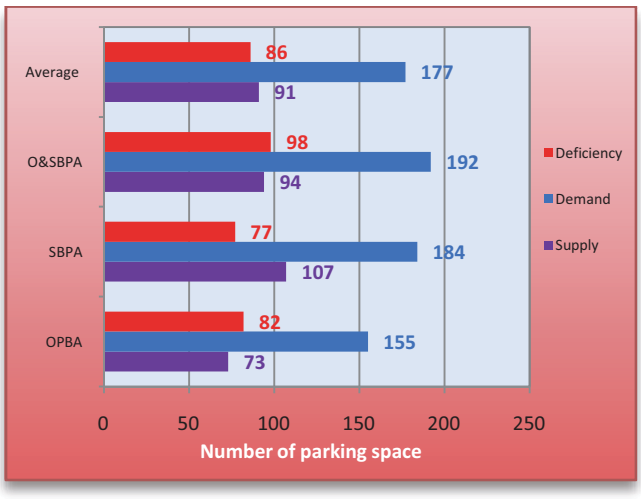

Figure-5 Gap between Demand and Supply

Given the occupancy study and demand calculation results, it is clear to see that parking lots in central Ulaanbaatar are extremely overloaded. For example, occupancy of study areas is over 85 percent and demand exceeds its supply at larger scale all selected parking lots.

From two points: 1/. The gap between supply and demand is very different in selected parking areas. 2/. Public parking supply is being increased from 2002 but not much (now, public parking is limited and investment for parking projects is very deficiency compare to number of increased vehicle). Then, guesstimate that shortage is from increase demand of old buildings (cause from the increasing of cars) and demand of new buildings under the cut-off line.

So, Government needs to have preferential policy to encourage investors to increase public off-street parking supply.

One rule was found out to reduce parking spaces that may be useful for parking system in Ulaanbaatar. That is shared parking. Shared parking means that parking spaces shared by more than one user, which allows parking facilities to be used more efficiently. From the survey, it is found that there is different peak demand between different land uses, so number of parking requirement can be reduced.

4. Conceptual Design

Conceptual design consists of preliminary site plans and floor plans that identify various alternatives for the basic components of parking structure. The goal is seek an opportunity to widen or restructure of existing parking lots will be discussed which allows to choose the best outcome of all possible alternatives and to plan in accordance with parking standards. It creates an opportunity to drivers to park conveniently. In this case, conceptual design is applied to O&SBPA, one of the three selected areas in this study and matrix analysis was conducted. In terms of parking lots where there is no possibility to expand its size or where the building density is high, it is appropriate to build parking lots nearby. In this case, parking behavior analysis should be considered for determining new parking lots. Conceptual design also covers numbers and sizes of geometric parking are directly dependent from parking demand.

5. Conclusion

The actual behavior of parkers to choose a parking location is mainly influenced by trip purpose, walking distance and availability of parking space. The main potential factors that influence the preference of parkers a parking location choice are security, comfort ability, availability of parking space and closeness of parking place to their destination. Drivers are only willing to walk not more than 300m.

In general, driver's opinion about parking facility in the Central Business District of Ulaanbaatar is relatively not so good. Example: not easy to maneuver, security is not so reliable, and incomprehensible pavement marking of parking lot. It is needed to develop level of service standards for parking facilities.

Government should consider to the distance from parking to their service are when has plan to construct public parking. If distance is so far, people do not want to use it. The government can control the number of on-road parkers by parking fee and spaces to decrease the traffic congestion

The parking demand continues to increase while supply cannot keep with demand because of limiting land and investment fund.

To apply the parking requirement standard in Ulaanbaatar, the parking space required for buildings in Central Business District.

The gap cause from the public parking is not enough to cover all parking for old building and new buildings that under the cut-off line. So it is better to provide more public off-street parking in Ulaanbaatar city.

6. References:

JICA team, 1979. Technical report: Urban Transport Study in Greater Metropolitan Areas of Georgetown, Bukit Mertajam Malaysia.

Wells & Associates, LLC. 2003. Parking demand analysis for Washington Adventist Hospital

Donal Shoup, 2006. The practice of Parking Requirements, Zoning Practice, American Planning Association.

Michael Manville, Donal Shoup, 2005. Parking, People, and Cities, Journal of Urban Planning and Development. pp. 233-245

So Morikawa, Kohei Asao, Takahiro Igo. Institutional System and Current Problems of Car Parking in Tokyo, Japan, 2009

Urban Land Institute, 2010. Dimensions of Parking 5th edition

K.J Button &D.A. Hensher. Handbook of Transport Systems and Traffic control, Volume 3. 2004

Asian Development Bank, 2010. Parking Policy in Asian Cities

Rich and Associates, Inc. 2008. Parking Study

JICA team, Ministry of Road, Transport, Construction and Urban Development, ALMEC Corporation, Aero Asahi Corporation 2009. Final report: The study on Master Plan and Urban Development Program of Ulaanbaatar city

Xiuyuan Zhang, Yaming Shao, 2005. Parking demand in the High Tech Business District of Urban. Transportation study Vol. 5 pp 891-899

Common Council, 2007. Middleton, Wisconsin, USA. Off-street parking areas specifications and standards.

INFLUENCE OF THE IONS IN PORE SOLUTION AND AROUND THE STEEL BAR ON CORROSION OF STEEL IN BFS AND FA MORTARS

Student Number: 09M51620 Name: Anita II Alvarez ODCHIMAR Supervisor: Nobuaki OTSUKI

This research investigates the steel corrosion behavior in mortars with 40% blast furnace slag (BFS) cement replacement and 20% fly ash (FA) cement replacement to ordinary Portland cement (OPC), considering the concentrations of chloride and other ions present in pore solution and around the steel bar. Three methods were used to extract solutions wherefrom ions were measured. Results show that steel corrosion activity is lower for FA specimens than BFS specimens, both having better corrosion performances than OPC specimens. Correspondingly, Cl^- contents in all extracted solutions follow the trend OPC>BFS>FA specimens. The Cl^-/OH^- contents in the solutions obtained from around the steel bar correspond to the specimens' corrosion behavior, signifying the influences of Cl^- and OH^- on corrosion and the greater importance of investigating the ions around the bar than that in the pore solutions. In addition, concentrations of Na^+, K^+, Ca^{2+}, Si^{4+}, Al^{3+}, Mg^{2+}, Mn^{3+}, Ti^{4+}, Fe^{3+} and P^{5+} ions were investigated from the extracted solutions.

1. Introduction

Blended cements such as BFS and FA are now in popular use. Their production has even exceeded that of ordinary Portland cement in Asia and Europe. The popularity owes to the benefits in economy as well as in the environment, from reduction in wastes to reduction in CO_2 emissions. Despite these, there is still no general agreement in their performances with regard to corrosion of embedded steel bars. Reinforcing bar corrosion is the most common durability problem that concrete structures are facing. Some studies reported that the partial substitution of BFS and FA to OPC improves resistance to corrosion, while still others reported otherwise [1].

Chlorides are considered the major culprit for reinforcing bar corrosion. But in literatures, there is inconclusive data about chloride threshold value (C_{crit}) – the Cl^- content that initiates steel depassivation – and this is attributed to the unsuitability of the experimental procedures used, one of which is the method of extracting pore solutions wherefrom free chloride contents are measured. The existing methods extract the pore solutions from the bulk concrete, though some studies showed that the microstructure of the steel-paste interface differs from the bulk mortar [2]; thus the free Cl^- measured from pore solutions may not be indicative of the actual content affecting the steel. Moreover, Ghods et. al. reported that other ions aside from Cl^- also affect the steel's protective passive oxide film [3].

In the pursuit to eliminate these gaps in the research field, this present study aims to fulfill the following objectives: First, to investigate the corrosion behavior of steel in BFS and FA mortars. Second, to investigate the ion concentration in the pore solutions of the bulk mortar through "pore water expression" and "water-soluble leaching", and around the steel bar through a method of "washing the bar" developed by Nagataki (1993). Taking these ions as bases, this research also aims to obtain the correlation between the solution extraction methods, and the influences of the ion concentrations on steel corrosion behavior.

2. Experiment Details

2.1 Materials used

Mortar specimens have the configuration of ø50x100mm. Three types of binders were used: (a) 100% OPC, (b) OPC + 40% BFS replacement, (c) OPC + 20% FA replacement. Distilled water and natural river sand were used in the mix. Reinforcements were ø9x50mm SD295A Ordinary Carbon Steels.

2.2 Mixing, curing and exposure condition

The water/cement and sand/binder were 0.55 and 2.0, respectively. Cl^- were internally added during the mixing with amounts of 0, 0.5, 1.0 and 2.0% per binder weight. Table 1 shows the details of mix proportions. Specimens were moist cured in the molds for 24 hours using wet burlaps. After, they were submerged in distilled water at 20°C for the whole 3-month exposure duration.

Table 1.1: Mix proportions

Specimen Label	Binder ratio	Unit Weight (kg/m^3)					
		Water	OPC	FA	BFS	Sand	Cl^- (0, 0.5, 1.0, 2.0%)
OPC	100% OPC	337.46	613.57	-	-	1227.13	0, 3.07, 6.14, 12.27
FA	OPC:FA 80:20	333.23	484.70	121.17	-	1211.74	0, 3.03, 6.06, 12.12
BFS	OPC:BFS 60:40	334.36	364.76	-	243.17	1215.86	0, 3.04, 6.08, 12.16

2.3 Methods of Corrosion Monitoring

a. Corrosion current density, i_{corr}

Steel corrosion activity can be deduced from i_{corr}. High i_{corr} means high corrosion activity. I_{corr} was measured at certain intervals within the 3-month exposure using alternating current (AC) impedance technique.

b. Steel passivity

Passivity was interpreted from anodic polarization curves obtain from a technique of the same name, and graded based on a system developed by Otsuki et. al. Grade of 5 means excellent passivity and 0 means no passivity [4].

2.4 Methods of solution extraction

a. Pore water expression (PWE)

Pore solutions were squeezed out from the cylindrical mortar specimens by the application of 250MPa to a steel apparatus which contains the specimens (Barneyback, 1981).

b. Water soluble leaching (WS)

The method complies with JCI SC4 where mortar powder is digested in water for 30 minutes at 50°C. The leached solution contains the water-soluble chlorides which approximate the free chlorides in the pore solution.

c. Washing of Bar method by Nagataki et. al.[4]

This is a relatively new method which employs the simple procedure of washing of bar as shown below.

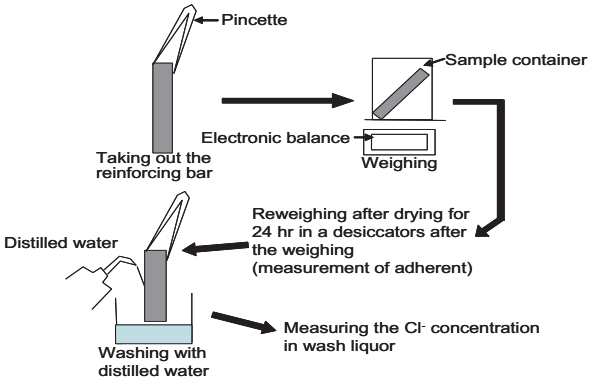

Figure 2.1: Extraction of Solution around the Bar

2.5 Methods of measuring ion concentrations

The following were used: Ion chromatography for Cl^-, pH meter for OH^-, and Induced Coupled Plasma (ICP) for the other ions.

2.6 Methods for investigating the properties of mortar and cement hydration products

Friedel's salt peak, indicative of the chloride-binding capacity of cement hydration products, was investigated through X-ray diffraction. Oxygen permeability was calculated from limited current measured through Cathodic Polarization technique.

3. Results and Discussion

3.1 Corrosion behavior

a. Corrosion current density

Low corrosion current density for FA and BFS mortars were measured for all amounts of Cl^- additions. OPC mortars with 2.0% Cl^- exhibited abrupt increase in corrosion activity (see Figure 3.2). For high Cl^- additions of 1.0 and 2.0%, corrosion current density is highest for OPC specimens, followed by BFS, and lowest for FA specimens (see graphs below).

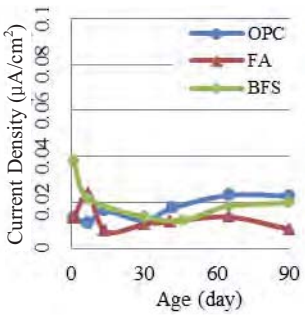

Figure 3.1: With 1.0% Cl^-

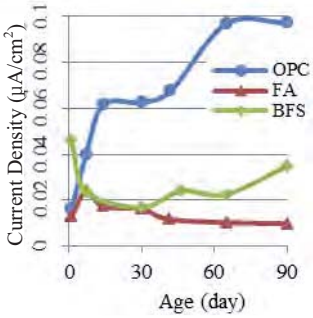

Figure 3.2: With 2.0% Cl^-

b. Steel passivity

Steel passivity results are in good agreement with that of i_{corr}. Only OPC specimens with 2.0% Cl^- exhibited significant steel depassivation, with very low passivity grade of 1 (see Table 3.1)

Table 3.1: Passivity Grades of Specimens

	Cl^- content (per weight of binder)			
	0%	0.5%	1.0%	2.0%
OPC	3	2	3	1
FA	3	3	3	3
BFS	3	3	3	3

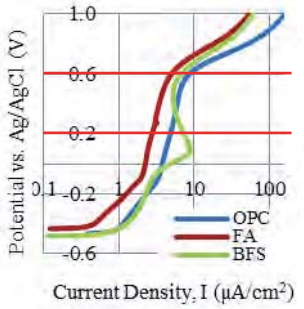

Figure 3.3: With 1.0% Cl^-

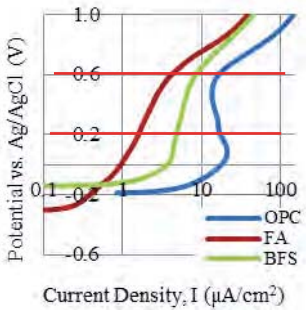

Figure 3.4: With 2.0% Cl^-

For high Cl^- additions of 1.0 and 2.0%, the specimens follow the same trend of anodic polarization curves. In Figures 3.3 and 3.4, OPC specimens exhibited the highest current densities between 0.2-0.6V, followed by BFS, then FA mortars. This trend is indicative of the magnitude of steel depassivation: OPC>BFS>FA specimens.

3.2 Free chloride content and chloride binding capacity

Figures 3.5 and 3.6 show the free Cl^- and Friedel's salt contents measured after 3 months of curing. Significant differences in free Cl^- contents were exhibited by specimens with 2.0% Cl^-, following the trend OPC>BFS>FA. This corresponds to the consistent trend in Friedel's salt contents, which is FA>BFS>OPC. This shows that the high chloride binding capacity of cement hydration products of FA mortars resulted to the presence of low free Cl^- in their pore solutions. Though free Cl^- of specimens with 0.5% Cl^- do not correspond to Friedel's salt contents, variations in free Cl^- measured are too small to be significant. High capacity of BFS hydration products to adsorb Cl^- may be responsible for their low free Cl^- content in this case.

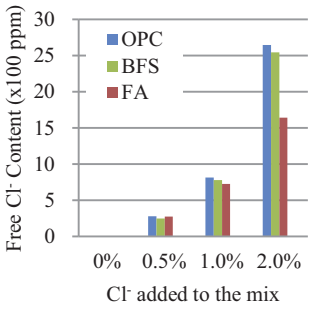

Fig. 3.5: Free Cl^- contents

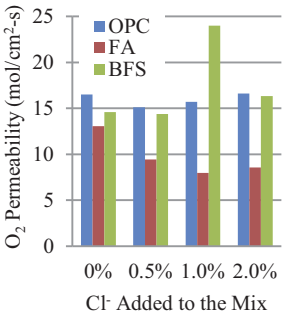

Figure 3.7: O_2 Permeability

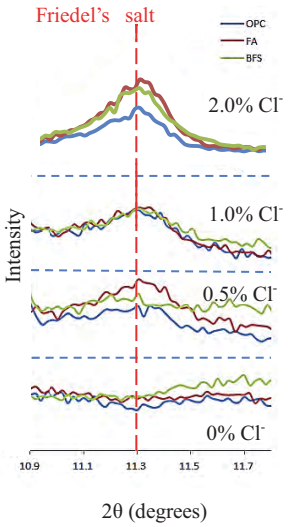

Fig. 3.6: Friedel's salt peaks

3.3 Oxygen permeability

Oxygen is necessary in the corrosion reaction. With not enough supply of oxygen at the level of the steel, corrosion will not proceed. FA mortars have the highest impermeability to oxygen (see Figure 3.7) which is a big contributing factor to their superior performance against reinforcement corrosion as presented in Section 3.1.

3.4 Ions detected from the pore solutions and their relation to corrosion behavior

At age 1 month of the specimens, solutions from the pores and around the steel bar were extracted using the methods presented in Section 2.4. The following are the ions measured from the said solutions:

a. Chloride ions

From Figure 3.8 with concentrations from PWE method as the basis, WS method measured lower free Cl^- contents with an average factor of 0.6392. While "washing of bar" method measured higher Cl^- contents with average factor of 2.8048. This indicates that higher concentrations of free Cl^- is found around the steel bar than in the bulk mortar, which is due to the difference in the microstructure composition between the two regions in the mortar.

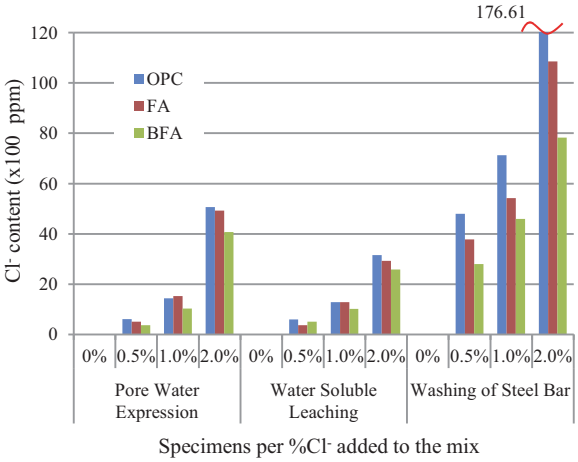

Figure 3.8: Cl^- contents vs. Method of Solution Extraction

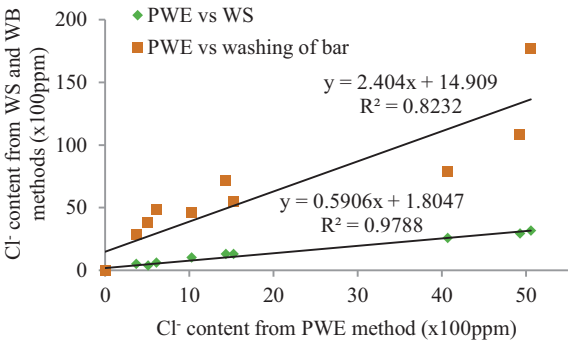

Figure 3.9: Correlation of the methods based on Cl^- contents vs. Method of Solution Extraction

Moreover, WS has a good correlation with PWE with coefficient of determination of 0.9788, while "washing of bar" method has lower correlation with PWE with R^2 of 0.8232 (see Figure 3.9).

b. Other ions

Concentrations of OH^-, Na^+, K^+, Ca^{2+}, Si^{4+}, Al^{3+}, Mg^{2+}, Mn^{3+}, Ti^{4+}, Fe^{3+} and P^{5+} were detected from the extracted solutions. As in Cl^- concentrations, ion concentrations measured from WS are lower and in good correlation with those of PWE, with R^2=0.9343 (Fig 3.10). While concentrations from "washing of bar methods showed poor correlation with those of PWE, with R^2=0.01(Fig. 3.11). This validates the differences in microstructure and cement hydration products between the bulk mortar and the steel-paste interface.

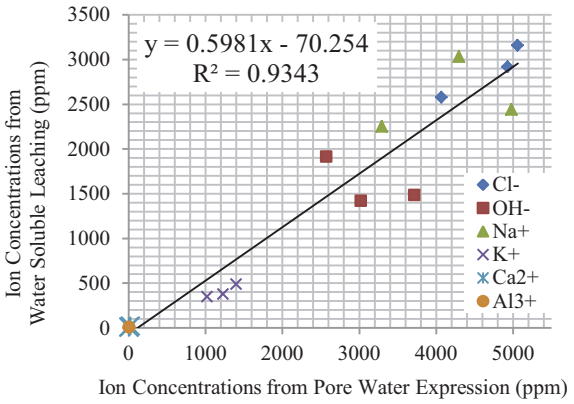

Figure 3.10 Pore water expression versus Water soluble leaching based on all ions

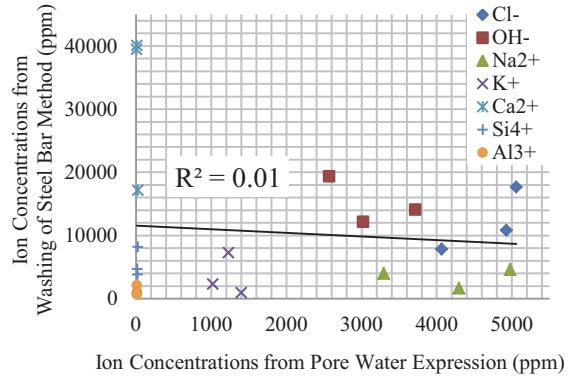

Figure 3.11: Pore water expression versus Washing of bar method based on all ions

c. Influence of ions on corrosion behavior

Correlation to rebar corrosion behavior is based on data measured during age 1 month of specimens. In general from Figure 3.8, OPC specimens has the most free Cl^- thus steel corrosion activity in these mortars are higher, as indicated by the apparent high corrosion current density at age 30 days of OPC-2.0% specimens (Figure 3.2). No general relation to corrosion was deduced from the concentrations of other ions except for that of OH^- measured from around the steel bar. Compared to OPC, FA and BFS mortars have lower OH^- contents around the steel, and the Cl^-/OH^- measured from "washing of bar" (WB) method corresponds to corrosion current density i_{corr}, with OPC having both i_{corr} and Cl^-/OH higher than the other specimens (Figure 3.12).

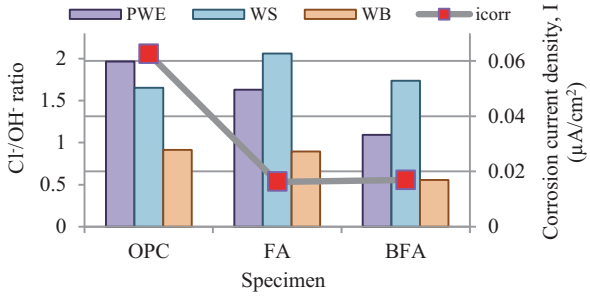

Figure 3.12: Cl^-/OH^- versus I_{corr}

Effective passivation of the steel's protective oxide film is obtained with high enough OH^- concentration around the steel. Though Ghods et al reported that pH might not be a determining factor for film quality [3], this present finding signifies that OH^- does affect the corrosion behavior, and that the ion concentrations around the bar are more indicative of corrosion behavior than those of the pore solutions in the bulk mortar.

4. Conclusions

The corrosion behaviors of steel in BFS and FA mortars, as well as the ions in the pore solutions and around the steel bar were investigated in this research. The following are the conclusions:

1. Mortars with blended cements BFS and FA have better steel corrosion performances than mortars with pure OPC.

   Superior steel corrosion performance of FA mortars is attributed to their high chloride binding capacity and low oxygen permeability. While, better corrosion resistance of BFS is contributed by their better chloride binding capacity than OPC mortars

2. Cl^- concentrations influence the corrosion behavior, as well as the OH^- concentrations measured in the solutions obtained from around the steel bar. More free Cl^- were measured from around the bar than from the pore solutions in the bulk mortar. Moreover, FA and BFS mortars have lower OH^- contents around the bar, with Cl^-/OH^- in agreement with corrosion activity. Relation to corrosion behavior of other ions cannot be deduced from the results of this research.

   Methods that extract the pore solutions from the bulk mortar (PWE and WS) have good correlation with each other. While the "washing of bar" method that extracts the solution from around the bar has poor correlation with PWE. This signifies that the microstructure composition in the steel-paste interface is likely different than in the bulk mortar, and the ion concentrations from around the bar are more significant to steel corrosion.

References

[1] U. Angst, B. Elsener, et. al., *Critical chloride content in reinforced concrete –A review*, Cement and Concrete Research, Vol. 39, pp. 1112-1138, 2009.

[2] L. Yue, et.al.,*The microstructure of the interfacial zone between steel and cement paste*, Cem. & Conc. Res.,Vol. 31, pp. 385-388.

[3] P. Ghods, O.B. Isgor, G. McRae and T. Miller, *The effect of concrete pore solution composition on the quality of passive oxide films on black steel reinforcement*, Cement and Concrete Research, Vol. 31, pp. 2-11, 2009.

[4] N. Otsuki, S. Nagataki et. al., *Evaluation of $AgNO_3$ solution spray method for measurement of chloride penetration into hardened cementitious matrix materials,* ACI Materials Journal, Vol. 89, pp.587-592, 1992.

LAND READJUSTMENT AND APPRAISAL IN GER AREA OF ULAANBAATAR CITY

Student Number: 09M51637 Name: Purevdorj ENKHMANDAKH Supervisor: Shinya HANAOKA

ウランバートル市ゲル地区における土地区画整理手法の適用と評価

プレブドルジ エンフマンダフ

This study proposes a land readjustment technique in to the Ger area of Ulaanbaatar city in which aims to convert disorderly allocated land parcels into suitable forms of development lots for public and private use accordance with city planning requirements. Thus, land value assessment and replotting methodologies are examined in the one of the urban fringe areas by case study.

1. Introduction

The importance of introducing land readjustment technique in to urban land use planning field has been emphasized for past years in Mongolia.

Mongolia shifted to a market-oriented economy at the beginning of 1990s. Because of the transition from a centrally planned economy to a market-oriented one and the private ownership of land used to be officially recognized and also Ger area, mostly traditional dwelling (Ger) and single storey houses surrounded with fences that situated in suburbs, is dramatically increased by the free migration from rural to urban as shown in Figure 1, in which strongly influence to environmental degradation such as air pollution, soil erosion and insanitary condition in Ulaanbaatar city over the past two decades.

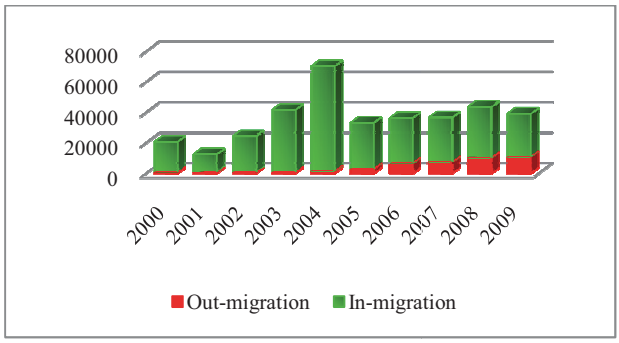

Figure 1. In and out migration of Ulaanbaatar

The significance to apply land readjustment methodology is to promote appropriate land use in urban fringe area that would be advantageous both for support to increase land use efficiency and to limit disorderly urban sprawl. There are two main objectives of this study. The first objective is to assess the land value of before and after the planning.

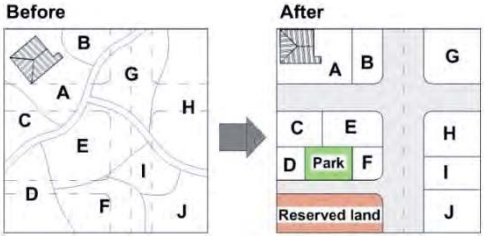

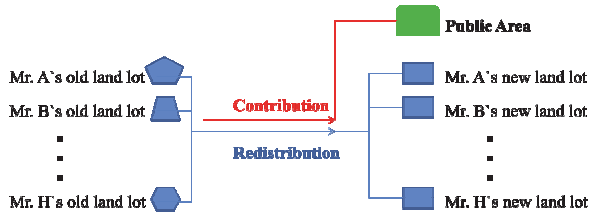

Figure 2. Land readjustment concept

The second objective is to determine readjusted land area and contribution ratio of landowners which would be described in replotting design.

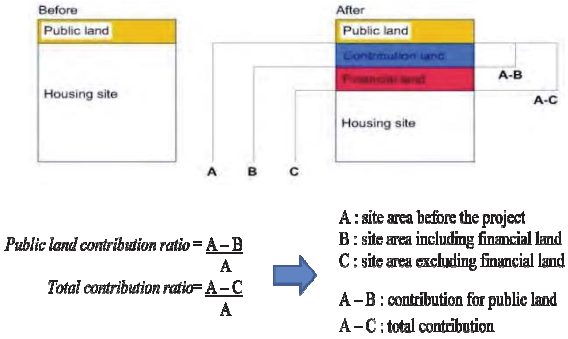

Figure 3. Contribution ratio

2. Questionnaire survey

Further questionnaire survey of the case study area is provided accordingly. Main purpose of questionnaire survey is focused more on to identify Ger area residents` perceptions of needs for basic infrastructure and willingness of improvements of the living environment. The survey of the study area clarifies opportunities and willingness to improve the living environment of the Ger area development, and the top priorities that the Ger area residents themselves have identified.

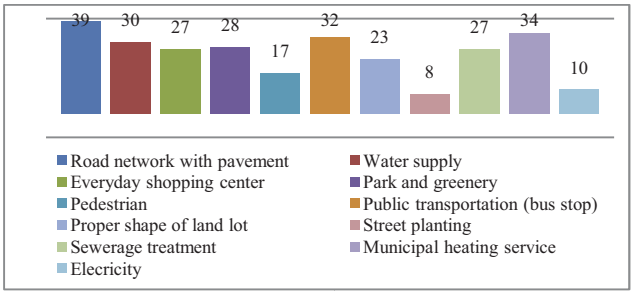

Figure 4. Important issues for improvement of living environment

Most of the respondents expressed a participation of Land readjustment project, and desire to stay after the implementation, if living environment improved. Among Ger area respondents, air pollution, solid waste and insanitary condition were the highest priority problems. Large scale investment in infrastructure, such as paved community road, pedestrian, park-greenery, water supply, sewerage treatment and municipal heating service were areas that the public reported should be improved a focus of public private partnership efforts.

3. Urban renewal design

A district plan consists of the vision statement and the district improvement plan that includes the location of community access roads, small parks and provision of public utilities.

The main vision of layout planning in the case study area will be comfortable and convenient residential area where residents will enjoy physical improvement of living environment. To achieve this vision, the case study area is planned as a layout planning according to Mongolian Norms and Ordinance of Building and City Planning.

Figure 5. Layout planning of the case study area

In the case study area, big trunk road is planned and approved by Municipality. Hence, the case study area is divided into two main zones that on the south side commercial area which is along the trunk road and on the north side residential zone.

Access road connections would improve travel within the community. Improved community road connectivity would also make get to the suburbs or downtown areas, supporting revitalization efforts. According to City planning standard, community access roads are planned two-way with 2 lanes that each has 3 meters wide in the case study area. Also it has 1.5 meters wide sidewalks and street planting along with in these access roads.

Moreover, residential zone park is planned in the case study area. Residential zone park area is 3044 m^2 or 4.5% of total planning area and per capita of green area is 8.5 m^2.

4. The concept of land appraisal

4.1 Basic idea of land appraisal

Land appraisal in land readjustment projects lies on measuring how residential land usage values change from before to after project implementation, in the other hand, measuring the rate of residential usage value increase.

Among the land appraisal methods of calculating land valuations for the land readjustment project, the road side value method is currently the most commonly used. This method presumes a standard frontage along a road and a shape for the residential land, derives a value per unit land area, and applies this to the roadway to obtain the road side value. Based on the road side value, corrections are made to calculate the final value, based on positioning with respect to the road, landscape, usage and other factors. Further, land valuation for the land readjustment project is not intended to be used for land transactions, but for uniformly measuring the mutual balance based on residential land usage.

Therefore, the road side value represents the usage value and utility of residential land, expressing this as the fundamental value set by area based on what the land in the area is to be used for and its maturity as urban land added to the value arising from functionality of facilities and their utilization. In the other hand, it is the sum of the road coefficient, the accessibility coefficient, the land coefficient, and the utility coefficient.

The road side value is expressed by the following equation.

Road side value = Street coefficient + Access coefficient + Land coefficient + Utility coefficient

$$= [(w-3)/w+\sum X] + [m\times(S-s)/(S-R)] + (Shape + LUT + legal) + (Elect+ Heat+ Water+ Sew) \quad (1)$$

Where: $F(W) = (w-3)/w+\sum X$ is a street coefficient,

$A = m\times(S-s)/(S-R)$ is access coefficient,

$L = Shape + LUT + legal$ is a land coefficient,

$U = Elect+ Heat+ Water+ Sew$ is utility coefficient.

4.2 Street coefficient

The street coefficient expresses the usage value originating only from the road that borders the land plot, given by the following equation.

$$F(W) = (w-3)/w+\sum X \quad (2)$$

Where: ***F(W)*** is road coefficient, ***w*** is road width, ***3*** is road shoulder and ***X*** is a road utility (pavement, pedestrian, street planting, etc.)

The F(W) equation has the following characteristics, first of all, F(W) increases as the road width W increases, reflecting the higher usage values of land plots along wide roads compared with these along narrow roads.

Secondly, increasing road widths boost the usage values of properties along narrow roads significantly, but have a comparatively smaller effect on wide roads. In other words, the rate of increase of F(W) gradually declines as W increases (Figure 6).

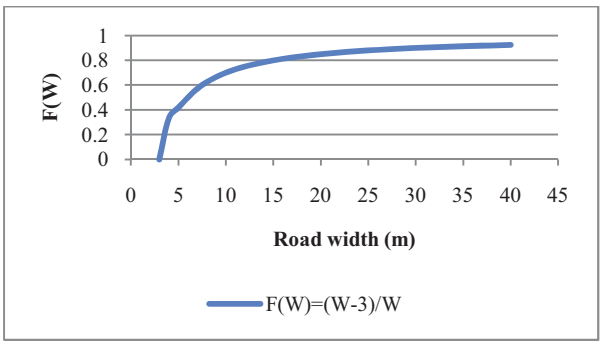

Figure 6. Street and road coefficient

4.3 Access coefficient

The access coefficient expresses the value of benefits arising from relative distance of a land plot to existing public and other facilities, as given by the following equation.

$$A = m \times (S-s)/(S-R) \quad (s \geq R)$$
$$A = 1 \quad (s < R) \qquad (3)$$

Where: ***A*** is the access coefficient, ***m*** is expressing the magnitude of the value of benefit arising from the relevant facilities, ***S*** is limit of the distance influence, ***R*** is constant distance (limit of distance for which ***m*** does not decrease but stays constant) and ***s*** is distance between land parcel and relevant facilities.

In urban areas, various city facilities are maintained to support land usage, and land use is predicated upon the usage of these city facilities. Therefore, the usage value of residential land is subject to differences based on the level of convenience afforded by using these city facilities. The access coefficient expresses such differences in the influences on usage value from various facilities.

4.4 Land coefficient

The land coefficient expresses the value arising from the usage status, legal rights, and physical condition of the land plot itself, given by the following equation.

$$L = Shape + LUT + legal \qquad (4)$$

Where: ***L*** is a land coefficient, ***Shape*** is a land parcel`s shape (regular or irregular), ***LUT*** is a land use type (commerce, residence), and legal is a legal rights` status of the land (ownership, possession, and usage).

4.5 Utility coefficient

The utility coefficient expresses the value arising from provision of public utility services such as water supply, sewerage treatment, electricity and municipal heating service in the project area, given by the following equation.

$$U = Elect + Heat + Water + Sew \qquad (5)$$

Where: ***U*** is utility coefficient, ***Elect*** is connection for central electricity network, ***Heat*** is provision of municipal heating service, ***Water*** is availability of central water supply system, and ***Sew*** is availability of sewerage treatment.

As a result of questionnaire survey of the case study area, the magnitude of the value of benefit arising from the relevant facilities and the highest values of land valuation indicators are defined as shown in Table 1.

Table 1. The magnitude of the value benefit arising from the relevant facilities

Indicators	Response of questionnaire	Share	Coefficient
Road network with pavement	39	12.4%	1.00
Heating	34	10.8%	0.87
Bus stop	32	10.2%	0.82
Water supply	30	9.6%	0.77
Park	28	8.9%	0.72
Shop	27	8.6%	0.69
Sewage	27	8.6%	0.69
Shape	23	7.3%	0.59
Pedestrian	17	5.4%	0.44
Electricity	10	3.2%	0.26
Street planting	8	2.5%	0.21

In addition, the decreased value of above mentioned indicators is calculated based on land market price survey of GTZ in Ulaanbaatar city which is defined for each indicator that significantly influencing land market price and its calculation is based on comparison between with or without their services of 1 m^2 average land price.

Consequently, the indicators and coefficients of street, access, land, and utility services are shown in below Table 2, which is used in land value assessment of the case study area.

Table 2. Indicators and coefficients of land value assessment

No.	Indicator	Condition	Coefficient
	Street coefficient		
1	Road width	20m over	0.9-1.0
		10-15m	0.7-0.8
		6-9m	0.5-0.6
		Under 6m	0.3-0.4
2	Pavement	Paved	1.00
		No pavement	0.50
3	Pedestrian	Available	0.44
		Unavailable	0.22
4	Street planting	Available	0.21
		Unavailable	0.10
Access coefficient			
5	Kiosk (water distributor)	Under 50m	0.80
		50-150m	0.50
		150-200m	0.10
		200m over	0.00
6	Daily shop	Under 100m	0.70
		100-250m	0.60
		250-500m	0.20
		500m over	0.00
7	Park and greenery	Under 100m	0.70
		100-250m	0.60
		250-500m	0.20
		500m over	0.00
8	Bus stop	Under 100m	0.80
		100-250m	0.70
		250-500m	0.30
		500m over	0.00
Land coefficient			
9	Shape	Regular	0.59
		Irregular	0.29
10	Land use type	Commerce	1.00
		Residence	0.57

11	Legal	Ownership	**1.00**
		Possession	**0.63**
		Usage	**0.35**
		No right	**0.00**
Utility coefficient			
12	Electricity	Available	**0.26**
		Unavailable	**0.13**
13	Heating	Available	**0.87**
		Unavailable	**0.58**
14	Water supply	Available	**0.77**
		Unavailable	**0.54**
15	Sewage	Available	**0.69**
		Unavailable	**0.48**

5. The procedure of land appraisal and replotting

The basic procedure for valuation of readjusted land is to determine the block value before and after the planning as the fundamental value, then calculate increased value with respect to the lot value before and after the planning and define the contribution ratio for the public facilities and reserved land. The principle of correspondence should be applied to replotting design.

Accordingly, the value enhancement is calculated on the basis of land value before and after the planning. Essentially, the following steps are taken for land valuation of case study area. These steps are as follows:

1) Confirm basic condition
2) Block evaluation
3) Calculate value increase
4) Lot evaluation before the planning
5) Lot evaluation after the planning and calculation of land area to be distributed
6) Designing the replotting plan

The replotting design of the case study area is drawn based on land valuation before and after the planning and the readjustment maps of before and after are shown in Figure 7 and 8.

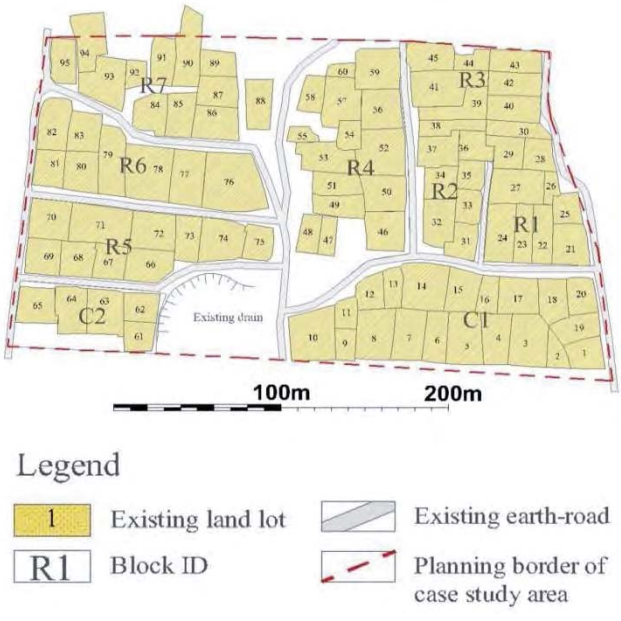

Figure 7. Existing land parcels before the planning

Figure 8. Replotting design map after the planning

6. Conclusion

The land readjustment approach in Ger area might solve problems of the shortcoming of basic infrastructure provision by involving the separated landowners in development, since they acquire the serviced urban land lots and increased value of land despite the area size reduction. In addition, the serviced and regularly shaped urban land lot promotes to the rational land use and its marketability.

Moreover, the local authorities might gain the profit from which they do not need to purchase overall land lots within the implementation zone. Besides, by through land readjustment project, municipality could be able to implement their responsibility of basic infrastructure provision in principal of better urban spaces for residents.

References

[1] Ito. S, "Outline of Land Readjustment Planning Manual in Japan", 1988.

[2] Deutsche Gesellschaft für Technische Zusammenarbeit (GTZ) GmbH in Land management and fiscal cadastre project, "Report on Land Market Price Survey in Ger Area of Ulaanbaatar City", 2009.

[3] JICA. Ministry of Land, Infrastructure and Transport. "Urban Land Use Planning System in Japan", 2007.

[4] Kim Moon Kyo, Tumursukh.Sh, Enkhmandakh.P, "Housing: Problems and Prospects", Ulaanbaatar city, 2007.

[5] JICA, Ministry of Road, Transport, Construction and Urban Development, Ulaanbaatar City Government, "The Study on City Master Plan and Urban Development Program of Ulaanbaatar city", 2009.

[6] Solongo Algaa, "Growth of Internal and International Migration in Mongolia", National University of Mongolia, 2007.

[7] Statistical Yearbook of Capital City 2010.

APPLICABILITY OF HIGH RESOLUTION WRF-ARW AND WEP ON SPATIALLY HETEROGENEOUS URBAN AREAS

Student Number: 09M51643 Name: Alvin Christopher Galang VARQUEZ Supervisor: Manabu KANDA

The performance of a weather forecasting model and hydrologic model was investigated on highly urbanized areas with complex topography and larger watershed, using high spatial and time resolution settings. To determine the contribution of urban parameters, different cases were set for WRF-ARW. With the addition of anthropogenic heat and displacement height static data at Nagoya, simulated localized rainfall distribution was improved but still underestimated the quantity. WRF-ARW was also used to differentiate the weather of Nagoya and Tokyo on summer. WEP was applied at Meguro and Nomikawa, two highly urbanized basins in Tokyo. Side-weir effect was considered. The models' performance details are explained and discussed.

1 Introduction

Urbanization has been growing at an unprecedented rate due to the rapid influx of people and population growth rate with Tokyo being classified with the highest agglomeration throughout the global decade. Urbanization's impact is phenomenal to the environment and has been topics of special issues of scientific journals [1]. Specifically, understanding the dynamics operating in urban environments may be especially important in developing mitigation tools for urban-induced calamities and disasters. In order to acquire at least the mechanisms of urban to basin and urban to mesoscale environment interaction, numerical models have been further improved or developed in terms of spatial and temporal calculation intervals [2].

Among the popular modern numerical models, The National Center for Atmospheric Research's (NCAR) Advanced Research Weather Research and Forecasting Model (WRF-ARW) and Japan's Public Works Research Institute's (PWRI) Water and Energy Transfer Processes Model (WEP) and its application to selected areas in Japan will be the focus of evaluation and application in this study due to its possibility for coupling.

Multiple model improvements and modules have been introduced for WRF. Among the latest are the inclusion of additional surface and urban physics options such as NOAH Land Surface Model (NOAH LSM) and Urban Canopy Model (UCM). These options have been proven to improve WRF simulations' accuracy well [3]. However, UCM provides very simple assumptions for urban parameters like roughness length, displacement height, and anthropogenic heat emission (AHE). As a remedy, available static inputs for displacement height and diurnal AHE information were included in the WRF-ARW simulation of localized rainfalls in Tokyo [4]. The impacts of the scale of available static inputs were not given enough attention. WRF-ARW's inclusion of high resolution AHE and displacement heights was only tested in Tokyo. It was necessary to try it in a smaller city with more complex surroundings.

WEP model has been improved by Kobayashi (2009) and applied at Nomikawa by simulating flows at a point near an observation gauge for verification. Despite this, the model still needed further evaluation at larger basins at similar parameterization to its neighbor Nomikawa. The model was also used to investigate how the channels responded to varying rainfall patterns.

2 Methodology

Fig. 1 summarizes the procedures conducted in this study. Study area for WRF-ARW was selected according to the degree of urbanization, availability of static datasets (for boundary setting), availability of observation data for evaluation, and the surrounding environment. For meteorological simulation, Nagoya city was selected suitable for the study because of its orographic location, and the growing concern for its rapid urbanization. After preparing the input static datasets, AHE and displacement heights, and calibration for WRF-ARW, cases were determined (e.g. varying level of input resolution, sensitivity to AHE, etc.). The cases were then compared with observation data. For hydrologic simulation, Nomikawa and Meguro basins were selected due to its high runoff values at relative rainfall events. Analysis was done in two parts: evaluate the accuracy of the model, and achieve additional knowledge on how urban areas affect meteorological and hydrologic parameters such as rainfall, runoff, sea/mountain breeze, heat flux, and diurnal heat evolution.

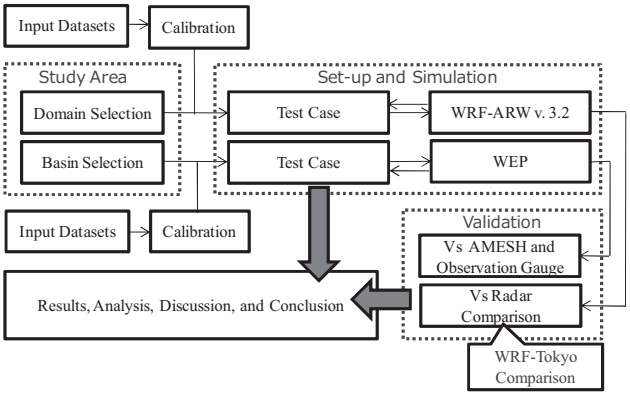

Figure 1: Research Flow

WRF-ARW is the next-generation mesoscale numerical weather prediction model designed to serve both operational forecasting and atmospheric research needs. It had become one of the popular NWP models recently [5].

WEP is a distributed hydrologic model developed to simulate spatially variable water and energy processes in watersheds with complex land covers successfully applied in countries like Japan, China, and Korea.

3 WRF-ARW Model Evaluation

3.1 Simulation Settings

Fig. 2 shows the domains selected. TOK D04 corresponds to the fourth domain in the previous simulation centered at Tokyo. Because of Nagoya's more complex surroundings compared to Tokyo, interaction of urban areas with its surrounding could also be determined. History interval at domain 4 is 10 minutes.

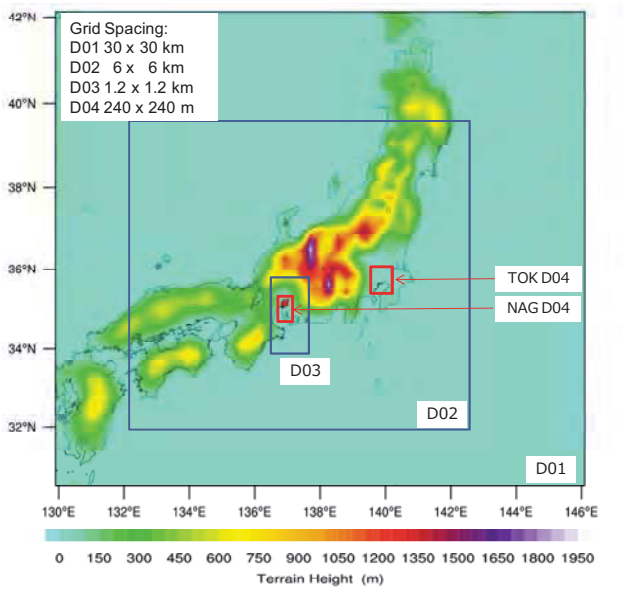

Figure 2: WRF Nagoya Domains

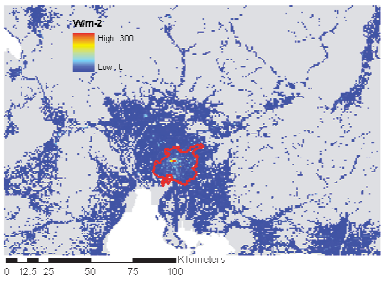

Figure 3: August 12-- JST 10-s AHE in rainbow color palette

Table 1: WRF Cases

CRITERIA	CASES			
	BASIC	DISP	DISPAHE MORI*	DISPAHE MORIKON
DISP. HGT.	X	O	O	O
AHE	X	X	O	O
*** - AHE Static Input set only for Nagoya City**				

From Table 1, BASIC uses only UCM. Displacement height (DISP.HGT.) was estimated by applying MacDonald's method [6] to 2009 CAD Center's 10-spatial information of Nagoya's Building height and plane area index. Highest in the region, AHE for Nagoya City was estimated in 30-s. using Moriwaki's method [7]. DISPAHE MORIKON includes not only Nagoya's but also acquired 22.5-s x 15-s AHE datasets of surrounding areas (fig. 3).

3.2 Simulation and Discussion

In fig. 4, Orange and green circles represent rain system near Fukushima and Aichi prefecture, respectively. Throughout the simulated time, differences in rain/surface pressure distribution could be seen. Same results could be seen in the August 13, 2009 simulation. Two reasons were cited to have caused these differences. First, urban areas have the capacity to affect synoptic weather. Second, applying chaos theory by Edward Lorentz, small changes in initial conditions in the simulation may produce large

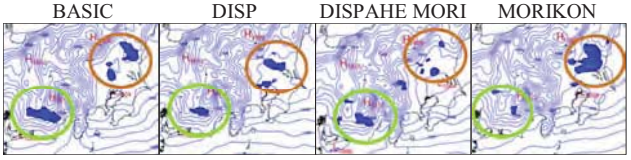

Figure 4: WRF Cases Domain 2 2-hr. Rainfall on 07/30/10 21:00

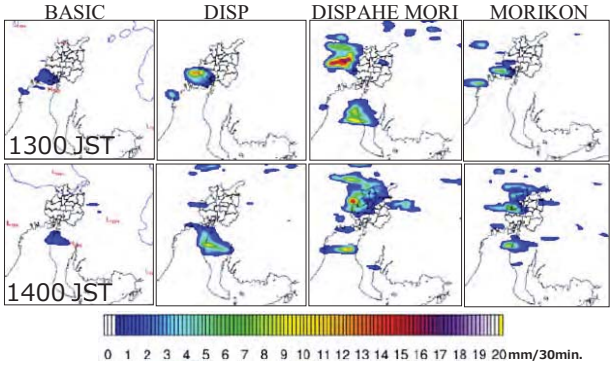

Figure 5: WRF Cases Domain 3 30-min. Rainfall on 07/30/10

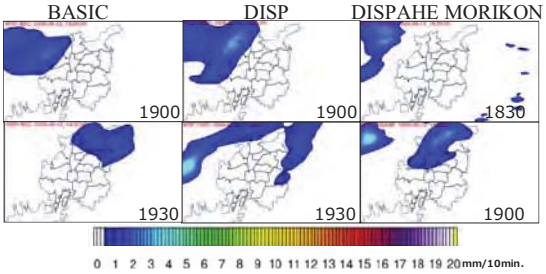

Figure 6: WRF Cases Domain 4 10-min Rainfall on 09/13/09

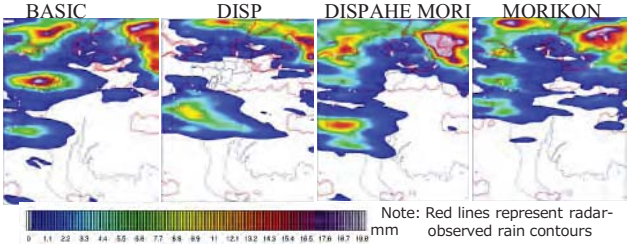

Figure 7: WRF Cases Total Rainfall from 1000-2100 on 07/30/10

changes in the long-term outcome. In the future, it is necessary to determine randomness or chaos in the physical processes. It became difficult for this study to point out whether the simulated values at finer scales were due to noises in domain 2 or the urban parameters. However, logical impacts of individual urban parameters were still determined at instances in the simulations.

On July 30, 2010 from 1300 to 1600 JST, BASIC case simulated the least amount of rainfall as shown in fig. 5. Urban areas causes rain system to bifurcate and avoid the city as shown in the DISP case. However, if the AHE is high enough like in DISPAHE cases, rain system is intensified in the city. August 13, 2009 rainfall simulation highlights how a passing rain is affected by AHE and displacement height of urban areas in fig. 6.

Because of the AHE included in the Northwest of Nagoya, rain was formed earlier by 20-min. for DISPAHE MORIKON case. Also, passing rain splits into two which can also be observed by radar for two dates, because of the strong surface forcing highly concentrated at Nagoya Center (fig. 3) which causes

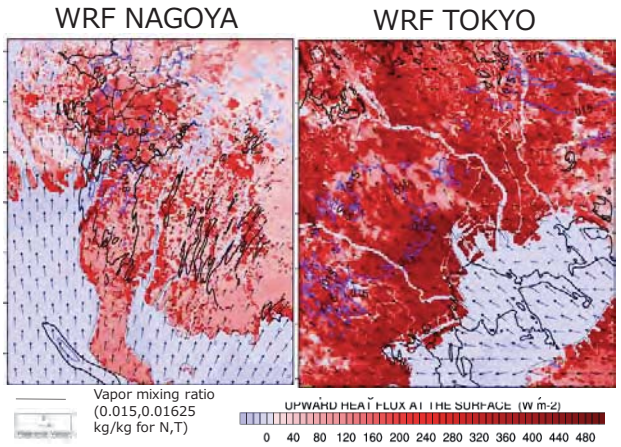

Figure 8: Nagoya and Tokyo Heat Flux at 100m. a.s.l.

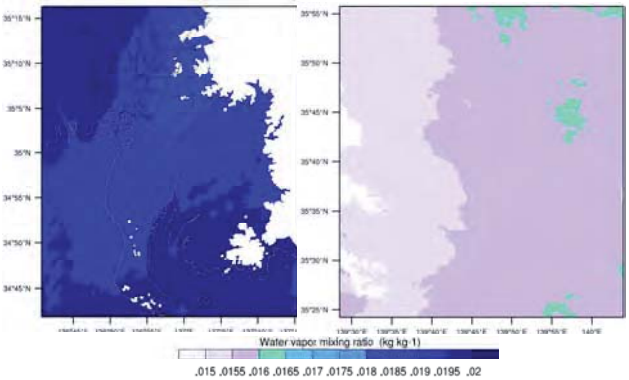

Figure 9: 10-min. Average Vapor Mixing Ratio in kg/kg: (L-R) August 13, 2009 Nagoya and July 29, 2007 Tokyo

updrafts to lift and separate passing moisture to upwind and downwind direction of rain system. Inclusion of AHE does not really improve the spatial rainfall total (not shown). WRF still remains to underestimate localized rainfall but occurs at the right time and improvements in rain distribution could be seen (fig. 8).

Fig. 8 shows simulation snapshots on July 30, 2010 at 1600 (Left: Nagoya) and July 29, 2007 at 1400 JST (Right: Tokyo). Mixing ratio transported by sea breeze could not penetrate the city for both cases. Tokyo generates wider heat flux than Nagoya City that's why advection of mixing ratio on Tokyo land was more difficult. Mixing ratio advected from the south is also hindered by the mountains located south of Nagoya City as shown by the stretched contour. In terms of moisture, Nagoya generates more moisture compared to Tokyo because of the surrounding vegetations' evapotranspiration (fig. 9). Furthermore, mountain breeze was found to arrive earlier due to sea breeze stagnation caused by heat flux rising from the urban surface. (image not shown)

4 WEP Model Evaluation

Affected by urbanization and urban-induced weather, the watershed's runoff response on rainfall must also be simulated with high accuracy. In this regard, WEP was tested in Nomikawa and Meguro Watershed. Previous evaluations of WEP were conducted at Nomikawa by Kobayashi (2009) [8]. In this research, simulation of channel flow rate distribution and application on

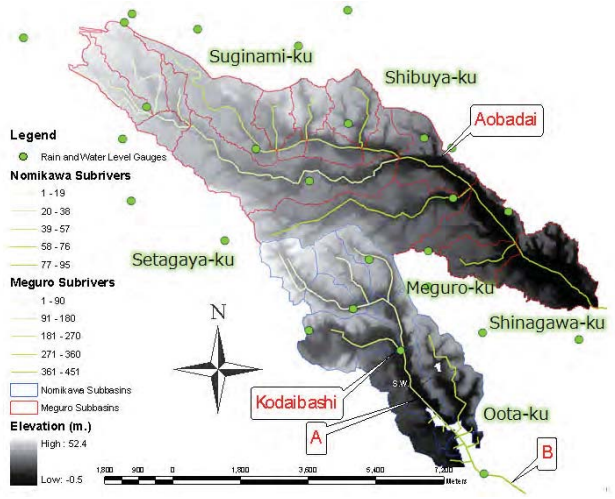

Figure 10: Nomikawa and Meguro Watershed

larger highly urbanized watershed was conducted. Both Nomikawa and Meguro are highly urbanized with impervious ratios of 0.70 and 0.68, respectively. Nomikawa basin (17.6 km^2) is twice wider than Meguro basin (40.7 km^2).

4.1 Model Settings, Simulation and Discussion

For WEP simulations along Nomikawa channel, side-weir (S.W.) overflows were considered using the empirically derived De Marchi Equation. This has caused a 16% flow reduction for the year 2007. Meguro watershed has 17 sub-basins and because of its 21 surrounding gauges, Thiessen method was used to calculate 10-min. spatial input rainfall data. Nomikawa has 18 sub-basins and uses 250-m. input rainfall data. 100 m. and 300 m. sub-rivers were set for Nomikawa and Meguro, respectively.

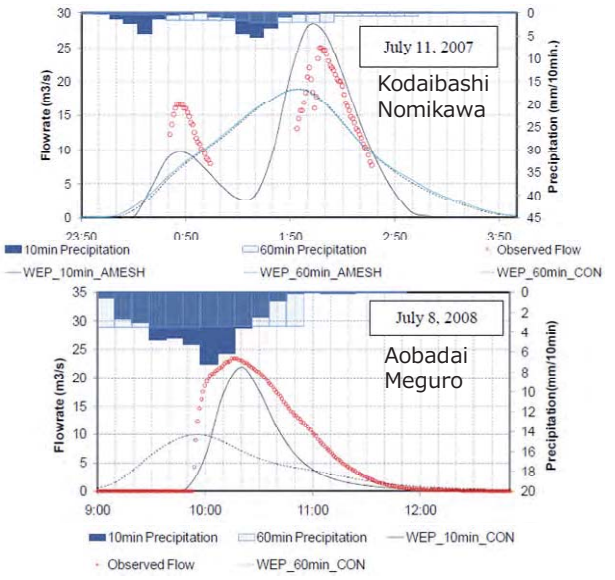

Figure 11: WEP Simulated Hydrographs

Simulations were conducted separately for both watersheds, Kodaibashi and Aobadai (fig. 10). Over-all, WEP performs well in simulating channel flows. Significant results are highlighted in

fig. 11 comparing various input resolutions and model time-stepping. Hyetographs correspond to rain occurring at sub-basins upstream from the simulated points. WEP_10min (10-min. rainfall inputs) shows an improvement in runoff for urban watersheds because of the fluctuating rainfall not reflected for 60-min. rainfall inputs, WEP_60min. Comparing Meguro and Nomikawa watersheds, at equal amounts of rainfall upstream, Nomikawa to Meguro discharge ratio is 3:1. The smaller the catchment the more critical is the effect of the input rain. It was recommended that for smaller catchments a higher spatial resolution of rainfall at finer time steps were necessary. The little difference observed between AMESH and CON at 60-min. time resolution runs was a given because CON, which stands for Tokyo Metropolitan Construction Bureau's Gauged Precipitation Data, was used to calibrate AMESH's rainfall radar data done by Kobayashi (2009). This means observation gauges' spatial resolution was sufficient enough for Nomikawa and Meguro watershed.

For WEP Meguro, flows at Aobadai still underestimates flow for all simulated dates because of insufficient parameterization and possible intrusion from unidentified sources.

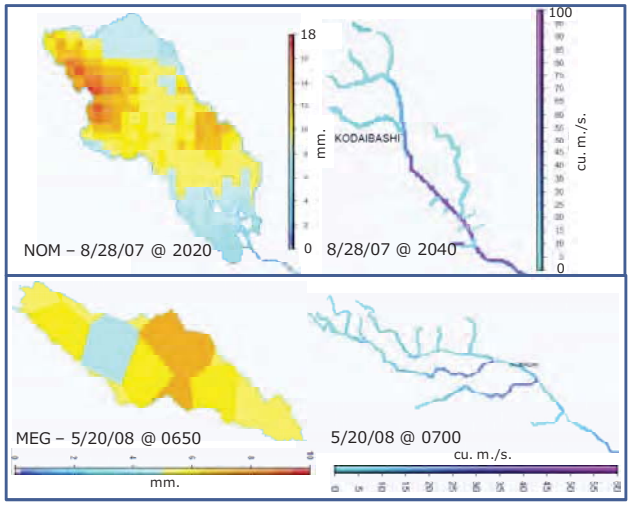

Figure 12: Rainfall Inputs and WEP Simulated Flow Distribution

From fig. 11, it can be seen that high flow rates could be observed at tributary channels especially at the point when flow enters the main channel. The reason behind this was the difference in hydraulics between the tributaries and main channel. Tributary channels have much smaller cross-sections than the main channel.

Basing from other simulation dates (not shown), Nomikawa shows high flow-rates downstream regardless of the rainfall distribution. It is because percolation into the ground was negligible at urban areas thus shortening the rainfall-runoff lag to 10 to 30 min. Also, flow tends to drop past the intersection points at Meguro basins simulations because the sub-river lengths are too short to accumulate 50-m. overland flow. Applying WEP model, the simulated critical locations can be investigated further by non-structural means.

5 Conclusion

WRF-ARW and WEP were evaluated and applied to urban areas for future applications and coupling at areas with poor observation data. WRF simulations were done for two dates evident of local surface forcing at Nagoya City. WEP simulations were conducted at Nomikawa and Meguro Watersheds using different levels of input and settings. Its performance in urban areas are concluded as follows:

WRF-ARW:

- Static inputs seem to affect weather at a synoptic scale.
- Inclusion of AHE still underestimates the total spatial rainfall although AHE together with orography generates rainfall at Nagoya City's leeward end.
- Rains downwind from the city center were not simulated.
- An earlier temperature rise in the morning can be attributed to AHE. Mountain breeze also arrives earlier.
- AHE and surrounding topography prevents advection of moisture into the city.

WEP:

- High spatial and temporal resolution initial inputs and model settings clearly captures the time of runoff, the rising, and recession limbs as shown at the simulation points for Nagoya and Meguro basins.
- Sub-river lengths longer than overland grid spacing provides a more accurate flow-rate distribution.
- Flow simulations are still underestimated at Meguro watershed brought about by possible unknown flow sources.
- The capacity for WEP to simulate runoff distribution proves useful. However, further improvements are needed if indirect coupling is needed.

6 References

[1] Duh, Jiunn-Der, Shandas, Vivek and Chang, Heejun, "Rates of Urbanisation and The Resliency of Air and Water Quality", Science of The Total Environment, vol. 400, pp. 238-256, 2008

[2] Chen, F., et al. "Challenge of forecasting urban weather with NWP models", WRF/14th MM5 Users' Workshop, pp. 34-42, 2004

[3] Kusaka, H., et al. "A simple single-layer urban canopy model for atmospheric models: comparison with multi-layer and slab models", Boundary-Layer Meteorology, vol. 101, pp. 329-358, 2001

[4] Shimoju, Ryo. "Investigation of The Mechanisms on Urban-induced Localized Heavy Rain usig WRF model", Tokyo Institute of Technology International Development Engineering, Masters Thesis. (in Japanese), 2009

[5] Lynch, Peter. "The origins of computer weather prediction and climate modeling", Journal of Computational Physics, vol. 227, no. 7, pp. 3431-3444, 2008

[5] Macdonald, R. W., Griffiths, R. F. and Hall, D. J. "An Improved Method for The Estimation of Surface Roughness of Obstacle Arrays", Atmospheric Environment, vol. 32., pp. 1857-1864, 1998

[6] Moriwaki, Ryo, et al. Anthropogenic Water Vapor Emissions in Tokyo. : Water Resources Research, vol. 44, W11424, 2008

[7] Kobayashi, Kenji. "Environmental Karte as a Tool for Regional Cooperation on Town Development in Watershed", TIT IDE, Masters Thesis. (in Japanese), 2009

Functional and Mechanistic Analysis of Kanamycin Biosynthetic enzymes

Hilda Sucipto 09M51650

Supervisor: Prof. Sachio Hirose **Sub supervisor: Prof. Tadashi Eguchi**

Kanamycin is a clinically important aminoglycoside (AG) antibiotic, which should be biosynthesized by a programmed molecular assembly line consisting of kanamycin biosynthetic enzymes, even though the logic of the biosynthetic machinery for kanamycin A is still in mystery. In my master course, I tackled to characterize the function of the kanamycin biosynthetic enzymes to elucidate the pathway. Understanding biochemical properties of these enzymes was supposed to provide important information to engineer proteins in generating structural diverse aminoglycoside antibiotics. This study mainly focused on the late stage of kanamycin A biosynthesis, which consists of a glycosylation of a pseudodisaccharide intermediate paromamine, two sets of amination, and a deamination. The candidate enzymes predicted by bioinformatic analysis were expressed in *Eschericia coli* and the enzymatic activities for the corresponding reactions were investigated. A glycosyltransferase KanM2 was found to catalyze the pseudotrisaccharide formation from paromamine with UDP-glucose. In addition, the final deamination process from kanamycin B to kanamycin A was facilitated by two unique enzymes KanJ and KanK, an α-ketoglutarate dependent dioxygenase and an NADPH dependent ketoreductase, respectively. Consequently, except for two amination processes, all of kanamycin biosynthetic enzymes have been characterized to show clear outline for the kanamycin biosynthetic pathway.

1. Introduction

Kanamycin is the most well known 2-deoxystreptamine (2DOS)-AG antibiotic because it possesses a broad range antibacterial activity. Although bacteria resistant to this antibiotic readily appear, investigations concerning bacterial resistant mechanism led to the development of semisynthetic kanamycin derivatives such as dibekacin, amikacin and arbekacin. These derivatives show good activities against kanamycin-resistant bacteria and except arbekacin, are used as chemotherapeutic agents against resistant bacteria of clinical importance.

Bioinformatics analysis of kanamycin biosynthetic gene cluster with the other 2DOS containing AG biosynthetic gene clusters revealed that *kan* gene cluster indeed encodes five conserved biosynthetic enzymes (*kanC,* 2-deoxy-*scyllo*-inosose synthase, *kanS1,* aminotransferase, *kanE*,

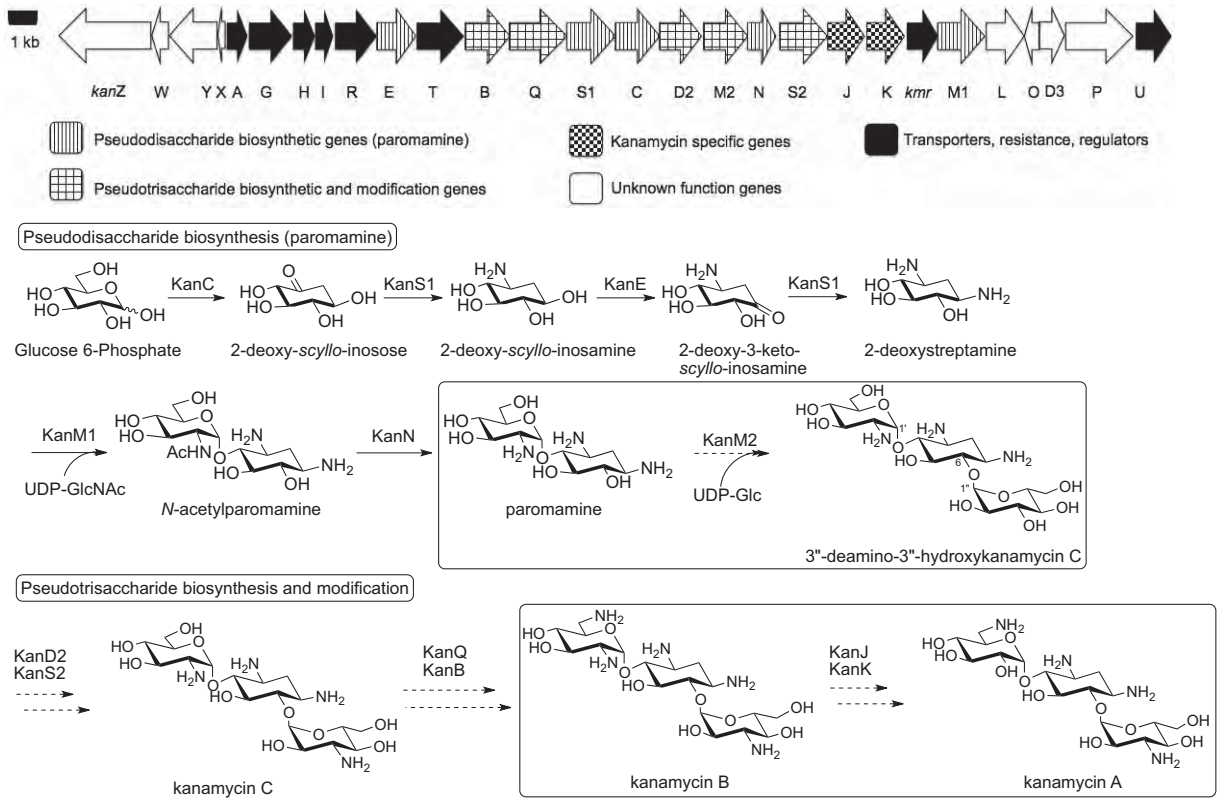

Figure 1. Kanamycin biosynthetic gene cluster identified from *Streptomyces kanamyceticus* and a proposed biosynthetic pathway for kanamycin A. Box showed the characterized enzymes in this study.

dehydrogenase, *kanM1*, glycosyltransferase, and *kanN*, deacetylase) for paromamine biosynthesis (Fig. 1). In fact, these five genes expressing *Streptomyces lividans* has been reported producing paromamine by a Korean research group.

Another deduced glycosyltransferase KanM2 was then presumed to be responsible for attaching a sugar at the C-6 of paromamine to form pseudotrisaccharide.

A set of FAD-dependent dehydrogenase (KanQ) and aminotransferase (KanB) is conserved in neamine containing AG biosynthetic gene cluster. Those homolog NeoQ and NeoB derived from neomycin biosynthesis were reportedly to catalyze the oxidation of hydroxyl group at C-6 of glucosamine moieties of biosynthetic intermediates. Therefore, KanQ and KanB seemed to be involved in the similar enzymatic reaction step in kanamycin biosynthesis (Fig. 1).

A set of NAD/NADP-dependent dehydrogenase (KanD2) and aminotransferase (KanS2) is conserved in kanamycin related pseudotrisaccharide AG antibiotic biosynthetic gene cluster. This family of AG has a characteristic amino group at C-3" of the third sugar. Thus, these seemed to be responsible for the amino group incorporation before or after the attachment of the third sugars.

Finally, KanJ, a putative phytanoyl-CoA dioxygenase and KanK, a putative NADP-dependent oxidoreductase remained to be assigned for the kanamycin A biosynthesis. Since C-2' position of kanamycin B is somehow converted to an amino group, KanJ and KanK were predicted to be responsible for this transformation. Based on the annotated function of these, KanJ seemed to catalyze the oxidation at C-2' and KanK reduces the presumable ketone intermediate to complete kanamycin A biosynthesis

In this study, those seven genes (*kanM2*, *kanD2*, *kanS2*, *kanQ*, *kanB*, *kanJ*, and *kanK*) were heterologously expressed in *E. coli* and their catalytic activities were investigated based on the above-mentioned hypothesis.

2. Results and Discussion

2.1 Functional analysis of KanM2[1)]

The cell-free extract of KanM2 expressing *E. coil* was reacted with paromamine and UDP-Glucose (UDP-Glc) at 28°C for 18 h. The enzymatic reaction products were treated with 2,4-dinitrofluorobenze to convert aminoglycosides to *N*-dinitrophenyl (DNP) derivatives. LC-ESI-MS analysis of the sample showed a new peak with *m/z* 982.4 which corresponded to $[M-H]^-$ for the derivative of glucosylated paromamine. Further, a large-scale KanM2 reaction with paromamine and UDP-Glc was carried out to isolate the product, whose structure was determined to be 3"-deamino-3"-hydroxykanamycin C by FABMS and NMR analysis.

Subsequently, substrate specificity of KanM2 was examined with paromamine and neamine as glycosyl acceptor, and UDP-Glc and UDP-N-acetylglucosamine (UDP-GlcNAc) as glycosyl donor. As a result, it was found that KanM2 prefer paromamine to neamine, supporting that paromamine is a likely intermediate in the biosynthesis of kanamycin. On the other hand, UDP-GlcNAc was not accepted by KanM2, indicating its strict substrate specificity. Since we cannot exclude UDP-kanosamine (3'-amino-3'-deoxyglucose) as a potential glycosyl donor which may be biosynthesized form UDP-Glc by KanD2 and KanS2 described below, substrate specificity with UDP-kanosamine should be investigated to elucidate the biosynthetic pathway.

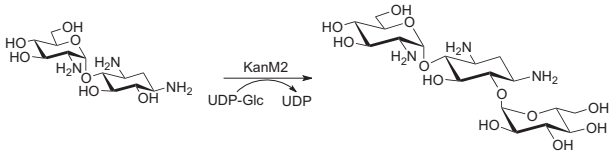

Figure 2. Enzymatic reaction catalyzed by KanM2

2.2 Functional analysis of KanD2/KanS2 and KanQ/KanB as dehydrogenase and aminotransferase

To introduce 3"-amino group of kanamycin C, two possible pathways were hypothesized; 1) conversion of UDP-Glc to UDP-kanosamine for KanM2 reaction, 2) conversion of 3"-deamino-3"-hydroxykanamycin C to kanamycin C, which were

presumably catalyzed by a set of KanD2 and KanS2 (Fig. 3).

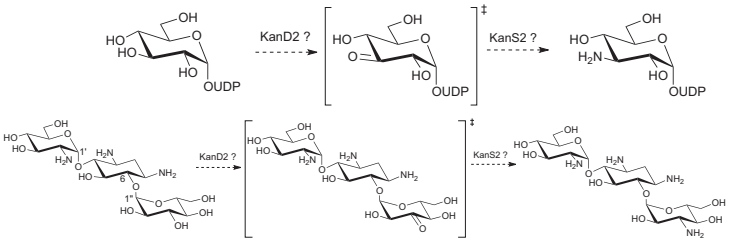

Figure 3. Proposed enzymatic reactions of KanD2/KanS2

Many expression systems including some KanD2/KanS2 co-expression systems were constructed to improve the solubility of the recombinant proteins. However, the expected transformations have not been detected yet, probably due to the expression problems.

To introduce 6'-amino group of kanamycin B, two possible pathways were hypothesized; 1) conversion of paromamine to neamine before KanM2 reaction, 2) conversion of kanamycin C to kanamycin B, which were presumably catalyzed by a set of KanQ and KanB. Since kanamycin C was not commercially available, paromamine was examined as a substrate for the KanQ and KanB reaction (Fig. 4). As a result, the expected oxidation activity of KanQ was not detected, probably due to its insolubility. On the other hand, when KanQ homolog NeoQ derived from neomycin biosynthesis pathway was coupled with KanB, neamine formation was observed. This result indicated that KanB recognizes 6'-oxo-paromamine and catalyzes transamination to give neamine. KanB is maybe a dual functional aminotransferase with 6'-oxo-paromamine and 6'-oxo-kanamycin C as its substrates. Substrate specificity of KanQ remained to be examined in order to determine the precise biosynthetic pathway for kanamycin.

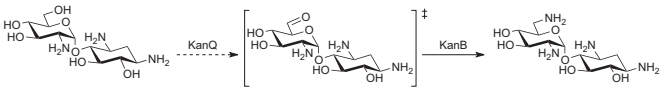

Figure 4. Proposed enzymatic reactions of KanQ/KanB

2.3 Functional analysis of KanJ and KanK

The recombinant KanJ and KanK proteins were reacted with kanamycin B and the DNP derivatives of the enzymatic reactions were analyzed by HPLC. As a result, it was found that KanJ and KanK catalyzed the conversion of kanamycin B to kanamycin A in the presence of α-ketoglutarate (α-KG), ferrous ions Fe(II) and NADPH, but not with NADH. The product from a large scale KanJ and KanK reaction was then confirmed to be kanamycin A by FABMS and NMR analysis. Even in the absence of KanK, the substrate kanamycin B was consumed and a new decomposed product was detected by LC-ESI-MS, indicating that KanJ somehow catalyzes the oxidation of kanamycin

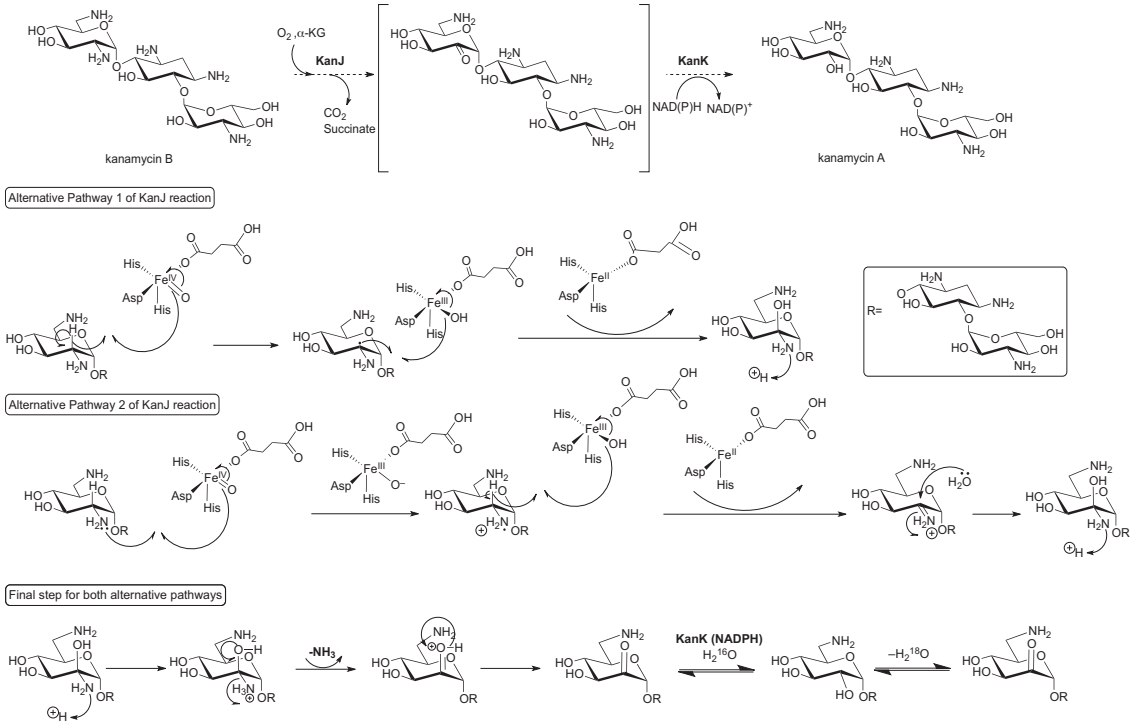

Figure 5. Proposed enzyme reaction for KanJ and KanK

B to form 2'-oxo-kanamycin, which is subsequently reduced to be kanamycin A by KanK (Fig. 5).

In order to clarify the ketone formation catalyzed by KanJ, the KanJ enzymatic reaction product was treated with $NaBD_4$. ^{1}H-NMR analysis revealed that this coupled reaction indeed afforded kanamycin A. Further, the deuterium atom incorporation into C-2' position was clearly detected by ^{1}H-NMR and ^{2}H-NMR. This result clearly demonstrated that the KanJ generated 2'-oxo-kanamycin, which was then reduced by $NaBD_4$. Another product, ammonia, was also clearly detected by the use of coupling assay with glutamate dehydrogenase. These results support that KanJ somehow synthesizes 2-oxo-kanamycin and release ammonia.

In the process of the ketone formation, two possible reaction mechanisms were hypothesized (Fig.5); (1) the formation of reactive [Fe(IV)=O] species breaks the inactivated C-2'-H bond in kanamycin B homolitically to produce kanamycin B radical at C-2' and facilitate its own reduction to an Fe(III)-OH species. Fe(III)-OH provides a hydroxyradical to afford a hemiaminal intermediate, which is simultaneously converted to 2'-oxokanamycin, (2) the reaction was initiated by the radical attack of ferryl oxo species to the lone pair of nitrogen atom at C-2' to form an nitrogen cation radical intermediate, which turns out to be an imine intermediate that is easily hydrolyzed to be a ketone. The presumed ketone intermediate formed by either pathway then was reduced to form kanamycin A.

To distinguish these reaction mechanisms, KanJ reaction coupled with KanK was conducted under ^{18}O-enriched atmosphere. As a result of LC-ESI-MS of the enzymatic reaction products, 7% of the produced kanamycin A was found to be labeled with molecular ^{18}O. This result clearly suggested that KanJ catalyzes the hydroxylation to afford a hemiaminal intermediate like usual α-KG dependent hydroxylase. The small amount of ^{18}O incorporation from $^{18}O_2$ appeared to be caused by the equilibrium exchange with ^{16}O from water of the ketone intermediate. Thus, this equilibrium event was confirmed in the presence of 50% ^{18}O-labelled water in the enzymatic solution. As expected, a significant amount of ^{18}O (16.7%) was clearly incorporated into kanamycin A, indicating that an equilibrium event between ketone intermediate with water from the buffer occurred.

Finally, the substrate specificity of KanJ was examined with several AGs that are structurally similar to kanamycin B. Among the alternative substrates tested, neomycin B, butirosin A, neamine and ribostamycin were converted to new products deaminated by KanJ and KanK within the conversion range 37 to 97%. Paromamine was the only tested substrate that was not accepted by KanJ. Thus, it was demonstrated that KanJ and KanK have relatively relax substrate specificity. Amino group at C-6' seems to be critical for KanJ reaction (Fig.6).

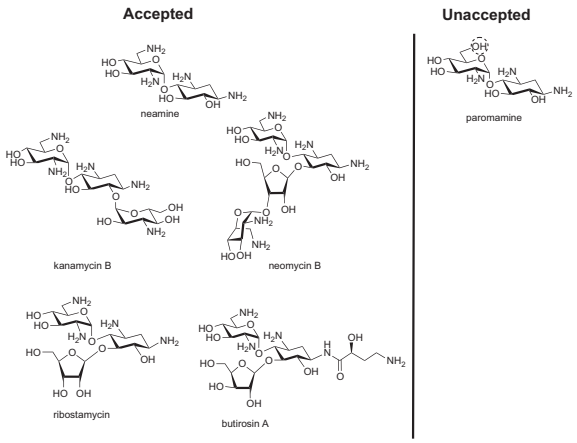

Figure 6. Substrate specificity for KanJ

3. Conclusion

In this master thesis, I characterized KanM2 as UDP-Glc: Paromamine glycosyltransferase, KanJ as α-KG dependent kanamycin B deaminase and KanK as NADPH-dependent 2'-oxokanamycin reductase. Although two amination steps are still unclear, most of the kanamycin biosynthetic enzymes have now been characterized to show clear outline for kanamycin A biosynthesis.

4. Reference

1. Kudo, F., Sucipto, H. & Eguchi, T. Enzymatic activity of a glycosyltransferase KanM2 encoded in the kanamycin biosynthetic gene cluster. *J. Antibiot.* **62**, 707-10 (2009).

Comparison of Corrosion Behavior of Paint-coated Steel in Real Structures and Experimental Results in Marine Environment

Student Number: 09M51666 Name: MYINT THET HTOO Supervisor: Nobuaki OTSUKI

Corrosion behaviour of circular steel plates using acceleration test covered with tar epoxy (TE) coating were conducted in this acceleration. This study includes investigation on degradation of paint by acceleration test was carried out. Then, the experimental data are compared to the data of experiment from real environment. As a result, it could be confirmed that paint is degraded more severely in the splashed condition. Macrocell corrosion is prominent in submerged whilst microcell larger in the splash zone. Also, painting starts deterioration after three month in acceleration test it took over 15 years in case of real environment.

Introduction

Being a material possessing versatile functionality, steel stands as an excellent choice for construction industry. Some of these steel structures have to be constructed in marine environment. There are various kinds of aggressive materials in this kind of environment, such as Cl^-, O_2 and OH^-, that causes deterioration of the structural members, mainly corrosion, leading undesirable structural failure.

To protect the steel against beset of these harmful species, surfaces of the structures are treated with various types of coating. Painting can isolate steel substrate from the aggressive matters acting as a barrier mechanism [1]. However these coating may encounter inevitable setbacks concerning chemical and mechanical injuries. After being damaged, aggressive chemicals from the surrounding can easily get in touch with the steel substrate. Once these chemicals invaded, they create the conditions for the corrosion reaction to initiate on the steel surface. Therefore, this study investigates corrosion behaviour in paint-coated steel plates with defect in the centre, using Tar Epoxy (TE), exposed to simulated marine environment, mainly for submerged and splashed zones, and compared the results to the data obtained from the real structures.

1. Overview of the Experiment

In this experimental series, deterioration of painting regarding submerged and splashed zone, corrosion behaviours of the steel underlain the paint coating are investigated using acceleration test.

Then the experimental data gained from the acceleration tests were compared to the outcomes from 20 years exposure test conducted in real environmental condition in Suruga Bay, Japan. The environmental conditions of Suruga Bay are 20˚C average temperature and amount of NaCl is around 3% NaCl.

2. Details of Experiment

3.1 Materials

The following materials, steel and type of coating shown in the **Table 3.1** and **3.2** were used in the experiment.

Table 3.1 Steel Composition

Fe (%)	C (%)	Si (%)	Mn (%)	P (%)	S (%)	Yield Strength (N/mm^2)
99.28	0.16	0.02	0.45	0.013	0.06	295

Table 3.2 Paint

Type	Tar Epoxy (T.E)
Thickness (μm)	250 ~ 300 μm
Surface Preparation	Sand Blasting
Primer Coating	None

2.2 Preparation of Specimen

Two types, divided and non-divided steel, specimens were used in the experiment. The

dimensions of specimens are in **Fig 3.1** and **Table 3.3**

Divided Circular

Fig 3.1 Steel Used

Ring	Inner Dia. (cm)	Outer Dia. (cm)
1	-	1.8
2	2.14	3.94
3	4.28	6.08
4	6.42	8.22
5	8.56	10.36
6	10.7	12.5

Procedure for preparation specimens were explained detail in the preceding section. Firstly surfaces of the specimens were properly cleaned by ethanol. Then the steel surfaces were wiped with abrasive sand paper. Lead wires were soldered on the surface of the steel. The soldered wires were checked for the electricity. Finally the soldered steels were covered with hard grey epoxy by leaving only one exposure surface, on which painting would be treated. All the prepared specimens were sent to the factory for painting process. Surfaces of the specimens were rubbed with sand paper to clean the impurities before the application of paint coating.

3.4 Exposure setting for Acceleration Test

As mentioned in the previous section, two regions of sea level, such as submerged and splashed are considered. For both of these regions, acceleration test were simulated. For the submerged zone, the specimens were immersed in 3% wt NaCl with ambient temperature of 50˚C accompanied with 2 lit/ min aeration. For splashed simulation, specimens were sprayed inside the brine spray chamber. All the environmental conditions were adjusted the same as submerged condition except spraying pressure inside chamber was set as 8 psi.

4 Results and Discussion

4.1 Paint Degradation

4.1.1 Paint Resistance using Acceleration Test

Regarding **Fig 4.1**, in splash zone, coating resistance increased in the second month. After 2month, coating resistance goes down in third and fourth months. Comparing submerged and splash zone, decrease in the paint resistance in splash

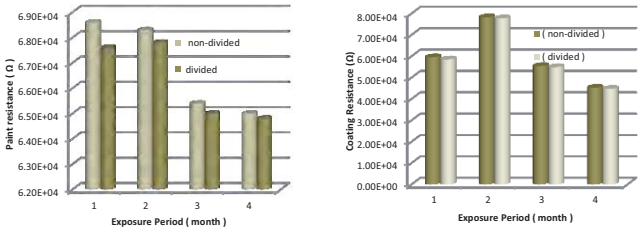

(a) Submerged (b) Splash

Fig 4.1 Paint Resistance using Acceleration Test

region is more severe than that in the submerged zone. This is because of change in temperature causes the paint to contract and expand due to cyclic dry and wet nature and also the availability of oxygen from the surrounding atmosphere.

4.1.2 Double Layer Capacitance from Acceleration Test

This part of experimental series also exhibits change in capacity of coating. Average values of double layer capacitance for 6 measurement locations are shown in **Fig 4.1 (a)** and (**b**) respectively**.** In this values, it shows that the divided and non-divided specimens possess the initially almost the same values of capacitance having order of 10^1. As the exposure period gets longer, the values of capacitance significantly become larger. After third month, the increase in the values becomes smaller. According to the **Fig 4.1**., these results have interdependency with the paint resistance discussed in the previous section. As the resistance of painting decreases, paint layer permits more aggressive ions from the surrounding including electrolyte. Consequently, this condition tends the capacitance of paint coating to be larger

leading to corrosion of steel substrate.

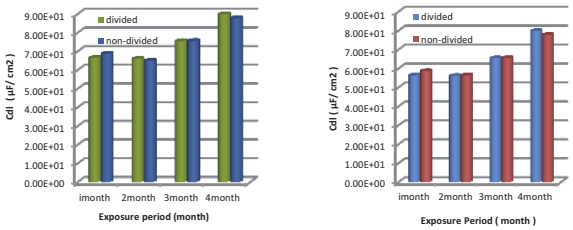

(a) Submerged (b) Splash

Fig 4.2 Coating Capacitance

4.1.3 Bode Plot Analysis

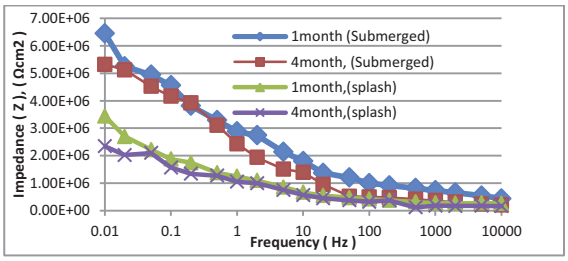

4.3 (a)Impedance vs Frequency

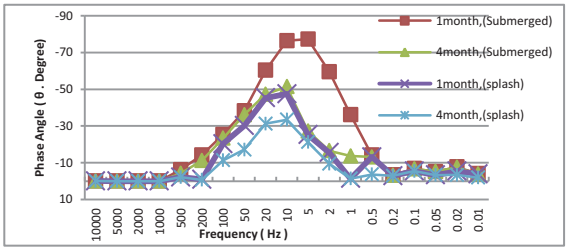

4.4 (b) Phase Angle vs Frequency

From **Fig 4.3 (a) and (b),** for Bode plots and phase angle (θ), the impedance of bode plot gradually decrease with time are shown. Impedance at lower frequencies found significantly lower with time. Also, in the first the graphs become flattened in both splash and immersed conditions even though the degradation of paint in splash zone is a little more severe than that in immersed zone.

4.1.4 Oxygen Permeability

As painting resistance decreases, its barrier property to oppose the invasion of corrosive ions, such as Oxygen, also get reduced. Therefore oxygen permeability through the paint was

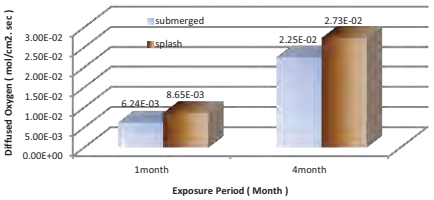

Fig 4.1.4Oxygen Permeability

investigated in this experiment. Here, one more correlated data showed that more oxygen ions had permeated into the paint layer by looking at the data from 1 month and 4 month exposure period. Similarly as in the above manners, splash found more harshly invaded by the O_2 in deterioration than in submerged zone.

4.1.5 Microcell and Macrocell Corrosion of Acceleration

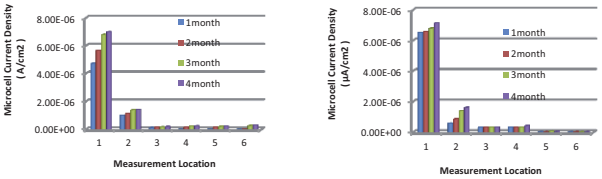

(a) Submerged (b) Splash

Fig 4.5 Microcell Corrosion (Circular)

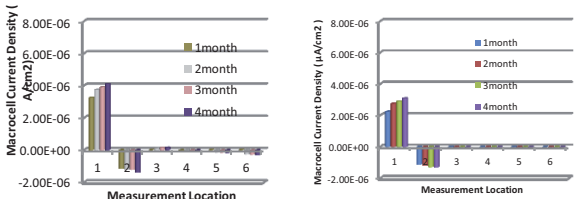

(a) Submerged (b) Splash

Fig 4.6 Macrocell Corrosion (Circular)

The results of microcell and macrocell corrosion investigation for TE coated steel plates are shown **Fig 4.5, Fig 4.6** and **Fig 4.7**. According to the figures, it was observed that microcell corrosion in submerged condition is lower than that in splashed

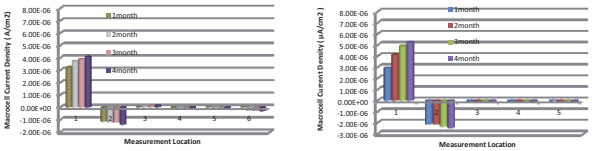

(a) Submerged (b) Splash

Fig 4.7 Macrocell Corrosion using Divided Steel

simulation.Contrastingly, higher macrocell corrosion in submerged simulation was found. This is attributed that there is high potential for electro-conductivity in the submerged condition due to the presence of electrolyte (3% wt. NaCl solution here) in the surrounding.

5 Comparison of Experimental and Data from Real Environment

In this section, the data from experiment and real environment of 20 years exposure were compared. In the case of real environment, it was reported that the deterioration was very slow up to 15 years exposure to the marine environment. Nevertheless, reactance (absolute value of alternating impedance at 1 kHz) started to decline after almost 20 year (19.5 years to be exact) exposure. Regarding **Fig 5.1**.

It could be found that the trend and nearly equal in values of reactance is similar for both of the experimental and real environment and also in comparing electrical potential for both situations the trend was similar but the the values are different. Moreover it could be said, through a brief comparison, that combination of both oxygen supply and temperature rise, double average sea water temperature in real environment, can accelerates the paint to deteriorate 60 times faster than that in normal condition.

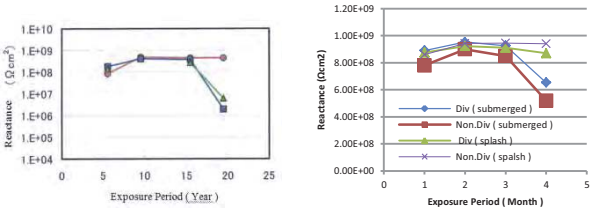

(a) Exposure Test (Real) (b) Acceleration Test (Experiment)

Fig 5.1 Comparison of Reactance between Real Exposure and Acceleration Test

6. Conclusion

Regarding the above results and discussions, following conclusions could be made.

Firstly, experimental outcomes are compared to the data obtained from the test samples exposed to the real marine environment, Suruga Bay, Japan. The average annual temperature of the site concerned is 20 to 30˚C, which is about half of the experimental temperature. As a result, painting started delamination and corrosion had initiated after 3 months exposure using acceleration test. Comparing it to the data from real environment of 15 years exposure for paint coating to delaminate, the experimental was 60 times faster than the corrosion initiation in real structures.

Secondly, microcell corrosion is more prominent in the splash condition due to comparatively abundant oxygen supply while macrocell corrosion is higher in the submerged region. It could be confirmed that presence of electrolyte in the surrounding for the current flow from cathode to distant anode.

Thirdly, comparing submerged and splash zone using acceleration test, it could be confirmed that decrement in the paint resistance in splash region is more severe than that in the submerged zone due to the changes in temperature and cyclic wet and dry condition of the zone.

References

1. Fontana,M.: Corrosion Engineering, McGraw-Hill, 1978.
2. Min, A.K., A Study on Corrosion of Paint Coated Steel with Defects in Marine Environment, Masters Thesis, Tokyo Institute of Technology, 2006.

Effect of operating conditions on water quality control in intensive shrimp mariculture ponds in developing countries by sterile seaweed

Student Number: 10M18016 Name: Yuichiro AOKI Supervisor: Ryuichi EGASHIRA

不稔性海藻による開発途上国型集約エビ養殖池の水質制御に対する操作条件の影響

青木　悠一郎

モデル海水中においてアオサ(横浜産)のアンモニア窒素(AN)摂取速度ならびに成長速度を実測した。アオサのAN摂取ならびに成長を確認した。AN、炭素、リンの濃度、光合成光量子束密度の増加、温度の上昇とともに、摂取、成長いずれの速度も増加した。AN濃度が特に高い範囲においてアオサの白化が観察された。これらの実験結果に基づいた計算において、エビ養殖池のAN濃度を低く抑えることができるとともに副産物として大量のアオサを得ることができた。

1 Introduction

Since the 1990s, the shrimp industry, which has given high profit and foreign exchange to developing countries, has suffered many viral disease outbreaks [1]. To avoid entering viruses from external water, some shrimp farmers introduced none or quite small water exchange culture system. However, this system caused the serious water deterioration and the water quality control became more important. Especially, ammonia-nitrogen (AN) is toxic to shrimp [2][3]. So, to control AN concentration is important for shrimp mariculture. However, because of low shrimp value, shrimp mariculture in developing countries can't pay away a lot of money for water quality control. In previous study [4], water quality control of shrimp ponds using sterile seaweed was proposed. However this system is affected on environmental conditions. So to examine effect of operating conditions is important. In this study, we examined effect of operating conditions on water quality control in intensive shrimp mariculture ponds in developing countries by sterile seaweed. First, we measured AN uptake rate by and growth rate of sterile seaweed and examined effect of operating conditions for growth rate. Second, we calculated water quality control and growth of seaweed in shrimp pond.

2 AN uptake by and growth of sterile seaweed

2.1 Materials

Sterile *Ulva* sp. collected from Umi no koen (Marine park) in Yokohama, Japan was used as sterile seaweed. Commercial sea salt was used to prepare artificial seawater (30 ‰). NH_4Cl, $Na_3PO_4{\cdot}12H_2O$, $NaHCO_3$ were used as sources of total ammonia-nitrogen (TAN), dissolved inorganic phosphorus (DIP), and carbon (DIC) in the seawater.

2.2 Experimental

Fig. 2.2-1 shows experimental apparatus. We measured TAN uptake rate by and growth rate of seaweed, and examined effect of total TAN concentration in culture medium, photosynthetic photon flux density (PPFD), and water temperature for growth rate. TAN concentration in liquid solution was determined by the indophenol blue method and growth rate of seaweed was calculated from mass increment of biomass.

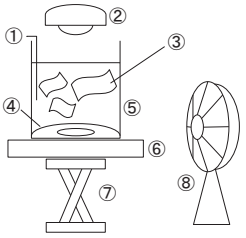

① Temperature indicator
② Metal halide lamp
③ Sterile *Ulva* sp.
④ Nylon mesh
⑤ Plastic beaker
⑥ Magnetic stirrer
⑦ Jack
⑧ Fan

Fig. 2.2-1 Experimental apparatus

2.3 Results and discussion

2.3.1 TAN uptake rate of sterile seaweed

The initial specific uptake rate of TAN by seaweed, $\pi_{TAN,0}$, was obtained by

$$\pi_{\mathrm{TAN},0} = -\frac{1}{\rho_{\mathrm{U}}}\frac{\mathrm{d}C_{\mathrm{TAN}}}{\mathrm{d}t}\bigg|_{t=0} \quad (1)$$

Fig. 2.3.1-1 shows the effect of initial TAN concentration on the initial specific uptake rate. It was reconfirmed that sterile *Ulva* sp. could take in TAN. The uptake rate increased, as TAN concentration increased. The relation between TAN concentration and uptake rate was fitted by Michaelis-Menten equation,

$$\pi_{\mathrm{TAN},0} = \frac{\pi_{\max} C_{\mathrm{TAN}}}{K_{\mathrm{M}} + C_{\mathrm{TAN}}} \quad (2)$$

with the maximum specific uptake rate of TAN, π_{max}, and the half saturation constant of TAN concentration for uptake, K_M, as shown by the solid line in Fig. 2.3.1-1. The relation was well represented by this equation with $\pi_{max} = 11.6 \times 10^{-3}$ kg-N kgDM^{-1} h^{-1} and $K_M = 2.3 \times 10^{-3}$ kg-N m^{-3}.

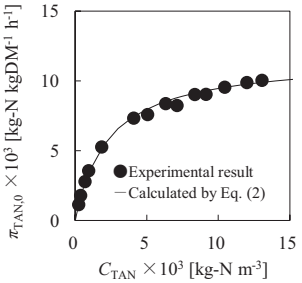

Fig. 2.3.1-1 Effect of TAN concentration on initial specific uptake rate

Table 2.3.1-1 Experimental conditions

$\rho_{U,0}$ [kgDM m^{-3}]	0.65
T [°C]	27 ± 1
I [μmol m^{-2} s^{-1}]	600
$C_{TAN} \times 10^3$ [kg-N m^{-3}]	0 - 13.1
$C_{DIP} \times 10^4$ [kg-P m^{-3}]	0
C_{DIC} [mM]	0

2.3.2 Effect of TAN concentration in culture medium on specific growth rate of sterile seaweed

The specific growth rate of seaweed, μ, was defined by,

$$\frac{\mathrm{d}\rho_{\mathrm{U}}}{\mathrm{d}t} = \mu\rho_{\mathrm{U}} \tag{3}$$

where ρ_{U} is density of seaweed in culture medium. Integration of this equation leads to,

$$\ln\frac{\rho_{\mathrm{U},t}}{\rho_{\mathrm{U},0}} = \mu t \tag{4}$$

where $\rho_{\mathrm{U},0}$ and $\rho_{\mathrm{U},t}$ are density of seaweed in culture medium at initial and t. **Fig. 2.3.2-1** shows time course of natural log of ratio of seaweed density to initial seaweed density in culture medium. The growth of the seaweed could be quantitatively detected in the range of this work. By eq. (4), the specific growth rate could be obtained from slope of Fig. 2.3.2-1.

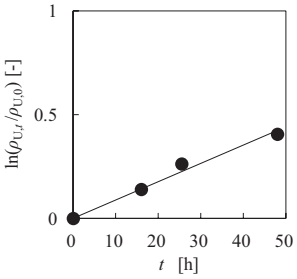

Table 2.3.2-1 Experimental conditions

$\rho_{\mathrm{U},0}$ [kgDM m^{-3}]	0.13
T [°C]	27 ± 1
I [μmol m^{-2} s^{-1}]	600
$C_{\mathrm{TAN}} \times 10^3$ [kg-N m^{-3}]	1.0
$C_{\mathrm{DIP}} \times 10^4$ [kg-P m^{-3}]	3.0
C_{DIC} [mM]	2.0

Fig. 2.3.2-1 Time course of natural log of ratio of seaweed density to initial seaweed density in culture medium

The specific growth rate is plotted against TAN concentration, C_{TAN}, in **Fig. 2.3.2-2**. The growth rate increased with increasing TAN concentration. In this study, effect of TAN concentration, PPFD, I and water temperature, T for specific growth could be described by,

$$\mu = \mu_{\max}\frac{C_{\mathrm{TAN}}}{K_{\mathrm{S}} + C_{\mathrm{TAN}}}\frac{I}{I_{\mathrm{S}} + I}\exp\left[-\frac{E}{R(T+273)}\right] \tag{5}$$

where $\mu_{\max}$ is the maximum specific growth rate. K_{S} and I_{S} are the half saturate constant of TAN concentration and PPFD for growth. E is the apparent activation energy for growth of seaweed, R is gas constant.

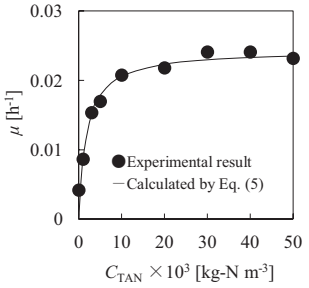

Table 2.3.2-2 Experimental conditions

$\rho_{\mathrm{U},0}$ [kgDM m^{-3}]	0.13 - 0.18
T [°C]	27 ± 1
I [μmol m^{-2} s^{-1}]	600
$C_{\mathrm{TAN}} \times 10^3$ [kg-N m^{-3}]	0 - 50.0
$C_{\mathrm{DIP}} \times 10^4$ [kg-P m^{-3}]	3.0
C_{DIC} [mM]	2.0

Fig. 2.3.2-2 Effect of TAN concentration on specific growth rate

2.3.3 Effect of PPFD on specific growth rate of sterile seaweed

The effect of PPFD on specific growth rate of seaweed is given in **Fig. 2.3.3-1**. When PPFD was 0 μmol m^{-2} s^{-1}, the seaweed did not grow. The specific growth rate increased with PPFD.

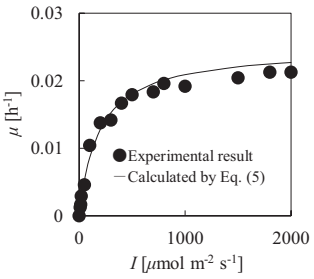

Table 2.3.3-1 Experimental conditions

$\rho_{\mathrm{U},0}$ [kgDM m^{-3}]	0.13 - 0.18
T [°C]	27 ± 1
I [μmol m^{-2} s^{-1}]	0 - 2000
$C_{\mathrm{TAN}} \times 10^3$ [kg-N m^{-3}]	4.0
$C_{\mathrm{DIP}} \times 10^4$ [kg-P m^{-3}]	3.0
C_{DIC} [mM]	2.0

Fig. 2.3.3-1 Effect of PPFD on specific growth rate

2.3.4 Effect of water temperature of culture medium on specific growth rate of sterile seaweed

Fig. 2.3.4-1 shows the effect of water temperature on specific growth rate. The growth rate had the maximum at around 30 °C over temperature. In higher temperature range, the chlorosis of seaweed was observed, which would result in the low growth rate. In this study, lower than 30 °C, effect of water temperature to the specific growth rate was fitted Arrhenius equation.

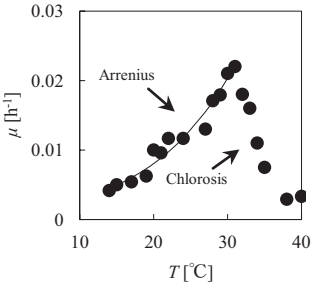

Table 2.3.4-1 Experimental conditions

$\rho_{\mathrm{U},0}$ [kgDM m^{-3}]	0.13 - 0.18
T [°C]	14 - 40
I [μmol m^{-2} s^{-1}]	600
$C_{\mathrm{TAN}} \times 10^3$ [kg-N m^{-3}]	4.0
$C_{\mathrm{DIP}} \times 10^4$ [kg-P m^{-3}]	3.0
C_{DIC} [mM]	2.0

Fig. 2.3.4-1 Effect of water temperature on specific growth rate

In this study, the maximum specific growth rate, $\mu_{\max}$, was 3 × 10^{10} h^{-1}. Half saturation constant of TAN concentration for growth, K_{S}, was 1.8 × 10^{-3} kg-N m^{-3}. Half saturate constant of PPFD for growth, I_{S} was 189 μmol m^{-2} s^{-1}. The apparent activation energy for growth of seaweed, E = 6.86 × 10^4 J mol^{-1}.

3 Calculation of water quality control and seaweed growth in shrimp pond

3.1 Nitrogen balance and growth of seaweed in shrimp pond

Nitrogen as the form of the shrimp feed is supplied into pond. Much of feed is eaten by shrimp and a portion of feed is uneaten. Shrimp excretes AN through respiration and other nitrogen metabolite (feces, shed shell etc.). AN also generate from sediment decomposition. On the other hand, in this study, AN in water column was removed by seaweed uptake only. Growth of seaweed is affected by AN concentration and environmental conditions (PPFD, water temperature).

3.1.1 Basic equation

Material balance;

The material balance of TAN in a unit volume of shrimp pond is given by,

$$\frac{dC_{TAN}}{dt} = r_{total,TAN} - r_{total,remove} \quad (6)$$

where $r_{total,TAN}$ is total generation rate of TAN, $r_{total,remove}$ is total removal rate of TAN.

3.1.2 TAN removal

The removal rate of TAN in a unit volume of shrimp pond is given by,

$$r_{total,remove} = \rho_U \pi_{TAN} \quad (7)$$

where ρ_U is density of seaweed in shrimp pond, π_{TAN} is the specific uptake rate of TAN by seaweed.

Growth yield of seaweed against TAN;

The specific uptake rate of TAN by seaweed, π_{TAN}, is described by,

$$\pi_{TAN} = \frac{\pi_{max} C_{TAN}}{K_M + C_{TAN}} \quad (8)$$

the maximum specific uptake rate of TAN, π_{max}, in eq. (8) is described by,

$$\pi_{max} \propto \mu_{max} \frac{I}{I_S + I} \exp\left[-\frac{E}{R(T+273)}\right] \quad (9)$$

given $K_S = K_M$, π_{max} could be represented by,

$$\pi_{max} = \frac{\mu_{max}}{Y_G} \quad (10)$$

where growth yield of seaweed, Y_G, was 2.1 kgDM kg^{-1}-N.

The specific growth rate of seaweed;

The specific growth rate of seaweed is given by,

$$\mu = \mu_{max} \frac{C_{TAN}}{K_S + C_{TAN}} \frac{I}{I_S + I} \exp\left[-\frac{E}{R(T+273)}\right] \quad (11)$$

the value of specific growth rate is changed with TAN concentration and environmental conditions in shrimp pond.

Environmental conditions;

Time course of PPFD in shrimp pond;

Time course of PPFD in shrimp pond is given by,

$$I = I_{max} \sin^2\left[\frac{\pi(t-6)}{12}\right] \quad (6\ \text{h} \le t < 18\ \text{h}) \quad (12)$$

$$I = 0 \quad (0\ \text{h} \le t < 6\ \text{h},\ 18\ \text{h} \le t < 24\ \text{h}) \quad (13)$$

with PPFD at the time of maximum solar height (midday), I_{max} is 1800 μmol m^{-2} s^{-1} in fine days, is 100 μmol m^{-2} s^{-1} in cloudy or rainy days.

Time course of water temperature in shrimp pond;

Time course of water temperature in shrimp pond is given by,

$$T = T_{min} + (T_{max} - T_{min}) \sin\left(\pi \frac{t - LSH + \frac{DL}{2}}{DL + 2P}\right) \quad (6\ \text{h} \le t < 18\ \text{h}) \quad (14)$$

$$T = \frac{T_{min} - T_S \times \exp\left(-\frac{\eta}{\tau}\right) + (T_S - T_{min}) \times \exp\left(-\frac{t - t_S}{\tau}\right)}{1 - \exp\left(-\frac{\eta}{\tau}\right)} \quad (0\ \text{h} \le t < 6\ \text{h},\ 18\ \text{h} \le t < 24\ \text{h}) \quad (15)$$

with maximum daily water temperature, T_{max} = 30 °C, minimum daily water temperature, T_{min} = 25 °C, the time of maximum solar height (midday), LSH = 12 h, day length, DL is 12 h, the delay in T_{max} with respect to LSH, P = 2 h, sunset temperature, T_S = 28.5 °C, sunset time, t_S = 18 h, time coefficient, τ = 4 h^{-1} and night length η = 24 h - DL. **Fig. 3.1.2-1** and **Fig. 3.1.2-2** show time course of PPFD and water temperature in shrimp pond.

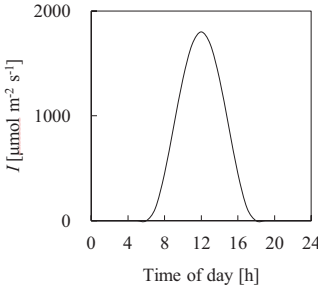

Fig. 3.1.2-1 Time course of PPFD

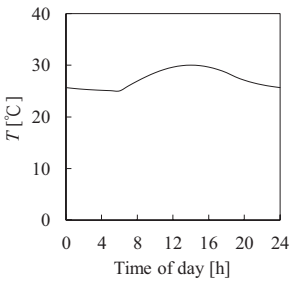

Fig. 3.1.2-2 Time course water temperature

Water balance in shrimp pond;

Water balance in shrimp pond is given by,

$$\Delta h = f_{Rain} + f_{Run} + f_{In} - f_{Evap} - f_{Out} - f_{Seep} - f_{Over} \quad (16)$$

where f_{Rain}, f_{Run}, f_{In}, f_{Evap}, f_{Out}, f_{Seep}, f_{Over} are water flow rate to and from shrimp pond, each is rainfall, runoff, inflow, evaporation, outflow, seepage, and overflow. In this study, f_{Run} = 1.25 × 10^{-5} m h^{-1}, f_{Evap} = 1.29 × 10^{-4} m h^{-1}, f_{Seep} = 2.17 × 10^{-4} m h^{-1}, f_{In} = f_{Out} = f_{Over} = 0 m h^{-1}, and on rainy days, f_{Rain} = 5.20 × 10^{-4} m h^{-1} and f_{Evap} = 0 m h^{-1}.

3.1.3 TAN generation

Total generation rate of TAN is given by,

$$r_{total,TAN} = r_{Shr,TAN} + r_{Sed,TAN} \quad (17)$$

where $r_{Shr,TAN}$ is rate of TAN excreted by shrimp respiration, $r_{Sed,TAN}$ is rate of TAN generated by sediment decomposition. $r_{Shr,TAN}$ is given by,

$$r_{Shr,TAN} = q_{TAN} r_{mtb,N} \quad (18)$$

where q_{TAN} is TAN fraction from shrimp respiration to total nitrogen metabolite. $r_{mtb,N}$ is excretion rate of nitrogen metabolite from shrimp per unit volume of shrimp pond and given by,

$$r_{mtb,N} = a_{mtb,N} \rho_S M_S^{\gamma} \quad (19)$$

where $a_{mtb,N}$ is nitrogen metabolite from shrimp per unit shrimp mass. ρ_S is culture density of shrimp. M_S is average shrimp mass and estimated from growth model. γ is allometric scaling of shrimp metabolism. On the other hand, $r_{Sed,TAN}$ is given by,

$$r_{Sed,TAN} = r_r M_{Sed,N} \quad (20)$$

where r_r is rate constant of decomposition. $M_{Sed,N}$ is

amount of nitrogen contained in sediment per unit volume of shrimp pond. $M_{Sed,N}$ include the sediment derived from uneaten feed and nitrogen metabolite from shrimp.

3.2 Main calculation conditions

In this study, *Penaeus monodon* was selected as model shrimp and cultivated 90 days. $C_{TAN,0}$ and $M_{Sed,N,0}$ were estimated 0 kg-N m^{-3}. $\rho_{U,0}$ was 1.0 kgDM m^{-3} and culture density of shrimp, $\rho_{S,0}$ was 40 m^{-3}. Pond area, A and depth, h were 4000 m^2 and 1.0 m.

3.3 Results and discussion

In developing countries, recommended maximum TAN concentration in shrimp ponds is 1.0×10^{-3} kg-N m^{-3}. **Fig. 3.3-1** shows daily variation of TAN concentration in shrimp pond at 06:00 a.m. and 12:00 p.m. On each day, TAN concentration has large difference over the time of day. Since seaweed could take in TAN efficiency around 12:00 p.m., TAN concentration in shrimp pond was very low. On the other hand, from night to morning, seaweed could not take in TAN very well, so TAN concentration in the morning is high. However, using seaweed, TAN concentration was controlled under the recommended maximum concentration. **Fig. 3.3-2** shows time course of seaweed density in shrimp pond. Seaweed increased from 1.00 kgDM m^{-3} to 1.12 kgDM m^{-3} in 90 days. On this cultivation, we obtained 480 kgDM seaweed as by-product. However, since shrimp pond is large in area, seaweed density in shrimp pond did not increase excessively. So harvest of seaweed is not necessarily often times.

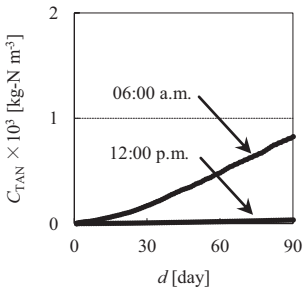

Fig. 3.3-1 Daily variation of TAN concentration in shrimp pond at 06:00 a.m. and 12:00 p.m.

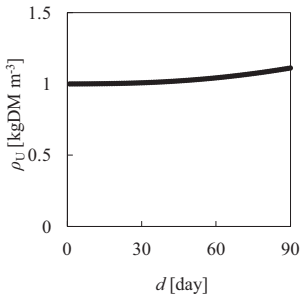

Fig. 3.3-2 Time course of seaweed density in shrimp pond

4 Conclusion

We could measure and quantitatively detect AN uptake and growth of sterile seaweed and examine the effect of operating conditions for specific growth rate and modeled mathematically. Next, the water quality control method by using sterile seaweed could remove AN in shrimp pond effectively and this method allows us to obtain a large amount of seaweed as by-product.

Nomenclature

A	Shrimp pond area [m^2]
$a_{mtb,N}$	Nitrogen metabolite excretion rate [kg-N kg-shrimp^{-1} h^{-1}]
C_{TAN}	Total ammonia nitrogen (TAN) concentration [kg-N m^{-3}]
d	Cultivation time [day]
DL	Day length [h]
E	Apparent activation energy for growth of seaweed [J mol^{-1}]
f_{Evap}	Flow rate of evaporation water from shrimp pond [m h^{-1}]
f_{In}	Flow rate of inflow water to shrimp pond [m h^{-1}]
f_{Out}	Flow rate of outflow water from shrimp pond [m h^{-1}]
f_{Over}	Flow rate of overflow water from pond [m h^{-1}]
f_{Rain}	Flow rate of rainfall water to shrimp pond [m h^{-1}]
f_{Run}	Flow rate of runoff water to pond [m h^{-1}]
f_{Seep}	Flow rate of seepage water from pond [m h^{-1}]
h	Depth of shrimp pond [m]
I	Photosynthetic photon flux density (PPFD) [μmol m^{-2} s^{-1}]
I_{max}	PPFD at the time of maximum solar height (midday) [μmol m^{-2} s^{-1}]
I_S	Half saturation constant of PPFD for growth [μmol m^{-2} s^{-1}]
K_g	Growth coefficient of shrimp [h^{-1}]
K_m	Existence coefficient of shrimp [h^{-1}]
K_M	Half saturation constant of TAN concentration for uptake [kg-N m^{-3}]
K_S	Half saturation constant of TAN concentration for growth [kg-N m^{-3}]
LSH	Time of maximum solar height [h]
M_S	Shrimp mass [kg-shrimp]
$M_{S,0}$	Shrimp mass at initial [kg-shrimp]
$M_{S,max}$	Shrimp mass at maximum grown [kg-shrimp]
$M_{Sed,N}$	Nitrogen in sediment per unit volume of pond water [kg-N m^{-3}]
P	Delay in T_{max} with respect to LSH [h]
q_F	Feed rate per shrimp mass [kg-feed kg-shrimp^{-1} h^{-1}]
q_{TAN}	TAN fraction from shrimp respiration to total nitrogen metabolite [-]
R	Gas constant [J mol^{-1} K^{-1}]
r_F	Feed rate per unit area of shrimp pond [kg-feed h^{-1}]
$r_{mtb,N}$	Nitrogen metabolite excretion rate by shrimp [kg-N m^{-3} h^{-1}]
r_r	Rate constant of sediment decomposition [h^{-1}]
R_S	Fraction of shrimp assimilation in feed [-]
R_{Sed}	Fraction of leftover in feed [-]
$r_{Sed,TAN}$	TAN generation rate from sediment [kg-N m^{-3} h^{-1}]
$r_{Shr,TAN}$	Excretion rate of TAN by shrimp respiration [kg-N m^{-3} h^{-1}]
$r_{total,remove}$	Total TAN removal rate [kg-N m^{-3} h^{-1}]
$r_{total,TAN}$	Total TAN generation rate [kg-N m^{-3} h^{-1}]
t	Time [h]
T	Water temperature [°C]
t_{max}	Cultivation time [h]
T_{max}	Maximum daily water temperature [°C]
T_{min}	Minimum daily water temperature [°C]
t_S	Sunset time [h]
T_S	Sunset temperature [°C]
Y_G	Growth yield of seaweed against TAN [kgDM kg^{-1}-N]
γ	Allometric scaling of metabolism [-]
η	Night length (24 h - DL) [h]
μ	Specific growth rate of seaweed [h^{-1}]
μ_{max}	Maximum specific growth rate of seaweed [h^{-1}]
π_{max}	Maximum specific uptake rate of TAN [kg-N kgDM^{-1} h^{-1}]
π_{TAN}	Specific uptake rate of TAN [kg-N kgDM^{-1} h^{-1}]
$\pi_{TAN,0}$	Initial specific uptake rate of TAN [kg-N kgDM^{-1} h^{-1}]
ρ_S	Culture density of shrimp [m^{-3}]
ρ_U	Density of seaweed in culture medium [kgDM m^{-3}]
$\rho_{U,0}$	Density of seaweed in culture medium at initial [kgDM m^{-3}]
$\rho_{U,t}$	Density of seaweed in culture medium at t [kgDM m^{-3}]
τ	Time coefficient [h^{-1}]

Literature Cited

[1]Primavera, J.H.; "Tropical Shrimp Farming and Its Sustainability," *Tropical Mariculture*, S. S. De Silva ed., pp. 257-289, Academic Press, San Diego, U.S.A. (1998)

[2]Haywood, G.P.; "Ammonia Toxicity in Teleost Fishes: A Review," Can. Tech. Rep. *Fish Aquat. Sci*., 1177, 1-35 (1983)

[3]Chen, J. C. and C. C. Tu; "Influence of Ammonia on Growth of Penaeus monodon Fabricius Post–Larvae," *Aquaculture and Fisheries Management*, 22, 457-462 (1991)

[4]Sato, K., Eksangri, T., Egashira, R.; "Ammonia-Nitrogen Uptake by Seaweed for Water Quality Control in Intensive Mariculture Ponds," *J. Chemical Engineering of Japan*, 39, 247-255 (2006)

[5]Burford, M. A., Lorenzen, K., "Modeling nitrogen dynamics in intensive shrimp ponds: the role of sediment remineralization," *Aquaculture*, 229, 129-145(2004)

EXPERIMENTAL INVESTIGATION ON INFLUENCES OF STEEL AND PRESTRESS ON THE EFFECTIVITY OF DESALINATION METHOD

Student Number: 10M18039 Name: Masato Kubota Supervistor: Nobuaki Otsuki

脱塩工法の有効性に及ぼす鋼材およびプレストレスの影響に関する実験的検討

久保田　昌登

本研究では、丸鋼、異形鉄筋、PC 鋼棒、PC より線を用いて、(1)脱塩前の防食性能に及ぼす鋼材の種類及びプレストレスの影響、(2)脱塩後におけるコンクリート中の塩分分布に及ぼす鋼材の種類及びプレストレスの影響、(3)脱塩後の RC 及び PC 試験体の防食性能に及ぼす鋼材の種類及びプレストレスの影響について実験的に検討することを目的とした。その結果、(1)プレストレスの影響により鋼材の防食性能は低下する可能性が示された。また、(2)鋼材の種類及びプレストレスの影響により脱塩後におけるコンクリート中の塩分分布に影響はないことが確認された。(3) RC 試験体及び PC 試験体において脱塩による防食性能の向上が確認され、RC 試験体の方が効果は大きいことが示された。

1. Introduction

Desalination method is one of the electrochemical corrosion control methods. And it is effective for deteriorated structures by chloride attack. Figure 1 shows principle of desalination method. Direct current is applied between external electrode and reinforcing bar in concrete members. And chloride ion is taken out by electrophoresis[1]. Desalination can recover corrosion protection performance of deteriorated members. Therefore it is applied for Reinforced Concrete (RC) and Prestress Concrete (PC) structures[2]. However, there was no research to investigate the influences of types of steel and existence of prestress on corrosion protection performance after desalination.

This research focus on four different types of steel such as round bar, deformed bar, PC steel rod and PC strand. In the case of PC steel rod and PC strand, the existence of prestress are also focused.

Objectives of this research are (1) to investigate corrosion protection performance of each steel bar,(2) to investigate distribution of chloride ion in concrete after desalination and (3) to investigate corrosion protection performance of RC and PC specimen after desalination depending on types of steel and existence of prestress.

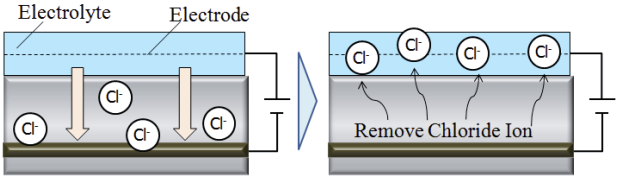

Fig.1 Priciple of Desalination Method

2. Experimental Procedure

2. 1 Specimen

2.1.1 Mortar Specimens

By using each type of steel, mortar specimens, 40×40×160mm with rectangular cross section, were casted including 0 to 9kg/m^3 chloride content with early strength portland cement. After casting, each specimen was cured for 50 days in distilled water.

2.1.2 Concrete Specimens

Table 1 shows the details of specimens. RC specimens were constructed with early strength portland cement by using round bar and deformed bar, and PC specimens were constructed by using PC steel rod and PC strand. Concrete specimens, 100×100×500mm with rectangular cross section, were casted with 9kg/m^3 chloride content. After curing specimens, desalination method has been carried out for 8weeks with 1A/m^2 or 3A/m^2 direct current. After desalination method, specimens have been exposed to corrosion acceleration environment (wet and dry) for 40 weeks.

Table 1 Details of Specimen

Types of Steel	Chloride Content	Current Density
Round Bar SR235 Ø13mm	9kg/m^3	-
		1A/m^2
		3A/m^2
Deformed Bar SD295A D13	9kg/m^3	-
		1A/m^2
		3A/m^2
PC Steel Rod SBPR930/1180 Ø13mm	9kg/m^3	-
		1A/m^2
		3A/m^2
PC Strand SWPR7B Ø12.7mm	9kg/m^3	-
		1A/m^2
		3A/m^2

2.2 Evaluation Method

In the test for chloride threshold content, corrosion current density was calculated by polarization curve. After calculation, existence of passive firm was evaluated by the value refer to CEB standard[3].

Distribution of chloride ion in concrete was evaluated based on extraction of total chloride content following JIS A 1154.

Corrosion protection performance after desalination was evaluated by electrochemical measurement such as corrosion potential and polarization resistance, and direct evaluation of internal steel bar such as corrosion weight loss and visual observation.

3. Corrosion Protection Performance of each Steel Bar before Desalination

3.1 Influence of Types of Steel Bar

Figure 2 shows corrosion current density for each type of steel with 0 to 9kg/m^3 chloride content. Based on CEB standard, passive firm is deteriorated in the case that value of corrosion current density is more than 0.1μA/cm^2. Therefore, value of chloride content, when corrosion current density is over more than 0.1 μ A/cm^2, can be defined as value of chloride threshold content for each types of steel.

From these results, value of chloride threshold content for round bar was 2 to 3kg/m^3, for deformed bar was 0 to 2kg/m^3 for PC strand was 0 to 1kg/m^3. In the case of PC steel rod, chloride threshold content was not able to evaluate exactly. And PC steel rod and PC strand have corrosion protection performance in 7 to 9kg/m^3 chloride content in the case of no prestress specimen.

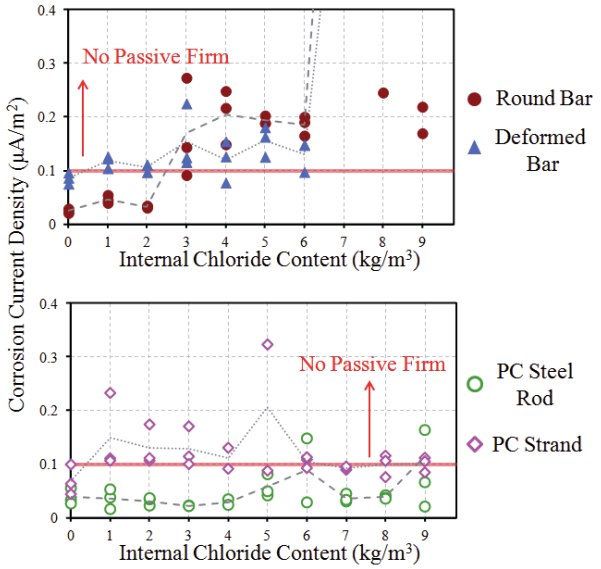

Fig.2 Relationship between corrosion current density and chloride content for each type of steel

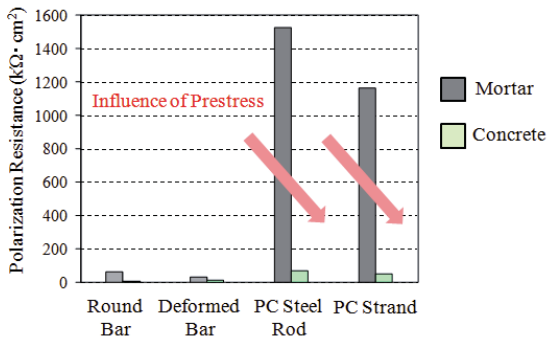

Fig.3Polarization Resistance depending on existence of prestress (Cl$^-$ 9kg/m^3)

3.2 Influence of Prestressing

Figure 3 shows comparison between polarization of Mortar and that of PC specimen with 9kg/m^3 chloride content in the case of PC steel rod and PC strand.

From the result, polarization resistances of Mortars were much higher than those of PC specimens used in PC steel rod and PC strand. Therefore it is verified that corrosion protection performance is lower by influence of prestress.

4. Distribution of Chloride Ion in concrete after Desalination Depending on Types of Steel Bar and Existence of Prestress

Chloride content in concrete was measured for RC specimen used in round bar and deformed bar and PC specimen used in PC steel rod and PC strand. Figure 4(a) shows distribution of chloride content in concrete immediately after desalination with 1A/m^{2}for each type of steel. And Figure 4(b) shows that after exposure test for 40 weeks. Figure 5 shows in same

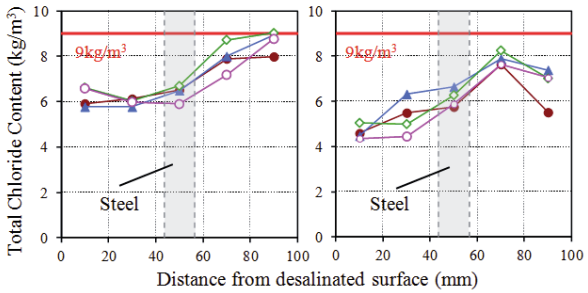

(a) After Desalination (b) After 40 weeks

Fig. 4 Desalination with 1A/m^2

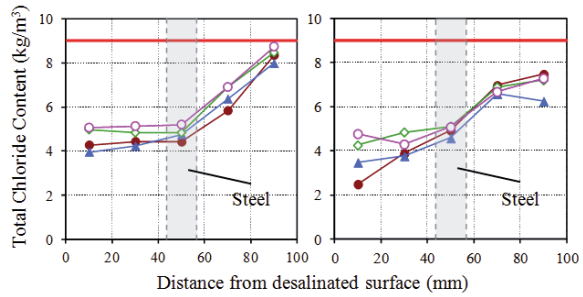

(a) After Desalination (b) After 40 weeks

Fig. 5 Desalination with 3A/m^2

: Round Bar : PC Steel Rod : Before Energization

: Deformed Bar : PC Strand

case of desalination with 3A/m^2. From Figure 4(a) and 5(a), in the case of 1A/m^2, desalination rate in all types of steel was 25 to 35% near the location of steel bar and it was more than 40 to 50% in the case of 3A/m^2. From this results, it could be verified that desalination rate in all types of steel found to be same.

As a result of Figure 4(b) and 5(b), total chloride content near the location of steel bar remained about 5 to 6kg/m^3 and 4 to 5kg /m^3. Therefore, it could be verified chloride contents near the location of steel bar after exposure test are almost same as immediately after desalination.

From the results, it is verified that types of steel and existence of prestress don't influence on distribution of chloride ion in concrete.

5. Corrosion Protection Performance of RC and PC specimens after Desalination Depending on Types of Steel and Existence of Prestress

5.1 Influence of Prestressing

Comparing between prestressed specimens and non prestressed specimen, it would be verified how corrosion protection performance was influenced by existence of prestress. Figure 6 shows polarization resistance depending on existence of prestress using in PC steel rod and PC strand on 4th week under exposure test. Based on CEB standard[3], at > 130kΩ· cm^2, passive firm around steel bar is exist.

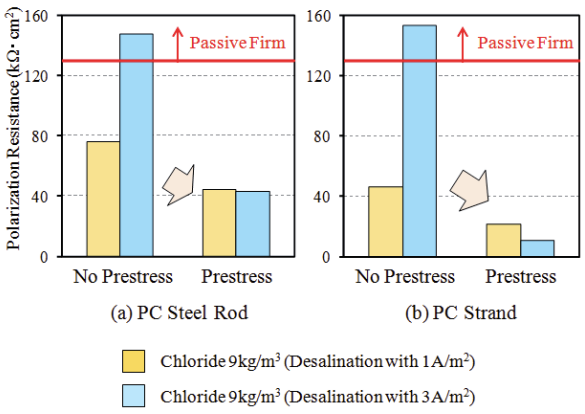

Fig.6 Polarization resistance depending on existence of prestress on 4th week under exposure test

In the case of desalinated specimen used in PC steel rod, polarization resistances of non prestressed specimens were smaller than prestressed specimens. In the case of PC strand, polarization resistances of non prestressed specimens were also smaller than prestressed specimens. Therefore, from the results by electrochemical measurement, it was partly proved that corrosion protection performance after desalination was influenced by prestressing.

5.2 Corrosion Protection Performance of RC and PC Specimen

5.2.1 Evaluation by Electrochemical Measurement

In corrosion monitoring, corrosion potential which can evaluate corrosion protection performance qualitatively was measured for 40 consecutive weeks. Based on ASTM-C 846[4], more than 90% no corrosion at > -326mV (vs Ag/AgCl), and more than 90% corrosion at < -479mV (vs Ag/AgCl).

Figure 7 shows corrosion potential for each type of steel under corrosion acceleration environment. In the case of round bar and deformed bar, corrosion potentials of desalinated specimen were higher than those of non desalinated specimens including 9kg/m^3. It was partly proved that desalinated specimens remain corrosion protection performance. On the other hand, in the case of PC specimens used in PC steel rod and PC strand, corrosion potentials of desalinated specimens were found to be almost same tendency as non desalinated specimens. From the results, corrosion protection performance improved in the case of both RC and PC specimens by desalination. Especially, RC specimens show higher performance than PC specimen.

5.2.2 Evaluation by Corrosion Weight loss and Visual Observation of Internal Steel

As direct evaluation of internal steel bar, corrosion behavior for each specimen was evaluated by weight loss due to corrosion and visual observation.

As a result of Figure 8, for all types of steel, corrosion weight loss of desalinated specimen was smaller than non desalinated specimen including 9kg/m^3 chloride content. Therefore, desalination

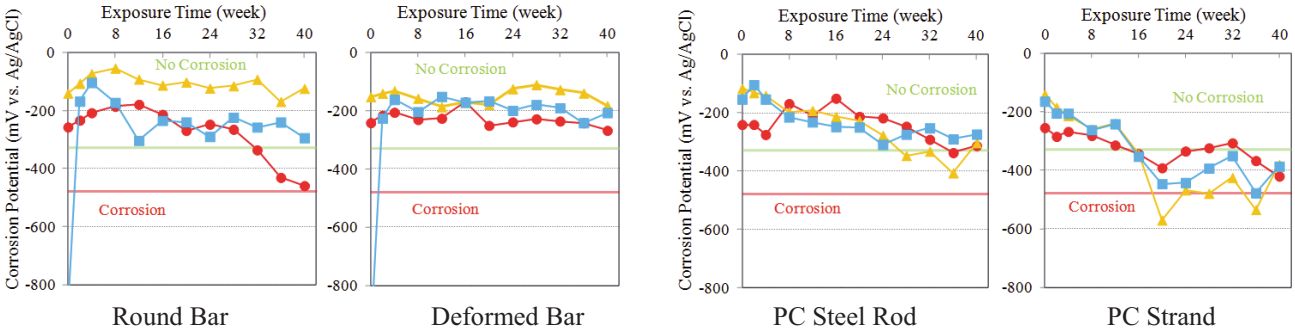

● : Cl- 9kg/m^3 No Desalination ▲ : Cl- 9kg/m^3 Desalination with 1A/m^2 ■ : Cl- 9kg/m^3 Desalination with 3A/m^2

Fig.7 Corrosion Potential for each type of steel under corrosion acceleration environment for 40 weeks

method had effects on improvement of corrosion protection performance for all types of steel. Based on CEB standard[3], at > 0.116mm/year is high corrosion rate. Weight loss due to corrosion in the case of desalinated RC specimens using round bar and deformed bar was smaller than PC specimens using PC steel rod and PC strand. Therefore, RC specimens had effects on desalination rather than in the case of PC specimens. Especially, in the case of round bar, desalination had highest effect on improvement of corrosion protection performance after desalination in all types of steel.

Figure 9(a)~(d) shows visual observation of internal steel in the case of round bar, deformed bar, PC steel rod and PC strand for non desalinated specimens and desalinated specimens with 1A/m^2 and 3A/m^2. As a result of visual observation, it was also verified that round bar in desalinated specimen was not corroded rather than non desalinated specimen. In the case of PC specimen, desalinated specimen was not corroded as much as non desalinated specimens. However there were many pitting corrosion holes in surface of steel. And PC strand in desalinated specimen, behavior of macro cell corrosion could be found.

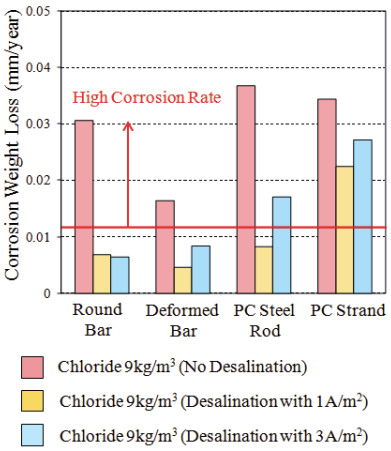

Fig.8 Corrosion weight loss after exposure test for 40 weeks

No Desalination

Desalination with 1A/m^2

Desalination with 3A/m^2

(a) Round Bar

No Desalination

Desalination with 1A/m^2

Desalination with 3A/m^2

(b) Deformed Bar

No Desalination

Desalination with 1A/m^2

Desalination with 3A/m^2

(c) PC Steel Rod

No Desalination

Desalination with 1A/m^2

Desalination with 3A/m^2

(d) PC Strand

Fig.9 Visual Observation of Internal Steel after exposure test for 40 weeks

6. Conclusions

Objectives of this research are (1) to investigate corrosion protection performance of each steel bar, (2) to investigate distribution of chloride ion in concrete after desalination and (3) to investigate corrosion protection performance of RC and PC specimen after desalination depending on types of steel and existence of prestress.

(1) By electrochemical measurement, it is partly proved that value of chloride threshold content in the case of round bar is 2 to 3kg/m^3, in the case of deformed bar is 0 to 2kg/m^3 and in the case of PC strand is 0 to 1kg/m^3.In the case of PC steel rod, chloride threshold content was not able to evaluate exactly.

Using in PC steel rod and PC strand, it is partly proved that corrosion protection performance was influenced by prestressing.

(2) From investigation of total chloride content in concrete after desalination and exposure test, distribution of chloride ion was not affected by types of steel and existence of prestress.

(3) Using in PC steel rod and PC strand, it is partly proved that corrosion protection performance after desalination was influenced by prestressing.

By evaluation of electrochemical measurement, weight loss due to corrosion and visual observation of internal steel, desalination method have effects on improvement of corrosion protection performance in the case of RC specimens rather than PC specimens.

[Reference]

[1] Japan Society of Civil Engineers : Electrochemical Corrosion control method, Concrete Library107, 2001

[2] K. Ashida, et.al : Research on Desalination of Concrete by Electrochemical Method, Docter thesis in Kyoto University, 1999

[3] CEB Working Party, commissions5 : Strategies for Testing and Assesment of Concrete Structures Affected by Reinforcement corrosion, ISBN2-88394-040-01, 2004

[4] ASTM C876-09 Standard Test Method for Half-Cell Potentials of Uncoated Reinforcing Steel in concrete

THERMAL IMAGE VELOCIMETRY (TIV) AND APPLICATIONS

Student Number：10M18045 Name：Hideaki KUMEMURA Supervisor：Manabu KANDA

熱画像風速測定法（TIV）の開発と応用

久米村秀明

本論では，複雑な都市境界層における乱流場の定量的把握を目的として，連続した熱画像を用いて物体表面近傍の二次元速度場を推定する Thermal Image Velocimetry （TIV）法を提案する．本手法を時空間スケールの大きく異なる３つの都市大気現象に適用し，以下の知見を得た．1．TIV 手法は建物スケールから大気境界層スケールの乱流の時空間構造を取得可能であること，2．TIV 速度は超音波風速計風速と良好な相関を有し，測定精度が十分あること，3．キャリブレーションにより，超音波風速計高度に対応する二次元風速を TIV 速度から同定可能であること，である．

1. Introduction

It is widely recognized in many big cities that urban heat island and urban localized heavy rain has become a serious problem. Recently, urban meteorology has made rapid progress owing to many cross-sectional researches and projects. However, the capture of complicated turbulent fields in urban boundary layer is still a big challenge in modelizations and systematizations[1].

Numerical simulations such as Large Eddy Simulation are one way to better understand the urban atmospheric turbulent fields. However, the validation data is very poor and the applicability of numerical methods in complicated urban boundary layers is questionable. The lack of validation data is mainly coming from the restriction of measurements system; most of field data is on the basis of point measurements using sonic anemometer.

One promising way to overcome the limitation is through Particle Image Velocimetry (PIV); it can obtain 2D spatial distribution of turbulences. Recently, PIV was used for a wide range of visualization of flows; flows around cars and airplanes in wind tunnels, river channel flows or coastal currents, medical tubing and apparatus of respiratory models. These applications of PIV are mostly for indoor model experiments. Recently, Takimoto et al. successfully applied PIV to outdoor experiments[2]. However, a significant limitation of PIV in real fields is that it can only be used during nighttime as it utilizes laser lights.

In very recent years, some researchers have tried to use thermal imaging to capture complicated turbulent flows[3-5]. However, these are still trial stage; just seeing the temporal and spatial images of thermal camera and discussing qualitatively in relation to turbulent structure. The authors came up with the idea of Thermal Image Vecocimetry (TIV) by combining with the previous PIV technology and the progressing high-frequency thermal video imagery. A high-frequency infrared camera is hopefully used to quantify the velocity field.

The objectives of this study are as follows: (1). To develop the algorithm of thermal image velocimetry to quantify airflows and turbulences. (2). To evaluate the accuracy of the quantifying TIV velocities in comparison with the conventional sonic anemometers. (3). To make a physical interpretation of the quantified velocities using meteorologically observed data.

2. Methodology

The velocity distribution near a surface is estimated based on the same algorithm of PIV but with usage of temperature images instead of tracer concentration. Then, special method is necessary to detect clear images of temperature fluctuation purely corresponding to turbulent motions. For this purpose, this section descries utilization of Styrofoam™ and a preprocess using short time averaging.

2.1. Utilization of Styrofoam™

An infrared camera takes continuous thermal images. It is preferred that anomaly temperatures of each grid are bigger. Therefore, it is not simple to apply this method for building walls because concrete and other construction materials have high heat capacities and the temperature fluctuations are small.

Styrofoam™RB-GK- Ⅱ (Dow Chemical Company Co., Shinagawa, Japan), which has small heat capacity was attached on a building wall. Styrofoam™ surface temperatures respond quickly to wind due to its small heat capacity and low thermal conductivity.

2.2. Averaging time of anomaly tem-

peratures

Not only wind but also surface shapes cause heterogeneity in surface temperature distribution. It is necessary to remove the latter's influence in order to identify the surface temperature fluctuations purely attributed to turbulent motions.

This was done by subtracting a local and short time mean temperature from the raw temperature, because the influence of the surface shapes always stays in the same position as a background noise.

3. Experiment

TIV was applied to three different surfaces: (1). in roof of a 1/5 scale model building (COSMO; Comprehensive Outdoor Scale Model experiment for urban climate), (2). full-scale building wall, (3). in artificial turf. One of the motivations of the choice of these areas is the difference of spatio-temporal scales (Table 1). The applicability of TIV in various scales of field and phenomena should be examined.

Table 1. Experimental data

	Date	Image capture area	distance from the surface
COSMO	09/13/2011	1.5 m×1.5 m	0 mm
Building wall	12/16/2010-12/18/2010	3 m×11 m	35 mm
Field	10/12/2011 01/18/2012	60 m×80 m	1300 mm

3.1. Scale model building (COSMO)

COSMO is made up of 512 concrete cubes, which is 1.5 m on a side, on a flat plate extending 50 m by 100 m horizontally. The cubes are aligned regularly. Styrofoam™ was attached on the entire roof surface of a cube and its surface temperature image is taken by an infrared camera (FSV-1100; Apiste Co., Osaka, Japan) in 30 Hz. The experiment was conducted on 13 September 2011.

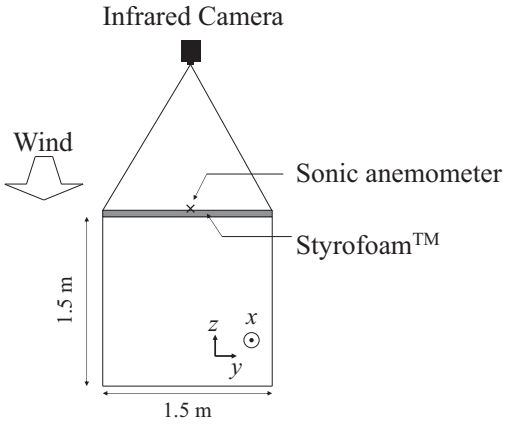

Figure 2. The observation setup. (COSMO)

3.2. Full-scale building wall

The TIV method was applied to a real building wall. The target wall is Ishikawadai 3rd building in Tokyo Institute of Technology (Tokyo Tech). Styrofoam™ were painted black and attached to the vertical wall (Figure 3a). Thermal images were taken in a section of 3 m horizontally and 11 m vertically at a frequency of 30 Hz. Figure 3b shows the example of the temperature image taken in the building wall. This experiment was conducted on 16-18 December 2010.

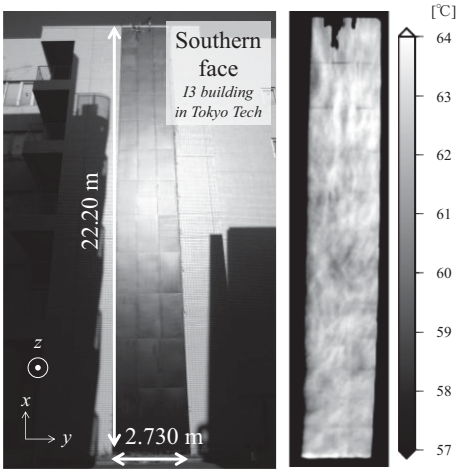

Figure 3(a). The observation wall (Left)
Figure 3(b). A thermal image (Right)

3.3. Artificial turf (Tokyo Tech ground)

TIV method was also applied to geophysical ground surface to obtain a footprint of boundary layer-scale phenomena. This experiment was conducted in Tokyo Tech ground whose surface is made of artificial turf. The test area was set to 60 m ×80 m.

The experiment was conducted two times, 12 October 2011 and 18 January 2012. One of the experiments was done with that a ground based observation which includes the measurement using a sonic anemometer installed at 130 cm from the surface (Figure 4).

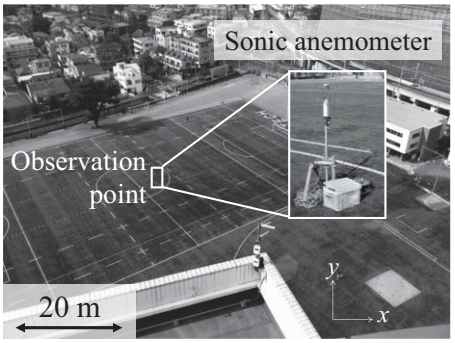

Figure 4. The observation setup (Tokyo Tech Field).

4. Results and discussion

4.1. Accuracy

Figure 5 shows the TIV velocity plotted with wind velocity measured by sonic anemometers which are installed from the surface as explained in the previous section. This figure demonstrates that TIV velocity is almost proportional to the wind velocity with correlation coefficients higher than 0.7 for all cases. This implies that the wind velocity can be estimated from the TIV velocity multiplying by a constant coefficient.

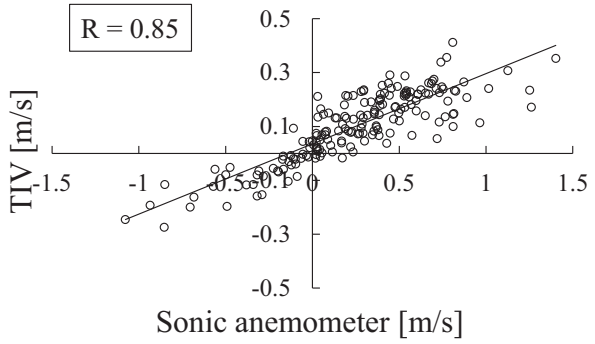

Figure 5(a). Point diagram of TIV velocities and wind velocities (COSMO).

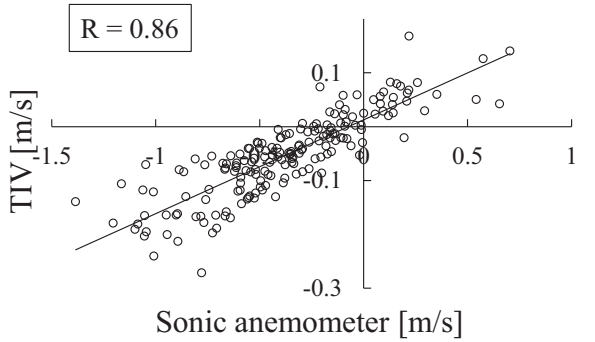

Figure 5(b). Point diagram of TIV velocities and wind velocities (Building wall).

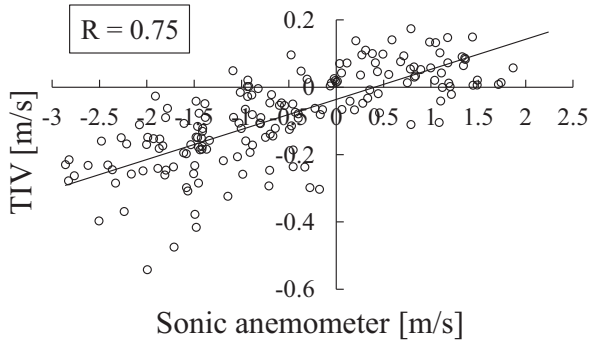

Figure 5(c). Point diagram of TIV velocities and wind velocities (Tokyo Tech Field).

It is also shown that the TIV velocity is always smaller than the wind velocity measured at higher elevation than the surfaces.

TIV velocity can be physically interpreted as the advection velocity of coherent structure passing over the surface. The advection velocity of the structure is large if the size of the structure is large since larger structure is affected by faster wind velocity at higher elevation from the surface. If the height of the turbulent structure which is tracked by TIV is lower than the location of the sonic anemometer, the TIV velocity becomes lower than the wind velocity measured by sonic anemometer. This situation possibly occurs because the large structure on the surface temperature fluctuation is effectively high-pass filtered by subtracting short-time average, and smaller structure is only tracked by TIV.

4.2. Turbulence formation

(a) COSMO

Figure 6 is the 2D distribution of velocity vectors obtained in the experiment in COSMO. In this figure, distinctive 2D-structures of turbulent motion can be seen: (a) Irruptive motions from left below edge are visible, (b) A divergence and (c) a convergence adjoiningly arises.

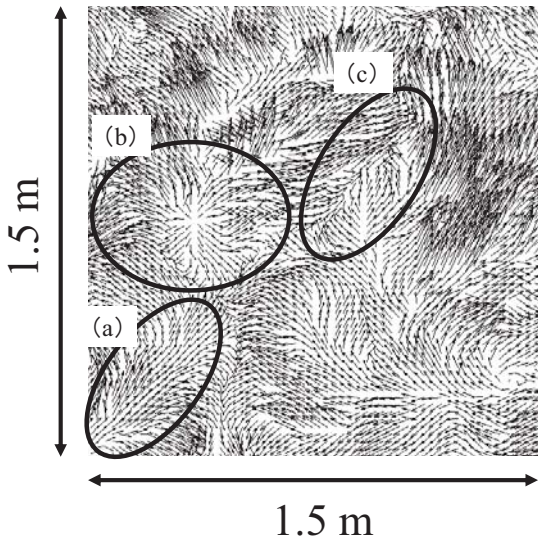

Figure 6. TIV vectors(COSMO). (a). Incursion into the area. (b). Divergence. (c). Convergence.

(b) Building wall

Anomaly temperatures and TIV vectors were calculated (Figure 7 and 8). Figure 7 shows an anomaly temperature. An area of +1 °C deviations move from bottom up. The same movement of temperature +1 °C deviations was observed in TIV vectors which lead upward flow of heat from bottom up (Figure 8).

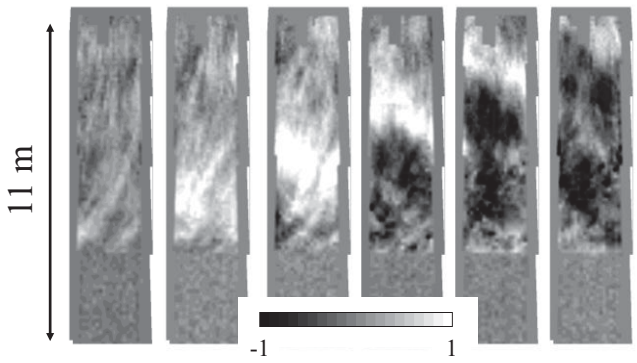

Figure 7. Thermal image of anomaly temperature (Building wall).

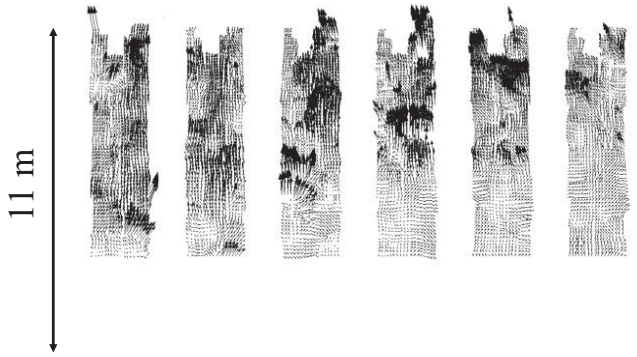

Figure 8. TIV vectors (Building wall).

(c) Artificial turf

Figure 9 shows an example of TIV vectors on the Tokyo Tech field. Convergence regions in the lower right area are clearly visible.

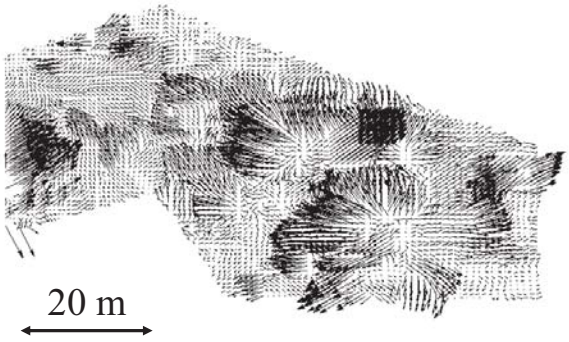

Figure 9. TIV vector of a field experiment (Tokyo Tech field).

6. Conclusion

A new technology to estimate velocity fields very close to a ridged wall by using a sequence of thermal images of the wall is proposed. We call this method Thermal Image Velocimetry (TIV). The principle TIV is utilizing thermal images instead of particle images. Although TIV can potentially obtain highly fluctuated turbulent fields, the surface temperature of the target wall should be sensitive to the velocity fluctuation nearby. We apply TIV to a model city, a building wall, and field, and discuss the performance of TIV. The wind variations estimated by TIV correlate very well with those observed by a sonic anemometer.

Acknowledgments

This work is supported by the Research Program on Climate Change Adaptation (RECCA). This research was partially supported by the Scientific Research, Young Scientific Research (B), 23760454, 2011. The Dow Chemical Company provided some Styrofoam^{TM}s.

References

[1]. Manabu Kanda : Progress in urban meteorology: A Review, *Journal of the Meteorological Society of Japan*, **85**, 365-383, 2007.

[2]. Hiroshi Takimoto, Ayumu Sato, Janet F.Barlow, Ryo Moriwaki, Atsushi Inagaki, Shiho Onomura, and Manabu Kanda : Particle Image Velocimetry Measurements of Turbulent Flow Within Outdoor and Indoor Urban Scale Models and Flushing Motions in Urban Canopy Layers, *Boundary-Layer Meteorology*, **140**, 295-314, 2011.

[3]. Christen, Andreas, Meier, Fred, Scherer, Dieter : High-frequency fluctuations of surface temperatures in an urban environment, *Theoretical and Applied Climatology*, Online First, DOI 10.1007/s00704-011-0521-x, 2011.

[4]. Christen A. and Voogt, J. A.: Inferring turbulent exchange processs in an urban street canyon from high-frequency thermography, *9th Symposium on the Urban Environment*, J3A.3, 2010.

[5]. Christen A. and Voogt, J. A.: Linking atmospheric turbulence and surface temperature fluctuations in a street canyon, *The 7th International Conference on Urban Climate*, A3-6, 2009.

QUANTITATIVE ANALYSIS OF SWARM OF MOSQUITOES BASED ON IN-SITU OBSERVATION IN RELATIONSHIP WITH ATMOSPHERIC ENVIRONMENT

Student Number: 10M18051 Name: Rai KONNO Superviser: Manabu KANDA

定量観測に基づいた都市河川周辺で発生する蚊柱濃度の時空間挙動と大気環境場との関連性の検討

今野　雷

都市河川で大量発生するユスリカの蚊柱が近隣住民の生活環境に不快な影響を及ぼしている．この問題に対し本研究では，既往の生物学的観点からではなく気象学的・流体力学的観点に基づく実測によって，大気環境場と蚊柱の関係性について検討を行った．その際，ユスリカ個体数を観測する手法を新たに提案した．

蚊柱を定量観測するための機器として，レーザーセンサー利用した非接触式のユスリカ個体数のカウンターを開発した．これを用い，定性的な観察・観測による知見を定量的に把握するために，都市河川においてカウンターによる観測を行った．以下が得られた知見である．

(1) 日の入り時刻の25分前に蚊柱発生量のピークを確認した．
(2) 河川側道の丁字路では頻繁に高濃度の蚊柱が観測された．
(3) 摂氏22.5℃付近を観測期間における蚊柱発生の適温帯として確認した．

1. Introduction

This is an experimental study to investigate the movement or deformation of swarms from a perspective of aerobiology. The movement of the swarm is not only affected by the active motion of the individual insects but also the surrounding flow field, which is especially focused on this study. The aim of this study is to construct an experimental basis on the prediction of their movement.

There are some experimental studies on the movement of swarms. Mathumura and Kusunoki (1998) detected aerial planktons in non-precipitation echo using the Doppler radar at 300~500m height. Seino (1987) verified that the planthoppers traveling long distances from Vietnam to China and Japan are flying in low-level jet stream pattern.

These studies are mainly focusing on the seasonal variation of large swarms at macro-scale, which extends more than few km horizontally. However, previous studies did not consider fluid mechanical feature in swarms' behavior.

The area of study is Nomikawa river where swarms of mosquitoes appear at a large scale sometimes causing disturbance in the surrounding neighborhood.

Traditionally, mosquitoes are trapped, collected, and observed in laboratories apart from their natural environment which weakens the reliability of results..

The objective of this study is to identify the relationship between the meteorological field and behavior of a swarm of chironomids with accordance to fluid mechanics. In order to achieve this, the swarm distribution must be preserved and observed remotely. A new method of observation and analysis was proposed without affecting the natural flight of mosquitoes.

2. Methodology

The first step was to identify the location of swarm. The selection criteria depended on the swarms' presence, wind velocity fluctuation and rainfall occurrence. The area selection was based on a series of primary observations done along Nomikawa River.

For a quantitative observation, a non-contact type counter was developed using 10 laser sensors to measure number of swarms.

Ten laser sensors were laid out vertically as shown in Fig.1. The center-to-center spacing of the sensors is 50m, and the length of the laser path is 500mm. The distances were optimized to capture large swarms without causing noise (Fig.2). The accuracy of the instrument was validated. The final counter was also calibrated.

For safety purposes, the counter was attached on a bicycle to maintain observation height and to

minimize the time lag of counting each swarm around the river. The observer did not mount on the bicycle.

To measure selected meteorological parameters of the surrounding environment, two thermocouples (φ=0.05mm) were attached on the counter. A video camera and electric switch were also installed to log the bicycle's location at an instant. Rechargeable batteries were used to power the whole set-up. Data was logged at 50Hz(Fig.3).

3. Observation

The observation points were located above the fence surrounding Nomikawa's upstream bounded by Kodai bridge and Sakai bridge at Meguro ward, Tokyo. Observing period was from 9/27 to 10/28 in 2011 autumn.

The observation height ranges from 180-230 cm from ground immediately above the 1.8m-high fence. The moving observation to measure the swarm of chironomids was conducted on the road-side surrounding the upstream part of Nomi-kawa river (Fig.4).

Observations were conducted three (3) laps for each day, initiated 30-min before sunset time (by NAOJ). Each lap has a 10-min interval. On average, one (1) lap took about 6 minutes. The observation conducted on September 27, 2010 was an exception with seven (7) laps without intervals. The results are also cited. Chironomid number of 16 sections on each side of the river were counted for every lap (refer to Fig.4)

An ultrasonic anemometer (Climatec CYG-81000) and thermo couples were installed at Tokyo Institute of Technology ground (red mark in Fig.4) for reference fixed-point observation.

10-min data of precipitation and water level at kodai bridge from tokyo metropolitan government were also obtained .

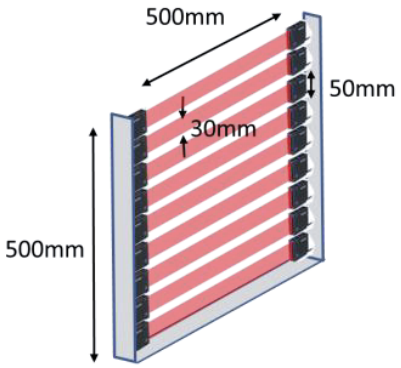

Fig.1 Layout of lasers

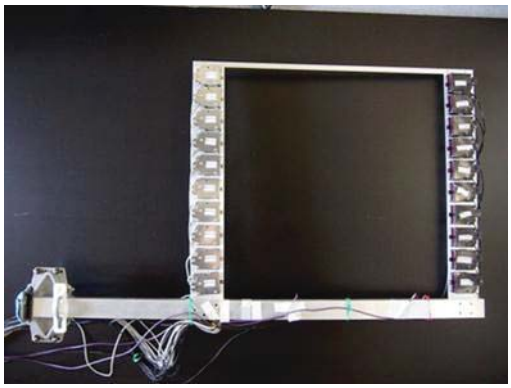
Fig.2 Counter part


Fig.3 Overview of the equipment

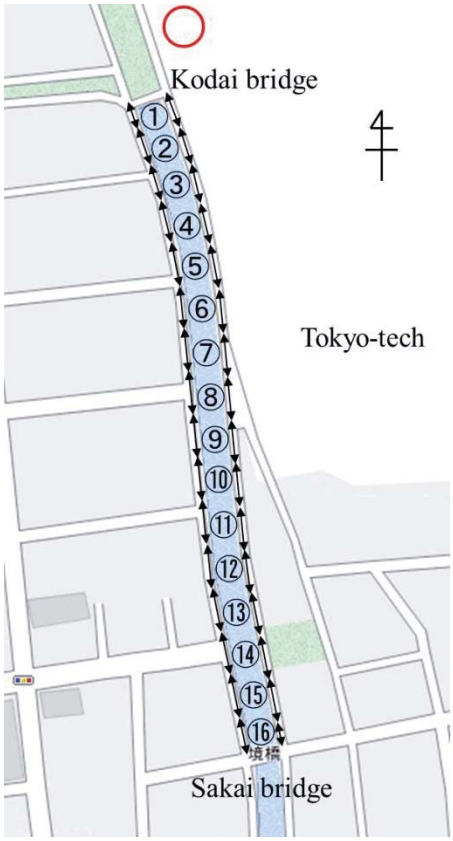

Fig.4 Observation area

4. Spatiotemporal dynamics of swarms

4.1 Time variation

The seasonal amount of increase and decline of the mosquitoes is shown in black line in Fig.5. The fluctuation of number of chironomids about for every 2-days is regarded as the life cycle of the chironomids.

The number of mosquitoes on each side of the river is also represented with red and blue lines. Constant deviation between the west side and east side was not observed for longer than 3 days.

Swarming of mosquitoes is restrained just after rainfall during day time. On the other hand, the swarms were not affected by rainfall occurring the night before the observation such as the observation conducted during October 8.

The concentration of swarm of mosquitoes in the observation area peaked 25-min on average before the sunset (Fig.7).

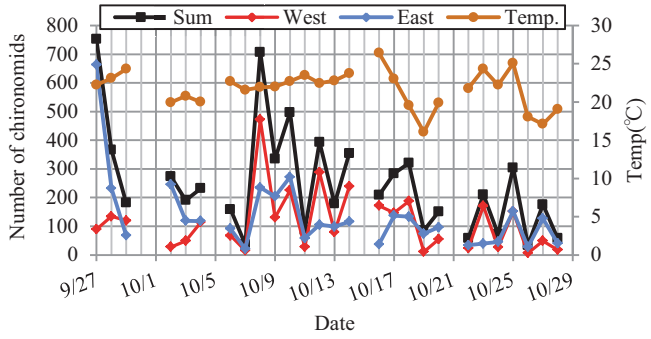

Fig.5 monthly change of number ofchironomids, temperature

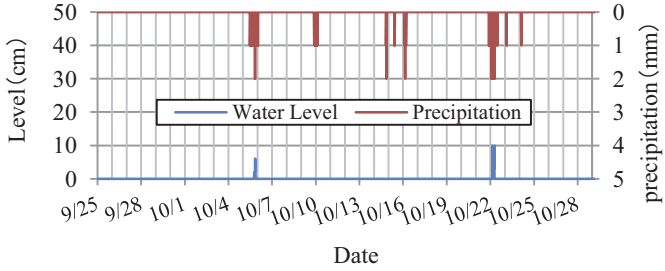

Fig.6 precipitation and water at kodai bridge

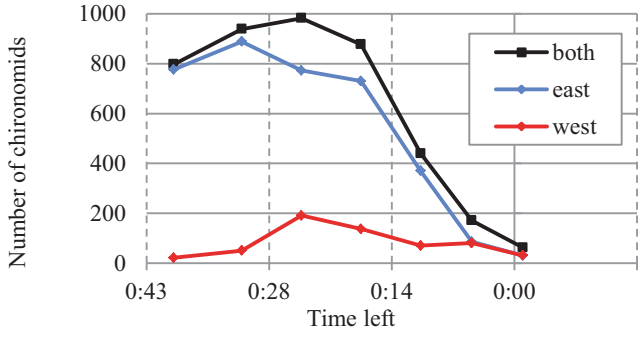

Fig.7 Daily change of number of chironomids

4.2 Spatial distribution

The area where a swarm of mosquitoes reached highest concentration could be seen in Figure 8. The swarms frequently occur on 3 points on 6 T-junctions on the roadside west of the Nomikawa (Fig.8: 11w, 14w, and 16w). This phenomenon was seen through the observation period.

The high concentration distribution spatially wasn't always seen in fixed section. There were also points with concentrations independent of time and space which means other factors could be influencing the swarms' presence.

T-junction points have common sunshine distribution just before sunset. This is because the T-junction provides minimum shade from the surrounding buildings. Previous studies also pointed out that man has higher sensitivity to ultraviolet rays than mosquitoes which is why light attracts mosquitoes more than humans. The existence of buildings may pose as a future threat to the mosquitoes survival.

4.3 Meteorological factor

The impact of weather and microclimate on the swarm was confirmed by the relationship between the temperature and the number of the chironomid.

A suitable temperature for swarm formation was observed. In Fig.9, it can be seen that 22.5-deg C had the highest occurrence of chironomids. This observation was also confirmed by the temperature histogram shown in Figure 10. Fig.11 shows the normalized number of chironomids by the number of sections for each temperature level.

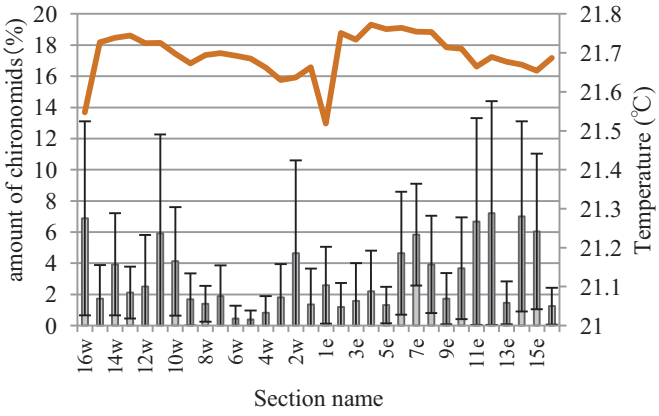

Fig.8 The sectionally-defined average appearance of the number of chironomid in observation period: e=east; w=west

In relation to the wind field, very low concentration of swarm of mosquitoes were observed when the wind velocity is large. Fewer than 50 chironomids were observed by a 1 observation round when the wind velocity exceeds 1.5 m/s (Fig.12). The effect of the direction of the wind couldn't be confirmed since southerly wind dominated throughout the duration of the observation (Fig. 13).

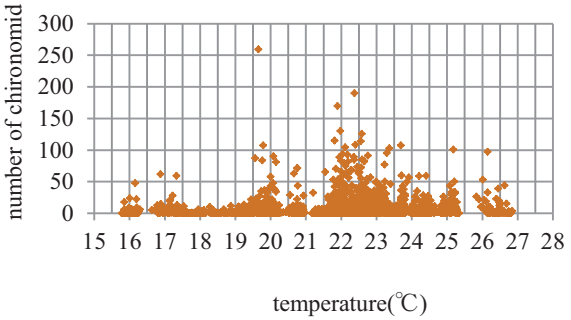

Fig.9 Number of chironomids vs. temperature

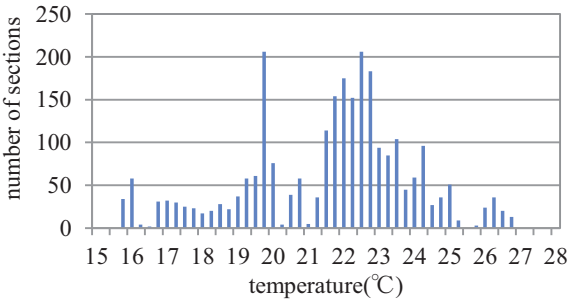

Fig.10 Histogram of Temperature

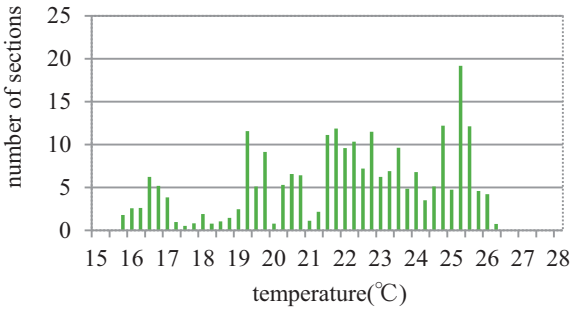

Fig.11 Average number of chironomid(every 0.25℃)

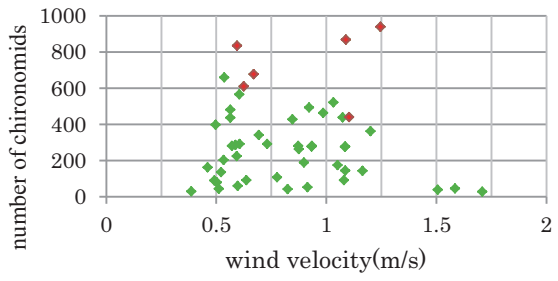

Fig.12 Number of chironomids v.s. wind velocity

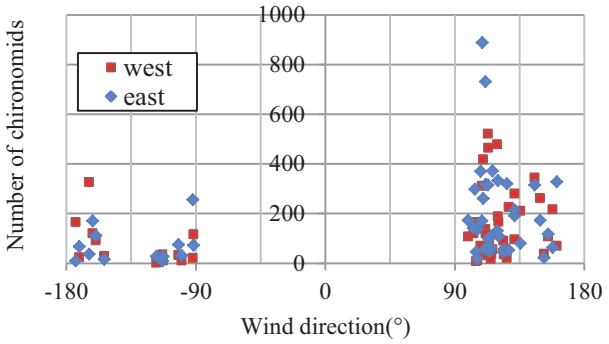

Fig.13 wind direction

5. Conclusion

The distribution of swarms were observed on consecutive days to investigate their seasonal concentration at the upstream of Nomikawa. To accurately identify the number of swarms, a portable counter was developed comprising of laser scanners.

The results showed the concentration of swarms peak 25 minutes before the sunset. Furthermore, the area where a swarm of mosquitoes reached high concentration was identified. The high concentration distribution was confirmed frequently in 3 points on 6 T-junctions near Sakai bridge. It was necessary to obtain different information as well as observational data in this research to specify the reason why the density of the swarm of mosquitoes rises at a T-junction. Another possible factor which may affect the swarm is the sunshine as affected by the surrounding buildings/land.

Reference

1) 村上行啓，五十嵐隆夫，佐伯陽子，足立雄一，松野正知，岡田敏夫，河合幸一郎，熊谷朗，佐々学：ユスリカ喘息に関する研究. 第 II 報　ユスリカ種別間の交叉抗原性について．アレルギー，36, 81-85, 1987.

2) 平林公男：諏訪湖地域における“迷惑昆虫”ユスリカの大発生とその防除策　第一報：アカムシユスリカ（Tokunagayusurika akamusi）成虫の大量飛来，日本衛生学雑誌，46 (2)，652 -661，1991.

3) 平林公男，中里亮治，沖野外輝夫：諏訪湖におけるユスリカ研究　(2)不快昆虫としての成虫とその防除策に関する検討，山地水環境教育センター研究報告，1，53-62，2003.

4) Kanda, M: Progress in urban meteorology: A Review, *Journal of the Meteorological Society of Japan*, Vol.85, pp.365-383, 2007.

5) 近藤繁生，平林公男，岩熊敏夫，上野隆平：ユスリカの世界，培風館，2001.

6) Kon, M.: Swarming and Mating of Chironomus yoshimatsui (Diptera: Chironomidae): Seasonal Change in the Timing of Swarming and Mating, *J. Ethol.*, Vol.2, pp.37-45, 1984.

EXPLANATION SYSTEM BASED ON WISDOM OF CROWDS ON ANDROID

Student Number: 10M18074 Name: Norihisa TAKEMURA Supervisor: Yukihiko YAMASHITA

Android 端末で動作する集合知を利用した説明システム

竹村典久

近年，e-ラーニングの重要性が増しているが，教材の作成・維持管理に大きな問題を抱えている．そのため集合知を用いてこの問題を解決した tobe システムが提案されているが，学習のためにパーソナルコンピュータを用いる必要があり，通勤・通学などの移動中に学習することは難しい．そこで最近保有率が高まってきたスマートフォンやタブレット端末に着目し，シェアが高く開発が容易である Android 端末を利用することを提案する．

1 Introduction

Recently, more and more people use electronic learning (e-learning). It has been common not only for students but also for company workers. However, most of e-learning softwares are for a personal computer (PC). Because PC is still large and heavy, time and place for e-learning are restricted. To solve this problem, mobile learning (M-Learning) has been introduced. A definition of M-learning is given as

> Any sort of learning that happens when the learner is not at a fixed, predetermined location, or learning that happens when the learner takes advantage of the learning opportunities offered by mobile technologies [1].

In other words, M-learning decreases limitation of learning location by the mobility of general portable devices.

Another problem of e-learning is that it takes much time or needs cost to make and maintain course materials. If we want to publish an e-learning software, we have to make all the course materials each time. To solve this problem, tobe (text oriented bi-stream explanation) system has been developed [2]. By using wisdom of crowds, it enables to reduce effort of individuals to make the materials. I will apply the concept of tobe system to M-Learning on Android.

2 Backgrounds and related studies

I explain backgrounds and related studies needed for my research.

2.1 E-learning

E-learning comprises all forms of electronically supported learning and teaching. The information and communication systems, whether networked or not, serve as specific media to implement the learning process.

E-learning has two types of contents:

1. Online-learning (ex: explaining with images and movies)
2. Online-training (ex: quiz)

These are usually mixed.

2.1.1 M-learning

The term M-Learning, or "mobile learning" covers learning with portable technologies including but not limited to handheld computers, MP3 players, notebooks and mobile phones. M-learning focuses on the mobility of the learner, interacting with portable technologies, and learning that reflects a focus on how society and its institutions can accommodate and support an increasingly mobile population.

M-learning is convenient in that it is accessible from virtually anywhere. In addition, it is simple to utilize M-learning for a more effective and entertaining experience [3].

2.2 Wisdom of crowds

The wisdom of the crowd refers to the process of taking into account the collective opinion of a group of individuals rather than a single expert to answer a question. This process, while not new to the information age, has been pushed into the mainstream spotlight by social information sites such as Wikipedia and Yahoo! Answers, and other web resources that rely on opinion of crowds.

2.2.1 Wiki

A wiki is a website whose users can add, modify, or delete its content via a web browser using a simplified markup language or a rich-text editor. Wikis are typically powered by wiki software and are often created collaboratively by multiple users [4]. But the markup language is different in each Wiki. Therefore, there is a tendency to standardize them.

2.3 Android

Android is a software stack for mobile devices that includes an operating system, middleware and key applications. Google Inc. purchased the initial developer of the software, Android Inc., in 2005. Android's mobile operating system is based on the Linux kernel.

Table 1: Worldwide Smartphone Sales to End Users by Operating System in 3Q11 [5]

company	3Q11 Units	3Q11 Market Share(%)	3Q10 Units	3Q10 Market Share(%)
Android	60,490.4	52.5	20,544.0	25.3
Symbian OS	19,500.1	16.9	29,480.1	36.3
iOS	17,295.3	15.0	13,484.4	16.6
RIM	12,701.1	11.0	12,508.3	15.4
Bada	2478.5	2.2	920.6	1.1
Windows mobile	1,701.9	1.5	2,203.9	2.7
Other OS	1,018.1	0.9	1,991.3	2.5
Total	115,185.4	100.0	81,132.6	100.0

Figure 1: XO-3 [6]

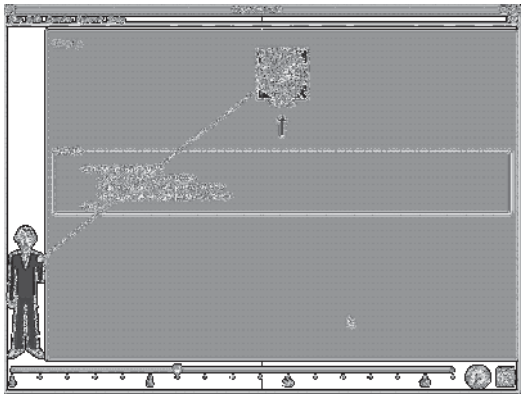

Figure 2: Expositor [2]

There are two reasons why I use Android for my research.

1. Android is the most popular mobile OS in the world (Table 1).

2. Android applications can be developed by Java.

2.3.1 OLPC

One Laptop per Child (OLPC) [6] is a project supported by the Miami-based One Laptop per Child Association (OLPCA) and the Cambridge-based OLPC Foundation (OLPCF), two U.S. non-profit organizations set up to oversee the creation of affordable educational devices for use in the developing world.

OLPC has just announced that the organization's promised under $100 XO 3.0 (Fig. 1) tablet will be shown off. The XO tablet will ship with the OLPC developed Sugar operating system but will also support Android and Linux. My proposing system may be useful for children in developing countries by using XO 3.0.

There are many statements that this project is failure. They say this project only provided personal computers for children. And they ask volunteers to build the infrastructure and maintain the personal computers. Some teachers cannot use the computer for the lecture, and some students use a computer only for games. I hope that my system will change the situation.

2.4 XML

Extensible Markup Language (XML) is a markup language that defines a set of rules for encoding documents in a format that is both human-readable and machine-readable. It is defined in the XML 1.0 Specification produced by the W3C, several other related specifications and all gratis open standards [7].

2.5 Tobe system

Tobe system is an e-learning system for which anyone can make the contents. The contents are described using tobeML (tobe markup language). The process of creating and studying contents is as follows.

1. Creators all over the world describe the tobeML documents using text editor on the web.

2. The tobeML documents are stored in the server.

3. Users receive the tobeML documents from the server, and load them into Expositer, that is a lecture style player of tobeML documents.

The format of tobeML documents is based on XML. A virtual teacher in Expositer (Fig. 2) can point an important area in text or figure and read the explanation.

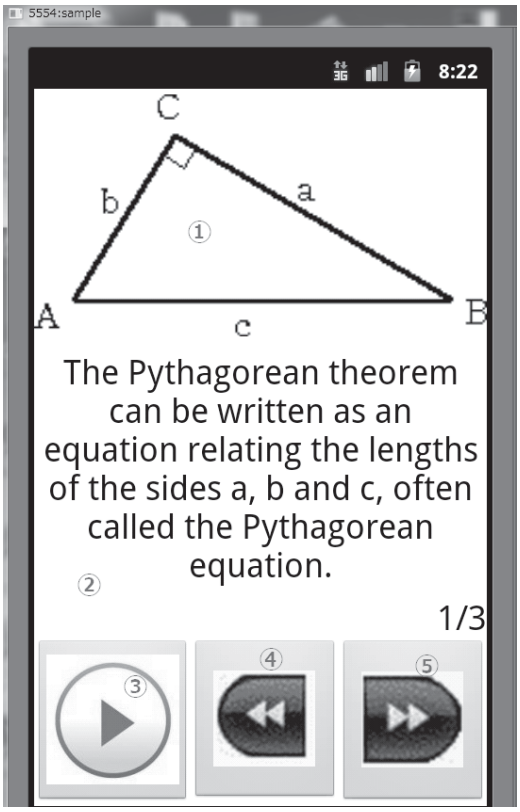

Figure 3: Display of the system

3 Tobe player on Android

In order to make easy to use tobe system outside, I focus not on PC but on smartphones and tablet computers, and propose a tobe player for M-learning. I develop a player on an Android device.

3.1 Text to speech

We use Text To Speech (TTS) to generate speech from text. The system sends text data to Google Translate [8], gets mp3 data, and plays the mp3 data on the device. To get sound data, the system needs to connect to Internet just only once, because mp3 data are saved in the device.

Android has an own TTS system, but its quality is not so good and the number of languages that Android can be applied to is less than that of Google Translate.

3.2 Structure of the player

The window of the proposing player is shown in Fig. 3. The explanation of each part is as follows:

1. Image area: show the image for explanation
2. Text area: show the text for explanation
3. Play button: start speech explanation
4. Back button: move to previous slide
5. Next button: move to next slide

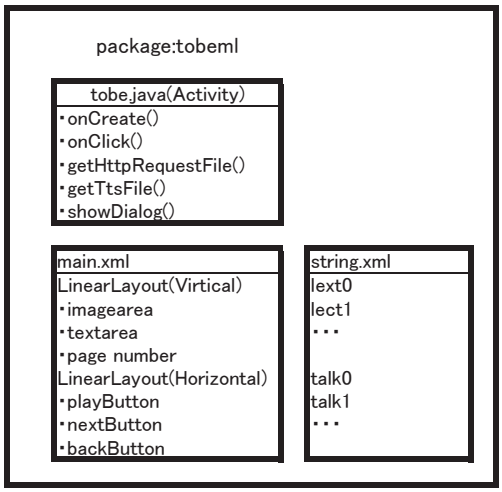

Figure 4: Class diagram

Android cannot set an image and a text at the same place. Therefore, I have to use images as back grounds.

The diagram of important classes in this player is shown in Fig. 4. I explain important methods and resources.

- onCreate(): This method is called at first when the application starts. In this application, the first resource is set and the language choice window is shown.
- onClick(): This method is called when a button clicked. In this application, when any button of three is clicked, this method is called and "play", "next", or "back" is run.
- getHttpRequestFile(): This method is called when the application sends the text to Google Translate. Its return is a mp3 file.
- getTtsFile(): This method save a speech file to the device and return a mp3 file to getHttpRequestFile().
- showDialog(): This method is called when the dialog is displayed such as "This is the last page".
- lect+number: This is resource text for display.
- talk+number: This is resource text for speech.

The process to use the proposing system is as follows:

1. Install the application.
2. Set the resources (texts for speaking, texts for display, images)
3. Start and choose language for speech explanation (Fig. 5).
4. Push the play button.

Figure 5: Window for language choice

4 Experiment

We conducted an experiment to evaluate the proposing system. Its outline is as follows:

- Compare Tobe Player to printed contents. “ Which is better to understand the content? ”
- The content explains some companies.
- The content is written in English. It is 8 pages of A4 document or 12 pages in player.
- Five subjects (2 Japanese, 1 Chinese, 1 Korean, 1 Vietnamese)

For the result, all subjects answered tobe player was better. Their impressions are as follows:

- Because the system explains using image and speech, it is easy to understand.
- I want to be said where I should look at such as “ Look at the graph. ”.
- The amount of information at one page is restricted.
- Listening to English explanations is a little difficult.

5 Conclusions

In this paper, we discussed about a tobe player on android that is an e-learning system using wisdom of crowds. I explained the system can solve the problem that tobe system needs PC.

The developed system can only do explanation. Then an editor using Wiki is necessary . And the proposing system can be use not only for e-learning but also for a manual. Because a manual is constructed by image and text, it is sometimes difficult to understand. By applying the proposing player to explain with speech, users can understand it more easily.

However, when we make the contents for e-learning, we have to consider educational engineering. Not everyone can make the contents for education easily. Therefore, we have to make contents that explains how to use this system and make good materials. Such an integration property is an advantage of the proposed system.

5.1 Future work

The proposing player has not been completed. So we have to do the following things:

- To improve the function to point an important point.
- To make contents in other languages.
- To play the contents automatically.

References

[1] C. O’Malley et al.: “Guidelines for learning/teaching/tutoring in a mobile environment”, MOBIlearn, pp. 6 (Oct. 2003).

[2] S. Tobe: “Research on Explanation Markup Language based on XML and its Lecture Style Player”, Master thesis of Tokyo Institute of Technology (Feb. 2005) (in Japanese).

[3] “Mobile learning is for everyone”, http://www.m-learning.org/ (accessed 2012-01-25).

[4] N. Matias: “What is a Wiki? Article”, http://www.sitepoint.com/what-is-a-wiki/ (accessed 2012-01-24).

[5] Gartner News, http://www.gartner.com/it/page.jsp?id=1848514 (accessed 2012-01-20).

[6] One Laptop per Child, http://one.laptop.org/ (accessed 2012-01-27).

[7] “Extensible Markup Language (XML) 1.0 (Fifth Edition)”, http://www.w3.org/TR/REC-xml/ (accessed 2012-01-24).

[8] Google Translate, http://translate.google.co.jp/ (accessed 2012-01-20).

A novel method for ammonia deodorization utilizing the anabolic activity of heterotrophic bacteria

Student No.:10M18080 Name:Masashi TANAKA Supervisor:Kiyohiko NAKASAKI Co-supervisor: Sachio HIROSE

従属栄養細菌の同化作用を用いた新規なアンモニアガス脱臭法

田中大志

悪臭問題を解決する方法として、従来から微生物による悪臭成分の分解いわゆる異化作用を利用する生物脱臭法が提案されてきた。本研究では臭気成分としてアンモニアガスを対象とし、従属栄養細菌が炭素源を消費すると同時にアンモニアを摂取して菌体合成する同化作用を利用して脱臭する新規なアンモニアガス脱臭法を開発した。カラム中に微生物を接種した有機物を充填し、1000 ppm のアンモニアガスを通気したところ、微生物の増殖(菌体合成)にともなってアンモニアが脱臭されることを確かめた。また、アンモニア 1000 ppm を 30 および 60 ^{o}C の条件で 5 日間通気したところ、平均アンモニア処理量はそれぞれ 7.72×10^{-4} g-NH_3/g-ds/d、7.31×10^{-4} g-NH_3/g-ds/d となった。

1. Introduction

In Japan, the Offensive Odor Control Act was enacted to control air pollution associated with nuisance odor in1971. Thereafter, nuisance odor caused many problems as a typical sensory environmental pollution at livestock farm, wastewater treatment plant and landfill.

At these point sources of the pollution, biofiltration is commonly used as a deodorizing method due to its low cost operation and construction. It is well-know that biofiltration is a technique to treat odor containing-air where microorgnisims in the supporting material degrade odorous components contained in the odor gas. Many reports have been focused on the removal of ammonia, hydrogen sulfide, and VOCs which are the typical components of the odor gas using compost and activated sludge as the supporting materials of the microorganisms[1][2].

Among these various components, ammonia gas is the most nuisance odor gas which has been generated in large quantities. So far, ammonia gas removal by the biofiltration has been carried out using the catabolism of the microorganisms during the nitrification. Two dominant kinds of bacteria, *Nitrosomanas sp.* which oxidizes ammonia to nitrite, and *Nitrobacter sp.* which oxidizes nitrite even to nitrate, proliferated with the progress of the nitrification[3]. Nitrogen oxide which is generated by these nitrifying bacteria inhibits their own growth. Therefore, in order to keep the activity of the nitrifying bacteria, the supporting material needs to be was had to remove nitrogen oxide and additional wastewater treatment facility is required to treat the solution used for washing of the supporting material.

This study aims to investigate ammonia deodorization utilizing the anabolic activity of heterotrophic bacteria where no byproducts that inhibit the bacterial activity facility are produced and no additional facility would be required.

2. Materials & methods

2-1. Solid filler material used for deodorization

In the present experiments, ammonia gas containing-air was introduced into a column which contained organic materials inoculated with microorganisms. It is expected that ammonia gas would be removed from the air by being used as the nitrogen source for the production of the microbial cell mass when heterotrophic microorganisms are incubating in the condition of less nitrogen source. It was thus considered that the organic materials with high carbon content was more advantageous and rice that was discarded as kitchen refuse was used as a raw material for the filler. Rice, sawdust, and seeding materials with the trade name Alles-G (Matsumoto Laboratory of Microorganisms, Matsumoto, Japan) with the mixing ratio of 10:20:1 on dry-weight basis were used as the filler in the column. The initial pH of the filler was 7 while the moisture content was adjusted to 60% by addition of distilled water. Some characteristics of the seeding materials are shown in Table 1.

Table 1 Some characteritics of Alles G

charcteristic		
Thermophilic	log(CFU/g-ds)	7.76 ±0.02*
Mesophilic	log(CFU/g-ds)	8.92 ±0.01*
pH	(-)	8.77
Moisture content	(%)	4.92 ±0.74*

*95%信頼区間(n=3)

2-2. Ammonia deodorization experiment using the filler material

Fig. 1 depicts a schematic diagram of the experimental set-up for ammonia deodorization. Air was first passed through a flask containing ammonia solution before introducing into the column. The aeration rate was maintained at 5.5 mL/min throughout the experiment. 15 g of the filler was placed into the column which was in-turn placed in an incubator (Model IS 800, Yamato Scientific Co., Ltd, Tokyo, Japan) in order to maintain the temperature at the constant level. The column was composed of a mini-reactor made of Pyrex glass cylinder which was 45mm in diameter, 100mm in height, sealed with silicone rubber stoppers with glass pipes for aeration.

In the first investigation of the ammonia deodorization at 60 ^{o}C, four runs namely Run A60 (column with filler), B60 (column with sterilized filler), C60 (column with no filler), and D60 (column with filler) were carried out. The NH_3 gas with 1000 ppm concentration was supplied from the bottom of the column in all runs except Run D60 where air was instead supplied. Similar runs were conducted at 30 ^{o}C namely A30, B30, C30, and D30. All runs were operated for 5 days and the filler was agitated every 24 h using sterilized spoon.

High concentration of ammonia deodorization with three kinds of experimental conditions (Runs A30+, B30+ and C30+) were taken in 30℃. Experimental set-up is the same as that in Run A30, B30, C30, although this test is taken by ammonia concentration 2000ppm. These runs called Run A30+, B30+ and C30+.

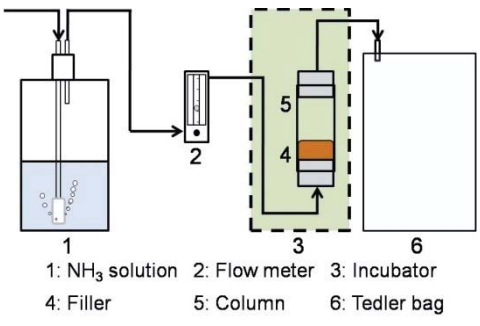

Fig.1 Schematic diagram of NH_3 deodorization setup

2-3. Analysis

The exhaust gas from the column was introduced into a 5L plastic bag(TedlarBag^{TM}; Omi Odoair Service Co. Ltd., Omihachiman, Japan) for 12 h, and the plastic bag was changed twice daily at 12 h intervals. The volume of exhaust gas captured in the plastic bag was measured, and the concentration of CO_2 was analyzed using Kitagawa gas detector tubes (KomyoRikagaku Kogyo K.K., Kanagawa, Japan). The quantity of CO_2 evolved during each 12 h period was determined by the CO_2 concentration and exhaust gas volume measured, and the cumulative CO_2 that had evolved up to a certain incubating time was calculated. A total of six reactors were used for each experimental run in order to measure the changes in cell densities of microorganisms and pH over time. These reactors were initiated at the same time, and the incubating process in subsequent reactors was interrupted at the point of 0, 1, 3 d and at the end of the incubating period. The concentration of ammonium was measured by enzymatic method with F-kit NH_3 (J.K.International Inc., Tokyo, Japan) and the concentration of nitrite and nitrate was measured by colorimetric method with Nitrite/Nitrate, Colorimetric Test(Roche Diagnostics K. K., Tokyo, Japan). Total nitrogen in the filler was measured by elemental analysis with organic micro analysor (MICRO CORDER JM-10, J-Science CO., Kyoto, Japan)

2-4. NH_3 deodorization by isolated microorganism

Two strains of the dominant bacteria were isolated from 3rd day samples of Run A60(C05T) and A30(C09T), respectively. C05T and C09T were pre-cultured in Trypticase-soy broth at 30and 60^{o}Cfor 1 day. Bacteria were then centrifuged and washed three times with medium solution prior being used as an inoculum.

300mL conical flask with M9G liquid medium including no nitrogen which was inoculated with precultured microorganism was used as the reactor instead of the column.

The NH_3 deodorizations in the M9G liquid medium with four runs (Runs E50, F50, E30 and F30) were conducted.NH_3 concentration of 700 ppm was supplied in the four runs. C05T and C09T were used as inoculum in Runs E50 and E30, respectively. Run F50

and F30 were without the liquid medium and used for the measurement of the NH_3 concentration.

3. Results & discussion

3-1. NH_3deodorization with solid filler material

The course of the cumulative NH_3 emission at 60 ^oC is shown in Fig.2. A clear difference of the cumulative NH_3 emissions between each run was observed. Lower cumulative NH_3 emission in Run B60 than that in Run C60 was due to the NH_3 adsorption to the filler. During the first 24 h, NH_3 seemed to be trapped in the column in Run A60 and B60. From 24 h, a sharp increase of cumulative NH_3 emission was observed in Run B60 while NH_3 emission in Run A60 was lower level than in RunB60 during which NH_3 was consumed by the microorganisms in Run A60.

The cumulative CO_2 emission in Run A60 at 24 h was higher than that in Run D60 in which air was instead introduced into the column (data not shown). The difference between A60 and D60 suggested that NH_3 induced the vigorous microbial activities as it was incorporated for the cell growth.

The courses of cell densities of microorganisms in Runs A60 and D60 are shown in Fig.3. At the end of the incubating period, cell density of microorganisms in Run A60 increased drastically to a value of $1.9x10^{10}$ CFU/g-ds which was over 2 orders of magnitude higher than that in Run D60. Due to high C/N ratio of the filler, it would be difficult for microorganisms in Run D60 to proliferate. However, the supply of NH_3 gas to the column could be an alternative source of nitrogen for the cell growth as in Run A60.

The mass balance of nitrogen of Run A60 is shown in Fig. 4. At the end of the incubating period, the increase of Org-N was observed and the difference of initial and final Org-N would be equivalent to the cell mass. Moreover, a part of Org-N has been decomposed in an early stage; therefore, higher cell mass would be produced than the present observation. Since the difference between ammonia gas input and sum of ammonia gas output and inorganic nitrogen should have converted to the microbial cell mass, at least 21.4 % of the supplied ammonia gas was served for the microbial growth.

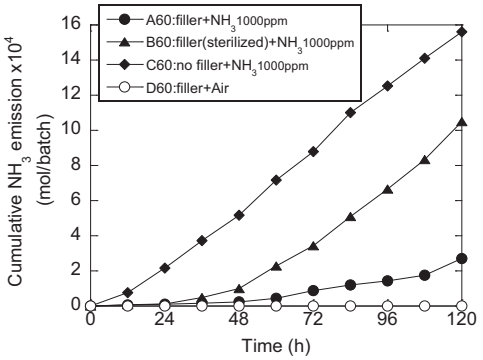

Fig. 2 The course of the cumulative NH_3 emission at 60 ^oC

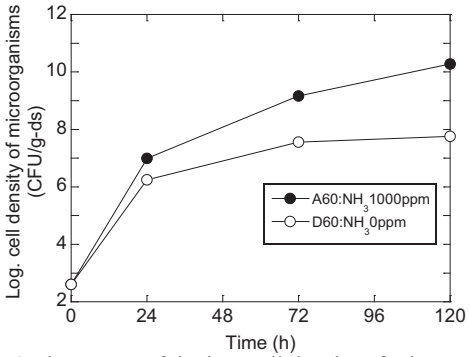

Fig. 3 The course of the log. cell density of microorganisms

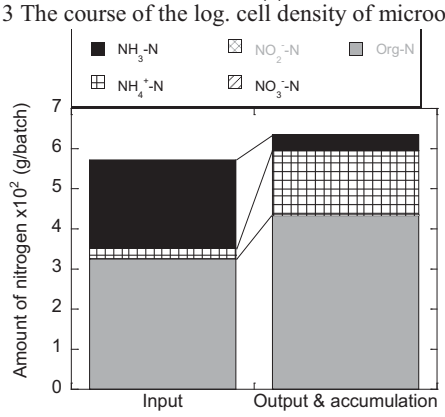

Fig.4 The mass balance of nitrogen in Run A60

The course of the cumulative emission of ammonia gas in the ammonia deodorization with solid filler at 30 ^oC is shown in Fig. 5. Since the difference of Run B30 and Run C30 become obvious at 48 h, and it was considered that ammonia gas is consumed by the microorganism in Run A30. Furthermore, NH_3 gas emissions was less, and 98.6% of the supplied ammonia gas was removed was checked by the end of the incubating period

Then, in Run A30 and D30, compared with ammonia gas or air which was aerated, the carbon dioxide evolution rate in Run A30 after 24 h was slowly increasing and carbon dioxide maximum evolution rate $8.0x10^5$ mol/g-ds/h in 96 h. Although the one in Run D30 was not increasing slightly after 24 h (data not shown). Difference between A30 and D30 suggested that NH_3 induced the vigorous microbial activities as it was incorporated for the cell growth.

The course of cell density of microorganisms in Runs A30 and D30 is shown in Fig.6.Compared to having been $3.6x10^9$ CFU/g-ds of cell density in Run D30 by 3 d, the microorganisms in Run A30 has increased well which aerated ammonia gas, and became $8.4x10^{10}$ CFU/g-ds.

The mass balance of nitrogen of Run A30 at 5 d is shown in Fig. 7.When it is calculated in similar way with Run A60, it is thought that 75.2 % of the supplied ammonia gas serves as a cell mass at least.

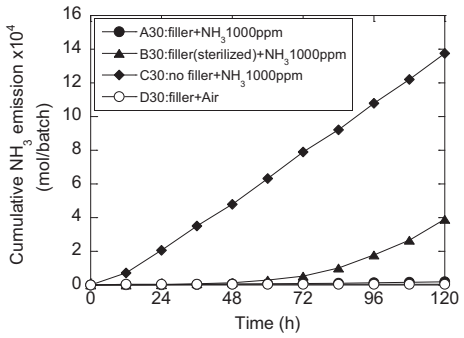

Fig. 5 The course of the cumulative NH_3 emission at 30 ^oC

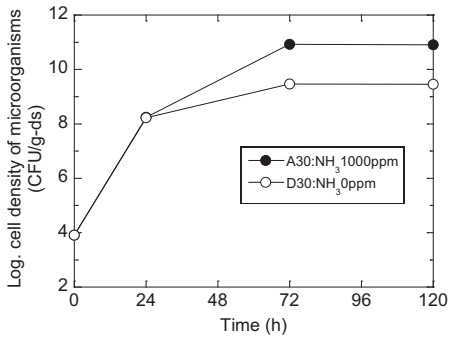

Fig. 6 The course of the log. cell density of microorganisms

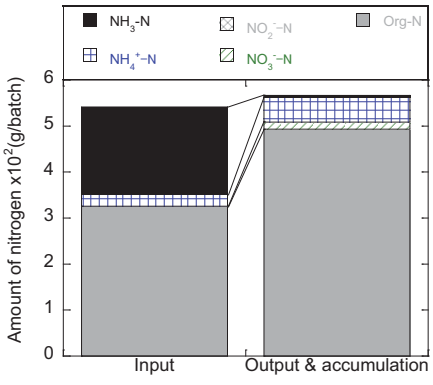

Fig.7 The mass balance of nitrogen in Run A30

When the concentration of ammonia gas, 2000 ppm, was aerated, Run A30+ which is inoculating the microbe was changing like Run B30+, and the effect of consumption of the ammonia gas by a microbe was nothing. Moreover, cumulative emission of the carbon dioxide was about 0 by 5 d, and the activity of a microbe was inhibited (data not shown). Since the cell density of Run A30+ increased only to 1/1000 at 3 d compared with the case where ammonia gas concentration 1000 ppm are aerated, Run A30, the effect of the ammonia gas removal by anabolism was not able to be expected. If it is to the ammonia gas loading dose around $1.0x10^{-3}$ g-NH_3/g-ds/d, in the case of aerating ammonia gas concentration 1000 ppm, Run A30.

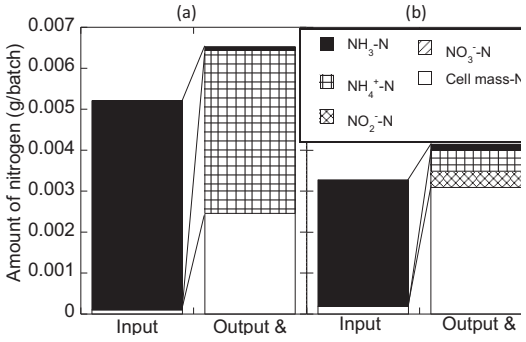

Fig.8 The mass balance of nitrogen at 50 ^oC (a), 30 ^oC

3-2. NH_3deodorization by isolated microorganisms

In order to clarify that the supplied ammonia gas is assimilated to the microorganisms, cultivation which aerated ammonia gas using M9G liquid medium adjusted to be nothing to use nitrogen except for the nitrogen from ammonia gas was performed.

The result of having calculated the mass balance of the nitrogen of the culture solution cultivated to 2 d in 50 ^oC, and to 1d in 30 ^oC was indicated with Figs. 7(a) and 7(b) respectively. It was ascertained that the microorganism propagated using the nitrogen supplied by the ammonia gas aerated in the both results.

4. Conclusions

The biofiltration using the present column packed with the solid filler containing the mixture of rice, sawdust, and seeding materials was effective in deodorizing ammonia gas with the loading rate of $1.0x10^{-3}$ g-NH_3/g-ds/d at the temperature of 30 ^oC. Moreover, ammonia gas deodorization by the anabolic activity of heterotrophic bacteria was demonstrated using the liquid medium without nitrogen source except the ammonia gas supplied.

Reference

[1] H. W.Ryu, et al., *J. Haz. Mate.* **168**(2009), 501–506
[2] Y. Jun, et al., *Biores. Tech.*, **100** (2009), 3869–3876
[3]Sakuma T., et al., *Water research*, **42**(2008), 4507–4513

Optimization of circuit and control parameters of a boost converter for Energy Harvesting

Student Number:10M18097　Name:Masanori TANAKA　Supervisor:Kunio TAKAHASHI

エネルギーハーベスティング用昇圧コンバーターの回路パラメータと制御パラメータの最適化

田仲　祐士

エネルギーハーベスティングの高効率化の為、昇圧コンバーターとキャパシターによるエネルギーハーベスターモデルが提案された。発電素子のポテンシャルエネルギーに対して蓄積されたエネルギーで定義されたエネルギー効率を理論的に解析する事で、回路パラメータ制御パラメータのエネルギー効率への影響が明らかにされた。最適な制御パラメータとしてデューティー比が解析的に、スイッチング周期が数値的に得られ、最適な回路パラメータが各パーツごとの様々な特性も含めて議論された。これをもとに設計された昇圧コンバーターと太陽電池を用いた実験により理論エネルギー効率の整合性が立証され、91 %の高いエネルギー効率を達成した。

1 Introduction

Energy Harvesting with small solar cells or thermoelectric generators requires an efficient storage method. A DC-DC converter which operates a generating device at its Maximum Power Point (MPP) should be implemented for high efficiency. Designing high efficient DC-DC converter for Energy Harvesting therefore requires considering not only transfer efficiency but also Maximum Power Point Tracking (MPPT) and stored energy amount. In [1], a Solar Harvester with a buck converter and a super capacitor is introduced and is optimized with the energy efficiency including the consideration. [1] achieves 85% of the energy efficiency at ∼400[mW] of a PV module's output with an experimental setup. Unfortunately, the energy efficiency in theoretical part of [1] is obtained as only numerical calculation so discussion for maximizing the energy efficiency for disigning a buck converter is poor. In [2] and [3], the energy efficiency is introduced and discussed but they do not optimize DC-DC converter to maximize the energy efficiency. Thus, this study introduced an Energy Harvester with a capacitor as a storage device which has low Equivalent Series Resistance (ESR) for high efficiency. Additionally, a boost converter is used for MPPT because it allows excellent transmission efficiency of electric power [3]. The objective is to introduce an equivalent Energy Harvester model, obtain the energy efficiency analytically and discuss methodology for maximizing the energy efficiency by focusing all parameters.

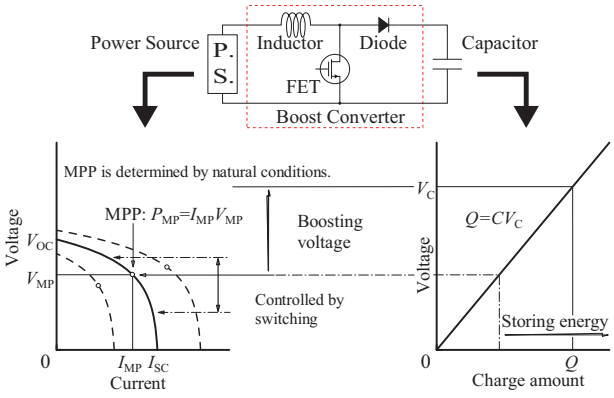

Fig 1: Maximum Power Point Tracking with a boost converter

2 Analytical energy efficiency

In order to analyze electric behavior of an Energy Harvester in several switching times, equivalent circuit model is introduced as Figure 2.

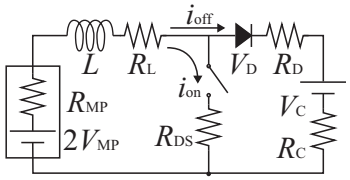

Fig 2: Equivalent circuit of an Energy Harvester

Power Source should be operated around its MPP, therefore the i-v characteristics can be assumed to tangential line at the MPP. The i-v characteristics is obtained as

$$v = 2V_{MP} - R_{MP}\, i$$

where V_{MP} and I_{MP} are power source's output voltage and current at MPP, and R_{MP} is defined as V_{MP}/I_{MP}.

In the same reason, the diode's forward voltage v_f for the current i is assumed as

$$v_f = V_D + R_D\, i.$$

Additionally, the capacitor as a storage device has large capacitance so that the capacitor's voltage can be assumed to be constant V_C in one switching. Moreover, low resistant components of the boost converter and the capacitor against R_{MP} are required in order to improve the energy efficiency. Thus, total resistance where current pass at switched on can be assumed to be nearly equal to total one where current pass at switched off. This condition is expressed as

$$\begin{aligned} R &= R_{MP} + R_L + R_{DS} \\ &\approx R_{MP} + R_L + R_D + R_C. \end{aligned}$$

Kirchioff's voltage law at switch on and switch off can be applied as

$$L\frac{di_{on}}{dt} + Ri_{on} = 2V_{MP}$$

when switch is on and

$$L\frac{di_{off}}{dt} + Ri_{off} = 2V_{MP} - V_C - V_D$$

when switch is off. In order to analyze current behavior, constant switch on time $T_{\rm on}$ and switch off time $T_{\rm off}$ are considered. When the number of switching is defined as n, current flow at switch on $i_{{\rm on}(2n-1)}$ is obtained as

$$i_{{\rm on}(2n-1)} = (I_{2n-2} - \frac{2V_{\rm MP}}{R})\,{\rm e}^{-\frac{Rt}{L}} + \frac{2V_{\rm MP}}{R}$$

where I_{2n-2} is a boundary condition at turning switch from off to on, and switch off $i_{{\rm off}(2n)}$ is obtained as

$$i_{{\rm off}(2n)} = (I_{2n-1} - \frac{2V_{\rm MP} - V_{\rm C,D}}{R})\,{\rm e}^{-\frac{Rt}{L}} + \frac{2V_{\rm MP} - V_{\rm C,D}}{R}$$

where I_{2n-1} is a boundary condition at turning switch from on to off and $V_{\rm C,D} = V_{\rm C} + V_{\rm D}$. Boundary conditions of I_{2n-2} , I_{2n-1} and I_{2n} have relationships of recurrence equations obtained as

$$I_{2n-1} = I_{2n-2}{\rm e}^{-\frac{RT_{\rm on}}{L}} + \frac{2V_{\rm MP}}{R}(1-{\rm e}^{-\frac{RT_{\rm on}}{L}}) \quad \text{and}$$

$$I_{2n} = I_{2n-1}{\rm e}^{-\frac{RT_{\rm off}}{L}} + \frac{2V_{\rm MP} - V_{\rm C,D}}{R}(1-{\rm e}^{-\frac{RT_{\rm off}}{L}}).$$

When initial condition I_0 is given as 0, the recurrence equations can be analyzed as

$$\begin{aligned} I_{2n-2} &= \Big(\frac{2V_{\rm MP}}{R} - \frac{V_{\rm C,D}(1-{\rm e}^{-\frac{RT_{\rm off}}{L}})}{R(1-{\rm e}^{-\frac{RT}{L}})}\Big)\Big(1-{\rm e}^{-\frac{(n-1)RT}{L}}\Big) \quad \text{and} \\ I_{2n-1} &= \Big(\frac{2V_{\rm MP}}{R} - \frac{V_{\rm C,D}{\rm e}^{-\frac{RT_{\rm on}}{L}}(1-{\rm e}^{-\frac{RT_{\rm off}}{L}})}{R(1-{\rm e}^{-\frac{RT}{L}})}\Big)\Big(1-{\rm e}^{-\frac{(n-1)RT}{L}}\Big) \\ &\quad + \frac{2V_{\rm MP}}{R}\Big(1-{\rm e}^{-\frac{RT_{\rm on}}{L}}\Big){\rm e}^{-\frac{(n-1)RT}{L}}. \end{aligned} \tag{1}$$

Analyzed current behavior can be obtained as Figure 3 with experimental specifications and optimized control parameters. Figure 3 indicates that top value and bottom value of boundary conditions converge from the initial condition immediately. Thus, steady state current can be obtained using boundary conditions of equation (1) at $n \to \infty$ as

$$\begin{aligned} i_{\rm on} &= -\frac{V_{\rm C,D}\Big(1-{\rm e}^{-\frac{RT_{\rm off}}{L}}\Big)}{R\Big(1-{\rm e}^{-\frac{RT}{L}}\Big)}\,{\rm e}^{-\frac{Rt}{L}} + \frac{2V_{\rm MP}}{R} \quad \text{and} \\ i_{\rm off} &= \frac{V_{\rm C,D}\Big(1-{\rm e}^{-\frac{RT_{\rm on}}{L}}\Big)}{R\Big(1-{\rm e}^{-\frac{RT}{L}}\Big)}\,{\rm e}^{-\frac{Rt}{L}} + \frac{2V_{\rm MP} - V_{\rm C,D}}{R}. \end{aligned} \tag{2}$$

Stored energy to the capacitor in one switching period can be calculated with equation (2). The energy $E_{\rm ci}$ is given as

$$E_{\rm ci} = V_{\rm C}\int_0^{T_{\rm off}} i_{\rm off}dt. \tag{3}$$

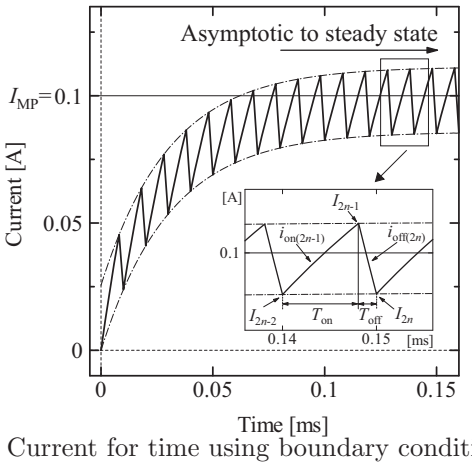

Fig 3: Current for time using boundary conditions of equation (1) and available specifications

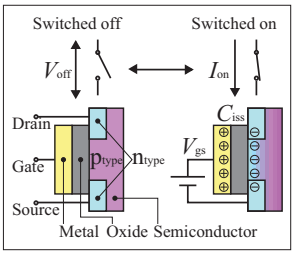

Fig 4: MOS-FET characteristics

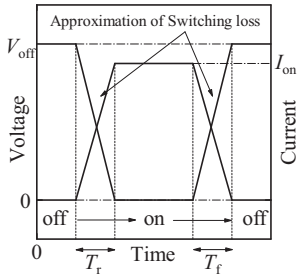

Fig 5: Switching loss at current rise time and current fall time

However the FET operates as an ideal switch without $R_{\rm DS}$ in the model. Gate drive loss $E_{\rm gd}$ and switching loss $E_{\rm sw}$ at the FET should be considered for Energy Harvesting. These energy loss are approximated as

$$\begin{aligned} E_{\rm gd} &= C_{\rm iss}V_{\rm gs}^2 \quad \text{and} \\ E_{\rm sw} &= \frac{I_{\rm on}V_{\rm off}T_{\rm r,f}}{6} \end{aligned} \tag{4}$$

where $C_{\rm iss}$ is input capacitance, $V_{\rm gs}$ is voltage of charging gate as shown Figure 4, $I_{\rm on}$ is current when the switch is turning from on to off, $V_{\rm off}$ is voltage of the diode and the capacitor, and $T_{\rm r,f}$ is total time of current rise time and current fall time required for turning switch as shown Figure 5. Stored energy to the capacitor should be considered with these energy loss give as equation (4). On the other hand, an ideal boost converter for Energy Harvesting must achieves operating an power source at its MPP and storing the energy to the capacitor without energy loss. Thus, the energy efficiency of the Energy Harvester model in one switching period T should be defined as

$$\eta = \frac{E_{\rm ci} - E_{\rm sw} - E_{\rm gd}}{I_{\rm MP}V_{\rm MP}T}. \tag{5}$$

Using equation (2) (3) (4), equation (5) can be expressed as

$$\eta = \frac{R_{\mathrm{MP}} V_{\mathrm{C}}}{R V_{\mathrm{C,D}}} \left(\frac{\widetilde{g}_{\mathrm{C,D}}^2 (1-\mathrm{e}^{-(1-d)\widetilde{T}})(1-\mathrm{e}^{-d\widetilde{T}})}{\widetilde{T}(1-\mathrm{e}^{-\widetilde{T}})} - \widetilde{g}_{\mathrm{C,D}}(1-d)(\widetilde{g}_{\mathrm{C,D}}-2) \right) - \frac{I_{\mathrm{on}} V_{\mathrm{off}} T_{\mathrm{r,f}} + 6 C_{\mathrm{iss}} V_{\mathrm{gs}}^2}{6 I_{\mathrm{MP}} V_{\mathrm{MP}} T} \tag{6}$$

where $\widetilde{g}_{\mathrm{C,D}} = \frac{V_{\mathrm{C,D}}}{V_{\mathrm{MP}}}$, $\widetilde{T} = \frac{RT}{L}$ and d is duty ratio expressed as $\frac{T_{\mathrm{on}}}{T}$. Duty ratio can be optimized analytically by differentiating equation (6) with respect to d. Optimized duty ratio d_{gt} is obtained as

$$d_{\mathrm{gt}} = 1 - \frac{1}{\widetilde{T}} \log\left(\left(\frac{1}{2} - \frac{1}{\widetilde{g}_{\mathrm{C,D}}}\right)(1-\mathrm{e}^{-\widetilde{T}}) + \sqrt{\left(\frac{1}{2} - \frac{1}{\widetilde{g}_{\mathrm{C,D}}}\right)^2 (1-\mathrm{e}^{-\widetilde{T}})^2 + \mathrm{e}^{-\widetilde{T}}} \right).$$

The optimum duty ratio d_{gt} operates fixing the center of the current oscillation on V_{MP}/R. It indicates that the power source's output point should be optimized by considering energy loss at the circuit resistance. This study defines the output point as Maximum Energy Harvesting Point as shown Figure 6.

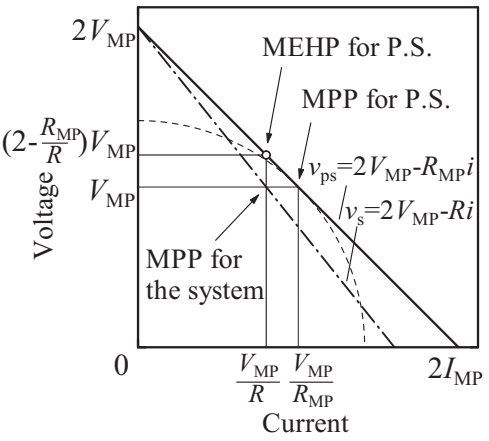

Fig 6: Maximum Energy Harvesting Point (MEHP) on i-v characteristics

Using optimum duty ratio d_{gt}, the part of equation 6 is defined as

$$\eta_{\mathrm{os}} = \frac{\widetilde{g}_{\mathrm{C,D}}^2 (1-\mathrm{e}^{-(1-d_{\mathrm{gt}})\widetilde{T}})(1-\mathrm{e}^{-d_{\mathrm{gt}}\widetilde{T}})}{\widetilde{T}(1-\mathrm{e}^{-\widetilde{T}})} - \widetilde{g}_{\mathrm{C,D}}(1-d_{\mathrm{gt}})(\widetilde{g}_{\mathrm{C,D}}-2).$$

Figure 7 shows that η_{os} is monotonic decrease for $\widetilde{T}$.Circuit resistance and the FET's energy loss should be small. Moreover, the FET and the diode should be considered with reverse voltage which typically prevent forward energy transmission. So these should be chosen as low reverse voltage as possible to exceed the capacitor's voltage V_{C}. On the other hand, lower switching period T improve η_{os} but also increase the FET's energy loss. Using optimum duty ratio d_{gt}, relationship between switching period T and energy efficiency η is plotted on Figure 9,12, 15 with solid lines. These figures indicate that optimum switching period achieving both of high η_{os} and low the FET's energy loss exist. Additionally, the inductor

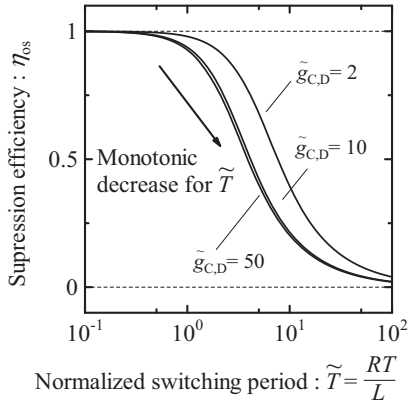

Fig 7: Relationship between $\widetilde{T}$ and η_{os}

with higher inductance L and lower resistance R_{L} requires high magnetic permeable core which cause DC superposition characteristics and iron loss with nonlinear inductance.

3 Experimental result and Discussion

To validate theoretical energy efficiency and optimum duty ratio, experimental energy efficiency for switching period T is obtained by measuring the capacitor's voltage. In the first experimental setup, constant voltage $2V_{\mathrm{MP}}$ =3.0[V] of MATSUSADA PL-36-2.2 and R_{MP} =15[Ω] of the resistance are used as a power source with linear i-v characteristics. Additionally, L =470[μH] and R_{L} =0.21[Ω] of Panasonic ELC18B471L, R_{DS} =78[mΩ], $T_{\mathrm{r,f}}$ =7.0[ns] and C_{iss} =480[pF] at V_{gs} =5.0[V] of TOSHIBA TPC6006-H, V_{D} =0.32[V] and R_{D} =0.20[Ω] at 100[mA] of forward current flow of TOSHIBA CMS16 are used for the boost converter. Moreover, C =219[mF] and R_{C} =6.0[mΩ] of BHC ALS3-224NP040 is used as the storage device and charged from 7.45[V] to 7.55[V].

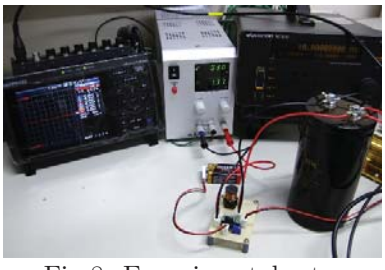

Fig 8: Experimental setup

The experimental result indicates that approximation error of the FET's switching loss occur at low switching period area on Figure 9. On the other hand, at high switching period area, the experimental result is nearly equal to theoretical one. In the second experiment, therefore, V_{MP} =2.35[V] and I_{MP} =74.6[mA] of the solar cells as shown Figure 10 is used as a power source with non-linear i-v characteristics as shown Figure 11.

The inductor is replaced to L =2.2[mH] and R_{L} =0.88[Ω] of Panasonic ELC18B222L. The capacitor is charged from 9.55[V] to 10.05[V]. The experimental result indicates that approximation error of

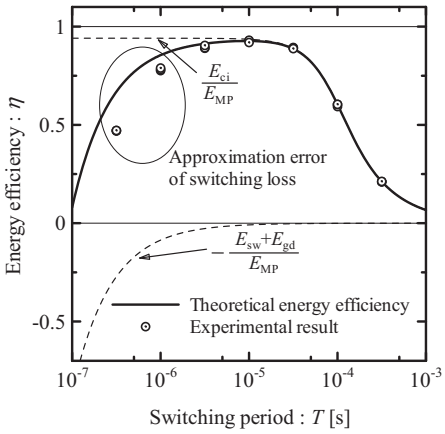

Fig 9: Experimental result with linear i-v characteristics

Fig 10: The solar cells and halogen lights

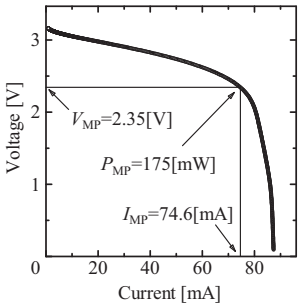

Fig 11: The solar cells' i-v characteristics

non-linear i-v characteristics occur at high switching period area on Figure 12. However, in high efficiency area from 3.16[μs] to 31.6[μs], both error is so small and achieving 94% at a maximum. Theoretical energy efficiency are validated experimentally at high efficiency area.

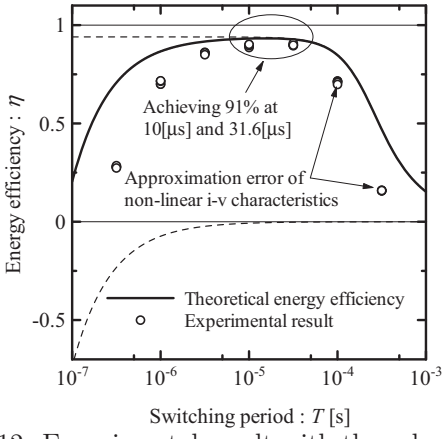

Fig 12: Experimental result with the solar cells

In the third experiment, to discuss possibility of an inductor with high magnetic permeable core, L =5.0[mH] and R_{L} =23[mΩ] of Nippon Chemi-Con LDFM05502MT-V0E is used. The frequency response of first order RL circuit as shown Figure 14 indicates that the inductor operates as high inductance under about 25[mA]. Therefore, constant voltage $2V_{\mathrm{MP}}$ =5.0[V] and R_{MP} =100[Ω] are used as a power source. The experimental result indicates that about 2% of energy efficiency decreasing is observed which previous experiments cannot observed. However, energy efficiency is over 90% at a maximum and possibility using high magnetic permeable core is validated. Maximizing energy efficiency requires optimization including magnetic permeability.

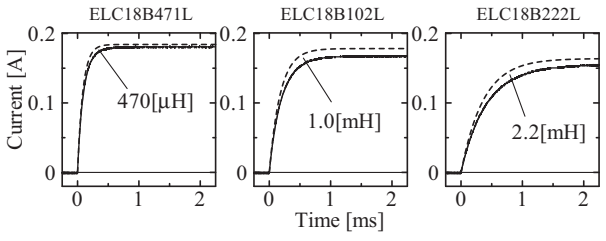

Fig 13: Inductors for experiments

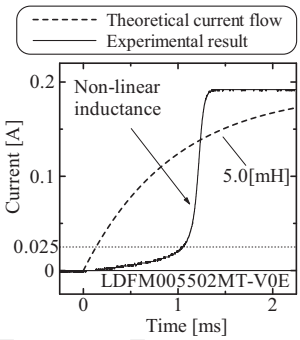

Fig 14: Frequency response of RL circuit

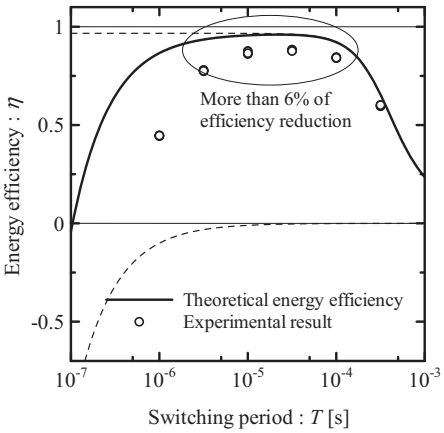

Fig 15: Experimental result with the high magnetic permeable core

4 Conclusion

This study focuses on optimum control parameters of the boost converter for Energy Harvesting. Optimum control parameters are obtained as optimum duty ratio analytically and optimum switching period numerically. Fundamental information of designing an switching controller for Energy Harvesting is obtained. Additionally, proposed Energy Harvesting model and theoretical energy efficiency can help components selection of boost converter designing.

References

[1] D. Dondi, et al., 2008, *IEEE Trans. Ind. Electron.*, **55**, 2759-2766.

[2] F. I. Simjee and P. H. Chou, 2008, *IEEE Trans. Power Electron.*, **23**, 1526-1536.

[3] A. Chini and F. Soci, 2010, *Electron. Lett*, **46**, 296-298.

Separation of Heavy metals from mine wastewater by adsorption using Mongolian natural zeolites

Student Number: 10M18105 Name: Saori TANABE Supervisor: Ryuichi EGASHIRA

モンゴル産天然ゼオライトを用いた吸着による鉱山廃水からの重金属の分離

田邉　沙織

まず、Tsagaan Tsav鉱床産のゼオライト試料のキャラクタリゼーションを行い、これらのゼオライトがカルシウム型のクリノプチロライト、モルデナイト、シャバザイトなどを主成分とすることなどを明らかにした。ついでOyu Tolgoi銅鉱山の廃水を想定して、銅ならびに付随する亜鉛、マンガンを含むモデル水溶液を、上記ゼオライト試料により処理した。いずれのゼオライトもこれらの重金属を吸着し、最大で99 %程度除去できた。また、他の金属共存条件下でもゼオライトによる吸着を確認した。

1. Introduction

In Mongolia, the large deposits of gold, copper ores, etc. have been found in 2000, discovered by Ivanhoe Mines Ltd. of Canada. The deposits of the metals were estimated as 340 tons of gold, and 15 million tons of copper, and they may have great influence on the commodity market in the world. For the future, an Oyu Tolgoi copper deposit, Tavan Tolgoi coal deposits and other ore deposit are to be developed and the trade of these metals is planned to drastically increase from around 2013. However, the environmental contamination due to the mining development has become serious.

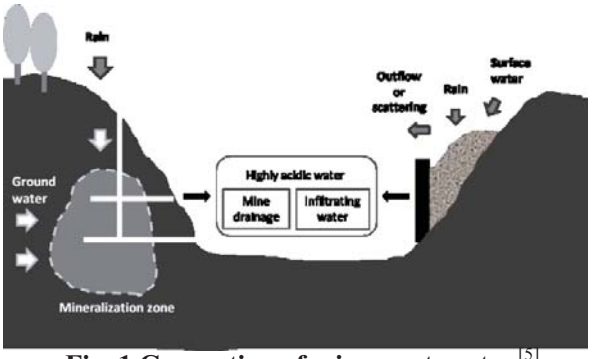

Fig. 1 Generation of mine wastewater [5]

When crushed or broken minerals in ore deposit contact with air and water, it generate acidic water called mine drainage. The sludge which has low metal concentration wastes is also cause of generation acidic water, infiltration water. Mine wastewater means both mine drainage and infiltrating water. It continues to flow out not only during mining development but also mine closing (**Fig. 1**).

The neutralization method is generally used for wastewater treatment. However this method has been pointed out to have many problems, such as generation of a lot of sludge, necessity of a large-scale facilities, high cost requirement, etc.

The use of alternative low-cost materials as potential sorbents for the removal of heavy metals has been emphasized recently. Treatment processes for metal contaminated waste streams include chemical precipitation, ion exchange, adsorption, ultra-filtration, etc; various treatment processes are available, among which ion exchange is considered to be cost-effective if low-cost ion exchangers such as zeolites are used.

Zeolites are microporous, aluminosilicate minerals commonly used as commercial adsorbents. The exchangeable cations in the zeolites can participate in ion-exchange processes. The fact that zeolite exchangeable ions are relatively innocuous and makes them particularly suitable for removing undesirable heavy metal ions from wastewater.

Mongolia is abundant in metal resources and the natural zeolite deposits have been developed. It was prospected that Tsagaan Tsav deposit of natural zeolites should have a potency to produce about 4.8 million tons of zeolite minerals. However the destination of the zeolite has not been fully examined.

The use of natural zeolites as an adsorbent has gained interest among many researchers. Although still in developmental stage, T. Motsi, *et al.* studied the actual treatment of mine wastewater from Wheal Jane Mine by using Turkey natural zeolite. They found that natural zeolite had the potential to effectively remove heavy metals from relatively dilute mine wastewater [2]. T. Bolortamir. *et al.* studied wastewater treatment including chromium by using Mongolian natural zeolites. They revealed that Mongolian natural zeolites have potential to remove chromium (III and IV) from solutions [1].

This study aimed at the application of adsorption using Mongolian natural zeolite to mine wastewater treatment. As in its early stage, the characterization of Mongolian natural zeolites and batch equilibrium adsorption of model wastewater were carried out.

2. Experimental

2.1 Characterization of natural zeolites

The used sample of natural zeolite was obtained from Tsagaan Tsav deposit in Dornogovi province, Mongolia (**Table 1**). The zeolites were crushed, ground and passed through 150×150 μm sieves and the moisture of the samples was controlled in the desiccators with saturated ammonia chloride.

Base component of the natural zeolites were

carried out using X-Ray diffraction (XRD). Surface elemental analysis was carried out with Energy Dispersive X-ray Spectroscopy (EDX). Surface areas were measured with nitrogen gas adsorption. The maximum quantity of total cations, Cation Exchange Capacity, was measured by Chapman method (1965). The aqueous phases were analyzed by ICP-AES (SPS 7800 Series, Seiko Instruments Inc.). Copper (Cu), Zinc (Zn), and Manganese (Mn) were selected as a model heavy metals. Since this study target at Oyu Tolgoi copper ore deposit, mine wastewater will contain copper and base metals such as Zn and Mn. Mine wastewater generally contains sulfate ions, and the analytical grade reagents of $CuSO_4 \cdot 5H_2O$, $ZnSO_4 \cdot 7H_2O$ and $MnSO_4 \cdot 5H_2O$ (Wako Pure Chemical Industries, Ltd.) were used as the sources of the metals.

2.2 Batch adsorption studies

Batch adsorption studies were conducted by the conditions shown in **Table 2**. pH of the initial solution was adjusted with sulfuric acid. The mixture was shaken in 100×10^{-6} m^3 Erlenmeyer flask in a shaker. The final concentration after suction filtration and filtration with 0.45 μm membrane filter was determined by ICP-AES. The material balances of metals are represented by,

$$L_0 \times C_0 = L \times C + S \times q \qquad (1)$$

where L_0 is the mass of initial solution, C_0 is the initial metal concentration, L is the mass of solution, C is the equilibrium metal concentration, S is the mass of adsorbent, and q is the adsorbed amount of metals per unit mass of zeolite. q was determined by Eq. (1) with the assumption of L=L_0.

To marshal the adsorption data, Langmuir adsorption model was used.

$$q = q_m \times K \times C / (1 + K \times C) \qquad (2)$$

where q_m is the saturated adsorbed mass and K is the Langmuir constant. The isotherms were expressed by this equation.

3. Result and Discussion

3.1 Characterization of natural zeolites

From XRD measurement the frameworks of the used natural zeolites could be classified into three species according to the major components, such as Clinoptilolite (CLP), Mordenite (MOR), and Chabazite (CHA). All zeolites have Ca type frameworks. The Si/Al molar ratios were measured by EDX analysis. The mass fraction of each oxidized metal was determined with the assumption that all metals should exist in form of oxide metal and is shown in **Table 4**. The measured cation exchange capacity and these results were shown in **Table 3**. As expected from the results of EDX and CEC, natural zeolites have impurity such as quarts, Sanidine, Muscovite, and so on. It found that there is general correlation between Si/Al ratio and CEC.

3.2. Batch adsorption studies

Table 1 Information of Mongolian natural zeolites[1]

Sample	Deposit	Sampling depth [m]	Sampling date
CLP	Tsagaan Tsav	60	09/2004
MOR	Tsagaan Tsav	60	09/2004
CHA	Tsagaan Tsav	150	12/2005

Table 2 Conditions of adsorption run

Mass of initial solution, L_0 [g]	20
Initial concentration of metals, C_0 [g/m^3]	100 – 5000
Mass of zeolite, S [g]	1
Contacting time, t [h]	240
Initial pH of solution, pH_0	2.5 – 5
Temperature, T [K]	300

Table 3 Principal characteristics of Mongolian natural zeolites

	CLP	MOR	CHA
Surface area [m^2/g]	31.7	7.8	164.1
Cation exchange capacity $\times 10^{-3}$ [mol/100g]	62 - 76	48 - 69	31 - 43
Si/Al molar ratio [-]	7.88	9.28	8.87

Table 4 The oxidized metal composition

Wt %	CLP	MOR	CHA
Al_2O_3	7.17	5.10	6.70
SiO_2	66.62	55.80	70.05
SO_3	2.32	1.96	4.10
K_2O	9.36	10.54	7.94
CaO	3.91	22.36	5.52
Fe_2O_3	9.34	3.27	4.88
TiO_2	1.28	0.96	0.19
Mn_2O_3	—	—	0.61

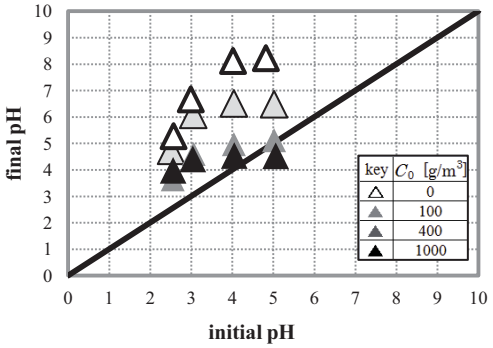

Fig. 2 pH change of CLP in Zn sol.

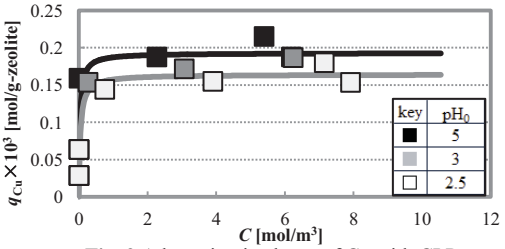

Fig. 3 Adsorption isotherm of Cu with CLP

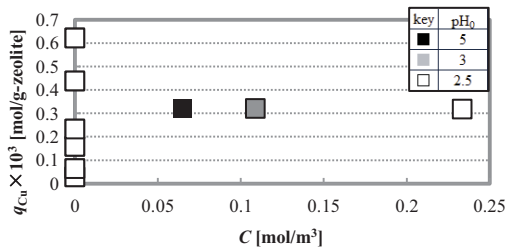

Fig. 4 Adsorption isotherm of Cu with MOR

The natural zeolite could adsorb all kinds of metals. The adsorption of sulfur content was measured as well and the used zeolites could not adsorb it at all. To attain the adsorption equilibrium it was found that 240 hours were needed. The pH was elevated from 3 to around 4-7 by the addition of zeolite since the zeolite preferentially may adsorb H^+ from solution [2], as shown in **Fig. 2**. The equilibrium pH decreased slightly with initial concentration of metals. Especially with MOR, the equilibrium pH tends to rise up. The pH influences precipitation and dissolution of metals. The addition of the zeolites causes the dissolved metals to precipitate, such as $Cu(OH)_2$, $Zn(OH)_2$, and $Mn(OH)_2$.

The adsorption isotherms of metals on the natural zeolite are shown in **Fig. 3 to 11**. q_m and K are shown in **Table 5**. The results of pH_0=5 and pH_0=3 are almost same. The adsorption amount increase with an increase in initial pH, pH_0. The reason for this is that competitive adsorption between H^+ ion and metal ions were occurred.

Cu In the case of adsorption with MOR, equilibrium concentration of metal was 0. Since the equilibrium pH tends to be higher and copper hydroxide has low solubility to water, it may produce precipitation. Then, the most of adsorption data on MOR were not fit to Langmuir adsorption isotherm. The adsorbed amount follows the order: MOR, CLP, CHA. The legal concentration of Cu^{2+} in effluent standard is 3 mg/L[4]. It is seen that 1 g of CLP, MOR and CHA are able to treat 20 g of 200 mg/L, 600 mg/L and 200 mg/L solutions to below the legal requirement, respectively.

Zn MOR may made zinc hydroxide precipitation. The adsorbed amount follows the order: MOR, CLP, CHA. The legal concentration of Zn^{2+} in effluent standard is 2 mg/L[4]. It is seen that 1 g of CLP, MOR and CHA are able to treat 20 g of 100 mg/L, 50 mg/L and 100 mg/L, respectively.

Mn The adsorbed amount follows the order: MOR, CLP, CHA. The legal concentration of

Table 5 Principal characteristics of Mongolian natural zeolites

		pH_0=high		pH_0=low	
metal	zeolite	$q_m \times 10^3$ [mol/g-zeolite]	K [m³/mol]	$q_m \times 10^3$ [mol/g-zeolite]	K [m³/mol]
Cu	CLP	0.20	32.13	0.16	23.07
	MOR	—	—	—	—
	CHA	0.18	10.17	0.13	70.95
Zn	CLP	0.15	5.62	0.14	1.67
	MOR	0.84	1.96	0.83	0.98
	CHA	0.11	8.50	0.07	2.46
Mn	CLP	0.15	2.12	0.13	1.87
	MOR	0.17	0.11	0.17	0.05
	CHA	0.12	0.32	0.11	0.43

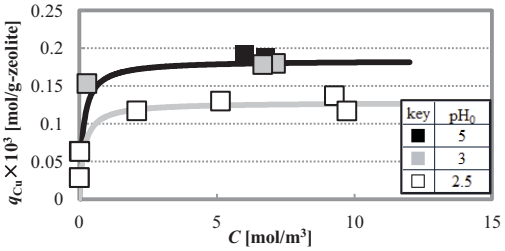

Fig. 5 Adsorption isotherm of Cu with CHA

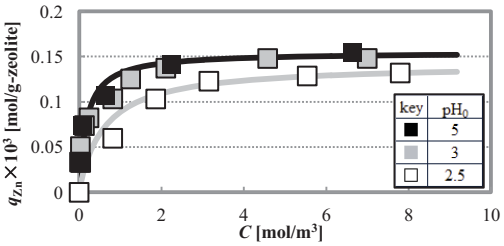

Fig. 6 Adsorption isotherm of Zn with CLP

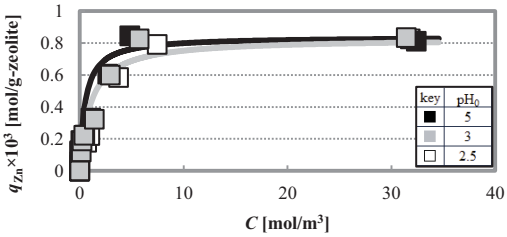

Fig. 7 Adsorption isotherm of Zn with MOR

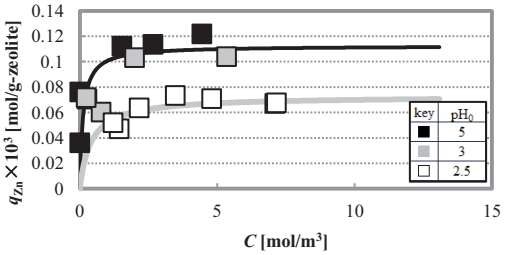

Fig. 8 Adsorption isotherm of Zn with CHA

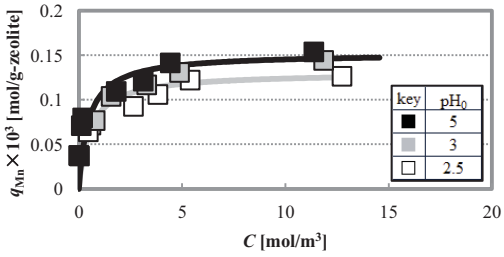

Fig. 9 Adsorption isotherm of Mn with CLP

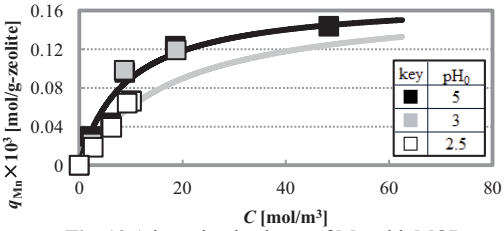

Fig. 10 Adsorption isotherm of Mn with MOR

Mn^{2+} in effluent standard is 10 mg/L[4]. It is seen that 1 g of CLP, MOR and CHA are able to treat 20 g of 200 mg/L, 50 mg/L and 50 mg/L, respectively.

Despite that the CEC follow the order: CLP, MOR, CHA, adsorbed amount didn't follow the same order. It is because that there is an effect of precipitation of metal hydroxide.

Adsorption from binary wastewater

The adsorption of Zn and Mn in the binary system with CLP was carried out (**Fig. 12**). The gray line and dashed line shows the adsorbed isotherms of Zn and Mn in the single system and black key shows total adsorption amount of Zn and Mn in binary system. The $q_{m,Zn}$ and $q_{m,Mn}$ have almost the same adsorbed amount to black key. It is considered that Zn and Mn are adsorbed on same adsorption site.

Adsorption from ternary wastewater

The results of adsorption from ternary wastewater were shown in **Fig. 13** to **Fig. 15**. It is clear that adsorbed amount from ternary solution were lower than from single solution. With CLP, it was considered that Zn and Mn were adsorbed on same adsorption site in binary system, however, the results in ternary system was different. Because there may be other effects, such as competitive adsorption between H^+ and metal ion, change of pore size, etc. With MOR, Cu may produce hydroxide and the concentrations after equilibrium were 0. The adsorption isotherm of total metal shown as black lines were inaccurate due to hydroxide precipitation, and there is not leaving much room for discussion.

4. Conclusion

XRD pattern showed that Mongolian natural zeolites have Clinoptilolite, Mordenite and Chabazite mainly with Ca-type. Silica/Alumina molar ratio was 7.88, 9.28, and 8.87, and Cation Exchange Capacity was 62-76$\times 10^{-3}$, 48-69$\times 10^{-3}$, and 31-43$\times 10^{-3}$ mol/100g-zeolite, and surface area were 32, 8, 164 m^2/g-zeolite with CLP, MOR, and CHA respectively. These zeolites could remove copper, zinc and manganese. The adsorption amount increase with an increase in initial pH. Removal of the heavy metal ions was not only due to ion exchange but also due to precipitation of metal hydroxides. In binary system of Zn and Mn, it was considered that Zn and Mn adsorbed on same adsorption site with CLP.

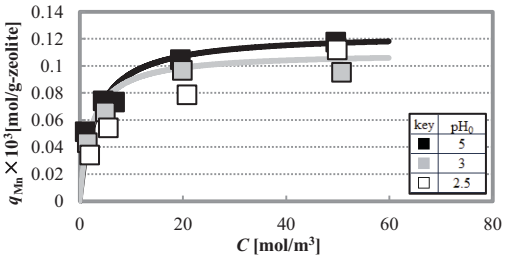

Fig. 11 Adsorption isotherm of CHA in Mn sol.

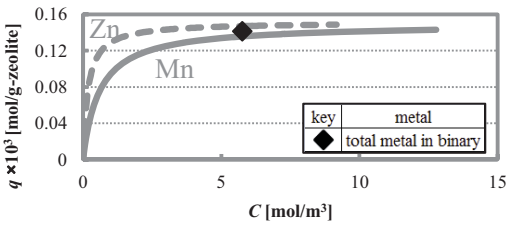

Fig. 12 Adsorption isotherm of Zn and Mn

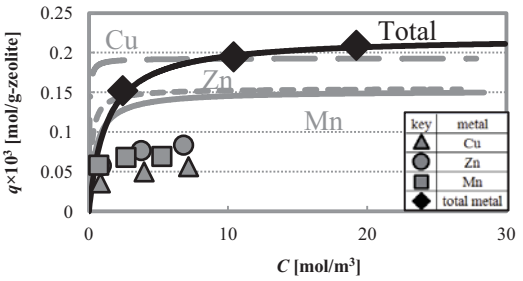

Fig.13 Adsorption isotherm with CLP from ternary system

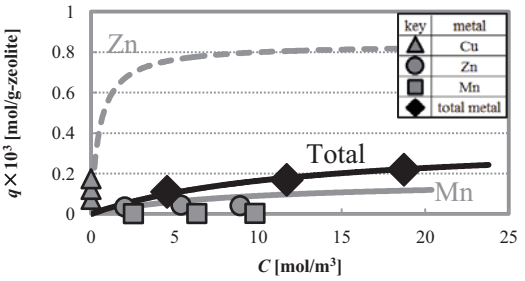

Fig.14 Adsorption isotherm with MOR from ternary system

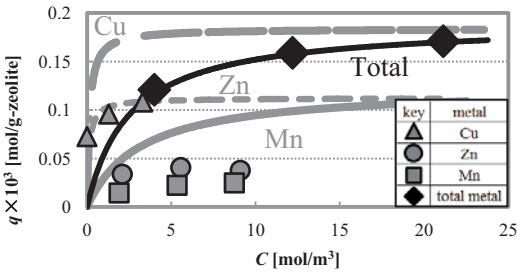

Fig.15 Adsorption isotherm with CHA from ternary system

Reference

[1] Bolortamir. Ts, *et al.*; *J. Chem. Eng. Japan*, **41**, 1003 (2008)
[2] Motsi, T.*et al.*; *Int. J. Miner. Process*, **92**, 42–48 (2009)
[3] Web site "Database of Zeolite Structures" http://www.iza-structure.org/databases/
[4] Environmental Bureau of the Tokyo Metropolitan Government http://www.kankyo.metro.tokyo.jp/water/pollution/regulation/emission_standard/hazardous_materials_except.html
[5] JOGMEC http://www.jogmec.go.jp/

Nomenclature

CLP: Clinoptilolite, MOR: Mordenite, CHA: Chabazite, L_0: Mass of initial solution [g], C_0: Initial concentration of metals [g/m^3], C: Final concentration of metals [g/m^3], S: Mass of zeolite [g], t: Contacting time [h], pH_0: Initial pH of solution, pH: equilibrium pH, T: Temperature [K], q: adsorbed amount [mol/g-zeolite], q_m: maximum adsorption amount [mol/g-zeolite], K: Langmuir constant [m^3/mol]

Study on the Sulfuric Acid Resistance of Cementitious Material
Using OPC-γ-C_2S-Quartz with Autoclave Curing

Student Number: 10M18111 Name: Yuriko TSUBURAYA Supervisor: Nobuaki OTSUKI

オートクレーブ養生した OPC-γ-C_2S-ケイ石微粉末系材料の耐硫酸性に関する研究
圓谷百合子

近年, γ-C_2S を混和材としてコンクリート材料に添加する研究が注目されている. すなわち, OPC-γ-C_2S-ケイ石微粉末系の材料にオートクレーブ養生を行うことで，寸法安定性及び化学的安定性を有するとともに外部劣化因子に対して高い抵抗性を示すことが提案されている．本研究では，γ-C_2S を混和しオートクレーブ養生したセメント系材料を用い，硫酸劣化に対する耐久性を実際の温泉地及び実験室環境にて検討した．その結果，最も耐硫酸性を有する最適なγ-C_2S の混和率を決定し，OPC-γ-C_2S-ケイ石微粉末系材料の実用化を示唆した.

1. Introduction

Nowadays, sulfuric acid attacks are found in the hot spring or sewerage pipe[1]. The sulfuric acid attack on the concrete structures are the serious problems. To obtain the durability, concrete needs to have dimensional stability, chemical stability, and high resistance against external aggressive ions. Furthermore, the use of concrete in engineered barriers is being considered in the construction of radioactive waste disposal facilities. In these circumstances, concrete needs the high durability. For these purposes, it is obvious that high durability concrete is in demand.

On the other hand, the research on the high durability of the cement-based material using γ-$2CaO{\bullet}SiO_2$ (hereafter"γ-C_2S") is focused. Initial compressive strength is small mixed γ-C_2S, because γ-C_2S does not react with water under normal curing. However it reacts in high temperature and high pressure. In the cement-based material mixed with γ-C_2S, the amount of tobermorite ($5CaO{\bullet}6SiO_2{\bullet}5H_2O$) which has high shrinkage resistance is increased after conducting the autoclave curing. Saito *et al.*[2] have proposed the concept of material design for high durability cement-based material in high shrinkage resistance. Using autoclave curing, tobermorite is generated in the hardened body and permeability resistance to external aggressive ions such as chloride ion and sulfate ion has been obtained and it becomes high shrinkage resistance in the hardened body.

However, the experiment on the durability performance especially in the sulfuric acid which is the severe environment, for concrete and mortar has not been investigated yet. Therefore, this study aims (1) to evaluate effects of the γ-C_2S and Quartz substitution ratio on the sulfuric acid resistance in autoclave cementitious material. And, (2) to evaluate the usefulness of a laboratory test, comparing an actual environment testing to an accelerating test in a laboratory has been carried out. (3) To propose the mixed proportions for improving the initial compressive strength when removed from molds.

2. Experimental Methodology

2.1 Materials and Mix proportions

The materials used in this study as binder are Ordinary Portland Cement (OPC), γ-C_2S and Quartz. Table.1 shows the chemical composition of these materials. Table.2 shows the mixed proportions of concrete specimens and the symbols. The name of cement paste and mortar specimens are also used same name with concrete. The mixed cement paste, mortar, cylinder concrete and concrete pile were cast in a mold that volume are 1cm×1cm ×8cm, 4cm×4cm ×16cm, ϕ10cm×20cm and ϕ20cm×30cm×thickness4cm respectively.

2.2 Curing

After casting, initial curing with 100% RH at 65ºC is done for 4 hours. Then the molds are removed from the specimen and autoclave for 8 hours under 1MPa at 180ºC. In addition, non-autoclave specimen, only OPC which is assumed generally cement-based material, was named after "Ref".

Table.1 Chemical composition and Physical property of materials

	SiO_2	Al_2O_3	Fe_2O_3	CaO	SO_3	f.CaO	Density (g/cm^3)	Blaine (cm^2/g)
OPC	21.6	5.08	2.93	64.5	1.95	0.4	3.16	3310
γ-C_2S	35.0	1.7	0.10	61.9	-	-	3.01	3060
Quartz	93.3	1.6	1.4	-	-	-	2.66	3870

Table.2 Mixed Proportions and Specimens Symbols

Name Q:γ-C_2S:OPC	W/B (%)	Quantities (kg/m^3)							Autoclave Curing
		W	OPC	γ-C_2S	S*	G*	Quarz	MT150	
Ref	32.9	148	450	0	924	907	0	0.00	×
50-0-50		148	225	0	906	889	225	3.37	○
50-20-30		148	135	90	904	887	225	2.88	○
50-30-20		148	90	135	903	881	225	2.68	○
50-40-10		148	45	180	902	886	225	2.56	○
40-0-60		148	270	0	910	893	180	3.37	○
40-36-24		148	108	162	906	889	180	2.59	○
30-0-70		148	315	0	913	896	135	4.27	○
30-42-28		148	126	189	909	892	135	3.00	○

*S : Fine aggregate, G : Coarse aggregate

2.3 Sulfuric Acid Exposure Test

After autoclave curing, the designed cement paste and mortar specimens were exposed to the solution of H_2SO_4 with pH1 at 20ºC for 38 weeks in the laboratory. In order to maintain pH value, the solution was exchanged every 1week. On the other hand, the concrete piles were exposure in the hot spring at Kusatsu in Japan with pH1.7-2.0 at 50-60ºC for 442 days (Figure.1).

2.4 Evaluation on Performance

Compressive strength test was carried out according to JIS A 1108 using cylinder specimen (ϕ10cm×20cm) before exposure. And after 38 week exposure, compressive strength test was also carried out. After that, remained ratio of compressive strength was calculated using following formula (1).

(After exposure / Before exposure)×100(%) (1)

During submerging test in the laboratory, the weight of specimens were measured on the 1, 2, 3, 5days, 1, 2, 3, 5, 7, 10, 13, 20, 26 and 38 weeks. And in the hot spring specimens were measured the weight on the 53, 115, 349 and 442 days.

The identification of amorphous material by using Fourier Transform Infrared Reflection (FT-IR) was conducted (frequency range 7800-350cm-1). In order to measure amorphous material like gel on the specimen surface, Attenuated Total Reflection (ATR) was conducted.

The identification of reactive products by using X-ray diffraction (XRD) was conducted. The samples were grinded to give a sample, which were cut at surface part (0-2mm) and core part (8-10mm) from exposed surface. The samples were scanned between 5˚-70˚ with an X'Celerator detector.

In order to measure the initial compressive strength when removed from molds, compressive strength test after demolded (before autoclave curing) was carried out according to JIS A 1136 using concrete piles (ϕ20cm×30cm×thickness4cm).

Fig.1 During exposure in hot spring

3. Result and Discussion

3.1 Compressive Strength Before exposure and After exposure

In figure.2, the left side bar shows compressive strength of concrete cylinder before exposure test. As can be seen, when replacement ratio of Quartz and γ-C_2S decreased, the compressive strength has increased. Figure.2 in right side bar shows compressive strength of concrete cylinder after exposure test. As can be seen, when replacement ratio of Quartz decreased, the compressive strength has increased. This result is the same tendency with compressive Strength of concrete cylinder before exposure. On the other hand, in case of before exposure, compressive strength is decreased, when percentage of γ-C_2S is increased. However in case of after exposure, compressive strength is increased, when replacement ratio of γ-C_2S is increased. Figure.2 in line graph shows remained ratio of compressive strength. It should be noted that effect of Quartz to compressive strength after exposure is small; however effect of γ-C_2S is very big and important. Remained ratio of compressive strength is increased, when percentage of γ-C_2S is increased. Therefore, it is confirmed that γ-C_2S is very important to increase the compressive strength after exposure.

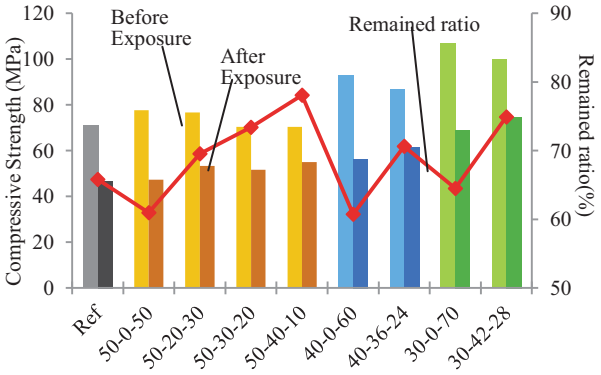

Fig.2 Compressive Strength Before and after exposure, and Decreasing ratio

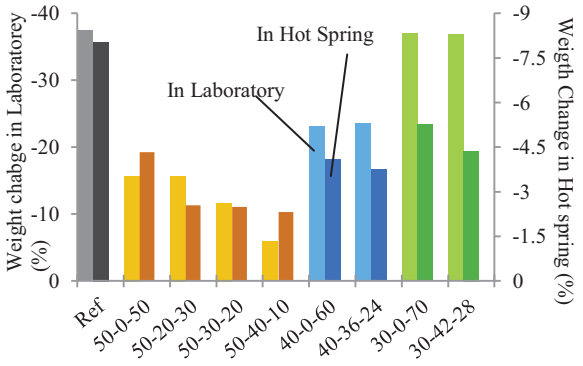

Fig.3 Weight Change After 38 weeks Exposure

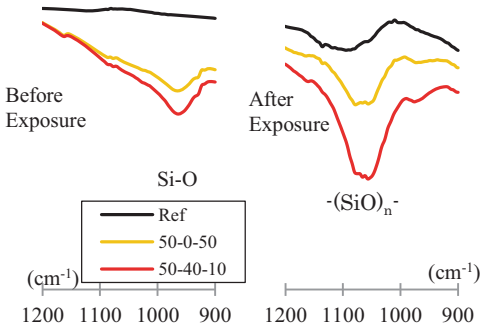

Fig.4 FT-IR spectra at Surface part

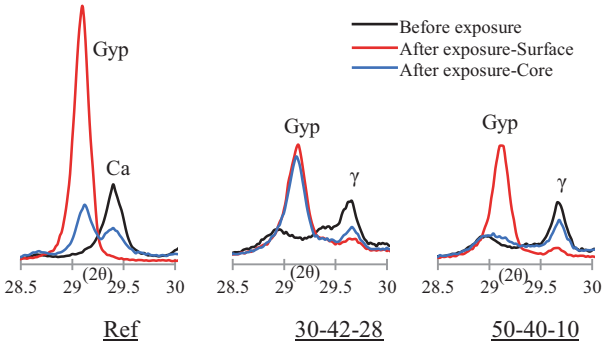

Fig.5 XRD pattern (28.5-30°)

3.2 Weight change Exposure

In figure.3, the left side shows weight change of mortar for 38 weeks exposure in the laboratory. In figure.3,
when Quartz percentage changed from 30% to 50%, the weight change is less. Furthermore, in case of same percentage of Quartz, it could be confirmed that the sulfuric acid resistance has improved by increasing the ratio of γ-C_2S. It is contemplated that hydration products which are tobermorite and other products are changed due to replacement ratio of γ-C_2S or Quartz. It means 50-30-20 and 50-40-10 specimens have high resistance against sulfuric acid. Particularly, in 50-40-10 specimen, weight loss reduced by 84% compared to Ref specimen.

Figure.3 in right side shows weight change of concrete pile for 442 days exposure in the hot spring. By comparison, in the laboratory and in the hot spring, the weight of specimens which exposed in laboratory is decreased more than in hot spring due to low pH. And in figure.3, the more amount of Quartz, the less weight change. And the more amount of γ-C_2S shows the less of weight change. This result is the same tendency with before exposure. Therefore, it is obvious that, the accelerating test in a laboratory is useful comparing the actual environment testing.

3.3 Reactive Products after Exposure test of cement paste

Figure.4 shows the FT-IR spectra of surface part before and after exposure. Before exposure, Si-O bonds which were comprised in tobermorite were observed except for Ref specimen. On the other hands, after exposure, -$(SiO)_n$- bonds which were comprised in silica gels were observed except for Ref specimen. And comparing 50-0-50 to 50-40-10 specimens, silica gel peak becomes strong in 50-40-10 after exposure.

Figure.5 shows the XRD patterns ranged from 28.5-30°. In the figure, "Gyp" corresponds to gypsum which is an expansive product, "γ" is γ-C_2S and, "Ca" is calcite.

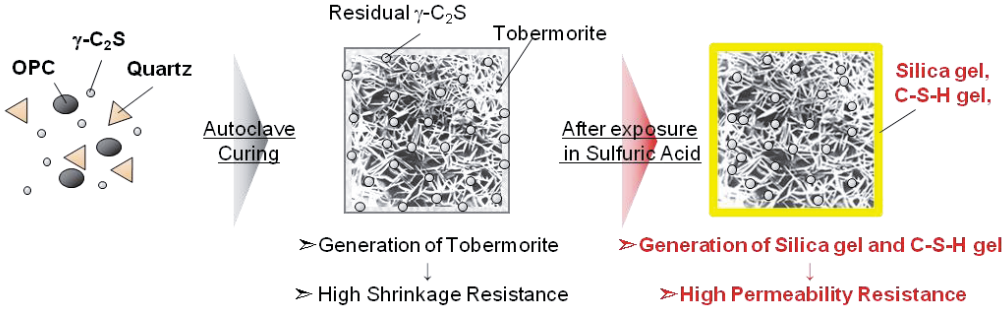

Fig.6 Concept of material deign for high resistance against sulfuric acid attack

Table.3 New Mixed Proportions and Specimens Name

	Name Q:γ-C_2S:OPC	W/B (%)	Quantities (kg/m^3)							Autoclave Curing
			W	OPC	γ-C_2S	Quartz	FA	S*1	G*1	MT 150	
Series W/B	*Ⅱ50-0-50*	26.0	148	285	0	285	0	790	787	5.69	○
	Ⅱ50-20-30		148	171	114	285	0	787	784	4.55	○
Series HC	*HC50-0-50*	32.9	148	225*2	0	225	0	855	851	3.37	○
	HC50-20-30		148	135*2	90	225	0	853	850	3.37	○

*1=S :Fine aggregate, G :Coarse aggregate *2=Early-strength cement

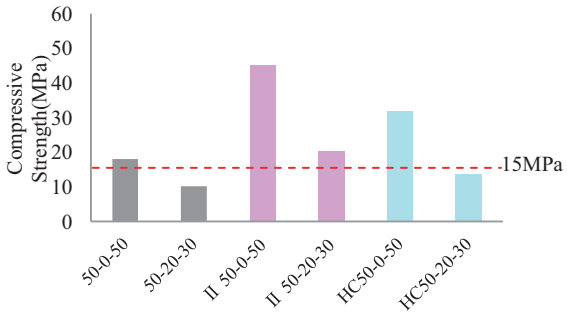

Fig.7 Compressive Strength when Remove from mold

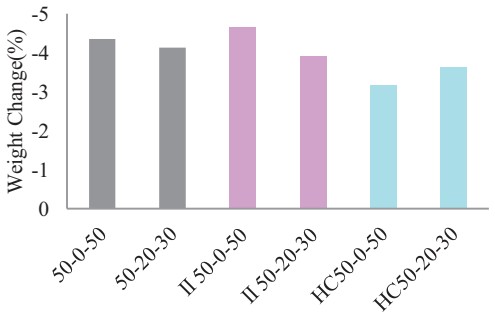

Fig.8 Weight Change After 20 weeks exposure

In 50-40-10 specimen, γ-C_2S was disappeared after exposure at surface part, on the other hand, γ-C_2S existed in the core part after exposure. However, in 30-42-28 specimen, γ-C_2S does not exist after exposure in surface and core part due to deterioration until core part. This result is attributed that dissolution of γ-C_2S and generation of silica gel like as shown in Eq.(1) .

$$\gamma\text{-}2CaO\bullet SiO_2+4H^+ +nH_2O \rightarrow 2Ca^{2+}+SiO_2\bullet nH_2O+2H_2O \quad (1)$$

From these results, it could be concluded that the amount of tobermorite or residual γ-C_2S after autoclave curing change to silica gel and C-S-H gel at the surface part. Therefore, it can be considered that the surface part was densified due to generation of silica gel and C-S-H gel in case of the high γ-C_2S and quartz substitution ratio (such as 50-30-20 and 50-40-10 specimens)(Figure.6).

3.4 The Improvement of initial compressive strength when removed from molds

In the pre-casted concrete pile, the initial compressive strength when removed from molds, needs more than 15MPa. Therefore, to improve the initial compressive strength when removed from molds, new mixed proportions which were low Water-Binder ratio (hereafter W/B) and use early-strength cement were proposed. Table.3 shows the mixed proportions of new concrete specimens and the symbols.

Figure.7 shows the initial compressive strength when removed from molds. 50-0-50 and 50-20-30 specimens are low compressive strength when removed from molds which are original mixed proportions. On the other hand, Ⅱ50-0-50, Ⅱ50-20-30, HC 50-0-50 and HC 50-20-30 are improved compressive strength.

Furthermore, figure.8 shows weight change after 20 weeks exposure. There is nothing much difference between original mixed proportions and new mixed proportions. Therefore, it was confirmed that low W/B and using early-strength cement show the good effect to improve compressive strength when remove from molds.

4. Conclusion

(1) In case of quartz substitution ratio 50% and γ-C_2S substitution ratio more than 30% with autoclave curing, the high sulfuric acid resistance has obtained. Because the sulfate ion penetration was small due to tobermorite or residual γ-C_2S change to silica gel and C-S-H gel at the surface part, then the surface part was densified due to generation of silica gel and C-S-H gel.

(2) The accelerating test in a laboratory and the actual environment testing show the same tendency.

(3) In order to improve the initial compressive strength when removed from mold, using low W/B with autoclave curing and early-strength cement showed the good effect to improve the initial compressive strength.

Therefore, in the view point of application, the cement based material using OPC-γ-C_2S-Quart can be able to put in the practice.

【Reference】

1) H. Matsusita *et al.*, : Classification of Probability of Deterioration of Concrete by Sulfate Attack Based on Investigation Results of Sulfate Content of Ground, Doboku Gakkai Ronbunshuu E,Vol.66, No.4, pp.507-519, 2010.12

2) T. Saito *et al.*,: Carbonation Reaction of Calcium Silicate Hydrates by Hydrothermal Synthesis at 150˚C in OPC-γ-$Ca_2\bullet SiO_4$- α‐quartz System, Journal of Advanced Concrete Technology, Vol.5, No.3, pp.333-341(2007)

Production of bioethanol from polysaccharides in the red seaweed

Student Number: 10M18134　Name: Kanami NAKAMURA　Supervisor: Kiyohiko NAKASAKI　Co-supervisor: Sachio HIROSE

紅藻中多糖類からのバイオエタノール生成

中村 奏美

近年、石油代替燃料として食糧と競合することのない原料からのバイオエタノール生成が期待を集めている。本研究では、食糧と競合せず、リグニンを含まないために高度の前処理を必要としない原料として海藻に着目し、酸・酵素を使用した糖化と酵母による発酵を組み合わせることで紅藻中多糖類から 55.0 g/L の高濃度バイオエタノールを生成した。さらに、酸や酵素を使用せずに、紅藻中多糖類を糖化することを目ざして、ガラクタン分解酵素を生産する遺伝子組み換え酵母を創製した。

1 Introduction

In recent years, bioethanol has attracted attention as an alternative to petroleum-derived fuel. The efficient production of ethanol from inedible biomass or biomass that people do not find palatable has long been considered a crucial requirement for the effective utilization of these materials. Many studies have been performed on the production of ethanol from lignocellulosic materials, such as wood, sugarcane bagasse, switchgrass, rice straw, and wheat straw. The presence of lignin in lignocellulosic materials makes cellulose and hemicellulose resistant to hydrolysis, and thus, various pretreatment methods to accelerate the saccharification of polysaccharides have been contrived. On the other hand, utilization of biomass without lignocellulosic materials such as corn and sugarcane for the ethanol production caused competition with the usage as food.

In this study, seaweed that is not utilized as food was proposed as one of the most promising biomass materials that can be easily converted to ethanol, since seaweeds are known to contain low concentration of lignin. It is expected that the production cost and energy can be saved by the use of the seaweed. Agar weed belonging to the red seaweed was used as the substrate and high concentration of bioethanol was produced in the following saccharification and fermentation. Then, for the purpose of the saccharification of the red seaweed without using acid and enzyme, recombinant yeast that produce galactan-degrading enzyme was developed.

2 Materials & Methods

2.1 Production of bioethanol from polysaccharides in the red seaweed

2.1.1 Red seaweed, enzyme, and yeast

Agar weed (*Gelidium elegans* Kuetzing) was used as representatives of red seaweeds (Fig. 1). The dried agar weed was washed once using distilled water in the laboratory, and dried again at 60 °C for 2 days. The dried agar weed was powdered using a mill to less than 0.5 mm in diameter before use.

Meicelase, a commercial enzyme was used for saccharification of the glucans in the seaweeds, such as cellulose, cellobiose and starch. The cellulase, cellobiase and amylase activities of Meicelase were 73.3, 227 and 13.6 units/g, respectively. It was ascertained that Meicelase does not contain galactan hydrolyzing enzyme.

Saccharomyces cerevisiae IAM 4178 was used in the fermentation of seaweed hydrolysate.

2.1.2 Enzymatic saccharification of red seaweed

Enzymatic hydrolysis was carried out to produce glucose from agar weed. Agar weed in 0.1 M citric acid buffer solution was added to the filtered and sterilized enzyme solution. The hydrolysis was carried out at 50 °C for 120 h under static conditions. Glucose concentrations were determined by the HPLC method.

2.1.3 Combined saccharification of red seaweed

Combined saccharification, that is, the acid hydrolysis of certain polysaccharides followed by the enzymatic hydrolysis of other polysaccharides, was applied to obtain high concentrations of sugars for use in the following fermentation with yeast. For the acid saccharification, agar weed was added to 2% sulfuric acid, and the mixture was autoclaved at 121 °C for 30 min. After autoclaving, the pH value of the reaction mixture was adjusted to approximately 5.5 by adding calcium carbonate. Next, the Meicelase solution was added aseptically to the reaction mixture. The enzymatic hydrolysis was carried out by incubating the reaction mixture statically at 50 °C for 120 h. After combined saccharification, concentration of glucose was measured using the HPLC and concentration of galactose was measured using the F-kit for Lactose/D-Galactose.

Composition	
Glucan Starch Cellulose	21.8%
Galactan Agarose Carrageenan	26.5%
Crude fiber	12.3%
NFE	70.9%
Crude protein	11.6%
Crude fat	0.7%
Crude ash	4.6%

Fig. 1　Composition of agar weed.

2.1.4 Fermentation of red seaweed hydrolysates

The seaweed hydrolysates obtained by the combined saccharification was mixed with Polypepton, yeast extract, and *S. cerevisiae* IAM 4178, which was precultured on an YM agar plate at 30 °C for 36 h and collected using a sterilized spatula to prepare the starting material for fermentation. The fermentation was carried out at 30 °C for 5 days under static conditions, and was ceased when almost all fermentable sugars were consumed. The concentrations of glucose, ethanol, galactose and glycerol, the byproduct in the fermentation with yeast in the substrate were measured.

2.2 Development of agarase producing yeast

Employment of acid and/or reagent grade of enzyme can increase the cost for the ethanol production. In order not to use the acid and enzyme, production of agarose degrading enzyme from yeast was attempted.

Structure of agarose was shown in Fig. 2. Agarose is derived from D-galactose and 3,6-anhydro-L-galactose units, which condense through α-1,3 and β-1,4 glycosidic bonds and hydrolyzation of agarose generates D-galactose, 3,6-anhydro-L-galactose and hetero-oligosaccharide composed of two or more saccharides. Agarase is the mixture of enzymes which hydrolyze α-1,3 and β-1,4 glycosidic bonds in the agarose and each of the are called α-agarase and β-agarase, respectivity. Hydrolyzation of agarose by α-agarase generates agaro-oligosaccharide of which component unit is agarobiose of non-reducing sugar and hydrolyzation of agarose by β-agarase generates neo-agaro-oligosaccharide of which component unit is neoagarobiose of reducing sugar.

At first, a β-agarase gene derived from agar-degrading bacteria was transformed to yeast and degradation of agarose by β-agarase produced by the recombinant yeast was carried out.

2.2.1 Strains and vector

The β-agarase gene was derived from agar-degrading bacteria, *Cellvibrio* sp. OA-2007. OA-2007 was isolated from activated sludge sampled in Kochi prefecture. DNA sequences of the genes encoding two kinds of β-agarase were determined and named *agaA* and *agaB*, respectively. DNA sequence of *agaA* doesn't include the sequence corresponding to the signal peptide and β-agarase produced from *agaA* accumulates inside the cell. On the other hand, DNA sequence of *agaB* includes the sequence corresponding to the signal peptide and β-agarase produced from *agaB* is secreted to outside of cells.

Saccharomyces cerevisiae YPH499 which is a histidine-requiring yeast strain was used as a host. A vector of pESC-HIS was used to introduce each of *agaA* and *agaB* gene into the yeast (Fig. 3).

2.2.2 Transformation of yeast by a plasmid including β-agarase gene

Genes of *agaA* and *agaB* were introduced to the pESC-HIS vector individually and pESC-HIS with *agaA* or *agaB* was introduced to YPH499. Preculture of OA-2007 was prepared using N. B. medium by incubating at 30 °C for 24 h and then, The strainOA-2007 was cultivated using liquid agarose medium at 30 °C for 48 h. Cells were harvested and genomic DNA was extracted. Genes of *agaA* and *agaB* were amplified by PCR. For the amplification of *agaA*, forward primer, *ACTAGTATGCAGCCAATCAGTTGG* and reverse primer, *GAGCTCTTAGTGGGTGAAGTTT* were used. For the amplification of *agaB*, forward primer, *GGATCCATGAAAAAAATCACTTCAT* and reverse primer, *GGATCCATGAAAAAAATCACTTCAT* were used. PCR amplified fragment of agarase genes and pESC-HIS were ligated using DNA ligation kit. The yeast, YPH499 was transformed by the constructed plasmid using Fast™-Yeast Transformation kit.

2.2.3 Degradation of agarose by crude enzyme from β-agarase producing yeast

Crude enzyme was prepared from β-agarase producing yeast and degradation of agarose using the crude enzyme was carried out. Recombinant yeast strains were inoculated to SD(-HIS) medium and cultured statically at 30 °C for 24 h. Then, the culture was inoculated to SG(-HIS) medium and shaken at 150 rpm at 30 °C for 48 h. After the cultivation, Cells were harvested by centrifugation (3000×g, 5 min) and were washed by phosphate buffered saline (pH=7.0). After the washing, cells were suspended phosphate buffered saline. Glass beads of 0.2 g with diameter of

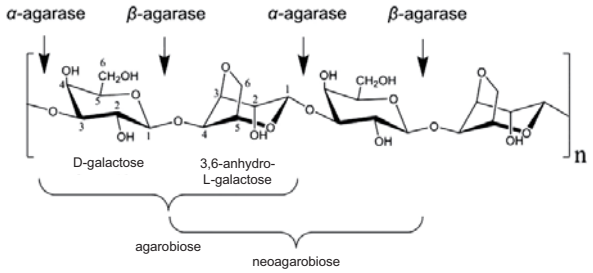

Fig. 2 Structure of the agarose molecule and two types of product derived from digestion with agarases [1].

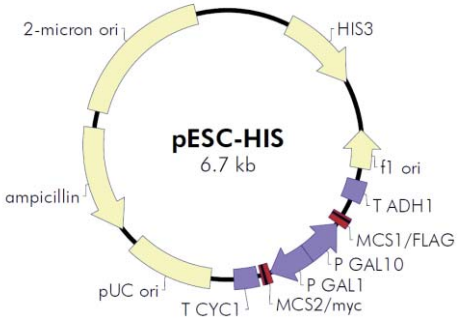

Fig. 3 Structure of the pESC-HIS vector [2].

0.5 mm was added to 1 mL of the suspension in 1.5 mL microtube. Then, vortexing of the microtube for 1 min followed by cooling down on ice for 4 min was repeated three times to disrupt the cells. After the disruption of the cells, the microtube was centrifuged and supernatant was used as crude enzyme.

Crude enzyme solution and agarose powder were added to phosphate buffered saline and shaken at 150 rpm at 30°C. Neo-agaro-oligosaccharide produced by the degradation of agarose was qualitatively analyzed by thin layer chromatography (TLC) using silica gel plate 60 [3].

3 Results & Discussion

3.1 Production of bioethanol from polysaccharides in the red seaweed

3.1.1 Saccharification of agar weed

Fig. 4 represents the glucose and galactose concentrations after the enzymatic saccharification and combined saccharification of agar weed. The concentration of glucose obtained after enzymatic saccharification and combined saccharification were 49.0 and 71.2 g/L, respectively, which corresponds to a conversion of 67.4 and 98.0% of the glucan, when the conversion of glucan is defined as the ratio of the amount of glucose produced by saccharification to the potential amount of glucose in the agar weed. From these results, combined saccharification was able to hydrolyze nearly all of glucan. In addition, the galactan that was not hydrolyzed in the enzymatic saccharification could be hydrolyzed to galactose by the acid saccharification.

More glucan was hydrolyzed by the combined saccharification than the saccharification with only enzyme. It was considered that starch in the agar weed was pregelatinized or hydrolyzed by the acid saccharification.

These results suggested that combined saccharification enables the production of fermentable sugars at high concentrations by thoroughly hydrolyzing the polysaccharides in the agar weed.

3.1.2 Fermentation of agar weed hydrolysates

The concentrations of cells, glucose, galactose and ethanol during the fermentation of agar weed hydrolysate after combined saccharification are shown in Fig. 5. Galactose was only consumed after the complete consumption of glucose. The phenomenon was considered to be caused because microorganisms have the characteristic to consume more easily available sugar (catabolite repression). The concentration of ethanol obtained after 48 h of fermentation was 55.0 g/L. The glycerol concentration increased with the progress of fermentation, and the ratio of glycerol produced to glucose and galactose consumed reached 0.08 g-glycerol/(g-glucose + g-galactose). The cell density of yeast was maintained at a high level, approximately $10^{8.2}$ CFU/mL, throughout the fermentation. As was not shown here for the sake of brevity, 19.2 g/L of ethanol was produced in the fermentation using the hydrolysate after only enzymatic saccharification and 0.03 g-glycerol/g-glucose of glycerol was produced. Therefore, it was confirmed that not only the ethanol but also glycerol concentration were increased by the additional acid saccarification of the agar weed. Higher productivity of glycerol was achieved in the fermentation with agar weed after combined saccharification than that after only enzymatic saccharification. It was considered that the yeast produced more amount of glycerol to regulate the osmotic pressure since osmotic pressure in the medium would have increased by the additional product generated in the acid saccharification.

These results suggested that the combined saccharification enables the production of fermentable sugars at high concentrations by thoroughly hydrolyzing the polysaccharides in the agar weed, thus increasing the ethanol concentration accordingly though productivity of glycerol as byproduct increased simultaneously.

3.2 Development of β-agarase producing yeast

3.2.1 Introduction of β-agarase gene into yeast

Fig. 6 shows the photograph of wild type yeast host strain YPH499, transformants YPH499 with *agaA* (YPH499-agaA) and the strain with *agaB* (YPH499-agaB) cultured on the SG(-His) agar

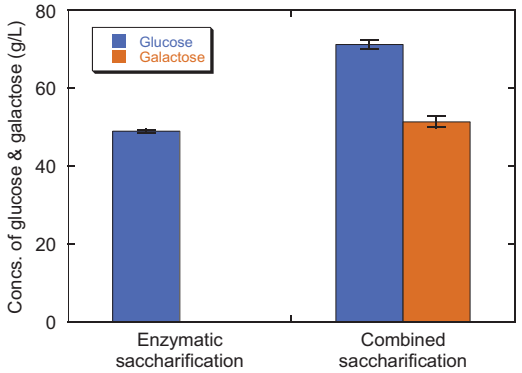

Fig. 4 Comparison of glucose and galactose concentrations after the enzymatic saccharification and combined saccharification of agar weed (n=3).

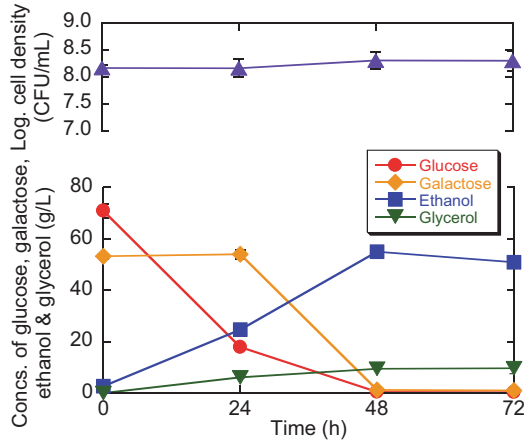

Fig. 5 The courses of cell density and the concentrations of glucose, galactose, ethanol, and glycerol during the fermentation of agar weed hydrolysate formed by combined saccharification (n = 3).

medium for 5 days. The size of the colony of yeast host strain YPH499 did not change during the glycerol cultivation indicating that wild type YPH499 could not grow on SG(-HIS) agar medium. On the other hand, the size of the colonies of YPH499-agaA and YPH499-agaB increased during the cultivation suggesting the growth of these transformants and furthermore, hollows around the colonies of transformants were observed and it was confirmed that agar was degraded by β-agarase derived from *agaA* and *agaB* introduced into the yeast. The size of the hollow around the colony of YPH499-agaB was larger than that of YPH499-agaA, which was consistent with the fact that *agaB* include the sequence corresponding to the signal peptide. Hollow around the colony of YPH499-agaA was supposed to be produced by β-agarase leaked from yeast cell.

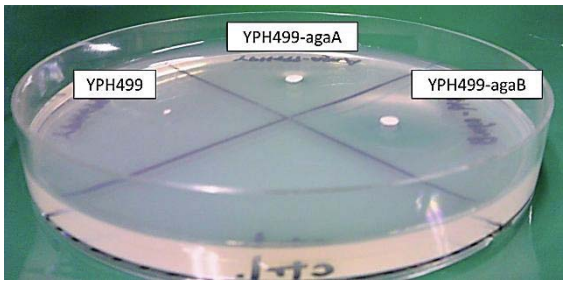

Fig. 6 Formation of hollow on SG(-His) by wild type yeast (YPH499) and two transformed yeasts (strain YPH499-agaA, YPH499-agaB).

3.2.2 Degradation of agarose by crude enzyme from β-agarase producing yeast

The course of TLC pattern for the agarose hydrolysate obtained by applying the crude enzyme derived from YPH499-agaA is shown in Fig. 7. Tetrasaccharide and hexasaccharide were detected after 6h degradation and disaccharide was also detected after 12h degradation and it was confirmed that the crude enzyme from YPH499-agaA can degrade agarose up to disaccharide. The course of TLC pattern for the agarose hydrolysate by applying the crude enzyme derived from YPH499-agaB is shown in Fig.8. Tetrasaccharide and hexasaccharide were detected after 6h degradation. Disaccharide could not be detected even after 48h degradation, suggesting that the crude enzyme from YPH499-agaB could degrade agarose up to tetrasaccharide. Different neo-agaro-oligosaccharides were produced by the degradation of agarose by the crude enzymes from YPH499-agaA and YPH499-agaB, therefore, it was suggested that *agaA* and *agaB* encode agarase with different agarose-degrading characteristics. As was not shown here for the sake of brevity, after cultivation of YPH499-agaB on SG(-His) medium where agarose powder was suspended, tetrasaccharide produced by the degradation of agarose could be detected and it was confirmed that agarose can be degraded by the β-agarase secreted by YPH499-agaB.

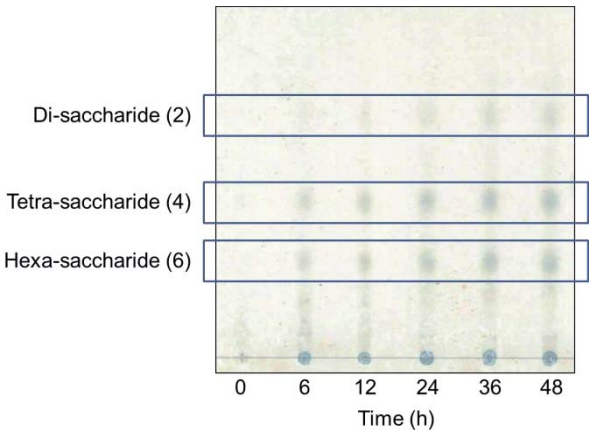

Fig. 7 TLC of hydrolysis products of agarose obtained by the crude enzyme agaA. Di-saccharide, neoagarobiose; Tetra-saccharide, neoagarotetraose; Hexa-saccharide, neoagarohexaose.

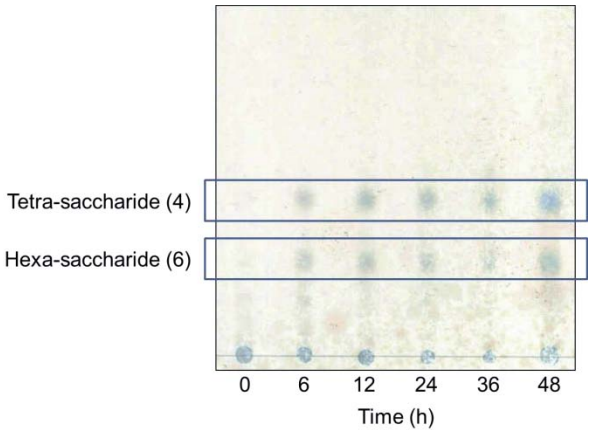

Fig. 8 TLC of hydrolysis products of agarose obtained by the crude enzyme agaB. Tetra-saccharide, neoagarotetraose; Hexa-saccharide, neoagarohexaose.

4 Conclusions

In this study, production of high concentration of bioethanol from agar weed belonging to red seaweed and development of transformed yeast producing agarase that degrade agarose contained in the agar weed were investigated. The concentration of ethanol as high as 55 g/L could be produced from agar weed by the combined saccharification using reagent grade acid and enzyme. Then, genes encoding two kinds of β-agarase were introduced into a yeast strain and agarose could be degraded by β-agarase produced by the transformed yeast strains.

References

[1] Kazłowski, B., *et al*.: Evaluation of HPSEC-ELSD method for precise measurement of β-agarase activity. Biomed. Chromatogr., 25, 570-578 (2011)
[2] STRATAGENE inc., pESG Yeast Epitope Tagging Vectors INSTRUCTION MANUAL Revision A.01.
[3] Yun E. J., *et al*.: Production of 3,6-anhydro-l-galactose from agarose by agarolytic enzymes of *Saccharophagus degradans* 2-40. Process Biochem., 46, 88-93 (2011)

Study on Effects of Body Shape on Propagation Characteristics in 2.45GHz Dynamic Wearable WBAN using Multi-Port VNA

Student ID : 10M18140 Name : Tetsuo Nukita
Superviser : Jun-ichi Takada, Takahiro Aoyagi

マルチポートVNAを使用した2.45GHzでのダイナミックウェアラブルボディエリアネットワーク伝搬特性における体格の影響に関する検討

貫田哲夫

本論文では、マルチポートネットワークアナライザを用いた、無線ボディエリアネットワークに関する屋内実験の結果を報告する。この実験により、人体の体格差が無線ボディエリアネットワークの伝搬特性にどの程度影響を与えるかを調べた。実験結果を分析した結果、無線ボディエリアネットワークの伝搬特性は、人体の体格差の影響を受ける事が判明した。具体的には、平均パスゲインが体格差によって部分的に説明できると結論づける事ができた。

I. Introduction

Wireless body area network (WBAN) denotes short-range wireless communication among electronic devices on the surface (wearable WBAN) and/or inside (implantable WBAN) of the human body. Both wearable WBAN and implantable WBAN are being discussed in the IEEE 802.15.6 standardization[1]. Their applications are highly expected especially in the medical treatment and the health care.

In order to realize these applications, comprehensive understanding of radiowave propagation characteristics is needed.

This task is quite challenging because a lot of factors have effects on the radiowave propagation in WBAN. For example, the interaction between antennas and human body, i.e. the changes in the antenna performance due to the presence of the body and power losses in the tissues[2]. In addition, human movement should be taken into account. When human body is in motion, received signal level is considerably fluctuating[3]. These factors lead to bad communication links between electronic devices. Among those elements which influence the propagation characteristics in WBAN, this paper focuses on the effect of body shape in wearable WBAN. There are only a few researchers who are addressing this topic. Accroding to [4], no significant difference is found in propagation characteristics among ZigBee WBAN devices for two female and two male subjects. However, the number of subjects is insufficient to provide statistical confidence. On the other hand, [5] measured 16 subjects. They examined the relationship between body shape and signal propagation using first order statistics (average and standard deviation) , level crossing rate (LCR) and average fade duration (AFD). Their conclusion is that men suffer higher path loss and more fade than women and that men's chest size is a parameter that affects signal propagation. In other words, physical characteristics are important parameters in WBAN channel model.

Extending these researches above, this paper tried to characterize the relationship by numerical value using analysis of variance (ANOVA) and regression analysis. This study provides the relationship more clearly.

II. Measurement Conditions

This on-body channel experiment aimed to measure the path gain between one transmitter antenna (Tx) and four receiver antennas (Rx) (Fig.1) using multi-port vector network analyzer. 12 males helped this experiment as a subject. Fig.2 indicates the measurement setup. The transmitter antenna was installed onto the navel of subjects. The four receiver antennas were installed onto the chest, arm, wrist and thigh of subjects. They are designed to operate at the frequency of 2.45 GHz. For these antennas to work properly for wearable body area communications, they should be placed with a sufficient gap from human body. Hence, a 15 mm gap was added between the antennas and the body surface of subjects.

In addition, this experiment took account of the antenna orientation and the body posture. As seen in Fig.2, two kinds of orientation were defined by vector v and vector h. At the analysis part of this paper, the relationship between these parameters and the propagation characteristics will be discussed. This experiment measured the path gain while subjects were still, walking, and sitting down/standing up for the follwing cases.

- Tx : v, Rx : v
- Tx : v, Rx : h

- Tx : h, Rx : v
- Tx : h, Rx : h

Notations Tx:v and Rx:v indicate that the the direction of the transmitter and the receiver antenna is parallel to vector v, and does not correspond to the polarization. Table I shows the summary of the measurement conditions.

Fig. 1. Antenna used in the experiment

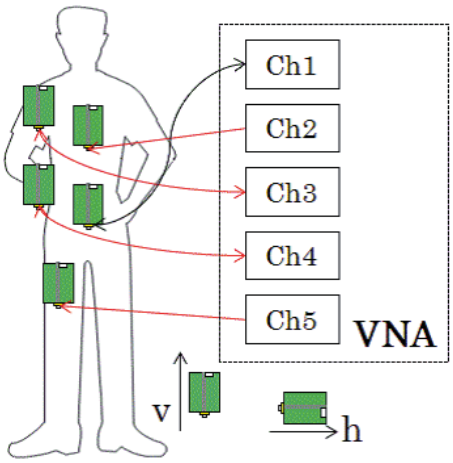

Fig. 2. Measurement Setup

TABLE I
MEASUREMENT CONDITION

VNA	ZVT20 (Rohde Schwarz)
Frequency[GHz]	2.45
RF Power[dBm]	13
Sweep Time[s]	11.18
Number of points	1801
IFBW[kHz]	1
Frequency Span[Hz]	1
Antenna	Chip Antenna × 5 (Mitsubishi Materials) Model : AHD1403-244SK01[6]
Antenna Dimension	50mm × 25mm × 1mm
Tranmitter Antenna	Navel
Receiver Antenna	Arm, Wrist, Chest, Thigh
Subject	12 males
Place	Empty Room (13.6m × 15.1m × 2.7m)
Posture	Still Walking on the spot Sitting down/Standing up

III. RESULT

Table II expresses body shape information of subjects and the average path gain obtained in the experiment. Other than them, fat percentage, body mass index (BMI), width across the shoulder, length of arm and leg, and circumference of arm, wrist and thigh were measured. Fig.3 to Fig.8 show the temporal path gain where the orientation of the transmitter and the receiver antennas is parallel to vector v. The distances between the transmitter antenna and the receiver antennas are denoted below.

- Tx and Rx (Chest) : 20〜27[cm]
- Tx and Rx (Arm) : 28〜37[cm]
- Tx and Rx (Wrist) : 23〜35.5[cm]
- Tx and Rx (Thigh) : 31.5〜42.5[cm]

TABLE II
BODY SHAPE INFORMATION AND AVERAGE PATH GAIN

Subject	Height [cm]	Weight [kg]	Chest Size[cm]	Waist Size[cm]	Average Path Loss[dB]
1	163	60.2	88	83	-46.2
2	163	54.9	76	71	-46.6
3	179	62.2	80.5	70	-43.8
4	159	60.4	84	80	-47.0
5	166.5	53	80.5	68.5	-44.1
6	166	55.7	82	71	-43.4
7	166	63.3	87	74	-40.7
8	175	66.8	85	75	-38.0
9	170.5	67.1	90	75	-40.3
10	178	65.8	85	71	-44.0
11	162	80	104	951	-47.0
12	180	71.1	87	80	-47.6
Average	169	62.8	85.6	76.1	-44.0
Standard Deviation σ	6.99	6.03	6.63	7.16	2.95

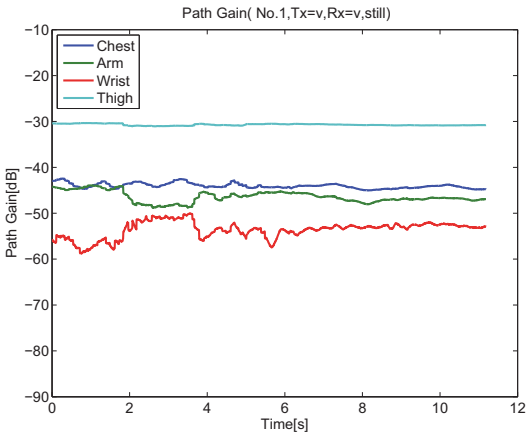

Fig. 3. Temporal path gain (No.1, Tx : v, Rx : v, Still)

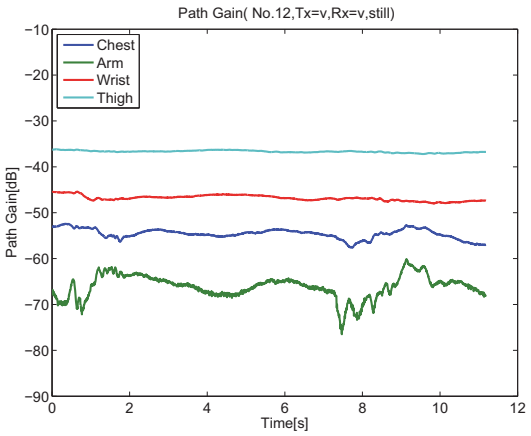

Fig. 4. Temporal path gain (No.12, Tx : v, Rx : v, Still)

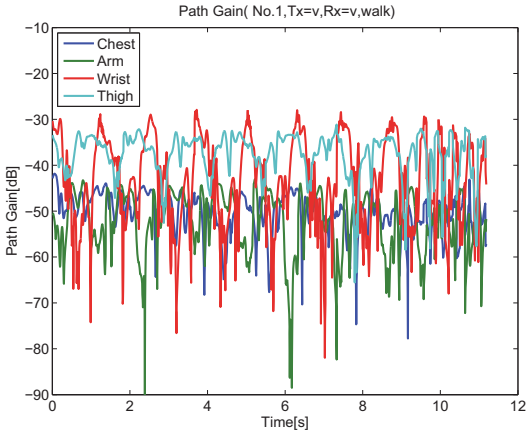

Fig. 5. Temporal path gain (No.1, Tx : v, Rx : v, Walk)

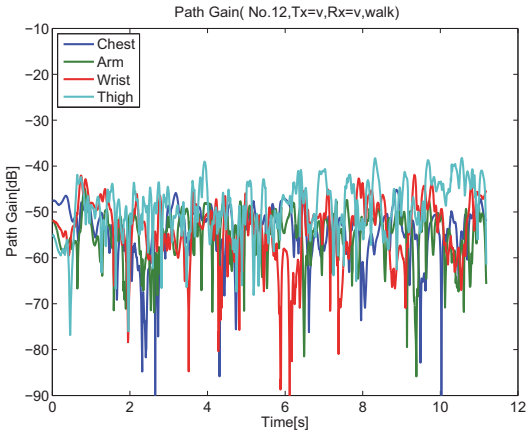

Fig. 6. Temporal path gain (No.12, Tx : v, Rx : v, Walk)

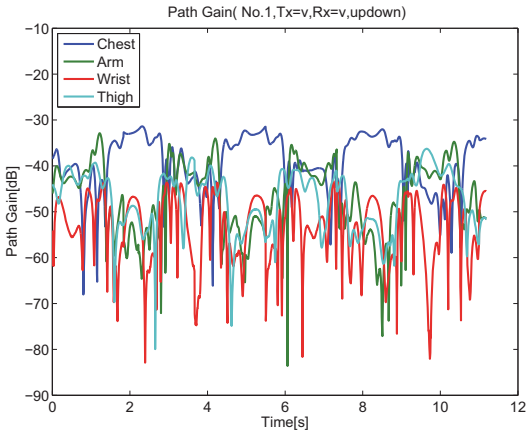

Fig. 7. Temporal path gain (No.1, Tx : v, Rx : v, Sit down/Stand up)

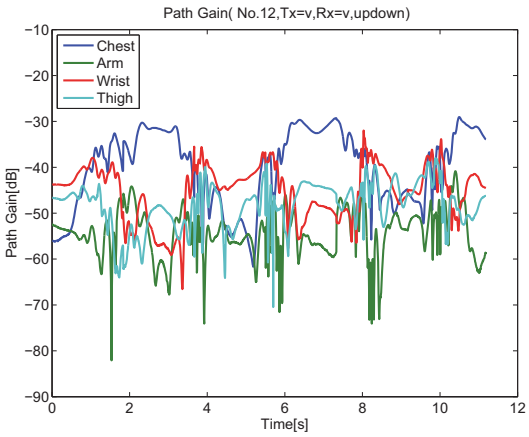

Fig. 8. Temporal path gain (No.12, Tx : v, Rx : v, Sit down/Stand up)

IV. Analysis

In order to characterize the relationship by numerical value, ANOVA and regression analysis were chosen as a means of analysis.

A. ANOVA to select the appropriate parameters for modeling

ANOVA can be used to examine which explanatory parameters are useful for modeling an observed data[7]. First the measurement data was divided into as many groups as the number of measurement conditions (antenna orientation, antenna position, subject posture and so on). Table III shows the F-value, the ratio of the variance within the data group and the one between the data group. In the table, "Ave"[dB] means the average of the path gain measured, and "Max-Min" means the difference between the maximum and the minimum value of the path gain. Larger F-value means the high dependency on the explanatory parameters. That is to say, the table prove which parameter is more critical for WBAN propagation channel. For example, as for the median of the path gain, antenna position has the most influence on it. P-value indicates the probability that F-value is observed by accident. The lower the p-value, the more significant the difference between the groups. The difference among subjects has strong relationship with the average path gain while the subject posture has little. Antenna position and orientation also have large effects on the path gain. With respect to the ANOVA on the height (weight) and the path gain, the data was separated into the two groups; a data group of subjects whose height (weight) is taller (heavier) than the median and the other data group whose height (weight) is shorter (lighter) than the median.

B. Regression analysis to clearfy the relationship between body shape and path gain

Regression analysis is a statistical technique for modeling an observed data set by explanatory parameters. By means of this technique, the path gain observed in the experiment was modeled on height or weight. In other words, the path gain y_{pg}[dB] can be expressed by height x_h[cm] or weight x_w[kg] in the follwing equations.

$$y_{pg} = a_0 + a_1 x_h \tag{1}$$

TABLE III
F-VALUE (** : P < 0.01、 *: P < 0.05)

	Median [dB]	Ave [dB]	Max [dB]	Min [dB]	Max-Min [dB]
Height	9.32(**)	10.34(**)	13.34(**)	4.69(*)	0.77
Weight	10.49(**)	10.94(**)	23.05(**)	1.86	6.56(*)
BMI	4.11(*)	4.58(*)	0.52	7.02(**)	3.88(*)
Waist	0.66	0.66	0.39	2.22	3.85
Chest	0.49	0.53	0.44	2.7	4.59(*)
Subject	7.4(**)	7.4(**)	8.09(**)	3.35(**)	1.2
Posture	1.75	1.04	81.2(**)	92.56(**)	826.84(**)
Antenna Position	56.18(**)	57.44(**)	34.81(**)	35.69(**)	2.42(**)
Antenna Orientation	25.78(**)	27.32(**)	19.41(**)	19.62(**)	19.37(**)

$$y_{pg} = b_0 + b_1 x_w \tag{2}$$

Table IV is the result of regression analysis on height and path gain. Table V is the result of regression analysis on weight and path gain. R^2 means the accuracy of the equations. This value should be 1 in an ideal case. Therefore, there is little relationship between weight and path gain. On the other hand, height accounts for 1.1 percent of the effects on the average path gain. Fig.9 and Fig.10 indicate the relationship between height (weight) and the path gain calculated by regression analysis.

TABLE IV
REGRESSION ANALYSIS ON HEIGHT AND PATH GAIN

y_{pg}	a_0	a_1	R^2	P(a_0)	P(a_1)
Average	-65.244	0.125	0.011	0	0.011
Max-Min	4.613	0.074	0.002	0.692	0.283
Median	-63.932	0.120	0.01	0	0.015
Max	-67.588	0.185	0.019	0	0.001
Min	-72.202	0.111	0.005	0	0.1

P(a_0) = P-value for a_0、 P(a_1) = P-value for a_1

TABLE V
REGRESSION ANALYSIS ON WEIGHT AND PATH GAIN

y_{pg}	b_0	b_1	R^2	P(b_0)	P(b_1)
Average	-45.762	0.027	0	0	0.635
Max-Min	6.137	0.174	0.008	0.22	0.028
Median	-45.11	0.024	0	0	0.68
Max	-44.823	0.135	0.007	0	0.039
Min	-50.96	-0.04	0	0	0.607

P(b_0) = P-value for b_0、 P(b_1) = P-value for b_1

V. CONCLUSION

This work has reported that the relationship between the body shape and the propagation channel in WBAN can be characterize by numerical value using ANOVA and regression analysis. Height accounts for about 1.1 percent effects on the average path gain. Therefore body shape is not the critical parameter in WBAN propagation channel. Result of ANOVA turns out which parameter is more dominant to the WBAN propagation channel. As for the average path gain, antenna position is most dominant and antenna orientation is the second.

The final goal of this work is to reduce the effect of body shape, subject posture and antenna position using antenna diversity. Generally, diversity technique is used to mitigate the effect of multipath fading or shadowing from buildings and objects in wireless communication systems. This technique is thought to be applicable in WBAN system. In order to achieve the goal, further investigation remains to be done.

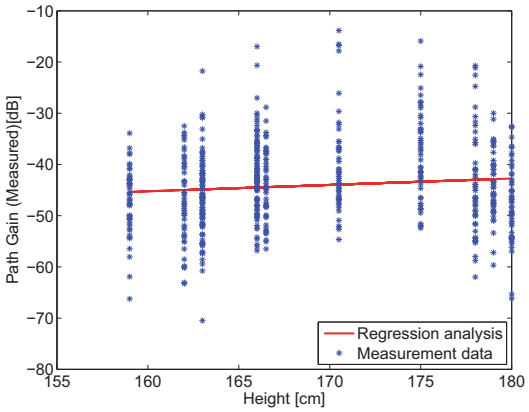

Fig. 9. Relationship between height and path gain

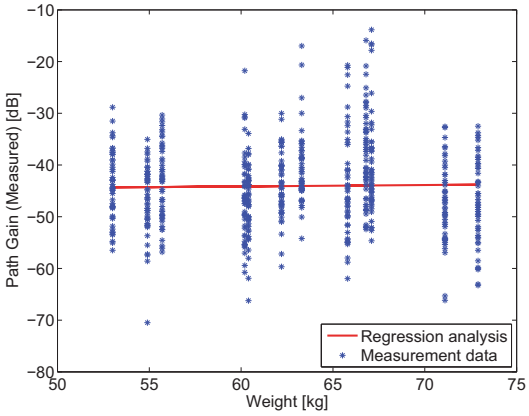

Fig. 10. Relationship between weight and path gain

REFERENCES

[1] IEEE 802.15 Task Group 6. [Online]. Available : http://ieee802.org/15/pub/TG6.html

[2] Y. Terao, M. Kim, Iswandi, J. Takada, "On antenna de-embedding in BAN channels-Measurement of reflection coefficient and radiation pattern of on-body antenna-," *IEICE Technical Report*, Jan. 2010.

[3] T. Aoyagi, M. Kim, J. Takada, K. Hamaguchi, R. Kohno, "Numerical Simulations for Dynamic WBAN Propagation Channel during Various Human Movements," Proc. 5th International Symposium on Medical Information and Communication Technology (ISMICT), Mar.2011.

[4] C. Oliveira, L. Pedrosa, R. Rocha, "Characterizing On-Body Wireless Sensor Networks," Proc. 2nd International Conference on New Technologies, Mobility and Security (NTMS), Aug. 2008.

[5] F. Di Franco, C. Tachtatzis, B. Graham, M. Bykowski, D. C. Tracey,N. F. Timmons, J. Morrison, "The effect of body shape and gender on Wireless Body Area Network on-body channels," 1st Middle East Conference on Antenna and Propagation (MECAP), Oct.2010.

[6] MITSUBISHI MATERIALS. [Online]. Available : http://www.mmc.co.jp/corporate/ja/index.html

[7] Yasushi Nagata, "Nyuumon Toukei Kaisekihou," Nikka Giren, Tokyo, 1992.

Separation of aromatic hydrocarbons from cracked kerosene by O/W/O emulsion liquid membrane

Student Number: 10M18170 Name: Masashi HARUNA Supervisor: Ryuichi EGASHIRA

分解灯油に含まれる芳香族炭化水素の O/W/O 乳化液膜分離

春名　将資

分解灯油を原料、Tween 80（ポリオキシエチレン(20)ソルビタンモノオレエート）水溶液を膜液、及びヘキサンを溶媒として回分透過を行った。原料中の直鎖飽和炭化水素成分に対して芳香族炭化水素成分が選択的に膜液を透過し、これらの成分間の分離が可能であった。既往の回分平衡抽出の場合と比較して、本分離法においては大幅に高い収率ならびに同程度の分離の選択性を得た。また、分離性能に対する主要な操作条件の影響を明らかにした。

1. Introduction

Cracked kerosene (CK) is one of the by-products from the process of cracking of heavier oil fraction to produce cracked gasoline in petroleum refinery. Nowadays, the supply of ordinary gasoline is decreasing. Because of this, whereas the quantity of cracked gasoline is decreasing, that of cracked kerosene is increasing. There are many kinds of chemical compounds contained in cracked kerosene, the alkanes such as octane (C8), nonane (C9), decane (C10); the aromatic hydrocarbons such as m,p-xylene (M,PX), pseudo cumene (PC), tetraline (T), etc. Since the content of aromatic hydrocarbons in the cracked kerosene is so high that this fraction does not meet the specification for the ordinary kerosene, the cracked kerosene is used as a low-value heavy oil blendstock. On the other hand, aromatic hydrocarbons are useful as raw materials of chemical industry. It is, therefore, desired to separate aromatic hydrocarbons from the cracked kerosene. The liquid-liquid equilibrium extraction[1] has been widely used for aromatics separation, such as, sulfolane process. The liquid membrane permeation[2,3,4] is expected as an alternative to the extraction. The liquid membrane separation is governed by the difference in permeation rates of the components through the membrane and the difference is attributed mainly to the solubilities of the components into the aqueous membrane liquid. In general, the solubility of aromatic hydrocarbon in water is about 200 times larger than that of alkane hydrocarbon, so that aromatic hydrocarbon permeates through the aqueous membrane preferentially rather than alkane hydrocarbon to be separated. In O/W/O emulsion liquid membrane process, the feed oil phase is emulsified in an aqueous solution of surfactant to prepare the stable O/W emulsion. This O/W emulsion is dispersed in a solvent oil phase to form O/W/O dispersion system, where the internal feed and external solvent oil phases are divided by the aqueous phase. This aqueous phase plays a role of the liquid membrane, through which the permeate transfers from feed to solvent phase and the separation takes place.

In this work, the separation of CK by the O/W/O emulsion liquid membrane technique was conducted. The effect on experimental condition for emulsion liquid membrane separation was studied.

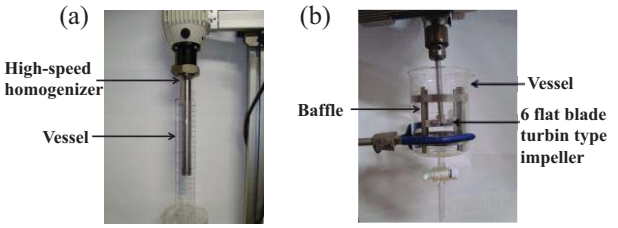

Fig. 1 Apparatuses for batch emulsion liquid membrane permeation (a) emulsifier with high-speed homogenizer (b) permeator

Table 1 Experimental condition of batch permeation

Feed	**Cracked kerosene**	
Solvent	**Hexane**	
Membrane	**Aqueous solution of surfactant**	
Surfactant	**Polyoxyethylene (20) sorbitan monooleate (Tween 80)**	
Stirring velocity in emulsification	N_E [h^{-1}]	1.1×10^{6}
Stirring velocity in permeation	N_P [h^{-1}]	1.8×10^{4}〜3.6×10^{4}
Total volume of liquid in permeator	V_T [m^3]	4.0×10^{-4}
Volume fraction of inner oil phase in O/W emulsion	$\phi_{O,0}$[-]	0.5
Volume fraction of O/W emulsion in O/W/O emulsion	$\phi_{OW,0}$[-]	0.25
Concentration of surfactant in a membrane liquid	C_S [-]	0.005〜0.2
Operation time	t [h]	0〜0.5
Operation temperature	T [K]	293±5

Table 2 Components in cracked kerosene

Component	Mass fraction [-]	Component	Mass fraction [-]
toluene	0.003	heptane	0.001
ethylbenxene	0.006	octane	0.017
m,p-xylene	0.024	nonane	0.074
o-xylene	0.016	decane	0.036
propylbenzene	0.004	undecane	0.034
mesitylene	0.015	dodecane	0.033
pseudocumene	0.013	tridecane	0.037
tetraline	0.009	tetradecane	0.027
naphthalene	0.004	pentadecane	0.02
hexylbenzene	0.01	hexadecane	0.009
2-methylnaphthalene	0.008	heptadecane	0.002
Aromatics	0.111	Alkanes	0.291

2. Experimental

CK was used as an inner oil phase. Aqueous membrane solution consisted of ion-exchanged water and polyoxyethylene (20) sorbitan monooleate as an emulsifying agent. Hexane was used as external solvent phase. The feed CK and aqueous membrane solution were stirred by a commercial high-speed homogenizer to prepare the stable emulsion. This prepared emulsion was brought into contact with the solvent by stirring vessel which was made of Pyrex glass equipped with a six-flat-blade turbine type impeller and four baffles. **Figure 1** shows appearance of the apparatuses for batch emulsion liquid membrane permeation (a) emulsifier with high-speed homogenizer (b) permeator. Stirring started to begin a permeation run (t=0) and continued for a specified operating time. The extract phases were sampled for analysis by a gas chromatograph (GC-2010, Shimazu Corp). This operation was repeated for the several different times to obtain the time courses of the compositions in the extract phase etc. **Table 1** gives the detailed experiment conditions.

3. Results and Discussion

Cracked kerosene contained a number of hydrocarbon components. **Table 2** summarizes several representative components and the respective contents identified, determined by gas chromatography.

The mass fraction in raffinate phase, x_i can be calculated by mass balance as follows:

$$R_0 x_{i,0} + E_0 y_{i,0} = R x_i + E y_i \quad (1)$$

E and R were obtained from the experimental data.

Yield of component i, Y_i, was defined as,

$$Y_i = \frac{E \cdot y_i}{R_0 \cdot x_{i0}} \quad (2)$$

where x_{i0} and y_i denote the mass fraction of component i in the inner oil phase at t=0 and that in the external extract oil phase after a run, respectively. R_0 refers to the initial mass of inner oil phase and E expresses the mass of out oil phase after the run.

Mass transfer rate of component i through ideal emulsion liquid membrane was expressed as,

$$\frac{dEy_i}{dt} = P_i a (x_i - y_i) V_T \quad (4)$$

In this equation, $P_i a$ expressed overall volumetric permeation coefficient.

When overall mass transfer is governed by permeation through the membrane, the overall permeation coefficient is qualitatively expressed as

$$P_i \propto D_i \cdot m_i \quad (5)$$

Separation selectivity of total aromatics by the ratio of overall volumetric permeation coefficients relative to total alkane was defined as,

$$\beta = \frac{P_{aromatics} \cdot a}{P_{alkanes} \cdot a} = \frac{P_{aromatics}}{P_{alkanes}} \quad (6)$$

Figure 2 shows the time courses of mass of raffinate and extract phase. The mass of raffinate phase

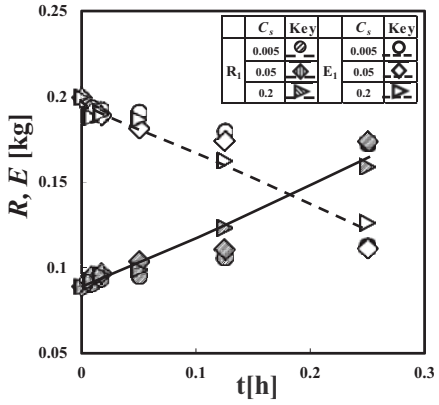

Fig.2 Time course of mass of raffinate and extract phase

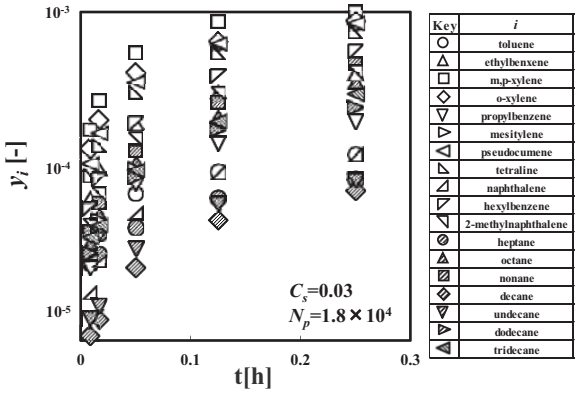

Fig.3 Time course of mass fraction in extract phase

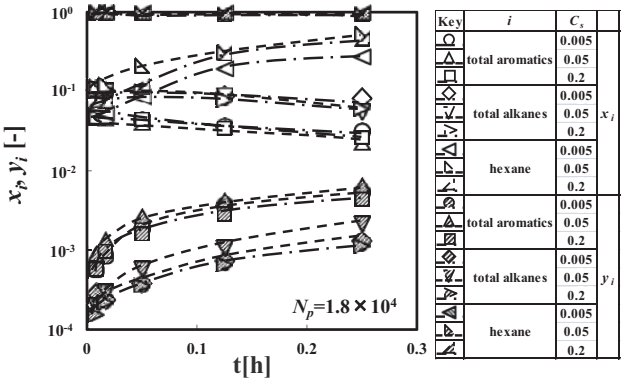

Fig.4 Time course of mass fraction in raffinate and extract phase

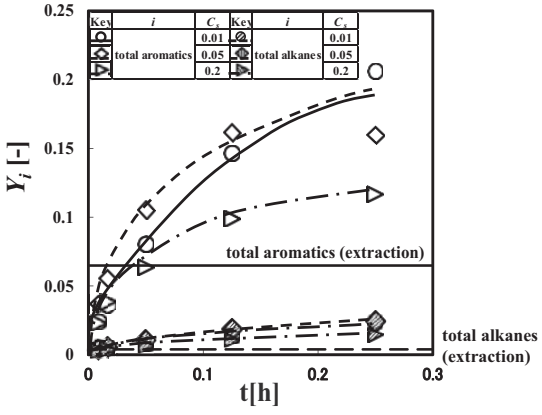

Fig.5 Time course of yield

increased as the mass of extract phase decreased with time. The extract phase transferred to raffinate phase. The variation of surfactant concentration didn't have much effect on *R* and *E*.

Figure 3 shows the time courses of mass fraction in extract phase. The mass fractions of all components which were identified by gas chromatography are shown on this figure. All of the mass fractions of extract phase increased with time. From next figure, the total aromatics and total alkane are shown to explain. Their variations are almost same as each compound.

Figure 4 shows the time courses of mass fraction in raffinate and extract phase about total aromatics, total alkane and hexane. The mass fraction of total aromatics and total alkane in raffinate phase decreased as those in extract phase increased with time. The mass fraction of hexane in raffinate phase increased as that in extract phase decreased with time. So the mass fraction of raffinate and extract phase approached each other. The difference of mass fraction which is driving force of permeation decreased with time.

Figure 5 shows the time courses of yields about total aromatics and total alkane. Under all conditions, Y_i of aromatic compounds were larger than those of alkane compounds, namely, it was confirmed that these compounds were separated into each other by the emulsion liquid membrane. The yield increased with time. This figure also shows comparison between emulsion liquid membrane and liquid-liquid extraction on yields. The yields in the case of liquid-liquid extraction method[1] about total aromatics and total alkane are expressed in a straight lines. The yields in the case of emulsion liquid membrane method were higher than those of liquid-liquid extraction. The yield of liquid-liquid extraction was 0.065 and that of emulsion liquid membrane was 0.30 at maximum about total aromatics.

Figure 6 shows the time courses of overall volumetric permeation coefficient, P_ia. In any case, P_ia decreased with stirring time. P_ia of the aromatic compounds was larger than those of alkane compounds. Aromatic compounds were selectively transferred through liquid membrane to extract phase and could be separated from alkane compounds.

Figure 7 shows the time courses of separation selectivity by the ratio of overall permeation coefficients, β. The separation selectivity decreased with time. This figure also shows comparison between emulsion liquid membrane and liquid-liquid extraction on separation selectivity. The separation selectivity in the case of liquid-liquid extraction method[1] about total aromatics is expressed in a straight line The separation selectivity in the case of emulsion liquid membrane method was higher than that of liquid-liquid extraction. The separation selectivity of liquid-liquid extraction was 12 and that of emulsion liquid membrane was 17 at maximum about total aromatics. Aromatic compounds were selectively

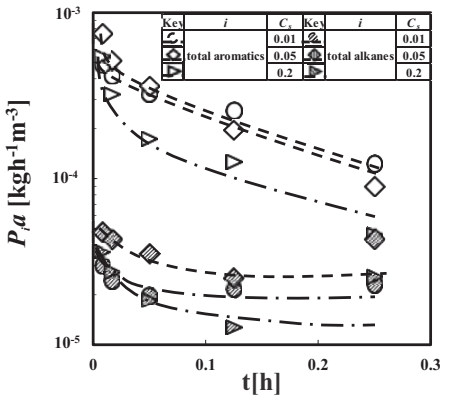

Fig.6 Time course of overall volumetric permeation coefficient

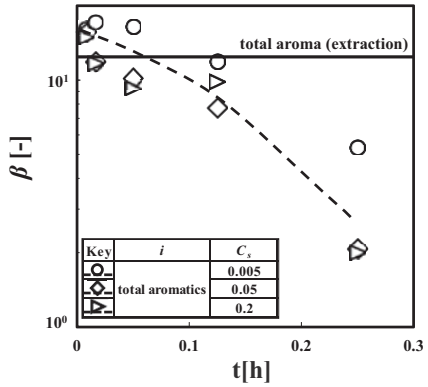

Fig.7 Time course of separation selectivity

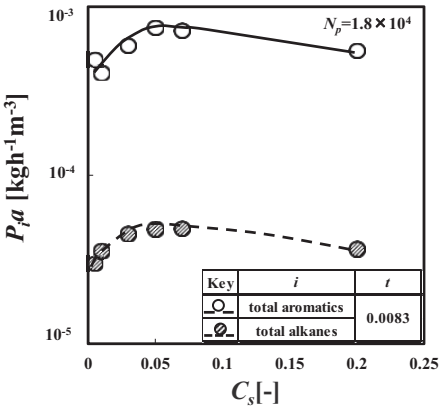

Fig.8 Effect of surfactant concentration on overall volumetric permeation coefficient

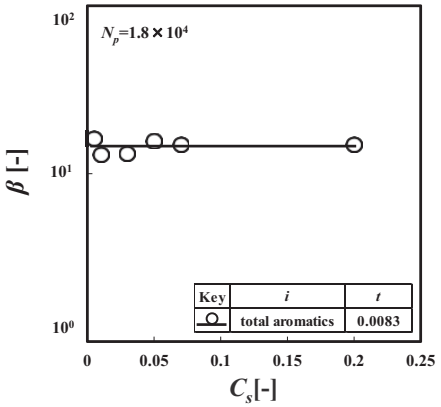

Fig.9 Effect of surfactant concentration on separation selectivity

transferred through liquid membrane to extract phase and could be separated from alkane compounds.

Figure 8 shows the effect of surfactant concentration on overall volumetric permeation coefficient, $P_i a$. While C_s was lower, $P_i a$ increased with C_s. And then while C_s was larger, $P_i a$ decreased with C_s. $P_i a$ had maximum value around $C_s = 0.05$.

Figure 9 shows the effect of surfactant concentration on separation selectivity by the ratio of overall permeation coefficients, β. The surfactant concentration didn't have much effect on separation selectivity.

Figure 10 shows the effect of surfactant concentration on interfacial tension between inner oil and surfactant solution phase and the effect of surfactant concentration on viscosity in surfactant solution from previous work[5]. The surfactant was Tween 20 in the previous work. The interfacial tension decreased with surfactant concentration. The decreasing trend became smaller from CMC (critical micelle concentration). The viscosity increased with surfactant concentration from CMC. While surfactant concentration was lower, it was supposed that the inner oil droplet decreased due to the decrease of interfacial tension. Therefore the $P_i a$ increased. While surfactant concentration was higher, it was supposed that diffusivity at liquid membrane decreased due to increase of viscosity from Wilke-Chang equation. Therefore the $P_i a$ decreased. The Wilke-Chang equation is shown as below.

Wilke-Chang equation

$$D_{\text{surfactant, water}} = \frac{2.946\times10^{-11}(\alpha M_{\text{water}})^{1/2} T}{\mu_{\text{water}} V_{b,\text{surfactant}}^{0.6}}$$

4. Conclusions

The aromatic hydrocarbon compounds were separated from cracked kerosene by the emulsion liquid membrane. Then the highest yield and separation selectivity were 0.3 and 17. These were higher than those of liquid-liquid equilibrium extraction. There was the appropriate surfactant concentration range.

Nomenclatures

a = specific interfacial area between O/W emulsion and extract phase [m^{-1}]
C_s = mass fraction of surfactant in membrane liquid [-]
E = mass of extract phase [kg]
N_E = stirring velocity in emulsification [h^{-1}]
N_P = stirring velocity in permeator [h^{-1}]
P_i = overall permeation coefficient [$kgh^{-1}m^{-2}$]
R = mass of raffinate phase [kg]
T = operation temperature [K]
t = operation time [h]
V_T = total volume of liquid in permeation vessel [m^3]
x = mass fraction in raffinate phase [-]
y = mass fraction in extract phase [-]

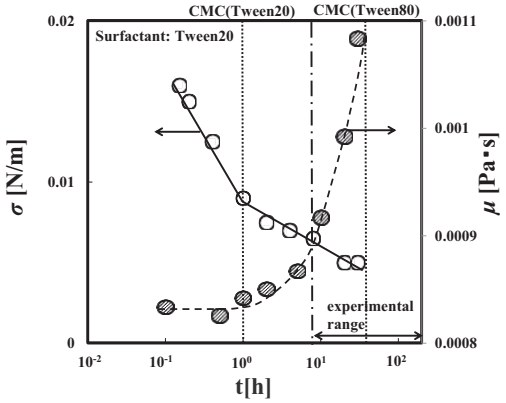

Fig.10 Effect of surfactant concentration on interfacial tension and viscosity

Y = yield [-]
D = diffusivity [m^2h^{-1}]
m = distribution coefficient [-]
α = degree of association [-]
M = molecular weight [-]
μ = viscosity [Pa · s]
V = molar volume [m^3/mol]
σ = interfacial tension [N/m]

<Greek>
β = separation selectivity of total aromatics by ratio of overall volumetric permeation coefficient relative to total alkane [-]
$\phi_{O,0}$ = volume fraction of inner oil in O/W emulsion [-]
$\phi_{OW,0}$ = volume fraction of O/W emulsion in total liquid [-]

<Subscript>
0 = at initial state
i = component i
CK = cracked kerosene
M,PX = m,p-xylene
PC = pseudocumene
T = tetraline
C8 = octane
C9 = nonane
C10 = decane

Literature Cited

[1] H. Habaki, M. Miyazaki, E. Egashira, "Liquid-liquid Extraction of Cracked Oil", S.C.E.J, March 2011.
[2] N. N. Li, "Separation of Hydrocarbons by Liquid Membrane Permeation", U. S. Pat. 3,410,794, November (1968).
[3] Kato, S. and J. Kawasaki; "Separation of aromatic hydrocarbons contained in reformate and kerosene by liquid membrane permeation," Sekiyu Gakkaishi, 30, (1), 1-6(1987)
[4] Kato, S. and J. Kawasaki; "Effects of lipophilic surfactants on liquid membrane permeation of hydrocarbons in naphtha and kerosene," Sekiyu Gakkaishi, 30, (4), 243-248(1987)
[5] Yamamoto, T and Tanaka, M; "Effects of surfactant concentration on drop sizes in O/W and W/O/W emulsions," J. Chem. Eng. Japan, 36, (8), 963-970(2003)

Study on fixing heavy metals by cementitious materials with Municipal Waste Combustion Ash, OPC, Blast Furnace Slag and Anhydrite

Student Number: 10M18186 Name: Takayuki FUKUNAGA Supervisor: Nobuaki Otsuki

実焼却廃棄物を混入したOPC－高炉スラグ微粉末－石膏系材料の重金属固定化に関する研究

福永隆之

本研究は，六価クロムを含む焼却廃棄物を混入した普通ポルトランドセメントに高炉スラグ微粉末および無水石膏をそれぞれ混和したセメント系材料を用いて， 1) 各材料が重金属固定へ与える影響を明らかにし，重金属固定能力を向上するための材料設計を提案し，2) 実用化への検討を行うことを目的とした.

その結果，1) について，高炉スラグ微粉末と無水石膏を同時に混和することにより，六価クロムの固定能力は向上した．これは，六価クロムを固定したモノサルフェートに加えて，六価クロムを含むエトリンガイトが生成したことに起因したものと結論付けた. 2) について，一般の実構造物には適さないがコンクリート二次製品には実用化の可能性があると結論付けた.

1. Introduction

Nowadays, it is difficult to get natural resources due to environmental issues. From that point of view, recycling Municipal Waste Combustion Ash (waste) is highly demanded in construction field. One of the effective methods is to use wastes as cementitious admixture. However, wastes include hexavalent chromium (Cr(Ⅵ)) which is a deleterious effect of health and difficult to remove it of all heavy metals. Therefore, it is necessary to fix Cr(Ⅵ) by using cementitious admixture.

Recently, Takahashi reported [1] that Cr(Ⅵ) can be fixed by aluminate hydration products such as AFm phase , and Yoda reported[2] that fixing Cr(Ⅵ) could be increased by using industrial waste such as blast furnace slag (BFS) and anhydrite (AH). However, these studies did not use existing waste.

For the above reason, this research are conducted to prevent leaching of Cr(Ⅵ) by using BFS and AH to generate AFm phase in early age. The purpose of this research is to prevent leaching of Cr(Ⅵ) from cementitious materials with waste-Ordinary Portland Cement (OPC)-BFS-AH and To consider possibility as a practical material.

2. Experimental procedure

2.1 Materials

The materials used in this study were waste, OPC BFS and AH. Waste was generated from rubbish disposal site and was used as an admixture. Table.1 shows chemical composition and physical properties of waste, OPC, BFS and AH. Waste has similar chemical composition as OPC. However, waste contains highest level of chromium ion (CrO_4^{2-} ion) in 60 samples. If thiswaste can be reused, there is a possibility that other waste (lower level) can be reused.

2.2 Specimens

2.2.1 Cement paste specimen

Table.2 shows the mix proportions of cement paste specimens. All mix proportions of cement paste specimens contain waste 50% by mass. Remained 50% are OPC: BFS = 60:40, 45:55 and 30:70% and AH=0, 2, 3, 5 and 7 mass%. Paste specimens were prepared with water binder ratio of w/b=0.4, 0.5, 0.6 and 0.7. Dimension of cement paste specimens is 1×1×8cm. All specimens were cured in air for 6 and 27- days, after demolding it at 24 hours.

Table.1 Chemical composition

Material	Ig.loss (mass%)	Chemical composition (mass %)						Heavy metal (ppm)	Specific surface area(cm^2/g)
		SiO_2	Al_2O_3	Fe_2O_3	CaO	MgO	SO_3	Cr(Ⅵ)	
Combustible waste	10-15	26.4	10.1	6.12	43.4	0.19	1.67	520	3700
OPC	1.07	20.37	5.57	3.38	63.17	2.04	2.48	-	3300
BFS	0.49	33.60	14.26	0.41	43.13	6.05	-	-	4550
AH	0.85	1.00	0.30	0.10	40.50	0.10	56.80	-	3990

2.2.2 Mortar specimen

All mix proportion contain waste 25, 50 % by (mass %). Remained 75, 50 % are OPC: BFS = 60:40, 45:55 and 30:70 % and AH= 5 mass%. The water binder ratio was 0.5. Mortars with sand-binder ratio of 2.0 and dimension of 4×4×16cm were made for compressive strength tests according to JIS R 5201[3]. All specimens were cured in the mold for 24 hours. After demolded, specimens were cured in air 6 and 27- days.

Table.2 mix proportions of cement paste specimens. (mass%)

w/b	waste	OPC : BFS	AH
0.4 0.5 0.6 0.7	50	100 : 0 60 : 40 45 : 55 30 : 70	0 2 3 5 7

2.3 Method

Fixed Cr(VI) was evaluated based on the amount of leaching chromium, which measured by the Japanese Leaching Test (JLT46).

In order to clarify influence of fixing ability of Cr(VI) by OPC, BFS and AH, hydration products of the cement pastes were examined using X-ray diffraction method (XRD). The cumulative pore volume was measured using mercury porosimeter (CE INSTRUMENTS Pascal240, pressure range: 0.1-200 MPa). Compressive strength were measured based on JIS R 5201[3]

3. Results and Discussion

3.1 Influence of mixing waste with OPC

Fig.1 shows relationship between water-binder ratio and the amount of chromium leaching on 7 day curing. All water binder ratios satisfy the environmental standard. Therefore, it is difficult to reduce the amount of chromium leaching by only mixing OPC.

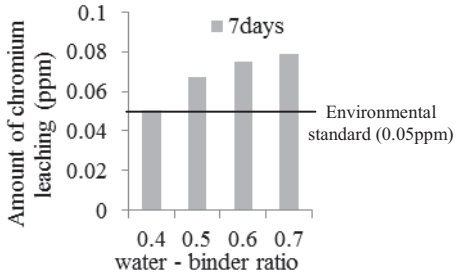

Fig. 1 Relationship between water - binder ratio and the amount of chromium leaching

3.2 Influence of mixing AH with OPC and waste

Fig.2 shows relationship between mixing ratio of AH and the amount of chromium leaching on 7day curing. In the case of mixing AH, Chromium leaching is decrease. Fig.3 shows the peak intensity ratio of ettringite. The amount of ettringite generation has increased by increasing the mixing ratio of AH. After increasing aluminate hydration products, the amount of chromium leaching has decreased. However, it is difficult to make the amount of chromium leaching below environmental standard value by only mixing AH.

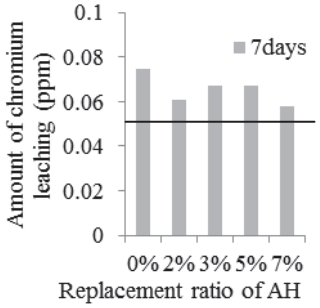

Fig.2 Relationship replacement ratio of AH proportion and amount of chromium leaching

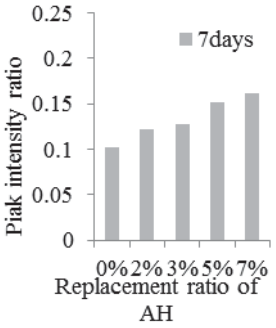

Fig.3 Peak intensity ratio of Ettringite

3.3 Influence of mixing BFS with OPC and waste

Fig.4 shows relationship between mixing ratio of BFS and the amount of chromium leaching on 7day curing. By mixing BFS, Chromium leaching has been decreased. Fig.5 shows XRD patterns of the specimens. [In this paper, "C" corresponds to calcium hydrate and "AFm (Cr)" is AFm phase including chromium.] In case of mixing BFS, AFm (Cr) is generated (AFm (Cr): θ=18.2°). Fig.6 shows the peak intensity ratio of AFm (Cr) and ettringite. The amount of AFm (Cr) has increased by mixing BFS, because concentration of aluminous component had increased in the specimen by mixing only BFS.

AFm (Cr) is produced by the reaction which occurs by anion exchange of SO_4^{2-} ion in monosulfate and CrO_4^{2-} ion as shown chemical equation (3.1).

$$3CaOAl_2O_3 \cdot CaSO_4 \cdot 12H_2O_{\ monosulfate} + CrO_4^{2-} \rightarrow 3CaOAl_2O_3 \cdot CaCrO_4 \cdot 12H_2O_{\ AFm(Cr)} + SO_4^{2-} \quad (3.1)$$

The amount of AFm (Cr) has been increased by mixing BFS. After increasing AFm (Cr), the amount of chromium leaching has decreased.

Therefore, fixing ability of Cr(VI) improved with mixing BFS because AFm phase which was taken Cr(VI) and changed into AFm (Cr), is able to increase in the early age.

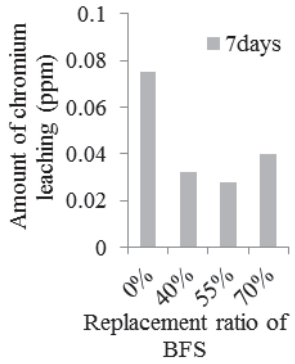

Fig.4 Relationship between replacement ratio of BFS and amount of chromium leaching

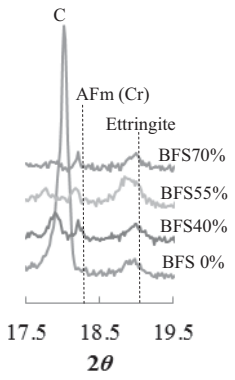

Fig.5 XRD pattern (2θ=17.5～19.5°)

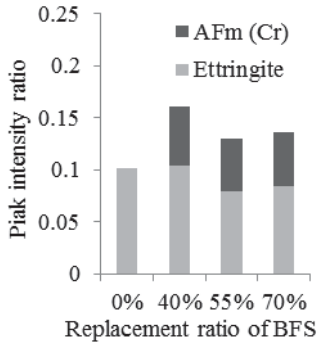

Fig.6 Peak Intensity Ratio of Ettringite and AFm (Cr)

3.4 Influence of mixing BFS and AH with OPC and waste

Fig.7 shows relationship between mixing ratio of AH and the amount of chromium leaching. In the case of (a) BFS 0%, chromium leaching had been decreased by mixing AH. In the case of (b) BFS 40%, it accompanies increase of mix rate of AH and amount of chromium leaching decreases. When mixing rate of AH is 5%, chromium leaching had shown the smallest value. In case of (c) BFS 55%, it accompanies increase of mix rate of AH and the amount of chromium leaching decreases. After mixing 3% of AH chromium leaching has decreased sharply. In AH5%, chromium leaching shows the smallest value. In the case of (d) BFS 70%, it was same trend with (c).

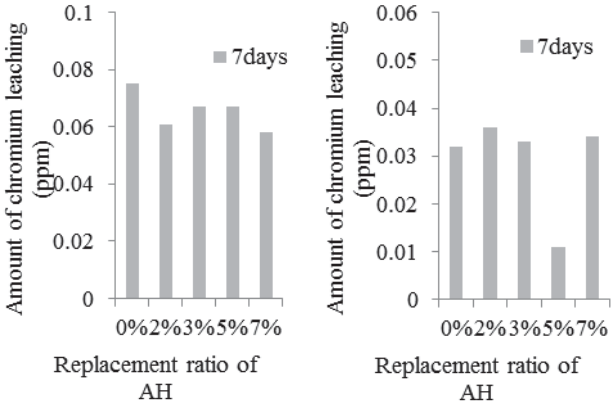

(a) BFS 0% (b) BFS 40%

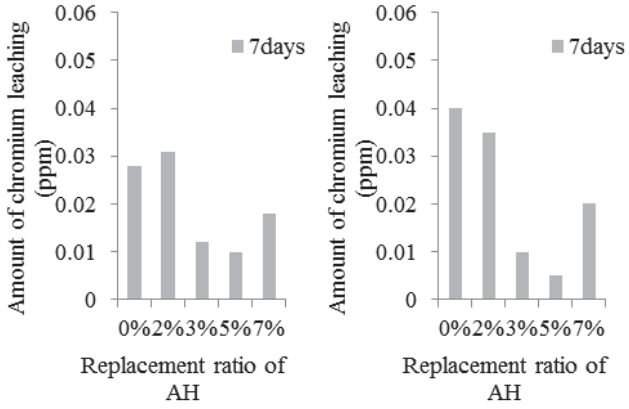

(c) BFS 55% (d) BFS 70%

Fig.7 Relationship between replacement ratio of AH and the amount of chromium leaching

Fig.8 shows the peak intensity ratio of aluminate hydration products. In the case of (a) AH 0% and (b) AH 2%, the amount of AFm (Cr) was small regardless of BFS replacement ratio, and ettringite was generated. In case of (c) AH3%, the amount of AFm (Cr) and ettringite has increased compared with AH 0%. Especially when mixing BFS is 55 and 70%, AFt (Cr) [AFt phase including hexavalent Chromium] had generated. In (d) AH 5%, the amount of aluminate hydration products such as AFm (Cr), AFt (Cr) and ettringite becomes the maximum. In case of (d) AH 7%, the amount of aluminate hydration products is decrease more than in case of mixing AH 5%. Fig.9 shows results of mercury intrusion porosimetry. In case of mixing AH 7%, pore volume is larger than mixing AH 5% because concentration of SO_4^{2-} ion in specimen was high and hydration product was not able to generate in early age.

Therefore, fixing ability of Cr(Ⅵ) was improved with including AH and BFS replacement ratio because AFm (Cr) and AFt (Cr) were generated in the early age.

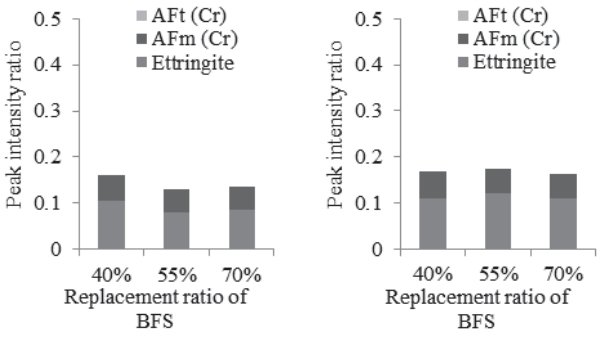

(a) AH 0% (b) AH 2%

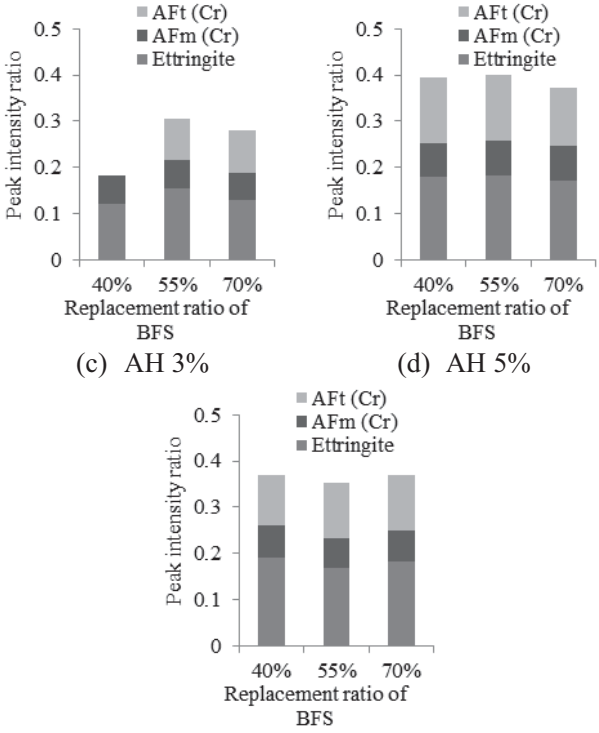

(c) AH 3% (d) AH 5%

(e) AH 7%

Fig.8 Peak Intensity Ratio of Ettringite, AFm (Cr) and AFt (Cr)

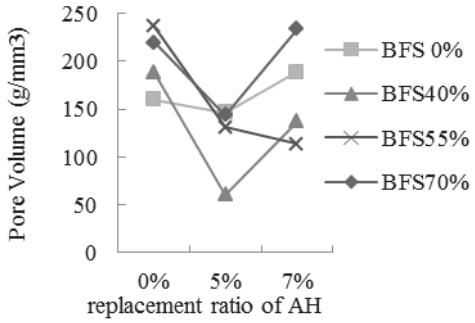

Fig.9 Relationship between Pore volume and replacement ratio of AH

4. Consideration to practical use

Fig.10 shows relationship between compressive strength and replacement ratio of BFS. In the case of mixing waste 25%, compressive strength was 30MPa on curing 28 days. On the other hand, in the case of mixing 50% of waste, compressive strength had decreased to 15MPa on curing 28 days. Compressive strength decreased by mixing waste. But, cementitious materials with waste – OPC – BFS - AH exceeds standard strength 15MPa[4)] in the precast concrete such as Interlocking Block. There is a possibility that the waste can be used as Interlocking Block.

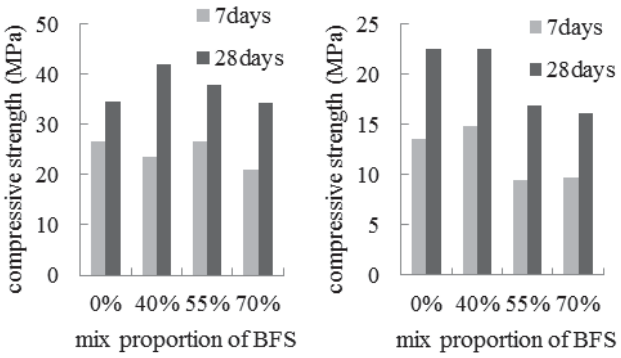

(a) Waste 25% (b) Waste 50%

Fig.10 Relationship between compressive strength and replacement BFS

5. Conclusions

The purpose of this research is to prevent leaching of hexavalent chromium (Cr(VI)) by cementitious materials with waste-OPC-BFS-AH and to consider possibility as a practical material. The experimental results could be concluded as follow.

1) In this research, when mixing 50% of waste, BFS 31.5%-OPC13.5%-AH5% (BFS70% - OPC30% - AH5%) showed the highest fixing ability of Cr(VI).
2) In the case of mixing only AH, fixing ability of Cr(VI) improved with including the AH replacement ratio because aluminate hydration such as ettringite was generated in early age.
3) In the case of mixing only BFS, fixing ability of Cr(VI) improved with mixing BFS because AFm phase which was taken Cr(VI) and changes into AFm (Cr), was able to increase in the early age.
4) In the case of mixing BFS and AH, fixing ability of Cr(VI) improved with including AH and BFS replacement ratio because AFm (Cr) and AFt (Cr) were generated in the early age. Therefore, it can consider that the generation of AFm(Cr) and AFt(Cr) in the early age is important to improve the fixing Cr(VI).
5) From the view of compressive strength, it is not enough to use as general structure material. However, there is a possibility that the waste can be used as Interlocking Block.

【References】

[1] Shigeru Takahashi et al., Hydrated Products in $Ca_3Al_2O_6$-$CaSO_4$・$2H_2O$-$CaCrO_4$ System, Journal of the Society of Inorganic Materials, Japan (2005)
[2] Yuya Yoda et al., Hexavalent chromium immobilization by high blast-furnace slag, Cement science and concrete technology (2010)
[3] Japanese industrial standards, JIS R 5201 Physical testing methods for cement, (2011)
[4] Japanese industrial standards, JIS A 5371 precast unreinforced concrete products, (2011)

URBAN AERODYNAMIC PARAMETERIZATION FOR URBAN DISTRICTS BY USING LARGE-EDDY SIMULATION WITH 3D BUILDING GIS

Student number : 10M18200 Name : Takashi MIYAMOTO Supervisor : Manabu KANDA

3 次元建物 GIS を用いた LES による都市街区の流体力学的パラメタリゼーション

宮本 崇史

東京都 23 区及び名古屋市から水平 1km 四方の領域を 110 か所選定し，GIS で表現された実都市における建物周りの流れ場の LES を行った. その計算結果からメソ気象モデルのための都市における地表面パラメータであるゼロ面変位及び運動量粗度を算定した．これらの結果を包括し，バルクな地表面幾何パラメータと関連付けることで，ゼロ面変位及び運動量粗度の新たな推定式を提案する．

1. Introduction

There are many researches on weather prediction such as the impact assessment of land surface parameter for urban climate using mesoscale weather prediction models. Numerical weather prediction model simulations are useful and important in investigating the characteristics of urban weather and climate. Since atmospheric phenomena over land are strongly influenced by surface properties and processes, the geometric properties and physical process of land surfaces should somehow be incorporated into numerical models. Furthermore, urban surface is a very complex type of land characteristic category.

However, most of them do not reflect the effect of real urban geometries because they assume rough geometry data using simple building shapes at low resolution (a few hundred meters at most).

In this study, two accurate urban aerodynamic roughness parameters displacement height(d) and roughness length(z_0) corresponding to actual urban geometries in Tokyo's 23 wards and Nagoya city were calculated from an output of the large eddy simulation (LES) in which the building canopy was explicitly resolved with fine grid spacing (Tokyo : 2.0m, Nagoya city : 2.5m). d is the effective height of the surface. This height is the level at which the mean drag on the surface appears to act. z_0, a non-substantial length, is considered as a length scale to represent the aerodynamic roughness of the surface.

Then, the two parameters calculated from an output of LES were compared with the popular and commonly utilized morphology-based model[1)] which calculates the two parameters based only on simple urban morphological information (such as average building height).

2. Theory

2.1. Ground surface drag

The average value of ground surface drag τ_0 in an entire numerical domain is calculated from the momentum conservation equation. The momentum conservation equation along x direction is written as Eq.(1);

$$\frac{Du}{Dt} = -\frac{1}{\rho}\frac{\partial P}{\partial x} - F_{\tau x} \tag{1}$$

where, $F_{\tau x}$ is the ground surface drag in x direction. By integrating Eq.(1) in the entire numerical volume and introducing volume velocity U and an area mean surface drag τ_0, τ_0 can be expressed as following Eq.(2);

$$\tau_0 = -\frac{1}{A}\left\{\frac{dU}{dt} + \frac{V}{\rho}\left(\frac{\partial P_{st}}{\partial x}\right)\right\} \tag{2}$$

in which, $dU/dt = 0$ in the case of constant volume flow and P_{st} is static pressure. By assuming a homogeneous static pressure gradient ($\partial P_{st}/\partial x = const.$), displacement height d and roughness length z_0 were calculated using the following logarithmic law for wind velocity profile (Eq.(3)).

$$u = \frac{u_*}{\kappa}\ln\left(\frac{z-d}{z_0}\right) \tag{3}$$

where u_* can be expressed using $u_* = \sqrt{\tau_0/\rho}$ and κ is the von Karman constant 0.4.

2.2. Morphological model equation

Aerodynamic roughness parameters d and z_0 of the morphological model were calculated according to the following two Eqs.(4a) and (4b) empirically derived from wind tunnel experiments.

$$\frac{d}{H} = 1 + 4.43^{-\lambda_p}\left(\lambda_p - 1\right) \tag{4a}$$

$$\frac{z_0}{H} = \left(1-\frac{d}{H}\right)exp\left[-\left(0.5\frac{C_D}{\kappa^2}\left(1-\frac{d}{H}\right)\lambda_f\right)^{-0.5}\right] \tag{4b}$$

λ_p is building coverage and λ_f is the ratio of the total areas of building facets facing the wind direction to the lot area. C_D is the drag coefficient 1.2, H is

average building height. κ is the von Karman constant 0.4.

3. Calculation condition

The calculation conditions in this work are as follows. By using the following conditions, Eq.(2) can be applied to calculate the average value of ground surface drag τ_0.

- Constant volume flow($dU/dt = 0$)
- Neutral stratification
- No Coriolis force
- Boundary conditions
  Upper surface: free-slip boundary
  Horizontal surface: periodic boundary
- Geometric data of the buildings in Tokyo's 23 wards and Nagoya city(in 2009)
- Resolution Tokyo's 23 wards: 2.0m, Nagoya city: 2.5m
- Initial horizontal wind velocity: 3.0m/sec
- Numerical domain (x, y, z) = (1000m, 1000m, 600m)

4. Calculated areas

Fig.1 shows the relation of λ_p and λ_f. λ_p and λ_f are building coverage and the ratio of the total areas of building facets facing the wind direction to the lot area, respectively. In Fig.1, the painted circles and triangles shown in Fig.1 were selected areas from Tokyo's 23 wards and Nagoya city respectively. Using this relationship, 100 areas in Tokyo's 23 wards and 10 areas in Nagoya city (total 110 areas) were selected to calculate the two aerodynamic roughness parameters.

5. Results

5.1. Vertical profiles of momentum flux and main wind velocity

Fig.2 shows signature vertical profiles of wind velocity and momentum flux with each aerial photograph. Table-1 shows the surface geometric parameters of the three areas and H_{uw_peak}(Height of momentum flux peak value). In Fig.2, solid lines, chain lines and gray zones show each H_{max} (Maximum building height), H_{ave} (Average building height) and $H_{ave} \pm \sigma_H$ (σ_H : Standard deviation of building height) respectively. In Fig.2, the peak values of momentum flux are located at much higher than H_{ave} and relatively close to H_{max}. This means that the momentum roughness parameters depend on H_{max} even though this parameter is not considered in the morphological model. In addition σ_H tends to obscure the peak value of momentum flux

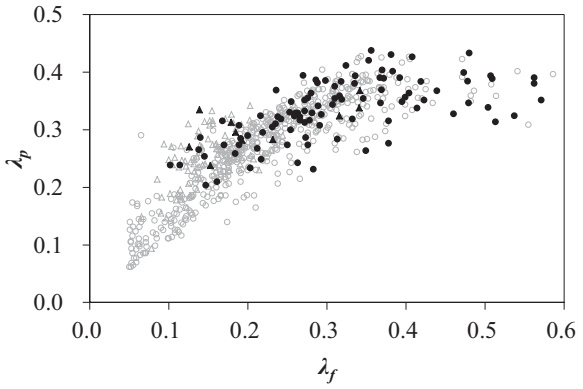

Fig.1 Relation of λ_p to λ_f

Table.1 Surface geometric parameters and H_{uw_peak}

	(a)	(b)	(c)
H_{ave} [m]	37.5	29.1	7.6
H_{max} [m]	154	188	40
σ_H [m]	41.4	21.2	3.3
λ_f	0.19	0.56	0.29
λ_p	0.31	0.38	0.38
H_{uw_peak} [m]	146	118	30

in Fig.2(b). The reason for this is that about 80% of the area's buildings have heights lower than 40m. Also, there are very few buildings of relatively similar heights to the tallest building in the area. In other words, the momentum flux of the lower buildings and that of the highest buildings are antagonistic to each other. Therefore, the area didn't have the clear value of momentum flux. The commonality of the areas is that the clear peak value of momentum flux is unclear similar to the characteristic of Shibuya area.

5.2. Displacement height

Fig.3 shows d/H_{ave} vs. λ_p. According to Fig.3, the result values of the LES showed larger than that of the morphological model because the model was adjusted so that d would not exceedH_{ave}. However, if building height is uneven, d, defined as action center of momentum, may exceed an H_{ave}. Therefore, it can be said that it is insufficient to calculate the aerodynamic roughness parameters in the actual city using the morphological model.

Fig.4 shows the new parameterization about d. The curves in Fig.4 are depicted the Eqs.$(5a\sim c)$ by a change of λ_p. Eq.$(5c)$ is the regression expression for staggered arrays with constant building height. By using Eqs. $(5a\sim c)$, d will be calculated more precisely than Eq.$(4a)$. The difference of Eq.$(4a)$ and Eq.(5) is shown in Fig.5.

$$d/H_{max} = -2\alpha x^3 + 3\alpha x^2 \qquad (5a)$$

$$x = (H_{ave} + \sigma_H)/H_{max} \qquad (5b)$$

$$\alpha = 1 + 176503.1^{-\lambda_p}(\lambda_p - 1) \qquad (5c)$$

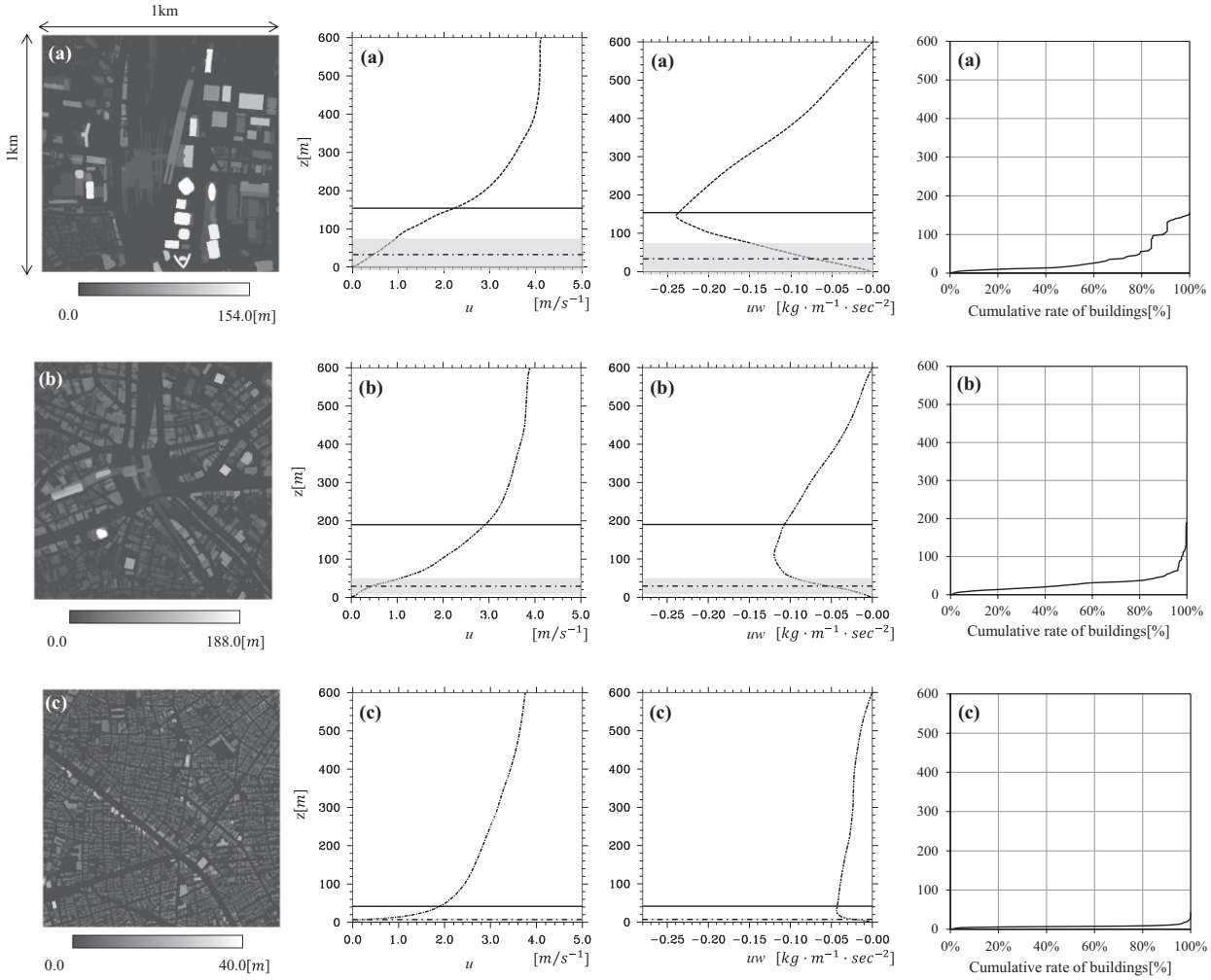

Fig.2 Vertical profiles of wind velocity u and momentum flux uw, ((a): Shinagawa, (b): Shibuya and (c): Senzoku)

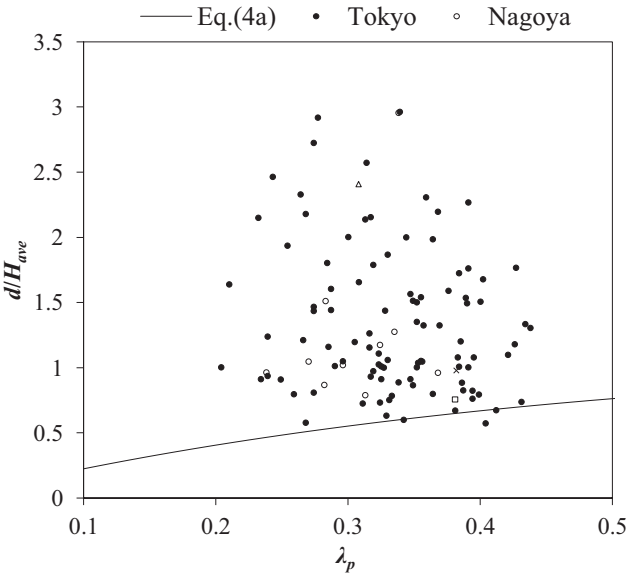

Fig.3 Relation of d/H_{ave} to λ_p, (△: Shinagawa, □: Shibuya and ×: Senzoku)

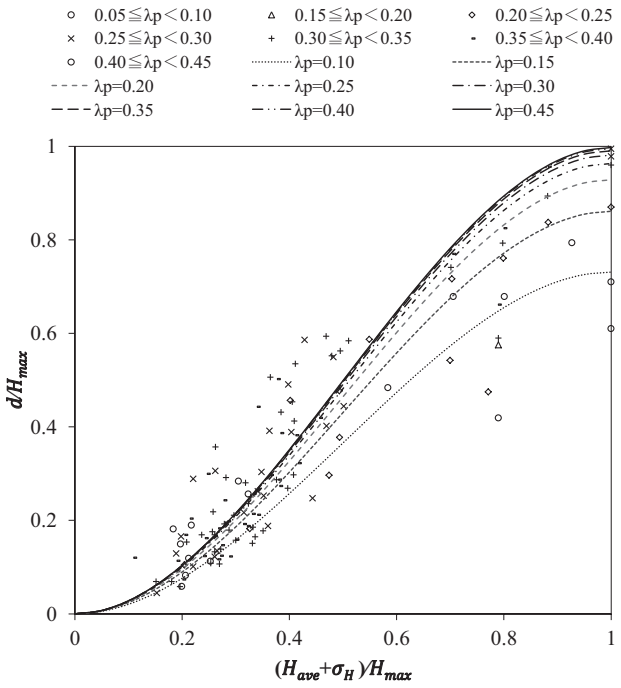

Fig.4 Relation of d/H_{max} to $(H_{ave}+\sigma_H)/H_{max}$

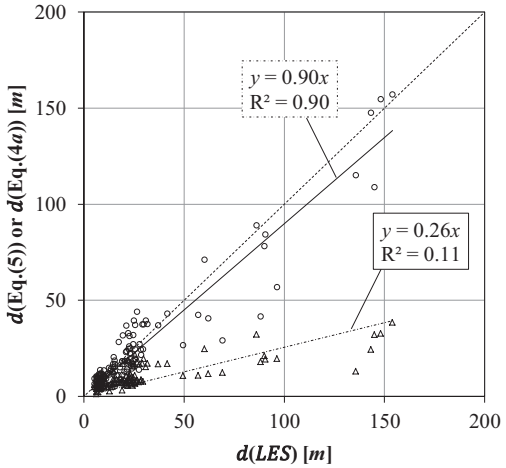

Fig.5 Comparison between Eq.(5) and Eq.$(4a)$, (○:Eq.(5), ∆:Eq.$(4a)$)

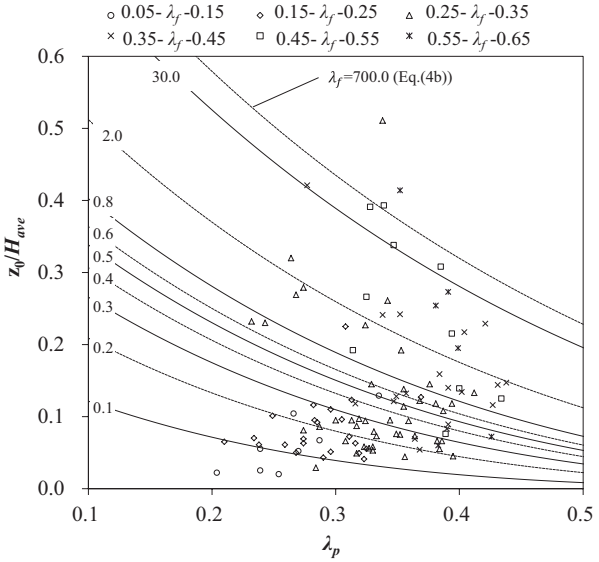

Fig.6 Relation of z_0/H_{ave} to λ_p

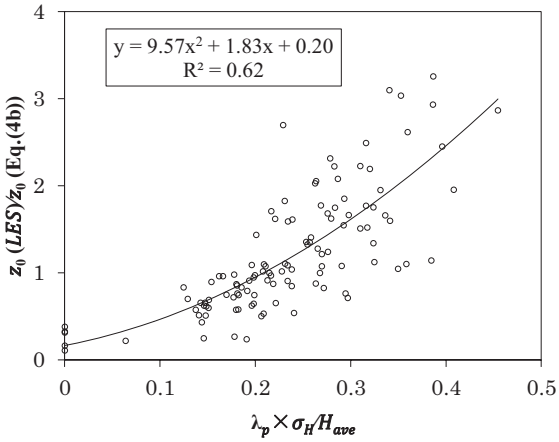

Fig.7 Relation of $z_0(LES)/z_0(\mathrm{Eq.\,(4b)})$ to $\lambda_p \times \sigma_H/H_{ave}$

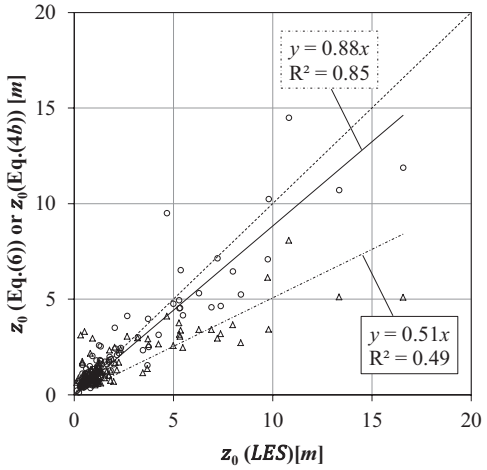

Fig.8 Comparison between Eq.(6) and Eq.(4b), (○: Eq.(6), ∆:Eq.(4b))

5.3. Roughness length

Fig.6 shows the relation of z_0/H_{ave} to λ_p. It should be noted that even if the $\lambda_f$of Shibuya has about three times as large as that of Shinagawa (cf. Table.1), the value of z_0/H_{ave} is almost equal to each other. In this regard, Xie *et al.* (2008)[2] pointed out that tall buildings have a significant effect on the total drag of a building array with non-uniform heights. It seems that areas that have a very large σ_H increase the momentum exchange.

Fig.7 shows the newly proposed parameterization of z_0. The curve in Fig.7 (Eq.(6)) is the regression expression to calculate z_0 more precisely. By using Eq.(6), z_0 will be calculated more precisely than Eq.$(4b)$. The difference of Eq.(6) and Eq.$(4b)$ is shown in Fig.8.

$$\frac{z_0}{z_0(Eq.(4b))} = 9.57x^2 + 1.83x + 0.20 \qquad (6a)$$

$$x = \lambda_p \times \sigma_H/H_{ave} \qquad (6b)$$

6. Conclusions

The methods for estimating two aerodynamic roughness parameters, displacement height and roughness length were discussed. The numerical results of vertical profiles of momentum flux and wind velocity were shown. It was found that drag coefficients, calculated from the numerical simulations, became significantly different from those calculated using the widely used conventional morphological models. On the basis of the discussion above, a new simple aerodynamic parameterization was proposed.

Reference

1) R. W. Macdonald, R. F. Griffiths, and D. J. Hall, An improved method for estimation of surface roughness of obstacle arrays, Atmospheric Environment, vol. 32, pp. 1857-1864, 1998.
2) Xie Z-T, Coceal O, Castro IP(2008), Large-eddy simulation of flows over random urban-like obstacles, Boundary-Layer Meteorol, 129:1-23

MODULATION CLASSIFICATION UTILIZING SPECTRAL CORRELATION FOR EMERGENCY RADIOS

Student Number: 10M18223 Name: Azril HANIZ Supervisor: Jun-ichi TAKADA

スペクトル相関を用いた災害時の緊急無線端末の変調方式の識別法に関する研究

アズリル・ハニズ

大地震のような天災が発生した場合、世界各国からの救助チームが被災地に駆けつけ、救命活動に参加すると予想される。同一周波数の使用による干渉問題を解決するためには、被災地における周波数利用状況および周波数を使用している緊急無線端末の同定が必要である。本研究では、変調信号の周期定常性およびスペクトル相関密度を用いた変調方式の識別法に注目した。同手法を利用した既存研究は本研究で想定する変調方式を識別するための議論が十分ではない。本研究では、スペクトル相関計算法の改善、および新たな特徴抽出法を導入することで、より多くの変調方式の識別を可能とした。さらに計算機シミュレーションにより提案手法の検証を行い、信号対雑音比 (SNR) が 4dB 以上あれば 0.9 以上の確率で 6 種類の変調方式が識別可能であることを示した。

1 Introduction

Whenever a large disaster occurs, damage to the telecommunication infrastructure can be expected, and emergency rescue teams from all over the world would have to set up their own mobile wireless network to communicate between their emergency personnel. As the number of rescue teams increases, the availability of unused frequency spectrum will become a problem, and once two different teams communicate on the same wireless channel, there is a high possibility of interference, which will then hamper their rescue operations.

In these kinds of situations, a radio surveillance system would prove to be useful. The system's main purpose would be to scan the radio environment and identify any transmitters on the scene. This identification may be performed by extracting parameters from the received signal, and recognizing the modulation scheme used by the transmitter. Modulation is the process of putting data such as human voice on a high frequency carrier signal which is suitable for wireless transmission. The main focus of these thesis will be on modulation classification.

A survey has been done on commercial wireless radio systems commonly used by rescue teams in the event of a disaster. In Japan, there still exists local councils which still utilize analog modulation (AM), although the government encouraged the use of digital radios since 2002. Elsewhere around the world, there have been a few efforts to standardize emergency radios, but unfortunately these efforts were only limited to certain parts of the world, and not worldwide. We have found that many different commercial systems utilize various modulation schemes such as AM, $\pi/4$-DQPSK, $\pi/8$-D8PSK, GMSK and 4FSK.

Automatic modulation classification (AMC) has been a long ongoing research topic, and different approaches have been taken to tackle this issue. [1] has conducted an extensive survey of recent AMC techniques. There exists much literature regarding modulation classification based on exploitation of signal cyclostationarity [2]. This research focuses on the technique which utilizes the spectral correlation density (SCD). Existing literature used the cyclic domain profile (CDP) to extract features from the SCD, but this resulted in an oversimplification of the SCD plot, leading to a loss of useful information to differentiate modulations [3].

The main objective of this study is to study the feasibility of exploiting signal cyclostationarity as a mean to classify a large number of modulation schemes commonly used by disaster emergency radios, and to obtain the optimum parameters for the system to successfully classify the targeted modulation schemes.

2 Cyclostationarity

2.1 Signal Model

For this thesis, we assume the received signal can be expressed by

$$x(t) = \mathrm{Re}\left\{h \cdot u(t) e^{j2\pi F_c t}\right\} + v(t)\,, \tag{1}$$

where $x(t)$ is the received real IF signal, h is time invariant channel response and F_c is the pseudo-carrier frequency. $u(t)$ and $v(t)$ denote the complex envelope of the transmitted signal $s(t)$ and noise respectively. Noise is assumed to be additive white Gaussian noise (AWGN) with zero mean and ${\sigma_v}^2$ variance. The signal-to-noise ratio (SNR) of the received signal is defined as the power of the signal divided by the in-band noise power.

2.2 Spectral Correlation Density (SCD)

Most communication signals can be modeled as cyclostationary processes that exhibit underlying periodicities in their signal structures. These periodicities can be exploited in order to differentiate between the transmitted signal and noise, and also between signals. A useful way to measure the spectral correlation of a cyclostationary signal is by using the spectral correlation density (SCD) [4]. The SCD is defined as

$$S_x^\alpha(f) = \lim_{T\to\infty} \lim_{\Delta t\to\infty} \frac{1}{\Delta t} \int_{-\frac{\Delta t}{2}}^{\frac{\Delta t}{2}} \frac{1}{T} X_T(t, f+\frac{\alpha}{2}) X_T^*(t, f-\frac{\alpha}{2}) dt\,, \tag{2}$$

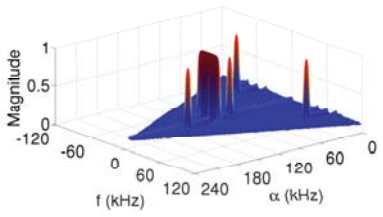

Figure 1: SCD plot of a BPSK signal

where

$$X_T(t,f) = \int_{t-\frac{T}{2}}^{t+\frac{T}{2}} x(u)e^{-j2\pi fu}du \tag{3}$$

is the Fourier transform of the input signal. Here, f is the spectral frequency and α is the cyclic frequency. The integrand in Eq.(2) is called the cyclic periodogram. In practice, the SCD can only be estimated using a finite set of samples. Frequency-smoothing was performed on the SCD to reduce any random fluctuations caused by this, and it can be expressed in the discrete domain by

$$S^{\alpha}_{x_T}(t,f)_{\Delta f} = \frac{1}{M}\sum_{v=-(M-1)/2}^{(M-1)/2} \frac{1}{T}X_T(t,f+\frac{\alpha}{2}+vF_s) X^*_T(t,f-\frac{\alpha}{2}+vF_s)\ . \tag{4}$$

Here, $\Delta f = MF_s$ is the width of the frequency-smoothing interval, $F_s = F_{\text{samp}}/L$ is the frequency sampling increment, and L is the FFT size. Next, the spectral coherence function was used to normalize the SCD plot, and can be expressed by

$$C^{\alpha}_{x_T}(t,f)_{\Delta f} = \frac{S^{\alpha}_{x_T}(t,f)_{\Delta f}}{[S^0_{x_T}(t,f+\frac{\alpha}{2})_{\Delta f}S^0_{x_T}(t,f-\frac{\alpha}{2})_{\Delta f}]^{1/2}}\ . \tag{5}$$

Finally, the SCD was also averaged over many blocks over time to improve reliability, and this operation can be written as

$$\tilde{C}^{\alpha}_{x_T}(f)_{\Delta f} = \frac{1}{N}\sum_{n=0}^{N-1} C^{\alpha}_{x_T}(t+nT,f)_{\Delta f}\ , \tag{6}$$

where N is the number of time-averaging blocks used. As an example, the SCD plot of a BPSK modulated signal is shown in Figure 1.

3 Implementation Issues in Discrete Time Domain

3.1 FFT Scalloping Loss

When the cyclic frequency α of the peak associated with the symbol rate does not fall exactly in the center of the FFT bin, scalloping loss occurs. The FFT can be thought of as a series of filters which are centered on the FFT bins. The filter responses will be attenuated as the frequencies move away from the center, and if a frequency is located exactly in between two adjacent FFT bins, then it would experience the largest scalloping loss. Instead of a rectangular window, we propose to use a Kaiser window ($\beta = 10$) to reduce this scalloping loss, and obtain a higher peak magnitude, as shown in Figure 2.

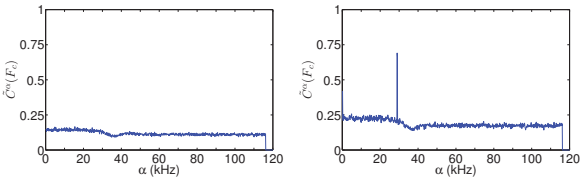

(a) Rectangular window (b) Kaiser window ($\beta = 10$)

Figure 2: Effect of various window functions on the SCD along the $f = F_c$ axis (BPSK signal, R_s = 29kSps, SNR= 20dB, F_{samp} = 240kHz, $L = 4096$, $M = 65$)

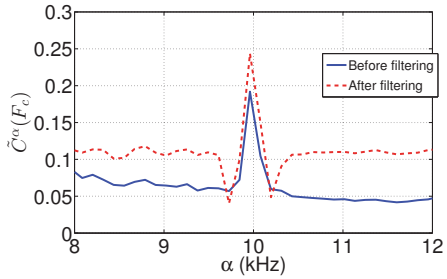

Figure 3: Effect of using emphasis filter (QPSK signal, R_s = 10kSps, SNR= 20dB, F_{samp} = 240kHz, $L = 4096$, $M = 65$, $K = 4$, Rect. window)

3.2 Dip in Noise Floor

One more issue that is faced when implementing the SCD discretely is there is a dip in the noise floor close to the symbol rate peak. This dip is a result of the frequency smoothing across the SCD. If the symbol rate peak magnitude is lowered due to this dip, it would be difficult to identify it. A simple filter is proposed to whiten the noise floor and emphasize the symbol rate peak, and we refer to this filter as an *emphasis filter*.

$$\hat{C}(\alpha) = \tilde{C}(\alpha) - \frac{1}{2}\left[\tilde{C}(\alpha - \frac{K\alpha_s}{2}) + \tilde{C}(\alpha + \frac{K\alpha_s}{2})\right] \tag{7}$$

Here, $\tilde{C}(\alpha)$ denotes the SCD in Eq.(6) when $f = F_c$, and α_s denotes the cyclic frequency increment. This filter averages the difference between the peak and the $K/2$-th cyclic frequencies from both the left and right side. A comparison between the SCD along the $f = F_c$ axis before and after filtering is shown in Figure 3. Here, the magnitude of the SCD after filtering is adjusted to match the noise floor of the original SCD for easier comparison.

4 Automatic Modulation Classification

4.1 Feature Extraction

Different modulation schemes produce distinct SCD plots which may be exploited for AMC, and the location of the peaks on the $f - \alpha$ plane is related to the carrier frequency (F_c) or the symbol rate (R_s). To reduce the amount of data, [3] took the cyclic domain profile (CDP) which is the maximum of the SCD taken over spectral frequency f. However, some peaks may overlap, resulting in ambiguity on the actual location of the peaks. In this research, we propose to calculate only certain points on the SCD to be used as features in order to avoid this ambiguity, and also reduce computational load.

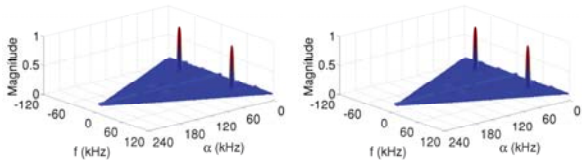

(a) QPSK (b) 8PSK

Figure 4: Comparison of SCD plots between several higher-order modulation schemes (R_s = 30kSps)

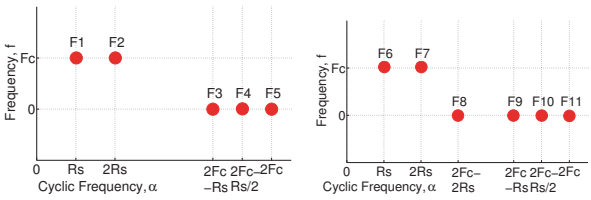

(a) Original received signal (b) Squared received signal

Figure 5: Feature locations on the f$-\alpha$ plane

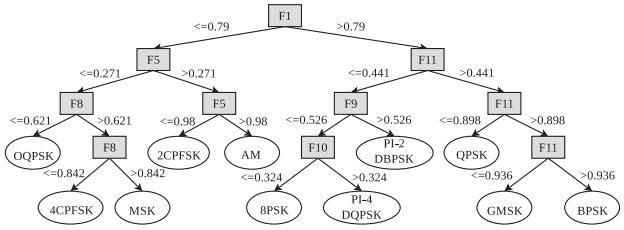

Figure 6: Decision tree (Numeric data, R_s = 30kSps, SNR= 20dB)

Higher-order modulation schemes such as QPSK and 8PSK do not exhibit second-order cyclostationary properties, and therefore have very similar SCD plots, and this is shown in Figure 4. Therefore, we propose to square the received signal before calculating the SCD, which will remove lower modulations orders and allow classification using the SCD. The location of the peaks on the SCD which are selected as features is shown in Figure 5.

4.2 Classification

There exists much literature which discuss the use of neural networks together with spectral correlation analysis [3]. In this research, the traditional binary decision tree was used because of its simplicity in implementation. A supervised learning algorithm is employed, where the system is trained beforehand with supervised training data to obtain an optimal decision tree. The C4.5 algorithm, which was used to build the decision tree, uses information gain ratio as the criterion in selecting the best features to be nodes in the decision tree [5]. The java implementation of the C4.5 algorithm is called J48 and is included in the WEKA data mining tool.

Two types of training data was used to generate decision trees. The first type is *nominal* (Boolean) training data, which consists of a *yes* or *no*, representing the presence or absence of a peak at feature locations shown in Figure 5. To decide the presence of a peak, the peak magnitudes were compared with a threshold, which was obtained empirically from additive white Gaussian noise data and based on a probability of false alarm (P_{FA}).

Table 1: List of simulation parameters

FFT Size, L	4096
Freq. smoothing interval, M	65 bins
No. of time-avg. blocks, N	100
Sampling freq., F_{samp}	240 kHz
Pseudo-carrier freq., F_c	60 kHz
Symbol rate, R_s	30 kSymbol/s
SNR	$-10 \sim$ 20dB
Window function	Rectangular window

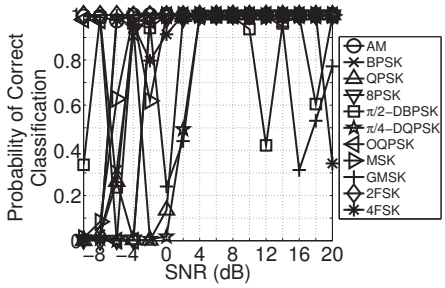

(a) Boolean data

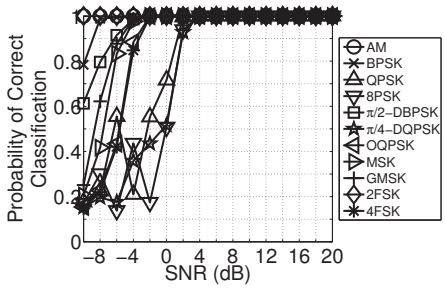

(b) Numeric data

Figure 7: Probability of correct classification for each modulation (R_s = 30kSps)

The second type is *numeric* data, where the peak magnitude itself was used as training data. Comparison between using these 2 types data will be shown in the results section. Figure 6 shows an example of a decision tree generated by WEKA using numeric training data.

4.3 Simulation Results

4.3.1 Simulation Setup

Monte Carlo simulations were run with AM, BPSK, $\pi/2$-DBPSK, QPSK, $\pi/4$-DQPSK, 8PSK, OQPSK, MSK, GMSK, 2CPFSK and 4CPFSK modulated signals. PSK signals used a raised cosine filter for pulse-shaping with a roll-off factor of 0.5, and GMSK used a Gaussian filter with a BT product of 0.5.

1000 sets of training data were used to build the decision tree. Using this decision tree, a Monte Carlo simulation of 1000 trials was performed on each modulation. A very low $P_{\text{FA}} = 0.1\%$ was chosen because training the system using data with many false alarms will hamper the training process.

4.3.2 Results

Figure 7 shows the probability of correct classification of 11 modulation schemes for 2 cases, using Boolean (nominal) data and numeric data. Performance using numeric data fared better than using Boolean data because WEKA

could catch smaller differences of peak magnitude when using numeric data. We can see that the system can correctly classify all 11 modulations with a high probability down to SNR= 4dB. At low SNRs, the feature peaks on the SCD plot diminish and is buried under the noise, thus reducing the probability of correct classification.

Figure 8 shows the results when the symbol rate is varied uniformly between $R_s = 1 \sim 30$ kSps at 1 kSps steps. It is assumed that R_s is known using a symbol rate estimator, and a decision tree was generated for each R_s. It can be seen that the performance is degraded, especially when utilizing Boolean training data. Scalloping loss reduces the magnitude of the peak on the SCD, and thus making it more difficult for the system to classify modulation schemes at small SNRs.

Figure 9 shows the probability of correct classification which is plotted against SNR and symbol rate R_s, when a Kaiser window is used. It can be seen that the performance at low symbol rates ($R_s < 5$kSps) is deteriorated. This is because if the signal bandwidth (which is roughly equal to R_s) is smaller than M, the peak will be smoothed out. This will result in a smaller peak magnitude, thus reducing the probability of correct classification.

5 Symbol Rate Estimation Utilizing SCD

In a ideal blind AMC system, the symbol rate R_s of the received signal is unknown, and it is necessary to estimate it beforehand. In this thesis, a technique to estimate the symbol rate R_s using the SCD plot is proposed. For many digital modulation schemes, the cyclic peak which appears along this $f = F_c$ axis is associated with the symbol rate R_s. Therefore, to estimate the symbol rate, first the SCD along the $f = F_c$ is calculated. Then the proposed emphasis filter of width $\Delta\alpha = K\alpha_s$ is applied, where α_s is the cyclic frequency increment, and K is the emphasis filter length. The cyclic frequency associated with the highest peak equals the symbol rate R_s of the received signal.

$$\tilde{R}_s = \arg\max_{\alpha} \hat{C}^{\alpha}_{x_T}(F_c)^{\Delta\alpha}_{\Delta f} \tag{8}$$

6 Whole System

In this section, the simulation results for the whole system is presented, where the proposed symbol rate estimation technique is used together with the proposed AMC technique. This brings the system one step close to *blind* AMC, where there is no prior information about the received signal. However, since there a several modulation schemes whose symbol rates cannot be properly estimated using the proposed symbol rate estimation technique, this simulation was performed with a smaller number of modulation schemes, which are BPSK, $\pi/2$-DBPSK, QPSK, $\pi/4$-DQPSK, 8PSK and GMSK. However, the decision trees used here are generated using all 11 modulation schemes in Section 4.3.

6.1 Results

Figure 10 shows the results of AMC with prior symbol rate estimation. The result presented here is the probability of correct classification averaged over all the 6 targeted modulation schemes. The proposed technique can correctly classify 6 modulation schemes with a probability of close to 1 down to SNR= 4 dB within symbol rate range of $R_s = 5 \sim 30$ kSps.

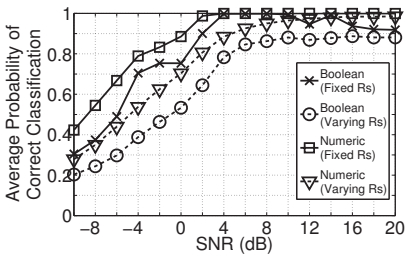

Figure 8: Comparison between fixed R_s and varying R_s

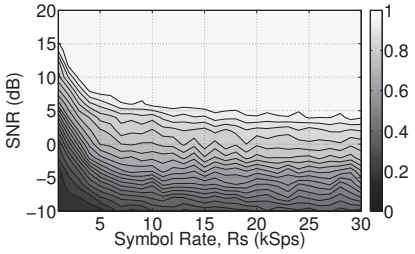

Figure 9: Avg. prob. of correct classification for proposed AMC technique with perfect knowledge of R_s (Kaiser window, numeric data)

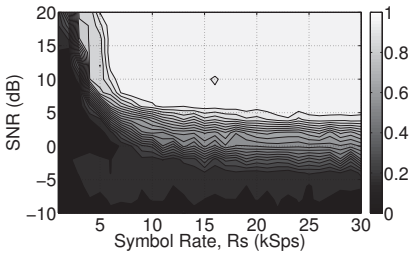

Figure 10: Avg. prob. of correct classification for proposed AMC technique with R_s estimation (Kaiser window, numeric data)

7 Conclusion

In this thesis, the modulation scheme of received signals is used to try to identify emergency radios in a disaster scenario. A novel AMC technique which utilizes specific features from the SCD plot of both the original received signal and the squared received signal was proposed. Several issues when implementing the SCD algorithm discretely were identified, and methods of compensation was also discussed. The performance evaluation of the whole system incorporating both the symbol rate estimator and the modulation classifier revealed that the overall system could correctly classify 6 modulation schemes down to an SNR of 4 dB. However, the optimum length of the frequency-smoothing interval M still remains an issue. The effect of the carrier frequency offset, and also multipath channel conditions will have to be addressed in future work.

References

[1] O. A. Dobre et al., "A survey of automatic modulation classification techniques: classical approaches and new trends," IET Commun., vol. 1, pp. 137-156, April 2007.

[2] B. Ramkumar, "Automatic modulation classification for cognitive radios using cyclic feature detection," IEEE Circuits Syst. Mag., vol.2, no.2, pp. 27-45, Second Quarter 2009.

[3] E. Like et al., "Signal Classification in Fading Channels Using Cyclic Spectral Analysis," EURASIP Journal on Wireless Communications and Networking, Volume 2009, 2009.

[4] W. A. Gardner, "Cyclostationarity in Communications and Signal Processing," IEEE Press, 1993.

[5] J.R. Quinlan, "C4.5 : Programs for Machine Learning," Morgan Kauffman Publishers, 1993.

THE DECOMPOSITION OF NITROUS OXIDE OVER RUTILE STRUCTURE TITANIA SUPPORTED METAL CATALYSTS

Student number: 10M18230　Name: Wanying HU　Supervisor: Hirofumi HINODE

ルチル型チタニア担持金属触媒による一酸化二窒素の分解

胡　婉瑩

本研究では、工業生産過程から排気された N_2O の分解を目的に、三種類のルチル型チタニアを担体として、チタニア担持金属（銀、セリウム、マンガン、マグネシウム）触媒を調製し、N_2O 分解に対する触媒活性を評価した。また、調製条件である金属担持量、担体の種類及び焼成温度による触媒活性の変化を検討した。調製した触媒の中で、550 ℃で焼成したルチル型チタニア(Toho-1)担持銀(10 wt%)触媒は最も高い触媒活性を示し、酸素がない場合、N_2O は 350 ℃から分解し始め、650 ℃において完全に分解した。酸素存在下では、N_2O の分解温度は高温側にシフトした。触媒のキャラクタリゼーションにより、比較的に小さい担持金属粒子径を持つ触媒は、より良い触媒活性を示したことがわかった。

1 Introduction

Nitrous oxide (N_2O) is one of the powerful greenhouse gases with a global warming potential per molecule of about 300 times that of carbon dioxide (CO_2) [1]. N_2O is also identified as a contributor to the destruction of ozone layer in the stratosphere. The major stationary sources of N_2O are agricultural byproducts and biomass burning [2]. Therefore, it is important to study the decomposition of N_2O from the environmental point of view.

Previous studies reported that the rutile structure titania had a better activity for the decomposition of N_2O to N_2 than the anatase structure [3].

In this research, to decompose the N_2O emission from industrial process, the decomposition of N_2O over rutile structure TiO_2 supported metal (silver, cerium, manganese and magnesium) catalysts was investigated.

2 Experimental

2.1 Catalyst preparation

M/TiO_2 (M=Ag, Ce, Mn and Mg) catalysts were prepared by impregnation method. Three types of TiO_2 (Toho-1, Toho-2 and Toho-3, Toho Titanium Co.) were used as supports. The characteristics of each TiO_2 were shown in Table 1. The precursors of four metals are $Ag(NO_3)$ (99.8%, Wako Co.), $Ce(NO_3)_3{\cdot}6H_2O$ (98.0%, Wako Co.), $(CH_3COO)_2Mn{\cdot}4H_2O$ (99.0%, Wako Co.) and $(CH_3COO)_2Mg{\cdot}4H_2O$ (99.9%, Wako Co.) respectively.

Table 1 Characteristics of each TiO_2

TiO_2 No.	Surface area (m^2/g)	Particle size (μm)	Rutile content (%)
Toho-1	32.8	≤0.42	93.3
Toho-2	50.5	≤6.02	91.7
Toho-3	73.8	≤3.48	95

In preparation, TiO_2 was impregnated in an aqueous solution of each precursor. Then, the solution mixture was stirred at room temperature for one day followed by drying up for 12 hours at 70 ℃. After that, the sample was calcined for 5 hours under air flow. In order to reduce the pressure drop, the sample was finally pelletized, crushed and sieved into between 0.71 mm to 1.00 mm.

The following nomenclatures for the catalyst samples are used: M (x wt%)/TiO_2 (y)-z ℃ where M means the loading metal, x means the loading level, y means the type of TiO_2 and z means the calcination temperature.

2.2 Catalytic activity experiment

The catalytic reaction was carried out in a fixed-bed flow reactor under atmospheric pressure. The reactant gas was prepared by mixing N_2O, O_2 and He as a balance gas. The mixed gas of 1000 ppm N_2O, 0%/10% O_2 and He was fed to the catalyst at a flow rate which correspond to a space velocity of 16000 h^{-1}.

Gas chromatography (GC323w; GL Science Co., with Porapak N, Porapak Q and Molecular Sieve 13X columns) was used to analyze N_2O, N_2 and O_2.

2.3 Catalyst characterization

Characterizations of the catalysts were performed by Thermogravimetric Analysis (TG8120), X-ray Diffraction (MultiFlex), Nitrogen Adsorption (Autosorb 1) and Scanning Electron Microscope (JSM-5310LV)-Electronic Data Systems (JED-2140).

3. Results and discussion

3.1 The effect of metal loading on catalytic activity for N_2O decomposition without O_2

Figure 1 shows the catalytic activity results of Ag/TiO_2 (Toho-1) - 600 ℃ and Ce/TiO_2 (Toho-1) - 600 ℃ with different metal loading levels for the decomposition of N_2O to N_2 without O_2. Compared to bare TiO_2 (Toho-1) which only decomposed 48% N_2O at 700 ℃, loading of Ag and Ce on TiO_2 improved catalytic activity.

Figure 2 shows the catalytic activity results of Mn/TiO_2 (Toho-3) - 500 ℃ and Mg/TiO_2 (Toho-3) - 400 ℃ with different metal loading levels for the decomposition of N_2O to N_2 without O_2. Compared to bare TiO_2 (Toho-3) which only decomposed 45% N_2O at 700 ℃, loading of Mn on TiO_2 improved catalytic activity. However, loading of Mg on TiO_2 showed no improvement on catalytic activity, the conversion of N_2O was even lower than bare TiO_2 (Toho-3).

Variation in metal loading levels showed optimum activity result using 10 wt% for Ag and Mn while 15 wt% for Ce. Ag (10 wt%)/ TiO_2 (Toho-1) - 600 ℃ showed the best catalytic activity. Since no NO and NO_2 were detected in all conditions, it could be concluded that N_2O was completely decomposed into N_2.

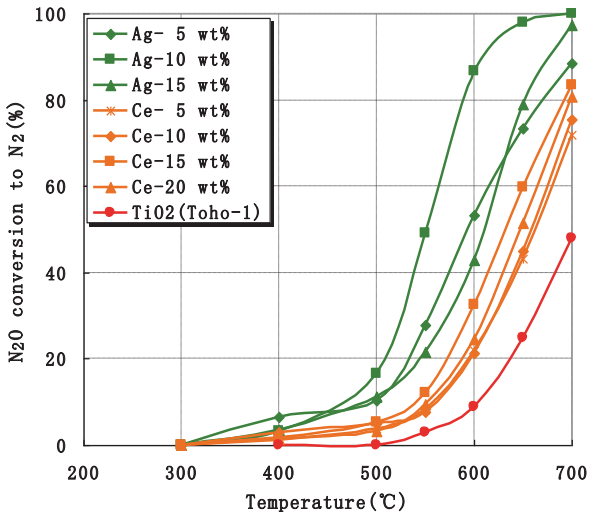

Fig. 1 The effect of metal loading of Ag/TiO_2 (Toho-1) - 600 ℃ and Ce/TiO_2 (Toho-1) - 600 ℃ catalysts on catalytic activity for the decomposition of N_2O to N_2 without O_2

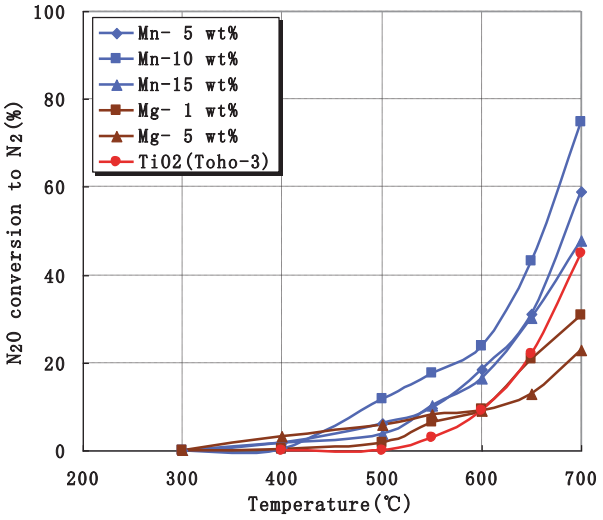

Fig. 2 The effect of metal loading of Mn/TiO_2 (Toho-3) - 500 ℃ and Mg/TiO_2 (Toho-3) - 400 ℃ catalysts on catalytic activity for the decomposition of N_2O to N_2 without O_2

3.2 The effect of support on catalytic activity for N_2O decomposition without O_2

Figure 3 shows the catalytic activity results of Ag(10 wt%)/TiO_2-600 ℃, Ce(15 wt%)/TiO_2-600 ℃ and Mn(10 wt%)/TiO_2- 500 ℃ with different support for the decomposition of N_2O to N_2 without O_2.

Variation in supports showed optimum activity result using TiO_2(Toho-1) for Ag and Ce, TiO_2(Toho-3) for Mn.

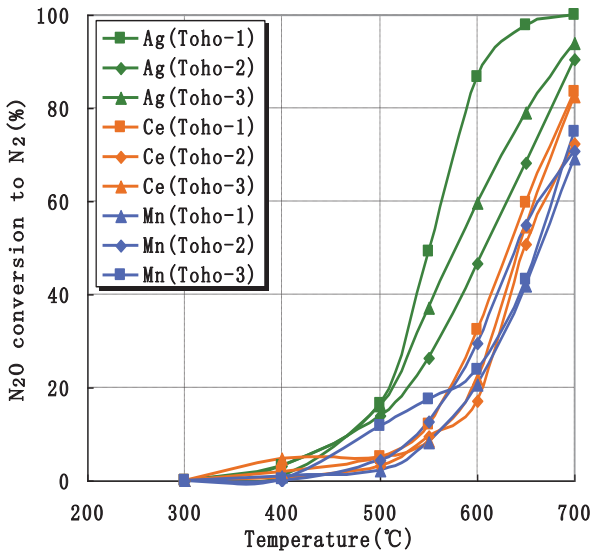

Fig. 3 The effect of support of Ag (10 wt%)/ TiO_2 (Toho-1), Ce (15 wt%)/ TiO_2 (Toho-1), and Mn (10 wt%)/ TiO_2 (Toho-3) catalysts on catalytic activity for the decomposition of N_2O to N_2 without O_2

3.3 The effect of calcination temperature on catalytic activity for N_2O decomposition without O_2

Figure 4 shows the catalytic activity results of Ag(10 wt%)/TiO_2(Toho-1), Ce(15 wt%)/TiO_2(Toho-1) and Mn (10 wt%)/ TiO_2 (Toho-3) with different calcination temperature for the decomposition of N_2O to N_2 without O_2.

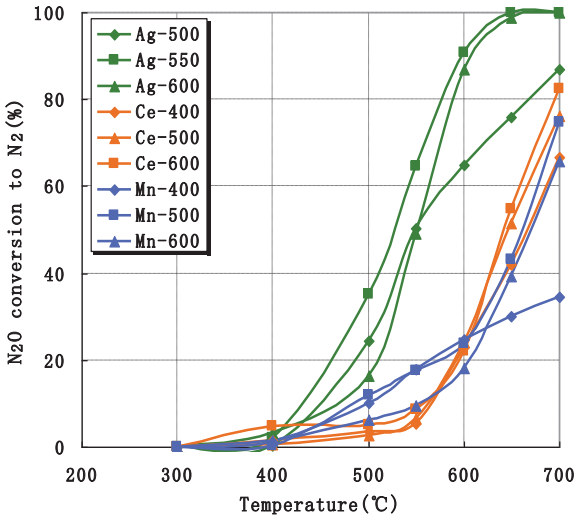

Fig. 4 The effect of calcination temperature of Ag (10 wt%)/ TiO_2 (Toho-1), Ce (15 wt%)/ TiO_2 (Toho-1), and Mn (10 wt%)/ TiO_2 (Toho-3) catalysts on catalytic activity for the decomposition of N_2O to N_2 without O_2

Variation in calcination temperatures showed optimum activity result using 550 ℃ for Ag, 600 ℃ for Ce and 500 ℃ for Mn.

3.4 The influence of oxygen on catalytic activity for N_2O decomposition

Figure 5 shows the catalytic activity results of Ag(10 wt%) /TiO_2 (Toho-1)- 600 ℃, Ce (15 wt%)/ TiO_2 (Toho-1)- 600 ℃ and Mn (10 wt%)/ TiO_2 (Toho-3)- 500 ℃for the decomposition of N_2O to N_2 in the presence of O_2 (10%) and without O_2.

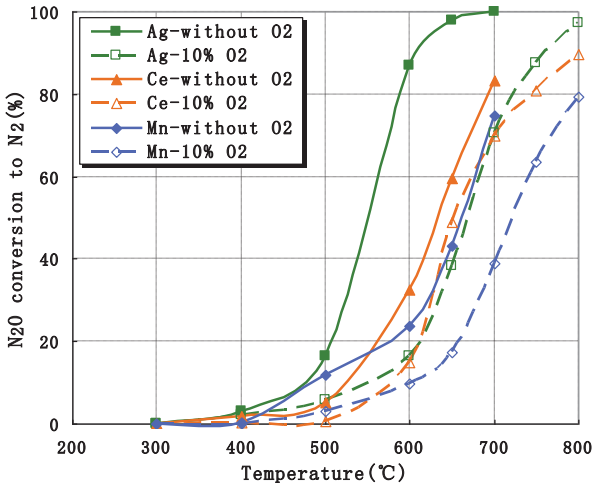

Fig. 5 The influence of oxygen of Ag (10 wt%)/ TiO_2 (Toho-1)- 600 ℃, Ce(15 wt%)/TiO_2(Toho-1)-600 ℃, and Mn (10 wt%)/ TiO_2(Toho-3)-500 ℃ catalysts on catalytic activity for the decomposition of N_2O to N_2

For all three samples, it is shown that the conversion temperature of N_2O was shifted to higher temperature in the presence of oxygen. This result indicated that the catalytic activity was inhibited by the presence of oxygen. The O_2 could compete with the N_2O in the process of adsorption on active site, reducing the contact of N_2O with the active site; thus reducing the effectiveness of N_2O degradation. [4].

3.5 XRD results

3.5.1 XRD patterns

Figure 6 shows the results of XRD patterns of Ag(10 wt%)/ TiO_2 (Toho-1)- 600 ℃, Ce (15 wt%)/ TiO_2 (Toho-1)-600 ℃, Mn (10 wt%)/TiO_2(Toho-3)-500 ℃ and Mg (1 wt%)/ TiO_2 (Toho-3)- 400 ℃.

In the cases of Ag, Ce and Mn loading, it is confirmed that each metal was supported in the form of metallic Ag, CeO_2 and Mn_3O_4 on TiO_2, respectively. Previous study suggested that the role of Ag, CeO_2 and Mn_3O_4 is to provide active site for N_2O

decomposition [3].

However, in the case of Mg loading, only $MgTiO_3$ peaks could be observed. Obviously Mg reacted with TiO_2 producing $MgTiO_3$ which has low activity towards N_2O decomposition.

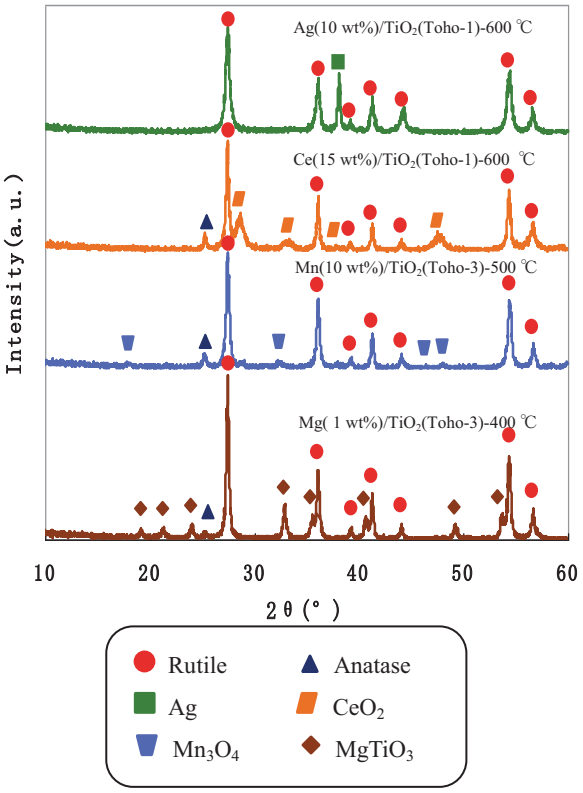

Fig. 6 XRD patterns of each sample

3.5.2 Supported metal particle size

The supported metal particle size could be calculated from XRD patterns. The Scherrer Equation was used in the calculation.

$$D=(K\lambda)/(\beta\cos\theta)$$

D: Particle size (nm)

K: The Scherrer constant (-)

λ: Wavelength (Å)

β: Full width at half maximum(FWHM) (rad)

θ: angle (°)

Table 2 shows the results of supported metal particle size and surface area of Ag (10 wt%)/TiO_2, Ce (15 wt%)/TiO_2 and Mn (10 wt%)/TiO_2 with different calcination temperature or support. The samples with higher catalytic activity of each metal were showed by deeper color. The catalysts with smaller supported metal particle size showed higher catalytic activity. It is possible that smaller supported metal particle size may increase the reactivity of the active site and also increase the area of active site exposed to N_2O. The catalysts with larger surface area showed higher catalytic activity to some extent. However, metal particle size seemed to be the prevailing factor instead of surface area on N_2O decomposition.

Table 2 Supported metal particle size and surface area of each sample

Catalyst	Supported metal particle size (nm)	Surface area (m^2/g)	N_2O conversion at 700 ℃
Ag/TiO_2(Toho-1)-500 ℃	6.27	22.02	87%
Ag/TiO_2(Toho-1)-550 ℃	5.61	24.46	100%
Ag/TiO_2(Toho-1)-600 ℃	5.79	18.34	100%
Ag/TiO_2(Toho-2)-600 ℃	6.90	16.94	90%
Ag/TiO_2(Toho-3)-600 ℃	5.71	17.88	94%
Ce/TiO_2(Toho-3)-400 ℃	4.61	51.18	67%
Ce/TiO_2(Toho-3)-500 ℃	2.49	45.83	76%
Ce/TiO_2(Toho-3)-600 ℃	1.73	57.06	82%
Ce/TiO_2(Toho-1)-600 ℃	1.60	28.21	84%
Ce/TiO_2(Toho-2)-600 ℃	3.17	26.86	72%
Mn/TiO_2(Toho-3)-400 ℃	3.38	58.15	34%
Mn/TiO_2(Toho-3)-500 ℃	2.78	41.40	75%
Mn/TiO_2(Toho-3)-600 ℃	4.76	26.00	66%
Mn/TiO_2(Toho-1)-500 ℃	4.46	19.42	69%
Mn/TiO_2(Toho-2)-500 ℃	4.98	30.85	71%

4. Conclusions

Loading of Ag, Ce and Mn onto TiO_2 improved catalytic activity compared to bare TiO_2. In contrast, loading of Mg showed no improvement. Ag(10 wt%)/TiO_2(Toho-1)-550 ℃ showed the best catalytic activity with the N_2O decomposition beginning at 350 ℃ and achieving 100% at around 650 ℃. By introducing oxygen, the catalytic activity was inhibited. The catalyst with smaller supported metal particle size showed higher catalytic activity.

References

[1]FAO, Livestock a major threat to environment (29 Nov. 2006.)

[2]IPCC AR4

[3]K.Yanagida, Master thesis, Tokyo Institute of Technology (2006)

[4] S. Suarez, M. Yates, A.L. Petre, J.A. Martin, P. Avila and J. Blanco, “Development of a new Rh/TiO_2-sepiolite monolithic catalyst for N_2O decomposition” Appl. Catal. B64 (2006), p.302

The situation of university electricity conservation through a focus on respondents' consciousness and action in Tokyo Tech

Student number: 10M18246 Name: Hongshan ZHAO Supervisor: Naoya ABE

東京工業大学における自主的節電意識・行動に着目した電力消費量抑制対策の実態分析

趙　紅姍

本研究は、東日本大震災後の学内利用者の節電意識・行動をアンケート調査により把握し、環境情報利用の有無に影響与える因子を分析した。これらの分析を通して、より効果的な環境情報提供方法を検討した。

1 Background and Objective

Due to electricity shortages after the accident at the Fukushima nuclear power plant last March of 2011, electricity conservation measures have been taken in Tokyo Tech. As an effect of such measures, electricity consumption was reduced by about 18% through Apr. to Dec. 2011 compared with the electricity consumption in the same period in 2010. Considering that most of the reduction was reduced by the conservation measures, the electricity consumption may probably rebound to the previous level. Therefore it is necessary to discuss long term electricity conservation.

The research about the relationship between energy conservation behaviors at home and energy consumption has been done (Katatani, 2004.)[1], the energy conservation actions such as air conditioner temperature controlling, and get together in one room with other family members are effective. But the situation in university is probably different, because of the little incentive to do the energy conservation actions. Therefore the relationship between mind-settings and behavioral change of electricity consumption at Tokyo Tech especially after 3.11 should be discussed.

The electricity consumption information was publicized in Tokyo Tech's homepage. Providing electricity consumption information is considered as a way to reduce electricity consumption by enhancing electricity users' consciousness (Maria Gleerup, 2010) [2]. But the actual situation of the information usage is unclear and it is possible that few respondents know about the existence of the information and even some information is not significant for other users. Therefore there are three main objectives of this research. The first one is to clarify the situation of electricity consumption reduction and the relationship with respondents' thinking about electricity measures. The second one is to determine how respondents change their energy conservation action at home and lab. The third one is to investigate the factors which influence usage of electricity consumption information.

2 Data Collection

Based on the electricity consumption data of Apr.~Dec. 2010 and the same data of 2011, area of building data of 24 mainly used buildings which are got from Facility Department of Tokyo Tech, the consumption reduction, the rate of the reduction were calculated.

A questionnaire survey was conducted from 30th Nov to 12th Dec. Questionnaires (petition and message with the link of survey) were sent to 426 individuals in O-okayama campus with a total population of about 5,500 respondents on the same campus.

242 responses with 233 effective responses were collected, including responses from 27 departments within 24 main buildings in O-okayama campus.

The contents of the questionnaire and response attribute were shown as Table 1 and Fig.1.

Table 1 Contents of the questionnaire

Qusetion Number	Q1:Attribution of the responders	Q2: (1)The thinking about the electricity measures taken in the lab	Q2: (2) The energy conservation action at lab and home before and after 3.11	Q3: The usage and thinking about the energy(electricity)information which is publicized in the homepage of Tokyo Tech
Qusetion	Department	Controlling the temperature of air conditoner	Controlling the temperature of air conditoner	The reason of using homepage
	Building which is studying in	Light efficiency	Light efficiency	The frequency of information usage
	gender	Using stairs instead of elevators	Using stairs instead of elevators	Satisfaction with enviromental information publicized in Tokyo Tech
	…	…		…
Number of question	18 questions	11questions	11questions×4	17 questions

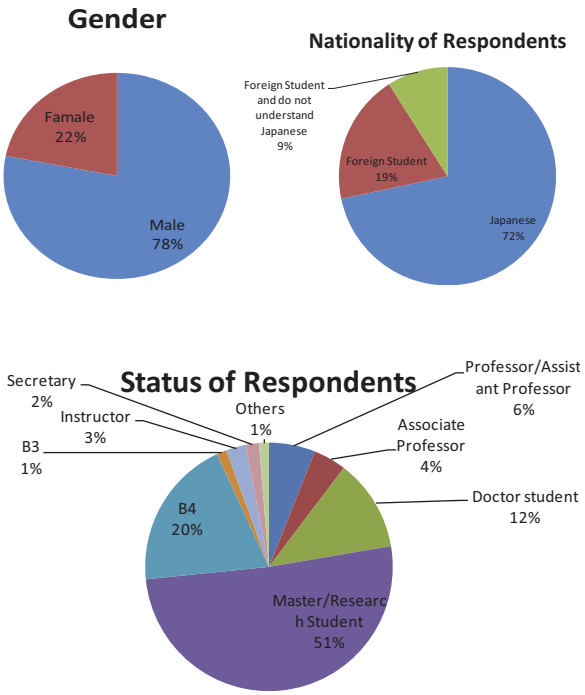

Fig 1 Response attribute

3 Methodologies

To clarify the situation of electricity consumption reduction and the relationship with respondents' thinking about electricity measures (objective1), PCA (Principle Component Analysis) and Cluster Analysis were used to group buildings. Correspondence analysis was also used to see the relationship.

About correspondence analysis, general indications for a contingency table with the two categorical variables V_1 and V_2 defined for n individuals ; individual l carries the categories i(for V_1)and j(for V_2): these are accounted for in x_{ij}. In correspondence analysis, we consider term $f_{ij}=x_{ij}/n$, the probability of carrying both the categories i(of V_1) and those of j(V_2). The margins of this table, which also known as marginal probabilities, are defined by

$$f_{i\circ} = \sum_{i=1}^{J} f_{ij} \quad f_{\circ j} = \sum_{i=1}^{I} f_{ij} \quad f_{\circ\circ} = \sum_{i,j} f_{ij} = 1$$

The χ^2test is used to test the significance of the overall deviation.

For objective 2, the cross session data was used to see respondents's behavior change after 3.11. To investigate the factors which influence usage of electricity consumption information (objective3), the logit model was used.

About the logit model, suppose the probability is π . The logit function of π leading to the model

$$\text{logit}(\pi) = \log\left(\frac{\pi}{1-\pi}\right) = \beta_0 + \beta_1 x_1 + \cdots + \beta_q x_q + \varepsilon_q$$

where β associated with explanatory variables x_j is such that exp(β j) is the odds that the response variable takes the value one when x_j increases by one, conditional on the other explanatory variables remaining constant.

The logit of a probability is simply the log of the odds of the response taking the value one. To see the relationship between parameters and probability, marginal effect is needed and can be calculated by

$$\frac{d\pi(Y=1)}{dX} = \frac{d(1-F(-\alpha-\beta X))}{dX} = bf(-\alpha-\beta X)$$

where F is cumulative density function of logistic distribution.

4 Results

The results of buildings grouping is shown as Fig.2. The variable of the horizontal axis is for the scores of the first component from PCA, the variable of the vertical axis is for the scores of second component. Reduction level can be seen as the first component, and reduction amount can be seen as the second component. The results of grouping are:

Group1: High reduction amount, low reduction level
Group2: Both reduction amount and level are large
Group3: Middle reduction amount, high level
Group4: Both middle reduction amount and level
Group5: Low reduction amount, middle level

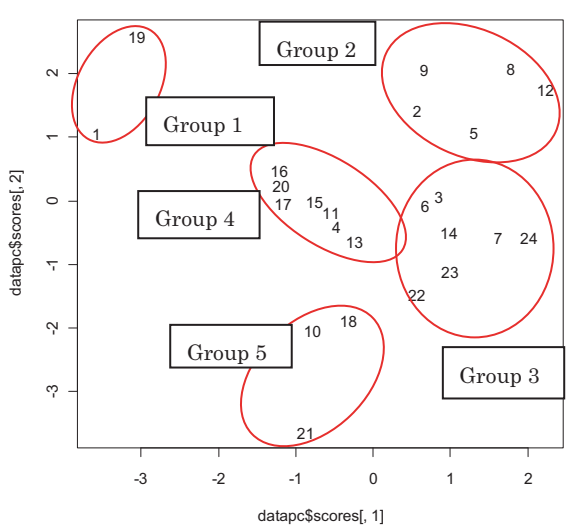

Fig2 Results of PCA and cluster analysis

The relationship between electricity reduction pattern and thinking about measures taken in lab was analyzed by correspondence analysis and results of group1 and group 5 were shown as Fig.3

For measures to control air conditioner temperature and to turn off the light when leaving the room, all of the groups' respondents think it is effective and will do them voluntarily. As for measures to work in "room together", responders think it is effective but will not do. In group 5 which has low electricity reduction amount, responders will not do them voluntarily. In group 1,3, and 4, although they think they are ineffective, respondents will do something about it.

About the energy conservation behavior change after 3.11, the percentages that respondents do the energy conservation action before 3.11 and after 3.11 results are shown in fig.4.

The results show that comparing before3.11 and after, the number of respondents who began to take the energy conservation action increased. The number of respondents who began to take the conservation actions at lab also increased. The electricity reduction measures taken in Tokyo Tech can be seen as an important reason of the increased respondent's number.

The number of respondents who began to take actions such as air conditioner temperature control, using light efficiently when in the room alone(such as use the desk light), using the stairs, PC efficiency setting, increased.

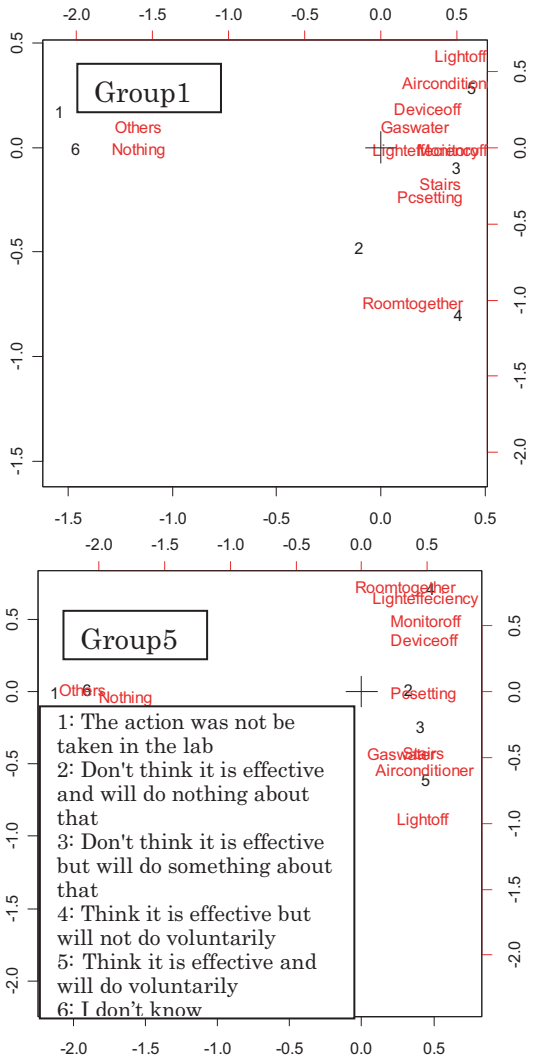

Fig.3 Results of correspondence analysis

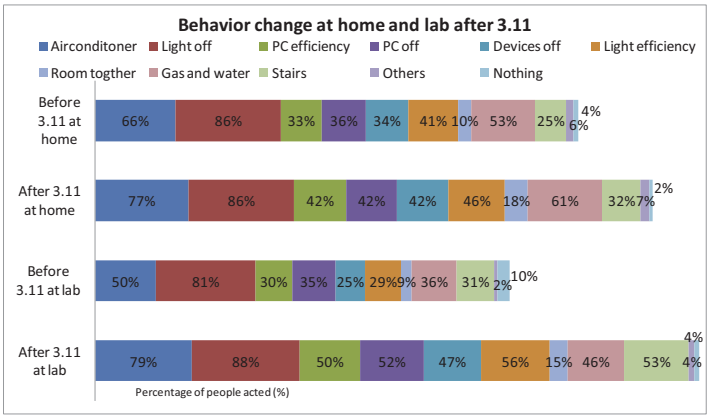

Fig. 4 Behavior change at home and lab after 3.11

About the factors which influence usage of electricity consumption information, the results of the logit model are shown below.

The factors that influence willingness of homepage electricity consumption information:

Dependent Variable: would like to use the information or not				
Independent Variables	coefficient	Std.Err.	Marginal effects	Std.Err.
Foreigh student who cannot speak Japanese	2.07**	0.67	0.48	0.13
Behavior changed after 3.11	1.00**	0.49	0.21	0.09
cons	−1.60**	0.43		

**Significant at 5% level

The factors that influence usage of electricity consumption information of visualization system:

Dependent Variable: using the visualization system or not				
Independent Variables	coefficient	Std.Err.	Marginal effects	Std.Err.
live alone	1.32**	0.58	0.29	0.11
cons	−0.04	0.28		

There is no significant variable that influence usage of electricity consumption information and willingness of visualization electricity consumption information.

Next, to see whether there is relationship between the electricity reduction pattern and information usage, correspondence analysis was conducted. Similarly with PCA, both variables of the horizontal axis and the vertical axis are for the scores of component. In Fig.5 and Fig.6, the component scores of the group and frequency or wishes of information usage are distributed in the same figure to see the relationship.

About information usage, the respondents in those groups which have large consumption reduction amount are always using the information and would like to use it.

5 Conclusions and Discussion

This study found the following points.

1: In smaller consumption building, respondents of the building also don't prefer to perform conservation actions.

2: An increase number of respondents who performed conservation actions were not only in laboratories (mandated by the university), but also at their houses (voluntarily.)

3: Foreign respondents, the respondents who have changed their behavior, and the respondents in the high consumption reduction group have been found to express willingness to use information system.

It is considered that respondents in Tokyo

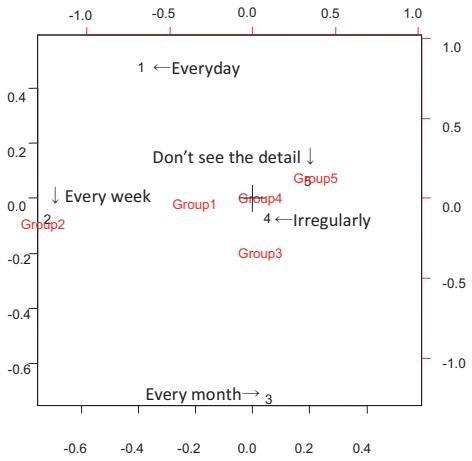

Fig.5 Homepage information usage

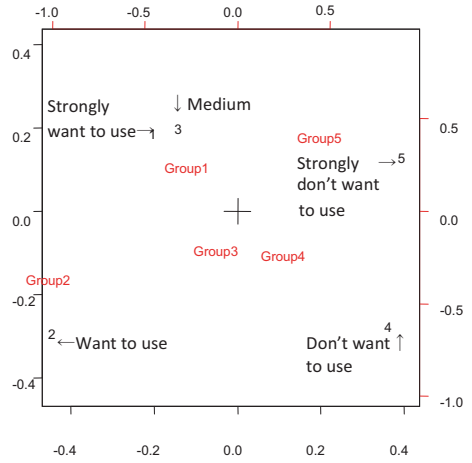

Fig.6 Wishes to use visualization information

Tech will change their perception and would like to do the energy conservation action when have incentive such as energy conservation measures. Providing the energy (electricity) information can be a way to provide the continuous incentive of energy reduction. As a science and engineering university, Tokyo Tech needs to consume a certain amount of electricity for experimental devices and various facilities so that it is crucial to investigate more where and for what we could conserve the electricity. There is potential to reduce electricity by people' voluntary action, without the sacrifice of doing research. And seeking the compatible way to reduce the electricity consumption is necessary.

References

[1] Katatani Noritaka: An Analysis of the Relationship between Household Electricity Consumption and Life-style, the Japan Institute of Energy (12), 456-457, 2003-07-30

[2] Maria Gleerup: The Effect of Feedback by Text Message (SMS) and Email on Household Electricity Consumption: Experimental Evidence, The Energy Journal, Vol.31, No3, 113-132, 2010

[3] Franois Husson: Exploratory Multivariate Analysis by Example Using R, CRC Press

OPTIMUM SPEED OF VESSELS CONSIDERING THE REDUCTION OF CO_2 EMISSION IN INTERNATIONAL MARITIME TRANSPORTATION

Student Number: 10M18252 Name: Jifang ZHANG Supervisor: Shinya HANAOKA

国際海運における環境を考慮した船舶の最適速度の推計

張　霽芳

本論文では、コンテナ船を対象として、船社の利益及び船舶からの CO_2 排出量の関係を考慮した最適航速を提案推計する。ケーススタディとして 3 航路を対象に計算した結果、5000TEU 以上の船舶では 18.5~19.5 ノット、それ以下の船舶では 13.2~18.3 ノットが最適航速という結果を得た。いずれも、現状より 13%~23%の減速が必要になる。また、航路の違いやサイズの違いが結果に与える影響を分析した。

1. Introduction

International maritime transportation response for 90% (ton-miles) of the world trade, while in 2007, emitted 3.3% of global CO2 emissions. Because the growth in the world seaborne trade, it is said that shipping's contribution to GHG emissions could reach 18% by 2050 [1].

In 2006, International Maritime Organization (IMO) made the frame work of a package of 3 measures to reduce emissions from shipping on global basis. Technical Measures including superstructure optimization, waste heat recovery, to make vessel themselves more environmental efficient. Operational Measures including weather-routing, speed management to make the voyages more efficient. Market based Measures including GHG Fund, EIS to encourage the GHG reduction by giving economic incentives.

IMO established a system of energy efficiency design indexing (EEDI) for new built vessels. In July 15th 2011, MEPC62 determined that all vessels built after January 1st 2013 need to satisfy the EEDI Index as an obligation. For operational measures, a template for a Ship Energy Efficiency Management Plan (SEEMP) allows companies to improve performance with regard to factors that may contribute to CO2 emission. But emitted CO2 during voyage would not be checked by any 3rd organizations. There is no regulation for the achievement of EEOI (Energy Efficiency Operational Index) at this moment.

Speed reduction considered as a mean to reduce fuel consumption and consequently reduce CO2 emissions. Generally, a 10% reduction in speed for all vessels would lead to a 19% reduction of emissions per ton-mile.[2] However, on the negative side speed reduction not only means longer delivery times, but also less reliable service schedules. During 2009, only 53% of vessels tracked on major East-West routes arrived on time, compared with 60% in 2008[2]. For carriers, speed reduction means a reduction in the number of miles traveled per year. In 2010 ton-mile per dwt was estimated to be declined 26% from 2008. [2]

Shipping companies insist that they reduce speed for CO2 emission reduction, while according to UNCTAD [2] speed reduction is only a consequence of overcapacity. From March 2007 to March 2009, around 240 new ships were being delivered, equivalent to a 10% increase in supply. While demand from containerized trade decreased by a similar amount. Speed reduction helped the carriers to reduce the need to lay off ships. When demand increase, shipping companies are possibly to resume higher speed to restore the vessel productivity.

Current speed reduction is burdened by many problems. It is necessary to define the optimum operational speed considering both the profit of shipping companies and the CO2 emissions.

IMO estimated the Marginal Abatement Cost (MAC) for 10% speed reduction of the world fleet in 2020, considered the cost as a sum of purchase new vessels and additional operational cost caused by new vessels. It was found that the cost would be 80~135$/ton CO2, and the world fleet have a 7.9% reduction potential to reduce 98.7 million tones. It was also mentioned that "The MAC curve adopts a social perspective. It doesn't represent the expenditures the ship operators would have to pay."

Currently, some research considered the optimal speed as the speed when profit of shipping company is maximized [3]. Some research considered optimal speed as the minimum cost speed, while considering the cost as a social cost [4].

2. Objective and Case Study

The objective of this research is to estimate the most reasonable speed for container vessels operated in specific routes, considering the relationship of profit of shipping company and CO2 emissions.

The effect caused by practicing the proposed speed, and the influence of vessel sizes and routes would also be discussed.

Three transportation routes have top seaborne trade amount were selected as case study routes. Shanghai to Los Angles represent Asia-North America routes, Shanghai to Rotterdam represent Asia-EU routes, and Shanghai to Singapore represent inside Asia routes. Container ships were selected as the case vessels, for their highest CO2 emissions in maritime transportation sector. In 2007, container ships transported 13% of the world freight while emitted 28.5% CO2 of the international maritime transportation sector.

3. Model Description

The model calculated the profit of shipping company, and emissions during voyages for individual ship classes as a function of speed. The model consists of 2 main equations, Eq (1) describes the profit as a difference between revenue and cost, when vessel k traveled from port i to port j. Eq (2) describes the emissions relative to fuel consumption when vessel k traveled from i to j.

Equation (1) Profit:

$P_{ijk} = P_t M$	(Revenue)
$-[MF_k(v_k/v_{kd})^3+AF_k](D_{ij}/v_k)]P_f$	(Cost of fuel consumption)
$-TC_{ijk}(T_{ijkb}+D_{ij}/24v_k)$	(Depreciation cost of the vessel)
$-MC_M/(T_{ijkb}+D_{ij}/24v_k)(C_{IR}/365)$	(Time cost of the freight)

Equation (2) Emission:

$\varepsilon = 3.17[MF_k(v_k/v_{kd})^3+AF_k](D_{ij}/24v_k)]$ (Relative to Fuel Consumption)

The model gave four assumptions. 1st, average freight rates remain generally constant. 2nd, load factor for global container vessels is around 70%. 3rd, coefficient 3.17 would be defined as fuel's carbon fraction 0.864 multiply a factor for converting carbon to CO2 (equal to 44/12). 4th, the depreciation of vessel and export value of freight remain constant. Parameters were described in Table 1.

Table1. Parameter Description

P_t: Freight Rate ($/TEU)	P_f: Fule Price ($/ton)
M: Average Transport amount (TEU Capacity*Load Factor%)	TC_{ijk}: Vessel Depreciation($/day)
MF_k, AF_k : Engine Fuel Consumption (g/h) =Engine Power (kw) *Fuel Consumption rate (g/kwh) *Load factor (%)	C_M: Export Value of Freight($/TEU)
	v_k: Operational speed (knot) v_{kd}: Design speed (knot)
D_{ij}: Distance between i and j (km) C_{IR}: Annual interest rate (%)	T_{ijkb}: Stopped time per voyage (day)
P_t: Freight Rate ($/TEU)	P_f: Fule Price($/ton)

4. Data Set

Data for container vessels operated in three target routes were used including vessel characteristic data and voyage data.

Table2. Data Description

Vessel Characteristic	Voyage
Engine Power (kw)	Distance (mile)
Engine Fuel Consumption (g/kwh)	Freight Rate ($/TEU)
Engine Load Factor (%)	Export Value ($/ton)
Designed Speed (knot)	Fuel Price ($/ton)
Vessel Depreciation ($/day)	Stopped time (day)
TEU Capacity(TEU)	Interest Rate (%)

According to IMO [1], main engine fuel consumption was set to be 175 to 195 g/kwh, and load factor was 67% or 65%. Auxiliary engine fuel consumption was set be 220 or 230g/kwh, and load factor was 60%.

Main engine power, Designed speed and TEU capacity for each vessel was bought from Lloyd's Marine Intelligence Unit, while stopped time per voyage was calculated from vessel movement data.

According to Japan Marine Center, Freight Rate P_t was set to be 2548$/TEU in LA route, 1718$/TEU in Rotterdam route, and 782$/TEU in Singapore route. Export value was set to be 5000$/ton, fuel price P_f was set to be 400$/ton and Interest rate was set to be 5%, Vessel Depreciation was set to be 10000$/day~30000$/day depending on vessel size [4]. Distance was referred from Google map, where LA route was 11632km, Rotterdam route was 21310km, Singapore route was 4141km.

5. Result and Discussion

5.1 Hypothesis Testing

5.1.1 Optimum Speed on Single and Annual Voyages

If set the annual transportation time T_a remain constant, the frequency would be $N=T_a/T_k$, where $T_k=T_{ijkb}+D/24v_k$. Annual profit and emissions could be calculated as Eq(1) and Eq(2) multiply N respectively.

According to IMO, the vessels are divided into 6 groups by size: Vessels larger than 8000TEU, between 5000and 7999TEU, 3000 to 4999TEU, 2000 to 2999TEU, 1000 to 1999TEU and vessels smaller than 999TEU.

Data of 90 vessels operated in Shanghai to LA route in 2010 was used to test this hypothesis. Results were described as follow. Figure 1 and 2 showed the relationship of speed and profit per trip, relationship of speed and annual profit, Figure 3 and 4 showed the relationship of speed and emissions per trip, speed and annual emissions.

Profit maximum speed and emission minimum speed were different by focusing on one voyage or annual voyages. This hypothesis only consist when the annual travel time remain constant, but in fact it is hard to predict the total travel time and this amount is also thought to change depend on transportation demand, thus the shipping companies would tend to optimize every voyage rather than annual voyages.

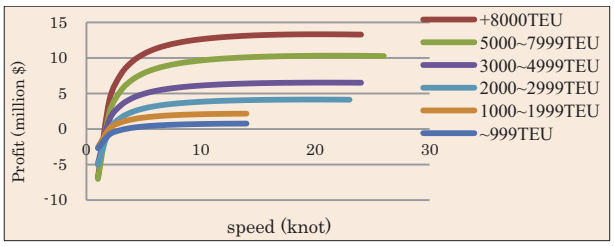

Figure1. Relationship of Speed and Profit per trip

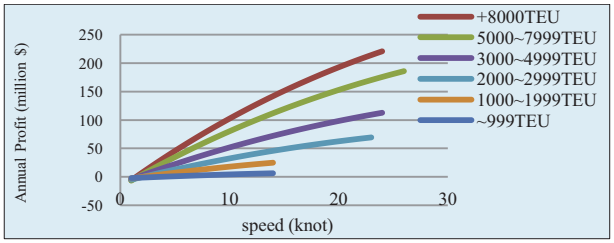

Figure2. Relationship of Speed and Annual Profit

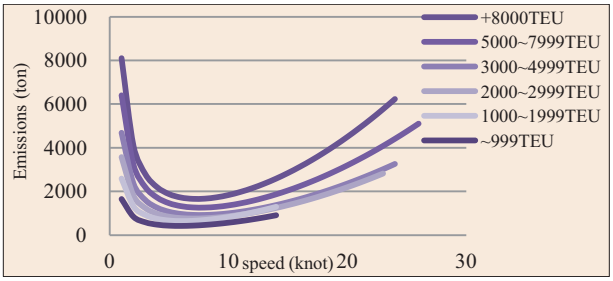

Figure3. Relationship of Speed and Emissions per trip

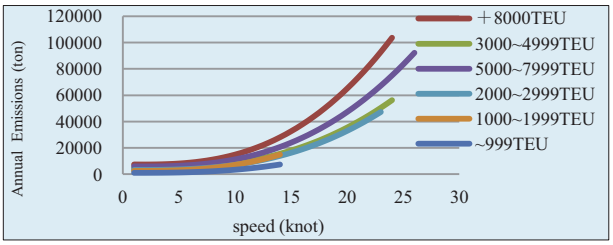

Figure4. Relationship of Speed and Annual Emissions

5.1.2 Speed of Profit Maximization and Emission Minimization

From Figure 1 and 3, it could be found that speed of maximum profits (V_{Pmax}) and speed of minimum emissions (V_{Emin}) are different in Shanghai to Los Angeles route. Similar results were obtained also in the other two routes. Table 3 shows the results of each route.

Table3. Max Profit Speed and Min Emission Speed(knot)

Shanghai to	Los Angeles **(LA)**		Rotterdam **(R)**		Singapore **(S)**	
TEU	V_{Pmax}	V_{Emin}	V_{Pmax}	V_{Emin}	V_{Pmax}	V_{Emin}
+8000	21	8	21	8	22	8
5~7999	21	8	21	7	21	8
3~4999	20	7			20	7
2~2999	18	7	21	7	20	7
1~1999	15.5	6	16.5	7	16.5	7
~999	13.5	6	14.5	6	15	6

It is thought to be hard to let the shipping company practice the minimum emission speed, because of the huge difference in profit. Take +8000TEU vessels in LA route as an example: under the speed of 21 knot, the profit was 13.3 million$, when the speed become 8 knot, the profit decline to 11.8 million$, which means a 1.5 million dollar loss in profit for shipping company.

It would be necessary to find the reasonable speed, which has less emission and small risk for the shipping company considering the relationship of profit and emissions.

5.2 Reasonable Speed Estimation

Objective functions to maximize profit Eq(3), and minimum emissions Eq(4) were defined, speed v_k was the variable.

Objective Functions :
Max (Profit)

$$P(v)= P_tM - [MF_k (v_k/v_{kd})^3+AF_k] (D_{ij}/v_k) P_f - TC_{ijk} (T_{ijkb}+ D_{ij}/24v_k) - MC_M (T_{ijkb}+ D_{ij}/24v_k) (C_{IR}/365) \quad (3)$$

Min (Emission)

$$E(v)=3.17 [MF_k(v_k/v_{kd})^3+AF_k](D_{ij}/v_k)] \quad (4)$$

Variable : Speed v

5.2.1 Smallest Profit Loss & Largest Emission Reduction

Speed v was the same variable for both profit and emission, the relationship of them could be found as Figure5.

The point with smallest change rate in profit and biggest change rate in emissions (**min (Δp/Δe)**) would be chosen as the most reasonable point in this part. The speed at that point would be defined as the most reasonable speed.

In the case of +8000TEU vessels in LA routes, relationship of Δp/Δe and speed was shown in Figure 6. The result was shown in Table 4. As Δp/Δe was biggest at Maximum Profit point, smallest at Minimum Emission point, the speed at Maximum Profit should be chosen as the most reasonable speed in this case.

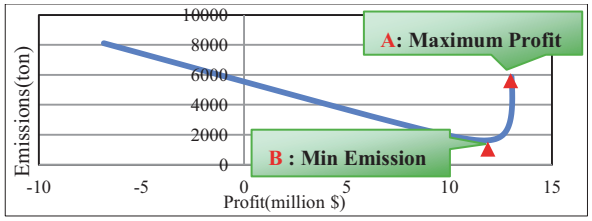

Figure5. Relationship of Emissions and Profit

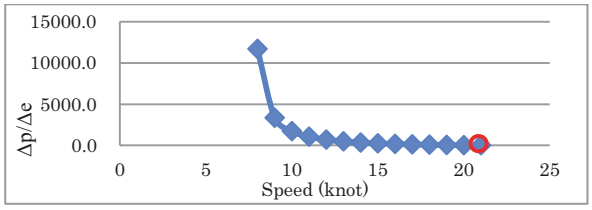

Figure6. Relationship of Δp/Δe and speed (speed ϵ V_{Pmax} ,V_{Emin})

Table4. Result of +8000TEU vessels (LA route)

	Speed (knot)	Profit (million $)	Emissions (ton)
✓1. Max Profit	21	13.06	4617.2
2.Min Emission	8	11.9	1626.3

This result implies that, if there is no regulation, even shipping companies consider the emission reduction, they will still choose the profit maximum speed. Same estimation was done with all vessels in the other 3 routes, similar results were obtained.

5.2.2 Monetize CO2 Emissions

Average CO2 trade price was around 22$ in 2010, in the case of Kyoto Credit. If monetize the emissions, by multiply the amount of emissions with CO2 price, relationship in Figure 7 could be obtained. Most reasonable speed was considered as some point between A and B in Figure 5 and 7.

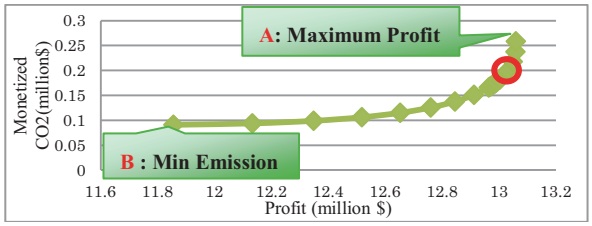

Figure7. Relationship of Monetized CO2 and Profit

Price of one ton CO2 reduction could control the scale of the vertical axis of Figure7, so the chose point would be different by changing CO2 price.

To choose any point x between A and B as the optimum point, it is considered to be necessary to satisfy the relationship in inequality (5), comparing with point A, saved cost for CO2 reduction must be larger than lost profit.

$$P_A - P_X \leq (E_A - E_x)* Eprice_X \quad \textbf{(5)}$$

In the case of +8000TEU vessels in LA routes, the chose speed and the CO2 price at that time was calculated as follow.

Table5. Result of +8000TEU vessels (LA route)

P&R Speed(knot)	Price of CO2 ($/ton)	P&R Speed(knot)	Price of CO2 ($/ton)
8	402.6	15	77.2
9	315.3	16	58.1
10	249.9	17	41.9
11	199.3	18	28.0
12	159.1	19	16.1
13	126.5	20	6.6
14	99.7		

If the price of CO2 was set to be 22$, the most reasonable speed would between 18~19knot, which was calculated to be 18.5knot.

This scenario considered the shipping companies need to pay an additional cost for CO2 emissions. The payment of this cost could be described as follow. At first, make the shipping companies to pay for the planned emissions amount, and then give back the paid amount to the companies operated under the proposed speed. Thus, it would become an incentive to the companies to achieve the proposed speed.

5.2.3 Results of Other Two Routes

Same estimation was done with all the vessels in target routes. Because most of vessels operated under service speed and some were under the 10% speed reduction, the comparison is shown in Table 6.

Table6. Comparison of Proposed Speed and Other Speed

TEU	Vservice (average)	$V_{-10\%}$ (average)	V profit Max(av)	$V_{P\&R}$ (LA)	$V_{P\&R}$ (R)	$V_{P\&R}$ (S)	Reduction from Vservice
+8000	24.6	22.1	21	18.5	19.5	19.3	-22.49%
5~7999	24.6	22.1	21	18.9	19.4	19.2	-21.89%
3~4999	23.3	21.0	20	17.5		18.3	-23.06%
2~2999	20.8	18.7	20	16.6	17.8	17.8	-16.33%
1~1999	17.0	15.3	16	14.3	14.9	14.5	-13.15%
~999	14.6	13.2	14	13.2	14.1	14.4	-5.07%

It could be found that, necessary percentage of speed reduction for most vessels were from 13% to 23% different by vessel sizes. 10% speed reduction was similar with profit maximum speed, which was not reasonable for all the world fleet.

5.3 Changes in Profit and Emissions under Proposed Speed

Table 7 shows the average change in profit and emissions. ΔE is the change in emissions under the proposed speed comparing with the profit maximum speed, which could be so called as reduction potential.

It could be found that with a small change in profit (-0.18% to -1.45%), a big reduction of emissions could be achieved (-10 to -17%). Shipping company should choose the proposed speed rather than 10% speed reduction or service speed.

Table7. Average change in Profit and Emissions

TEU	ΔP (%)	ΔE (%)	ΔP (million$)	ΔE (ton)
+8000	-0.18	-17.12	-0.015	725.6
5~7999	-0.21	-13.70	-0.013	527.2
3~4999	-0.23	-16.93	-0.011	315.1
2~2999	-0.45	-16.53	-0.009	378.4
1~1999	-0.81	-14.34	-0.006	199.1
~999	-1.45	-10.32	-0.005	97.3

5.4 Comparison of Three Routes

Changes in profit and emissions caused by practicing the proposed speed in three routes are shown in Figure 8 and 9.

If focus on vessels with same size, loss of profit (**ΔProfit**) in Singapore route was smallest, while in Rotterdam route was biggest. At the same time, emission reduction potential (**ΔEmission**) was smallest in Singapore route, and biggest in Rotterdam route.

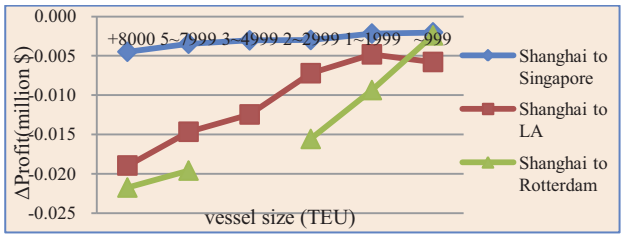

Figure8. Profit Loss (ΔP) in each route

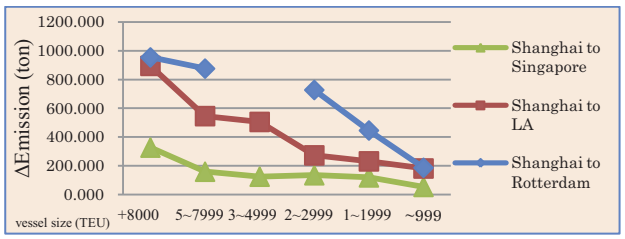

Figure9. Emission Reduction Potential in 3 Routes

Thus, in short-term vessels operated in Singapore route should work on speed reduction as soon as possible, while in long-term emission reduction in Rotterdam route should be addressed with.

Freight Rate, Stopped time, Distance were different by route, while distance was thought to be the factor influenced the result most. When speed reduced, route with longer distance would have more cost increase, consequently would be more sensitive.

5.5 Comparison of Vessel Sizes

5.5.1 Profit & Emissions per TEU Under Proposed Speed

Figure 10 and 11 show the profit and emissions per TEU under optimum speed. It could be found that bigger vessels are more profitable and have less emission per TEU.

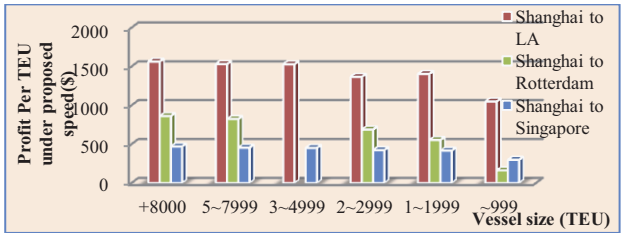

Figure10. Relationship of Size and Profit per TEU

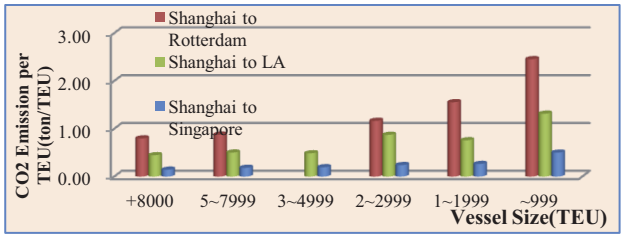

Figure11. Relationship of Size and Emission per TEU

5.5.2 Changes in Profit and Emissions per TEU

From Figure 12 &13, it could be found that smaller sizes tend to lose more profit, while have higher reduction potential at the same time.

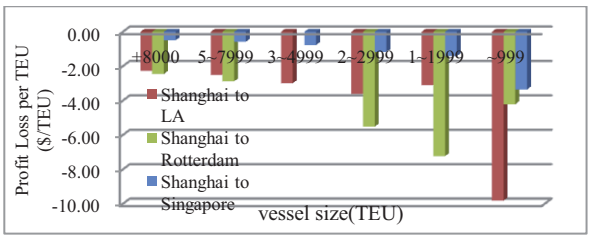

Figure12. Profit Loss per TEU (ΔP/TEU)

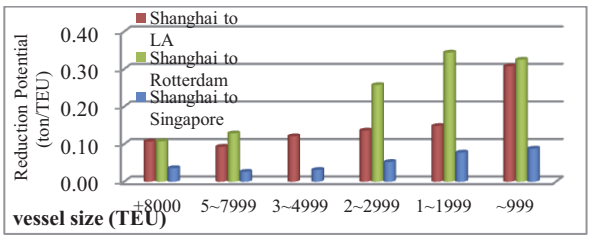

Figure13. Emission Reduction Potential per TEU (ΔE/TEU)

6. Conclusion

Speed that maximize profit and speed that minimize CO2 emissions were different. The relationship of profit and emissions could be found.

If consider the speed with smallest change rate in profit and biggest change rate in emissions (min (Δp/Δe)) as the most reasonable speed. Profit maximize speed would be selected.

If monetize CO2 emissions by multiplying the amount of emissions (ton) with the price of CO2 reduction ($/ton), some speed between max profit speed and minimum emissions speed could be selected. Comparing with profit maximum speed, saved emissions reduction cost must be larger than loss in profit by choosing this speed. Thus, this speed would be defined as the most reasonable speed in this research.

To let the shipping company operate with lower speed for less CO2 emission, CO2 price need to be kept higher. To make the shipping company practice the proposed speed, it would be necessary to combine the proposed speed with market based measure, which could give economic incentive to the companies.

Proposed reasonable speed was different by vessel size. Vessels larger than 5000 TEU were supposed to have optimum speed around 18.5~19.5knot, 2000~4999TEU around 16.6~18.3knot, vessels smaller than 2000TEU were 13.2~14.9knot..

Shanghai to Singapore route had least profit loss and least emission reduction potential under proposed speed, while Rotterdam route had both biggest. This imply that, in short-term vessels operated in Singapore route should work on speed reduction as soon as possible, while in long-term emission reduction in Rotterdam route should be addressed with.

Vessels with larger capacity were estimated to be more profitable and have less emission per TEU, while smaller vessels tend to lose more profit, but have higher reduction potential at the same time. It would be better to introduce new bigger vessels, while speed reduction for the current smaller vessels need to be started.

Reference

[1] International Maritime Organization (2009) "Second IMO GHG Study, 2009"

[2] UNCTAD SECRETARIAT (2011) "Review of Maritime transport 2010" United Nations Conference on Trade and Development Sales No. E.10.II.D.4

[3] James J.Corbett, HaifengWang (2009), "The effectiveness and costs of speed reductions on emissions from international shipping" "Transportation Research" Part D14, P593–598

[4] Haakon Lindstad (2011), "Reductions in greenhouse gas emissions and cost by shipping at lower speeds", Energy Policy 39, P3456–3464

Microwave-assisted Synthesis of Thalifendine

Student Number: 10M18269　Name: Dao Zhang
Supervisor: Prof. Sachio Hirose, Prof. Kiyohiko Nakasaki

マイクロ波加熱によるベルベリン誘導体タリフェンディンの生成

張　道

本研究では、ベルベリン誘導体タリフェンディンを生成するため、マイクロ波を用いてベルベリンからタリフェンディンの生成方法を検討し、反応温度、初期 pH、反応時間の反応への影響を明らかにする。オートクレーブによる加熱方法とマイクロ波による加熱方法とを比較する。次に、様々な添加剤を添加し、添加剤による反応への影響を明らかにした。Cu_20 を添加することにより、タリフェンディンを選択的に生成できることを明らかにした。

1. Introduction

Protoberberine alkaloids have various activities such as antimicrobial [1], anti-inflammatory [2], antimalarial [3], and anti-diabetic activities [4]. Among them, berberine (BER) has a long history of medicinal use in traditional medicine and it has been widely investigated. However, only few researches have been studied the activities of other protoberberines. Recently, it was reported that BER was metabolized to be protoberberines such as berberrubine (BBR), columbamine, dehydro-discretamine, demethylene-berberine (DMB), jatrorrhizine (JAT), and thalifendine (TLF), which were observed in human urine (Fig. 1) [5]. This evidence suggested that the pharmacological effect of BER could be derived from its metabolites. However, they are too complex for cost-effective chemical synthesis and the plants contain very small amount of protoberberines. Therefore, it is difficult to study the pharmacological effects of protoberberines.

Microwave energy has been widely used for heating food materials, and recently, there has been an increasing interest in using microwave as heat source for chemical synthesis. Microwave-assisted synthesis has been used for the synthesis of some chemical compounds, for example, for deacetylation [6], and for cross-coupling reaction [7]. In many cases, shorter reaction time and higher selectivity were observed comparing with conventional heating method. However, only an experiment for producing of DMB from BER was conducted using microwave at atmospheric pressure [8][9] and the characteristics of microwave-assisted synthesis are not fully understood. In addition, no method has been reported for the synthesis of TLF.

The purpose of this study is to synthesize TLF by using microwave. The effect of temperature, initial pH, radiation time, additives, and Comparison microwave synthesis with autoclave synthesis were investigated. In addition, the synthesis of other protoberberines those similar to TLF were also studied by using microwave.

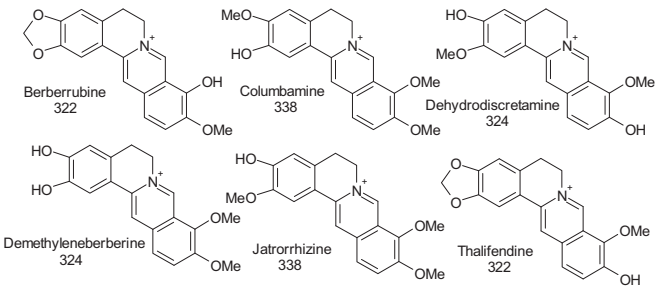

Fig.1 Metabolites of BER

2. Materials and Methods

2.1 Materials

All chemicals were purchased from Wako Pure Chemicals Co., Japan. Ultra pure water produced by the Milli-Q Advantage vessel (Millipore, USA) was used in this study.

2.2 Microwave-assisted synthesis

The microwave apparatus Mars-X (CEM, USA), as shown in Fig. 2, was used for microwave-assisted synthesis. It can be operated with an output power of up to 1600 W (2450 MHz). The temperature was measured using the fiber optic temperature probe RTP-300 Plus, and pressure was measured using the ESP-1500 Plus.

The microwave apparatus automatically adjusted the radiated power when the actual temperature reached the set temperature. The experiments were performed in a Teflon-made Green Chem vessel with a capacity of 100 mL, which could operate under a temperature of up to 180℃ and a pressure of up to 1.38 MPa (200 PSI). The initial output power was set at 300 W. A volume of 20 mL of BER solution (2 mmol / L) was put in the vessel and radiated by microwave. The reaction vessel was cooled down for 30 min before filtration.

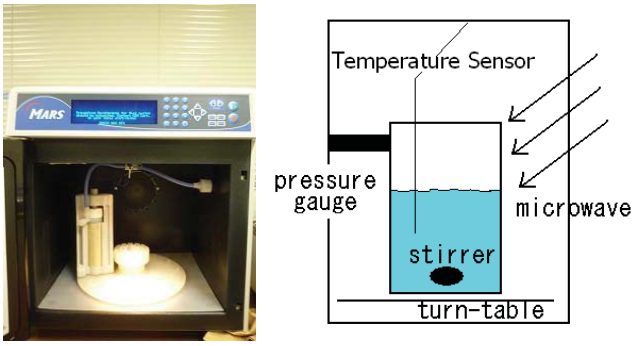

Fig. 2 Microwave apparatus

2.3 Autoclave synthesis

The autoclave used for autoclave synthesis was shown in Fig. 3. The temperature was measured using thermocouple and pressure was measured by pressure gauge. The autoclave automatically adjusted the output power when the actual temperature reached the set temperature. The output power was set at 100 V. A solution (20 mL) of 2 mmol/L berberine was used for the reaction. The reaction vessel was cooled down for 1 h before filtration.

2.4 Effect of initial pH

The initial pH of the solution was adjusted to 3-11 using sodium hydroxide and hydrochloric acid. The pH was measured by pH meter model F-55 (Horiba, Japan).

2.5 Effect of additives

Each additive (0.5g) was added into 20 mL of BER solution. After the reaction, the solution was filtered by No. 40 (Whatman, UK). The filtered additive was desorbed in methanol (20mL) for 24 h.

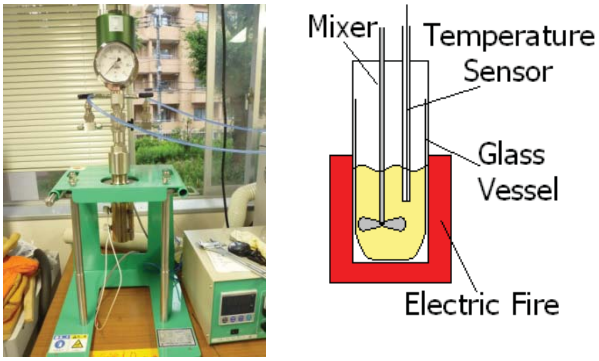

Fig. 3 Autoclave

2.6 Effect of weight of Cu_2O

The weight of Cu_2O was adjusted to 0.1-2.0g. All the sample was filtered through filter paper No.40. The filtrate was diluted 5 times in ultra pure water, and then filtered using a 0.45-μm membrane filter (Toyo Roshi Kaisha, Japan) for liquid chromatography mass spectrometry (LC/MS) analysis.

2.7 LC/MS analysis

The quantification of BBR, BER, DMB, and TLF was performed using LC/MS-2010EV apparatus (Shimadzu, Japan). The separation was carried out in a ZORBAX Eclipse XDB column (3.5 μm, 2.1 × 150mm) (Agilent Technology, USA). The mobile phase, which consisted of a 0.1% formic acid aqueous solution (A) and methanol (B), was delivered at a flow rate of 0.2 mL/min using the following gradient program: 25% (B) for 0–15 min, 25–30% (B) for 15–32 min, 30-70% (B) for 32–47 min 70% (B) for 47–52 min, and 25% (B) for 52–60 min. The sample injection volume was 1 μL, and the column temperature was maintained at 40°C. The UV spectra were obtained by scanning the samples in the range of 200–470 nm. The amounts of BBR, BER, DMB, and TLF were calculated from the peak area at 345 nm.

3. Results and discussion

3.1 LC/MS analysis

Fig. 4 shows HPLC at 345 nm of the BER solution after radiated by microwave for 30 min. DMB , TLF , BBR , and BER were observed at retention time of 14.5 min, 21.4 min, 29.3 min, and 29.9 min, respectively. The compounds were determined by its retention time, mass to charge radio (*m/z*) and comparing with literature.

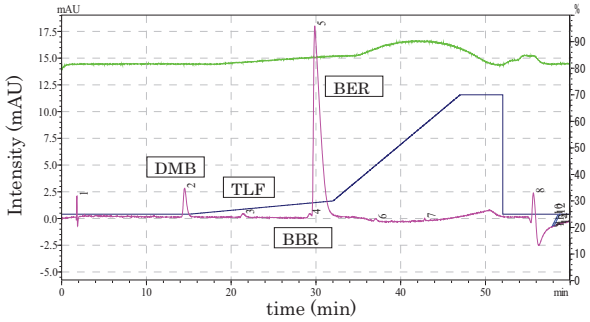

Fig. 4 HPLC at 345 nm

3.2 Effect of reaction time

Fig.5 shows the mechanism of temperature rise for microwave and autoclave. Microwave heated BER solution to 180℃ in 5 min. On the other hand, it took 30 min for the experiment by autoclave. So it's easily to control the temperature with the method of microwave than autoclave. Fig. 6 and Fig. 7 show the effect of reaction time by microwave and autoclave. The peak area of protoberberines increased with an increase in the reaction time. Microwave-assisted synthesis gave faster reaction than that of autoclave. But TLF couldn't be produded in large quantities.

3.3 Effect of temperature

Fig. 8 shows the peak area of protoberberines by microwave-assisted synthesis. TLF was not observed at the temperature up to 140℃. The TLF yield increased with an increase in the temperature above 150℃. The highest TLF yield was obtained at 180 degree centigrade.The reaction was performed at the temperature up to 180℃ because the limit thermal-resistance of microwave vessel is up to200 ℃.

3.4 Effect of initial pH

Fig. 9 shows the effect of initial pH. A larger amount of TLF was obtained in pH range from 6 to 8. DMB was produced when the experiment conducted in the initial pH from 3 to 8, but DMB peak area was the highest around the initial pH 6-7. However, DMB peak area was decreased at pH 9 and was not observed at pH 11. On the other hand, BBR was generated at pH 11 as a major production compound.

3.5 Effect of additives

The additive material such as cellulose and Iron oxide could absorbed microwave and increased the surface temperature. Thus, they can enhance the protoberberines. Fig. 10 and Fig. 11 show the effect of degradation of BER and increase the amount of other additives by microwave and autoclave. In microwave radiation, Cellulose gave higher yield of DMB compared to experiment without the additive. Fe and

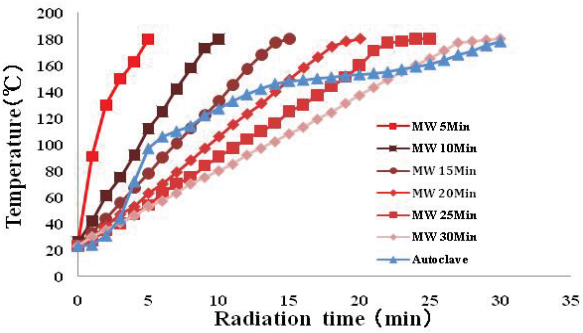

Fig. 5 the mechanism of temperature

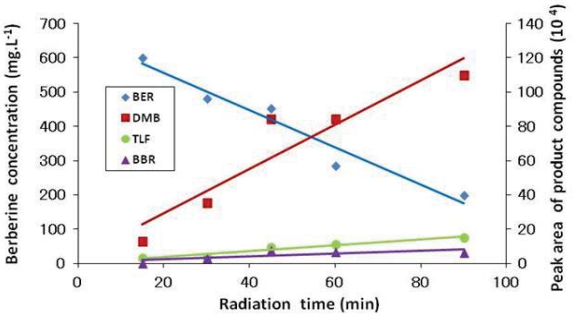

Fig. 6 Effect of reaction time (MW)

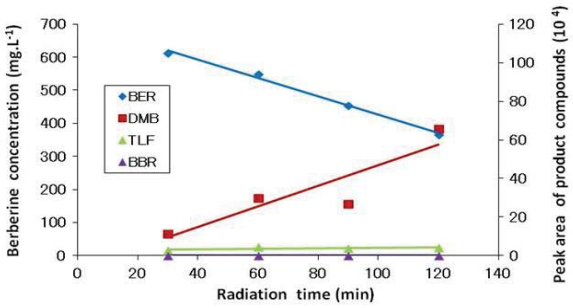

Fig. 7 Effect of reaction time (Autoclave)

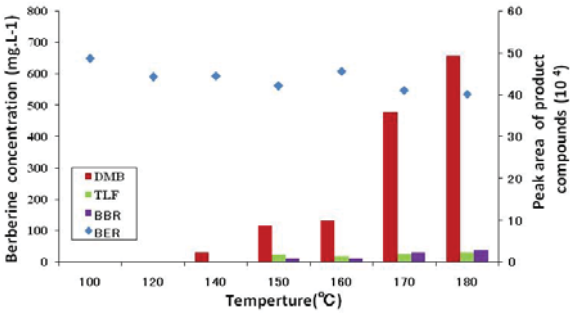

Fig. 8 Effect of temperature

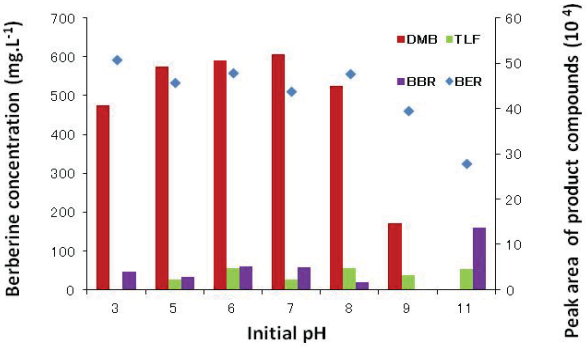

Fig. 9 Effect of initial pH

Co_3O_4 produced BBR as main product. SiC, Al, and Fe_3O_4 gave low yield of DMB. On the other hand, DMB was not observed when using CuO, CuI, Fe_3O_4, and Co. TLF was produced when using Cu_2O and CoO as the additives. From this result, only some additives increased protoberberines. The other characteristic of the additives rather than microwave absorbing ability could cause the difference in the amount and molecular structure of protoberberines.

In most experiment using the additives, microwave-assisted synthesis gave higher yields of protoberberines compared to those of autoclave synthesis. However, SiC, Al, and CuI gave lower yields of DMB.

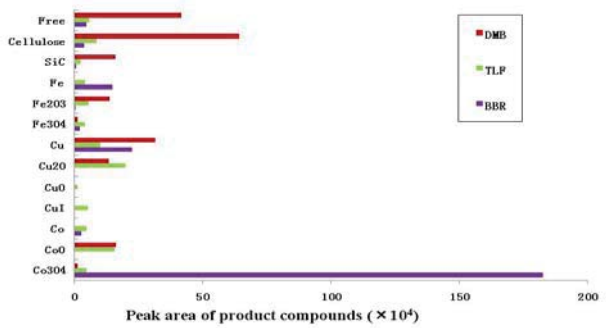

Fig. 10 Effect of additive (MW)

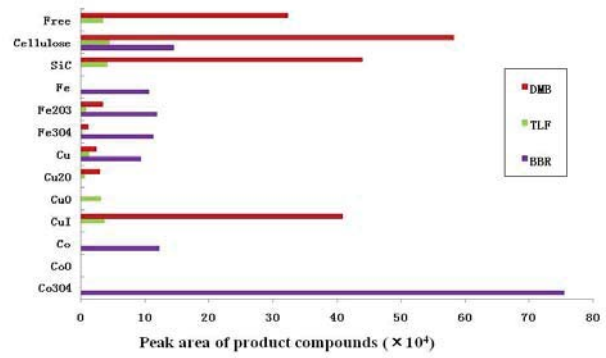

Fig. 11 Effect of additive (Autoclave)

Fig.12 shows a Comparison between the result of the effect of additives by microwave with the effect of initial pH, It was found that the effect of additives have larger influence than the effect of initial pH.

3.6 Effect of weight of Cu_2O

TLF was produced when using Cu_2O as the additives. Fig. 13 shows the effect of amount of Cu_2O on the degradation of BER and peak area of protoberberines. As the amount of Cu_2O increased to 0.8g, peak area of TLF was increased, while the peak area of DMB and BBR were decreased. In addition, the peak area of TLF by using 0.9 g Cu_2O was decreased compared to 0.6g.

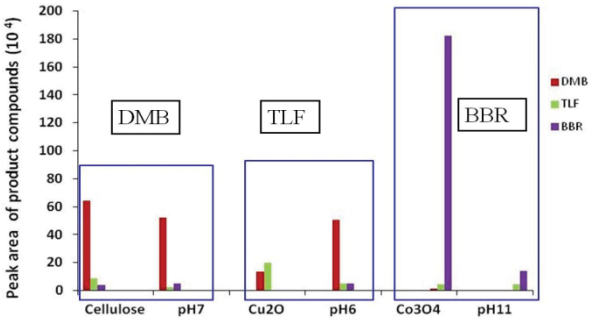

Fig. 12 Comparison additives and initial pH

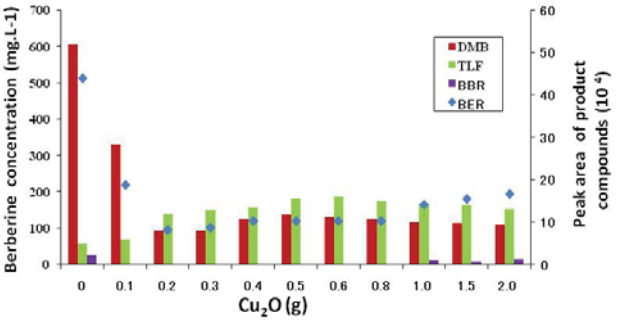

Fig. 13 Effect of Cu_2O weight (MW)

4. Conclusion

This study shows that it is possible to use microwave as a heat source for synthesis of TLF. The higher yield was obtained by using Cu_2O more than 0.2g at 180 ℃. Microwave-assisted synthesis gave fast and precise reaction for production of protoberberines than that of autoclave. Using additive Cellulose DMB was synthesized from BER with microwave radiation. BBR was produced selectively when using Co_3O_4 as the additive.

Reference

[1] Iwasa, et al..,J. Nat. Prod., 61, 1150-1153 (1998)
[2] Kuo, et al.,Cancer Lett., 203, 127-137 (2004)
[3] Iwasa, et al., Eur. J. Med. Chem., 34, 1077-1083 (1999)
[4] Ko, et al., Biol.Pharm. Bull., 28, 1431-1437 (2005)
[5] Feng, et al.: DMD., 36, 2159-2165 (2008)
[6] Varma, R. S. et al., J. Chem. Soc. Perkin. Trans. 1, 999 (1993)
[7]Kabalka. G. W, et al., Tetrahedron Lett., 41, 5151 (2000)
[8]Das, B. et al., Synth. Commun., 32, 19, 3027-3029 (2002)
[9]Zhang, D. Microwave-Assisted Synthesis of Demethyleneberberine. Bachelor Thesis (2010)

STUDY ON RELATIONSHIP BETWEEN ROAD TRANSPORT INFRASTRUCTURE AND REGIONAL ECONOMIC DEVELOPMENT IN CHINA

Student Number: 10M18275 Name: Tianxing BA Supervisor: Shinya HANAOKA

中国における道路整備と地域経済発展の関係

巴　天星

本研究は、中国における道路整備と地域経済発展の関係の分析を目的とする。1995 年から 2009 年までの期間を対象に、地域間の相互関係を考慮した上で、自地域内の道路整備と地域間道路の整備が地域経済の成長に与える影響について検証した。その結果、地域間道路が経済力に差がある隣接地域の GDP 成長に対し、ストロー効果あるいは分散効果をもたらすことを明らかにした。

1. Introduction:

There is one proverb in China – '要想富先修路' that means "if you want a country to be rich, build more roads there first." . The proverb gives us an idea that roads, as one of the major transport infrastructures, are indeed vital for a nation's economic growth, social development and security.

Since 1978, China has increasingly become aware of the benefits and the importance of road constructions. Its total length of roads increased from 890,200 km in 1978 to 3,683,600 km in 2008. In 2005, China's road investment ranked the first in the world. Recently, as the road infrastructures in China is developing rapidly, it is vital to conduct studies on relationship between road infrastructure and economic development in China.

While a number of studies on the topic have been done, studies using econometric model analysis are not enough. Here are three unsolved questions:

First, the previous studies generally focus on a certain type of road infrastructure such as highways, national roads. There is no comparison on the impacts of inter-regional roads and intra-regional roads.

Second, most of the literatures analyzed the relationship between road infrastructures economic development on the assumption that the regional economy is a closed. However, with the expansion of economic activities, the interdependent relationship among regions has been strengthened. Spillover Effect or Straw Effect of Inter-regional road infrastructures on economic growth may differ across regions.

Third, most studies have ignored that the impacts of road infrastructures on economic growth may differ in different periods.

Finally, most studies used nominal GDP to analyze the impact of road infrastructure. However, Real GDP and Nominal GDP are very different in China.

This study attempts to fill the gaps above. And it aims to analyze the relationship between road transportation infrastructure and regional economic development in China by econometric model analysis.

The specific objectives of this study:

1) Analyze the difference between inter-regional roads impacts and intra-regional roads impacts.

2) Verify whether the road infrastructures will bring spillover impacts on real GDP growth rate to several regions to make a difference in economy.

3) Compare the influences of road infrastructure on economic development in different periods.

The framework of this study is shown in figure 1.

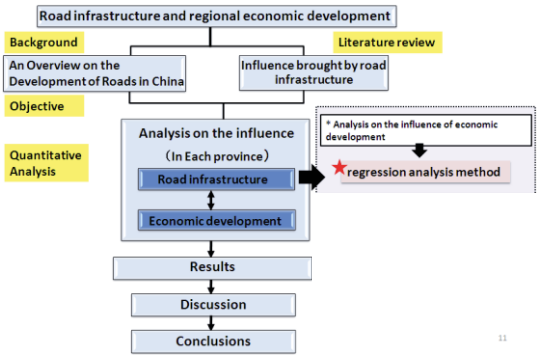

Figure 1: Study Framework

2. Research Methodology

2.1 Selection of Study Target

This study focuses on the inter-regional roads and intra-regional roads from 1995~2009 in 30 Chinese provinces. According to 'the orientation of Roads in China', (Ma, 2004), highways in China are defined as the inter-regional roads, and general national roads, provincial roads, prefectural roads and township roads are defined as the intra-regional roads.

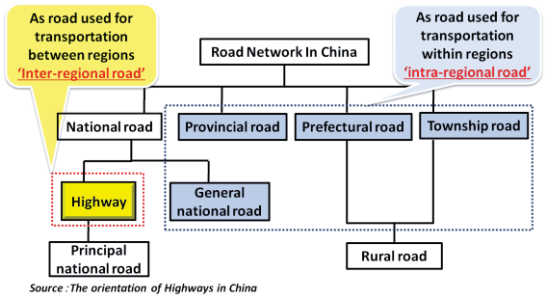

Figure 2: Inter-regional roads and intra-regional roads

2.2 Selection of Methodology

2.2.1 Barro Regression (Barro, 1991)

In Barro Regression, the region's rate of GDP per capita growth during a certain time period is regressed on an initial condition for GDP per capita and other potential output growth determinants. Barro Regression can verify which factors affect economic development.

Barro Regression also has been applied widely in analyses of convergence hypothesis. It can verify whether economic growth tend to convergence. In this model, the effect of road

infrastructure is reflected by GDP growth, and the quantitative distribution of roads corresponds to social and economic development can be calculated.

2.2.2 Estimating equation

In order to analyze the impacts of inter-regional roads and intra-regional roads on GDP growth rate in China, this study refers to the literature from Nakasato (2001). The equations are shown in Eq.(2.1).

$$\frac{1}{T}\left(\ln\left(y_{i,t+T}\right)-\ln\left(y_{it}\right)\right)=\alpha+\beta\ln\left(y_{it}\right)+\gamma DINFRA_{it}+\theta IINFRA_{it}\times\left(\ln\left(y_{it}\right)-\ln\left(y_{it}^{*}\right)\right)\times D_1 + \phi IINFRA_{it}\times\left(\ln\left(y_{it}^{*}\right)-\ln\left(y_{it}\right)\right)\times D_2+\varepsilon_{it} \quad (2.1)$$

Where, if $\ln(y_{it}) > \ln(y_{it}^*)$: $D_1=1$; otherwise: $D_1=0$;
.if $\ln(y_{it}) < \ln(y_{it}^*)$: $D_2=1$; otherwise: $D_2=0$;

Table 1 has explanations for the variables in the estimating equation.

Table 1: Explanations of variables

Dependent Variable	$\frac{1}{T}\left(\ln\left(y_{i,t+T}\right)-\ln\left(y_{it}\right)\right)$
Independent Variables	**Parameters**
Constant	Alpha
$\ln(y_{it})$	Beta
$DINFRA_{it}$	Gamma
$IINFRA_{it}$ $(\ln(y_{it}) > \ln(y_{it}^*))$	Theta
$IINFRA_{it}$ $(\ln(y_{it}) < \ln(y_{it}^*))$	Fai

Table 2 shows the definitions of major independent variables in Eq.(2.1).

Table 2: Definitions of major variables

Variables	**Definition**
y_{it}	Real GDP per capita of i Province in t time point;
$DINFRA_{it}$	Increase in intra-regional road density;
$IINFRA_{it}$	Increase in inter-regional road density;
y_{it}^*	Average of real GDP per capita of the surrounding provinces (the provinces next to i province) in t time point;

The inter-regional roads impacts depend on the economic gap between one region and other regions next to it with road infrastructure connections. In this estimating equation, cross terms are used '$\phi IINFRA_{it}\times\left(\ln\left(y_{it}^{*}\right)-\ln\left(y_{it}\right)\right)$', '$\theta IINFRA_{it}\times\left(\ln\left(y_{it}\right)-\ln\left(y_{it}^{*}\right)\right)$' as independent variables.

In China, road infrastructure constructed depending on traffic demand. The average traffic volume of national road is 20000 vehicles / day. There is serious traffic congestion in two-thirds cities of China with automobiles increasing. The utilization of road is relatively high, so this study refers to Nakasato (2001), using road density data as index of road infrastructure to analyze the impacts of road infrastructure in basic analysis.

2.3 Interpretation of parameters' sign

Table 3 shows the interpretation of each parameter's sign in Eq.(2.1).

Table 3: Interpretation of each parameter's sign

Parameters	**sign**	**Effects**
Beta	+	Divergence;
	-	Convergence;
Gamma	+	Positive effects;
	-	Negative effects;
Theta	+	Straw effects ;
	-	Spillover effect ;
Fai	+	Spillover effect;
	-	Straw effects;

Refer to Barro(1991) and Nakasato(2001) :

- Convergence:

It implies that poor regions (with lower GDP per capita) tend to grow faster than rich regions.

- Divergence:

It implies that rich regions (with higher GDP per capita) tend to grow faster than poor regions.

- Straw Effect:

As road construction is developing, more people and factories of the slow-growing regions will move to the fast-growing regions which more logistic centers, factories and technical economic zones have settle in.

- Spillover Effect

As road construction is developing, more people and factories of fast-growing regions will move to slow-growing regions depending on the expansion of trade area and the dispersion of economic activities.

Figure 3 shows the generalization of Straw Effect and Spillover Effect.

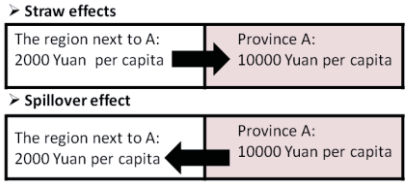

Figure 3: Straw Effect and Spillover Effect

2.4 Analysis step

Figure 4 shows the analysis steps of this study.

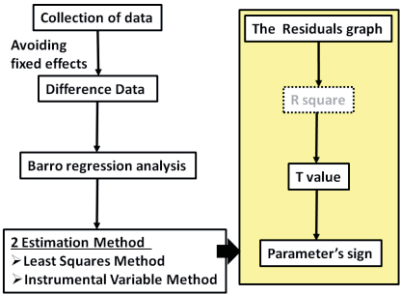

Figure 4: Analysis steps of this study

In this study, there are 2 estimation methods: Least Squares Method and Instrumental Variable Method. Figure 5 shows the image of 2 estimation method.

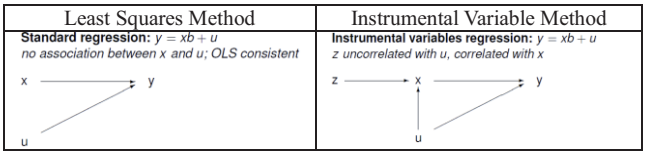

Figure 5: Images of 2 estimation method

In econometric model analysis, if we only verify whether the parameters are significant, comparing with T value, R square is not very important.

3. Results and Discussion

3.1 Results

Base on the three points of 'Possibility of Data Collection', 'Sufficiency of Study Analysis' and 'Difference of influences', this study analyze the impacts of road infrastructures in China.

The table 4 is the summary of basic analysis. In basic

analysis, this study refers to Nakasato (2001), using panel data (T=5) as input-data and road density data as index of road infrastructure to analyze the impacts of road infrastructure all over China by Least Squares Method.

Table 4: Summary of basic analysis

	Data	Data of road infrastructure	Parameters	Data sections	Method
A1	Panel data (T=5) 30 samples	Road density	Basic equation	All of the provinces (Except Hainan province)	Least Squares Method

The basic analysis indicates that most T-values are low. Therefore, from Discussion 1 to Discussion 5, this study changed the data, parameters and study sections over again to analyze the impacts of road infrastructure on GDP growth rate by Least Square Method.

Table 5 is the summary of Discussion 1 to Discussion 5 by Least Square Method.

Table 5: Summary of Least Square Method

	Data	Data of road infrastructure	Parameter	Data sections	Method
D1	Panel data (T=5) 30 samples	Road length	Basic equation	All of the provinces (Except Hainan province)	least squares method
D2		D2-1 Road density	Basic equation + stock		
		D2-2 Road length			
D3	Panel data (T=5) 23 samples	D3-1 Road density	Basic equation	Omitting 4 municipalities and 3 provinces in west.	
		D3-2 Road length			
		D3-3 Road density	Basic equation + stock		
		D3-4 Road length			
D4	Panel data (T=5)	New Barro regression refer to LIN (2010)			
D5	Panel data (T=1) 150 samples (each period) 420 samples (all periods)	Road density	Basic equation	All of the provinces (Except Hainan province)	

Discussion 1 to Discussion 5 indicate that most T-value are still low in any applied Least Squares Methods (Table 6). There are probably some endogeneity problems. In general, when estimating the impacts of road infrastructure on economic growth by Least-Squares Method, it should be noted that there is a potential for estimate bias. Also, there are Endogeneity problems caused by reverse causality.

Table 6: Results of Least Squares Method

Barro Regression	Least Squares Method			
	1995-2000	2000-2005	2005-2009	1995-2009
Alpha t-value	0.015 (0.358)	-0..039 (-0.874)	0.288*** (3.809)	-0.033 (-1.182)
Beta t-value	0.008 (1.537)	0.017*** (3.473)	-0.018** (-2.258)	0.015*** (4.868)
Gamma t-value	-0.025 (-0.565)	-0.003 (-0.159)	0.049 (1.193)	0.025 (1.390)
Theta t-value	-0.694 (-0.263)	-1.027 (-0.963)	-0.066 (-0.508)	-1.280 (-1.156)
Fai t-value	5.512 (1.049)	21.479** (2.586)	0.101 (0.923)	18.727*** (2.976)
Adjusted R square	0.026	0.086	0.064	0.087

Instrumental Variable Methods allow consistent estimation when the explanatory variables (covariates) are correlated with the error terms of a regression relationship. Such correlation may occur when the dependent variable causes at least one of the covariates ("reverse" causation). Therefore, it is essential to use Instrumental Variables Method for analyzing the impacts of road infrastructure on GDP growth rate in China. Table 7 shows the Instrumental Variables.

Table 7: Instrumental Variables

Instrumental Variables
Total population in initial period;
The ratio of employee population over total population in initial period;
Area ;
GDP per capita of the provinces next to the study province in initial period;
GDP per capita of study province in initial period
Road length in initial period;

Table 8 is Summary of Discussion 6 and Discussion 7 by Instrumental Variable Method.

Table 8: Summary of Instrumental Variable Method

	Data	Data of road infrastructure	Parameter	Data sections	Method
D6	Panel data (T=1) 150 samples (each period) 420 samples (all periods)	D6-1 Road density	Basic equation	All of the provinces (Except Hainan province)	Instrumental Variables Method
		D6-2 Road length			
D7	Panel data (T=1) 115 samples (each period) 322 samples (all periods)	D7-1 Road density	Basic equation	Omitting 4 municipalities and 3 provinces in west. .	
		D7-2 Road length			

Comparing the results from basic analysis to Discussion 7, some T-value of Discussion 6-1 are relatively significant.

Table 9 shows the results of Discussion 6-1.

Table 9: Results of Discussion 6-1

Barro Regression	Instrumental Variables Method			
	1995-2000	2000-2005	2005-2009	1995-2009
Alpha t-value	-0.294 (-0.621)	-0.739 (-1.169)	0.430*** (2.922)	0.212** (2.398)
Beta t-value	0.046 (0.787)	0.010 (1.337)	-0.034** (-2.163)	0.041)*** (2.842
Gamma t-value	-1.074 (-0.798)	-0.482 (-0.896)	0.103* (1.701)	-0.371 (-1.436)
Theta t-value	-12.283 (-0.282)	-21.097 (-1.420)	13.745 (1.368)	-42.769** (-2.349)
Fai t-value	96.330 (0.946)	123.469 (1.177)	0.029 (0.002)	14.478** (2.357)
Adjusted R square	0.096	0.162	0.070	0.039

1) *, **, *** indicate that it is statistically significant at 10%, 5%, 1% level.
2) The values in ( ) represent the T-values of each parameter.

3.1.1 Intra-regional Roads

In the 2005~2009 period, the parameter of intra-regional roads is significantly positive at 10% level. In China, 2005~2009 are the years in which road infrastructure grew rapidly. The average growth rate of intra-regional road length at that time is 22%. There are relatively sufficient construction comparing with the 1995~2000 period and the 2000~2005 period, so the intra-regional road impact on GDP growth in the 2005~2009 period is relatively obvious.

However, in other periods, the parameters of intra-regional roads are almost insignificant. One reason is that the road infrastructure construction of the 1995~2000 period and the 2000~2005 period are relatively insufficient. Another reason is that the growth rate of road length is slower than the real GDP growth rate.

Overall, in the 1995~2009 entire period, the intra-regional

roads did not have significant effects on GDP growth.

3.1.2 Inter-regional Roads

Comparing the 1995~2000, 2000~2005, and 2005~2009 periods, the inter-regional roads bring significant effects on GDP growth in the 1995~2009 period. It means the longer the opening of the inter-regional roads, the greater the effects on GDP growth rate in regions.

In the 1995~2009 period, the parameter of inter-regional roads in the regions with higher GDP per capita than the surrounding regions is significantly negative at 5% level. And the parameter of inter-regional roads in the regions with lower GDP per capita than the surrounding regions is significantly positive at 5% level.

Thus, based on the above results, in the 1995~2009 period, the inter-regional roads brought Spillover Effect on regional economic development and reduced economic disparities between regions through spillover effects. As road construction develops, more people and factories of fast-growing regions will move to slow-growing regions depending on the expansion of trade area and the dispersion of economic activities.

3.1.3 GDP per capita in initial Period

In the 2005~2009 period, the parameter of real GDP per capita in initial Period is significantly negative at 5% level, so according to the neo-classical growth theory, the development of economic growth tends to Convergence.

However, in the 1995~2009 entire period, the parameter of real GDP per capita in initial Period is significantly positive at 1% level, so according to the neo-classical growth theory, the development of economic growth tends to Divergence.

3.2 Discussion

3.2.1 Effect of Road Type

The significant economical influences brought by inter-regional roads and intra-regional roads in China are different in this study.

Today, with the expansion of economic activities, the interdependent relationship among regions has been strengthened. Under such a situation, in the 1995~2009 entire period, the inter-regional road impacts are greater than intra-regional road impacts. The economic effect of inter-regional roads in China is differed from region to region as a result of the Spillover Effect or the dispersion of economic activities.

3.2.2 Estimation Method

Referring to Barro econometric model analysis, this study aims to analyze the impacts of road infrastructures by using least-squares method and instrumental variables method.

Compare with the least squares method, T-value of instrumental variables method are relatively better.

In general, when estimating the impact of road infrastructure on economic growth by using least-squares method, there is a probability of bias estimation. There are also some endogeneity problems that occurred due to reverse causality.

As the interdependent relationship among regions has been strengthened, it is very likely that the development of road infrastructure will develop if the regional economic grows.

1).In regions with many opportunities for economic growth, the demand for road construction could increase to support the expansion of companies.

2).In some richer areas, their economy develops faster. Accordingly, the local governments have more funds for road constructions. There are more roads being built in those areas.

Therefore, a country in which road construction and economic development have reverse-causality, it is essential to use Instrumental Variables Method for analyzing in China.

3.2.3 Reasons for the less prominent promotion of road constructions

Except for the years of 2005 to 2009, the increase of road constructions in China has been smaller than the growth of GDP. To some degree, the road constructions did not meet the needs of the economic development during those years.

Figure 6 shows growth rate of real GDP PC and road length.

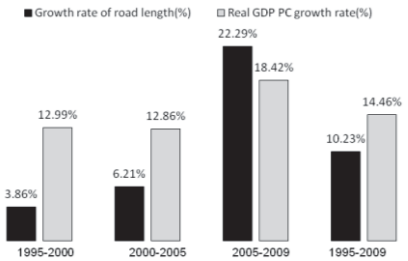

Figure 6: Growth rate of real GDP PC and road length

3.2.4 Comparison of road construction between China and other countries

Recently, the road constructions in China have been increasing rapidly. However, there is still a long way to go to be sufficient infrastructure with developed countries like Japan and UK, especially on road density. For example, average ratio of territory unit area to highway length of China in 2007 is equivalent to that of Japan in 1977 (Table 10). Thus road constructions in China require much more attention and promotion.

Table 10: The ratio of territory unit area to highway length

($km/1000km^2$)	China	Japan
Average ratio of territory unit area to highway length.	5.63 (2007)	5.81 (1977)

4. Conclusions

The significant economical influences brought by inter-regional roads and intra-regional roads in China are extensively discussed in this study. Only in the years of 2005 to 2009, the intra-regional roads brought significantly positive effects to GDP growth. In 1995~2009 period, the inter-regional road brought significant effects to GDP growth.

In China, it means the longer the opening of the inter-regional roads, the greater the effects on GDP growth rate in regions.

This study also estimates the impacts of inter-regional roads on regional economies by considering the interdependent relationship among regions. In the 1995~2009 entire period, the inter-regional roads brought Spillover Effect on regional economic development and reduced economic disparities between regions through spillover effects.

As the “five columns and seven lines” highway construction program progresses, it is expected that those road infrastructure would accelerate regional economies in China.

References

1.Barro (1991): Economic Growth in Cross Section of Countries, quarterly journal of Economics 106,P407-443

2.Nakasato(2001): Transport infrastructure and economic development, No43,P101-114

3.Abhijit Banerjee, Esther Duflo (2009):On the Road: Access to Transportation Infrastructure and Economic Growth in China

4. Jeffrey P(2010):The broad effects of transportation infrastructure: Spatial econometrics and productivity approaches, Transportation Research Part E 46, P317-326

DIRECTIONAL CHARACTERISTICS OF THE RADIO WAVE PROPAGATION THROUGH FOLIAGE

Student Number: 10M18306 Name: Le Vu Hung Supervisor: Jun-ichi TAKADA

樹木における電波伝搬の空間特性

レ ヴ フン

本研究は村落における移動通信サービスを主な対象とし，樹木による電磁波の散乱の角度広がりに関する実験的な検討を行う．広帯域チャネルサウンダによる信号を測定した．SAGE(Space Alternating Generalized Expectation)の超分解能到来方向推定アルゴリズムを適用した空間チャネル特性について検討を行った．結果はアジマスには水平偏波の角度広がりが垂直偏波の角度広がりより大きいが，逆にエレベションに対しては水平偏波の角度広がりが垂直偏波の角度広がりより小さいということが分かった．平均アジマス広がりが 25° で平均エレベションが 6° である．また，基地局の高さと角度広がりの関係は全く明らかにされていない．

1 Introduction

In recent years, the research of the radio propagation mechanism in the urban environment has been studied extensively. On the other hand, only a small amount of research on environments with low population density and large amounts of vegetation and foliage are present. Presence of foliage in propagation path plays a significant role in the propagation of radio waves. In many studies in the field of radio wave propagation through foliage, there have been a number of theoretical as well as empirical path loss models developed in the literatures [1–3]. A theoretical description of penetration into vegetation is given by the theory of radiative energy transfer [4]. These models are generic and applicable to any foliage wave propagation scenario, but are more complicated than the empirical models. The empirical models are based on specific measured data and fail to relate the foliage path-loss to the foliage dependent parameters such as tree species and density. All the models, as mentioned above, are focused mainly on path loss characteristics. An important aspect in the understanding of radio wave propagation in rural areas are the spatio-temporal characteristics of the channel. Of special note is the angular spread of the channel, which is an essential parameter for diversity and MIMO. Currently, there are few studies on the directional analysis of the dispersion effects of foliage in the radio channel. In [5], the delay characteristics and the polarimetric spatio-temporal channel characteristics have been studied in detail, but is limited only to V polarization and with both the base station (BS) and mobile station (MS) situated below the trees. Thus, from the viewpoint of the design of mobile communication systems, the investigation is insufficient. Based on the above background, the spatio-temporal channel characteristics at the MS side in the foliage environment based on measurements using channel sounder has been studied [6]. The results show that some large spreads in azimuth and the distance of the nominal azimuth values from zeros may be related to the dispersion caused by the foliage. However, this result had only investigated the direct path with the location of the MS fixed. Further investigation is essential to extract the effects of other paths that may be present in the environment.

The aim of this research is to evaluate the directional characteristics of radio wave propagation through foliage. A wideband channel sounder was employed to perform a directional measurement of polarimetric signal through dense forest in Kanagawa. Discrete plane wave model is deployed in the data modeling, where individual multipath component is represented as a discrete plane wave with specific complex amplitude, angle of arrival and delay time. To estimate these parameters, the SAGE algorithm is applied. The selection of the SAGE algorithm as the estimation technique is attributed to several factors: accuracy, rapid convergence, and robustness in low SNR scenarios. In order to understand the statistical characteristics, such as the direction spread, analysis of the multipoint mobile measurement acquisition results was performed.

2 Measurement

The measurement was performed using the channel sounder at the center frequency of 2.22 GHz and an operation bandwidth of 44.8 MHz. The sounder specification and measurement set up parameters are found in Table 1. A sleeve and a slot antenna were used to send the vertically and horizontally polarized signal. The receiver antenna array was installed on the roof-top of a measurement van with the horizontal distance between the transmitter and receiver ranging from 109 to 123 m. This antenna array is a stacked polarimetric uniform circular patch array (SPUCPA). It comprises of 4 stacked rings of 24 polarimetric patches yielding 192 ports in total. The MS was equipped with a differential global positioning system (GPS) to accurately track its location. A measurement campaign was carried out in a forest at Kanagawa on October 26–27, 2009 (Figure 1). The average height of the trees is 10 m and spread out with the average density of 0.32 per square meter. The measurement area is surrounded by other forests, low rise housing and a nearby sea, the physical feature of this forest mainly consist of 90 percent is a specie of Japanese pine tree. The BS antenna height was varied from 4 to 15 m by using a man lift, whereas the MS antenna was mounted on a van with a height of 2.8 m. The number of measurement points per each BS antenna height was 64 with 1 m interval. As indicated to Figure 1,

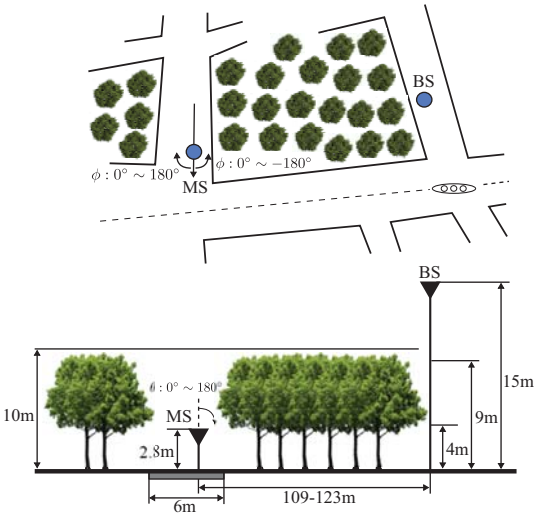

Figure 1: Measurement scenario.

Table 1: Specification of experiment

Center frequency	2.22 GHz
Bandwidth	44.8 MHz
Trans. power	40 dBm
Trans. signal	Wideband Multitone, 897 tones
BS antenna	sleeve, slot
MS antenna	SPUCPA (4 ring, 96 elements)
BS antenna height	4, 9, 15 m
MS antenna height	2.8 m
BS-MS separation	109–123 m
Average tree height	10 m
Number of meas. points	64
Number of snapshots per measurement point	20
The distance between the measurement points	1 m

the azimuth-of-arrival (AoA) ϕ relative to the movement direction of the MS was found to be $0 \sim -180°$ for left-hand side and $0 \sim 180°$ for right-hand side. Moreover, the co-elevation-of-arrival (EoA) θ was defined to have a value $0° \sim 180°$, $\theta = 0°$ corresponds to the zenith.

3 Analysis Approach

3.1 Signal Model

Figure 2 shows the signal model considering the directional information. In the data analysis, radio channel is modeled as the sum of impinging waves. Each impinging wave is represented as a discrete plane wave with specific complex amplitude, angle of arrival and delay time.

$$\mathbf{x}(t) = \sum_{l=1}^{L(t)} \alpha_l \mathbf{e}(\theta_l, \phi_l) s(t - \tau_l) + \mathbf{n}(t), \qquad (1)$$

where α_l, τ_l denote the complex channel gain, the propagation delay of l-th multipath component, respectively.

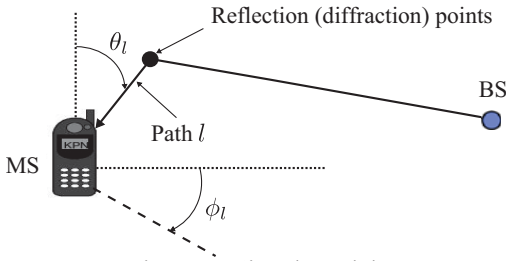

Figure 2: Signal Model.

$L(t)$ is the varying number of multipath components as the MS moves. Since α_l is complex valued, it can be written as $\alpha_l = |\sqrt{P_l}|e^{j\varphi_l(t)}$, where we assume $\varphi(t)$ are independent and uniformly distributed in the interval $[0, 2\pi)$, and $|P_l|$ is the received power of the path l. $s(t)$ is the transmitted signal and $\mathbf{n}$ represents the zero-mean complex Gaussian measurement noise with variance σ_n^2. $\mathbf{e}(\theta_l, \phi_l)$ is the array response of the receiver antenna array at θ_l in co-elevation and ϕ_l in azimuth.

3.2 Estimation of Channel Parameters

The parameters of each impinging wave are estimated from measurement data using the SAGE algorithm. This scheme is based on maximum likelihood estimation (MLE). A detailed description of the SAGE algorithm is shown in [7].

Although the SAGE algorithm is capable of estimating a large number of propagation paths, not all of these estimated paths are meaningful. There are two reasons for this. First, the received power of most of the paths after extracting 80-th path was less than the actual power level threshold of 25 dB, which had no significant contribution to the power transmission from BS to MS. Second, the detected paths were not always reliable due to the low SNR. In this regard, only paths falling within the 25 dB dynamic range were used find the delay and angular spreads. The paths that do not fall within the dynamic range were not used for further analysis.

3.3 Fleury's Direction Spread

Fleury [8] proposed an alternative approach to represent the angular spread to avoid the ambiguity of angular definition due to the rotational periodicity. In this paper, 2-dimensional definition of Fleury's direction spread is introduced:

$$\sigma_\phi = \sqrt{\frac{\sum_{l=1}^{L} \mid \exp(j\phi_l) - \mu_\phi \mid^2 \cdot P_l}{\sum_{l=1}^{L} P_l}}, \qquad (2)$$

with

$$\mu_\phi = \frac{\sum_{l=1}^{L} \exp(j\phi_l) \cdot P_l}{\sum_{l=1}^{L} P_l}, \qquad (3)$$

where P_l is the normalized azimuth angular power spectrum. It is noted that the direction spread in Eq. (2) is close to the root-mean-square (RMS) azimuth spread when the

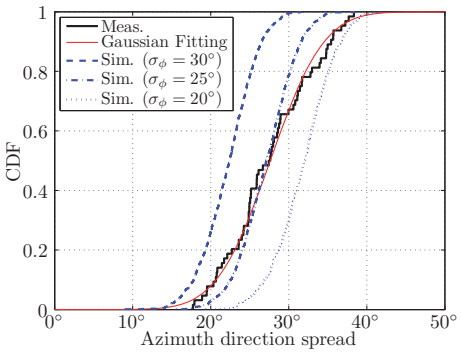

(a) CDF of azimuth direction spread

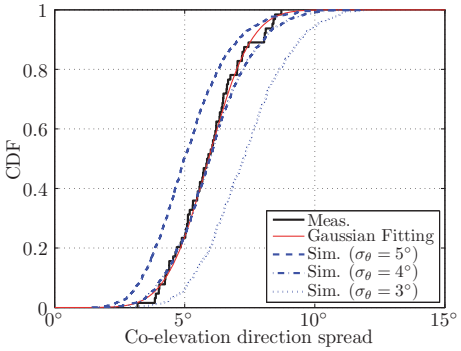

(b) CDF of co-elevation direction spread

Figure 3: Comparison of simulated and measured CDF of direction spread.

Table 2: Summary of direction spread statistics

Direction spread	Mean		Standard deviation	
	$\bar{\sigma}_{\text{sim}}$	$\bar{\sigma}_{\text{meas}}$	$\sigma_{\text{std,sim}}$	$\sigma_{\text{std,meas}}$
Azimuth	27.1°	27.6°	3.6°	5.4°
Co-elevation	6.0°	5.9°	1.5°	1.3°

impinging waves are highly concentrated within small azimuth range [8]. By replacing ϕ with the co-elevation angle θ in Eq. (2) and (3), we can compute the co-elevation direction spread σ_θ.

4 Results

4.1 Comparison Between Measurement and Simulation

Figure 3 shows the CDFs of the simulated and measured results of direction spread with its Gaussian fitting. The width of angle for simulation can be calculated. The widths of azimuth are 42°, 52°, and 62° corresponding to the azimuth spread of 20°, 25°, and 30° and the width of co-elevation are 8°, 10°, and 13° corresponding to the co-elevation spread of 3°, 4°, and 5°, respectively. The simulated CDF of direction spread with the azimuth spread of 25°, the co-elevation spread of 4° are in agreement with the measurements. Table 2 summaries the statistics of direction spread in case of of azimuth spread is 25° and co-elevation spread is 4°. It can be confirmed that the simulations results are in agreement with the measurements.

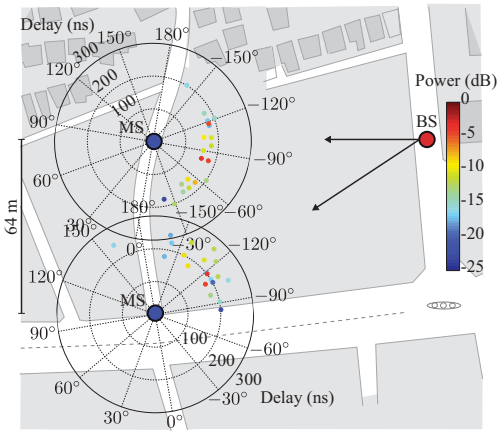

Figure 4: The obtained SAGE estimates of the mobile measurement at the first and last point (strongest 20 paths).

4.2 Direction Spread

The obtained SAGE estimates of the mobile measurement at the first and last points with a BS antenna heigh h_{BS} of 15 m are indicated by the red dots in Figure 4. In this case both ports V and H polarization were used for the estimation of the mentioned parameters. It can be confirmed that the nominal direction of arrival calculated by Eq. (3) seen from MS is quite close to the actual direction.

Figures 5, 6 show the cumulative distribution function (cdf) of direction spread for the azimuth and the co-elevation domains compared with Gaussian distribution fitting. It can be confirmed that the azimuth direction spread for H polarization is always greater than that for V polarization and the opposite is true in the case of co-elevation direction spread. It can be seen from the figures that changes in the BS antenna height produce no significant changes in the azimuth direction spread values for V polarization. The relatively high values of azimuth direction spread indicate that the incoming field at the MS is highly varying in azimuth. This is due to the dispersion caused by the absorption, scattering, and diffraction of the waves propagating through the foliage. For the EoA, the BS direction is set to 0°, 3° and 6° corresponding to the BS antenna height h_{BS} of 4 m, 9 m, 15 m, respectively. There is no clear relation found between h_{BS} and co-elevation direction spread. The relatively low values of co-elevation direction spread indicate that the incoming field at the MS is highly concentrated in co-elevation. Also on these figures, the mean, standard deviation of the direction spread $\bar{\sigma}, \sigma_{\text{sd}}$ are also shown. The mean azimuth direction spread is about 25° and the mean co-elevation direction spread is about 6°. This value is close to the average azimuth spread which was found to be about 25° in [9]. Furthermore, when the BS antenna height is 9 m, all the values are minimum. In this case, a better understanding of the mechanism of radio wave propagation is required to describe this result. To confirm the goodness of fitting between the Gaussian and experimental distributions, a Kolmogolov-Smirnov (KS) test has been applied. A Kolmogorov-Smirnov test is used to compare the values

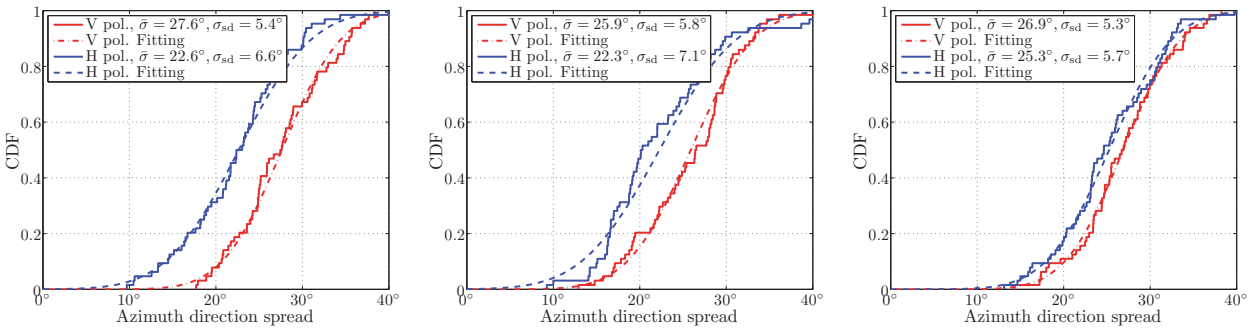

(a) $h_{BS} = 4$m (b) $h_{BS} = 9$m (c) $h_{BS} = 15$m

Figure 5: CDF of azimuth direction spread.

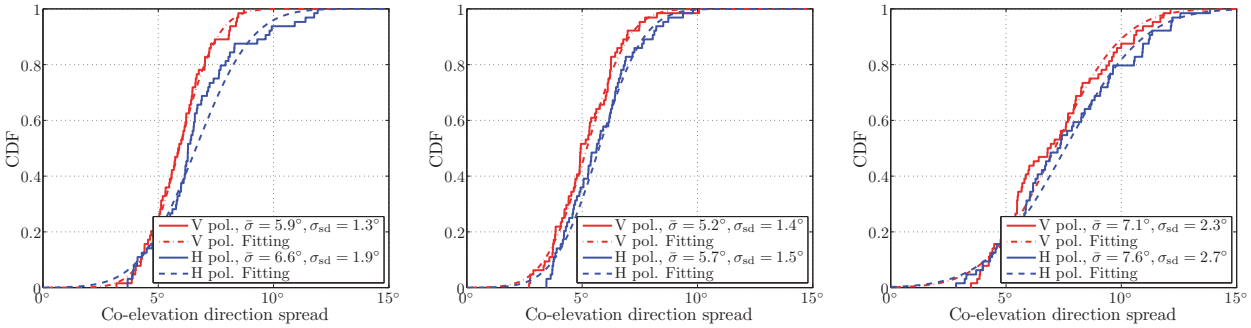

(a) $h_{BS} = 4$m (b) $h_{BS} = 9$m (c) $h_{BS} = 15$m

Figure 6: CDF of co-elevation direction spread.

Table 3: KS-Test results

Polarization		Height of BS		
		4 [m]	9 [m]	15 [m]
V	Co-elevation	A*	A	A
	Azimuth	A	A	A
H	Co-elevation	A	A	A
	Azimuth	A	A	A

* A: accepted, R: rejected (Confidence interval of 95%).

in the measured data to a Gaussian distribution. The null hypothesis is that the measured data has a Gaussian distribution. The alternative hypothesis is that the measured data does not have a Gaussian distribution. The result is A (accepted) if the test rejects the null hypothesis at the 5% significance level, R (rejected) otherwise. Table 3 summarizes the results of one-sample Kolmogolov-Smirnov test of Gaussian distribution for all the parameter sets. In all of the cases, empirical distribution was matched with the Gaussian distribution.

5 Conclusion

In this research, the effect of the foliage on the radio wave propagation has been analyzed by using a SAGE algorithm. The analysis result shows that the azimuth direction spread for H polarization is always more than that for V polarization and opposite is true in the case of co-elevation direction spread. The mean azimuth direction spread was found to be about 25° and the mean co-elevation direction spread was about 6°.

References

[1] International Telecommunication Union (ITU), "Attenuation in vegetation," Rec. ITU-R, Geneva, Switzerland, Tech. Rep., 2007.

[2] N. C. Rogers, A. Seville, J. Richter, D. Ndzi, N. Savage, R. Caldeirinha, A. K. Shukla, M. O. Al-Nuaimi, K. Craig, E. Vilar, and Others, "A generic model of 1–60GHz radio propagation through vegetation-Final report," *Radio Agency, UK*, 2002.

[3] G. M. Whitman, M. Y.-C. Wu, and F. K. Schwering, "Propagation and scattering of spherical wave pulses in vegetation using scalar transport theory," *IEEE Trans. Antennas Propag.*, vol. 58, no. 5, pp. 1662–1676, May 2010.

[4] A. Ishimaru, *Wave propagation and scattering in random media*. Wiley-IEEE Press, 1999, vol. 12.

[5] C. Oestges, B. Villacieros, and D. Vanhoenacker-Janvier, "Radio channel characterization for moderate antenna heights in forest areas," *IEEE Trans. Veh. Technol.*, vol. 58, no. 8, pp. 4031–4035, Oct. 2009.

[6] M. Ghoraishi, J. Takada, C. Phakasoum, T. Imai, and K. Kitao, "Azimuth and delay dispersion of mobile radio wave propagation through vegetation," in *4th European Conference on Antennas and Propagation (EuCAP 2010)*, Mar. 2010, pp. 1–4.

[7] B. H. Fleury, M. Tschudin, R. Heddergott, D. Dahlhaus, and K. Ingeman Pedersen, "Channel parameter estimation in mobile radio environments using the SAGE algorithm," *IEEE J. Select. Areas in Commun.*, vol. 17, no. 3, pp. 434–450, Mar. 1999.

[8] B. Fleury, "First- and second-order characterization of direction dispersion and space selectivity in the radio channel," *IEEE Trans. Inf. Theory*, vol. 46, no. 6, pp. 2027–2044, Sep. 2000.

[9] C. Phakasoum, M. Ghoraishi, J. Takada, K. Kitao, and T. Imai, "Frequency characteristics of angular spread for radio wave propagation through foliage," in *5th European Conference on Antennas and Propagation (EuCAP 2011)*, Mar. 2011, pp. 3289–3292.

IMPROVEMENT OF NOMIKAWA RIVER ENVIRONMENT THROUGH H_2S REMOVAL BY OXYGEN RELEASE COMPOUND (ORC)

Student Number: 10M18312 Name: Yuanzheng ZHU Supervisor: Hirofumi HINODE

酸素供給剤を用いた硫化水素除去による呑川水質改善

朱　遠征

東京を流れる呑川は東京湾に近い下流部分において淡水層および海水層からできている。大雨などの特殊な状況では川に大量の有機物を含む下水が流れ込んで、底泥などに存在する硫酸還元菌の活動によって硫化水素が多く生成され悪臭の原因となっている。本研究では呑川の縦断面のシミュレーション装置を用いて、硫化物イオン濃度、pH、DO および SO_4^{2-} の変化を観察した。硫化水素生成の抑制は酸素供給剤（ORC）を用いて行った。ORC は水との反応によって酸素を生成し、硫化物イオンを硫酸イオンに酸化させる機能を持っている。H_2S：MgO_2 の反応モル比はそれぞれ１：１、１：２、１：３、１：４を検討し、H_2S：MgO_2 の反応モル比は１：２の時、H_2S の除去速度が一番高い。H_2S：MgO_2 の反応モル比は１：１に基づいて、ORC による呑川の硫化水素除去に関する簡単なコストは 1.4×10^8 円/年間。

1 Introduction

Nomikawa River (Fig.1) flows through Setagaya ward, Meguro ward and Ota ward in Tokyo. Since Nomikawa River connects to Tokyo Bay, the section close to the sea has both fresh and salt water layers in the flow. At particular conditions where abundant of organic matters are present due to the flow of large amount of sewage water into the river, hydrogen sulfide (H_2S) is largely generated causing bad odor.

Fig.1 Nomikawa River

Hydrogen sulfide (H_2S) is one of the main states of sulfur in the natural sulfur cycle. The dominant source of H_2S is the reduction of sulfate, the most common state in the natural aquatic system, by sulfate-reducing bacteria (SRB) under anaerobic conditions [1]. H_2S may cause several problems to both sewers and the water supply system such as odor and toxicity [2].This study is focused on investigating the effective and economic method to remove H_2S from Nomikawa River in order to improve the river environment.

Eliminating the growth of SRB is a primary approach to inhibit the generation of H_2S in groundwater. Disinfectant is generally added to water to kill SRB. However, the H_2S level recovers rapidly. The growth pattern of SRB population is consequently changed since the SRB in suspension have been killed and from that point the immobilized SRB predominate in the water system. Therefore, the SRB population becomes more resistant to disinfectant [3]. In addition, many commercial disinfectants contain heavy metals and/or are toxic [4], which makes their use inappropriate when applied to an observational ground water system.

Addition of an oxidizing agent to the wastewater like hydrogen peroxide, chlorine gas, sodium/calcium hypochlorite, potassium permanganate etc. is another way to remove H_2S in wastewater [5][6][7]. H_2S can also be removed by precipitating with ferrous/ferric sulfate [8][9]provided the pH value is greater than 7.5.

The study deals with the evaluation of various chemicals like hydrogen peroxide, sodium/calcium hypochlorite, ferrous/ferric sulfate and a combination of sodium hypochlorite and sodium hydroxide for oxidation of dissolved sulfide in wastewater on laboratory scale.

At present, aeration technology [10] on treatment of polluted rivers was an adopted method in the world. Mechanized power must be needed for aeration technology in the oxygen supply system, construction cost and maintenance charge are also very high. So it is very difficult to enforce the process in actual application.

An oxygen release compound (ORC) is composed mainly of magnesium peroxide (MgO_2) and this was applied in this study. It can be reacted with water to release oxygen slowly to produce magnesium hydroxide ($Mg(OH)_2$). There are two major mechanisms by which ORC may be able to decrease H_2S concentration in water. One is the abiotic oxidation of sulfide to sulfate, and the other is biotic inhibition of SRB by reducing the generation of sulfide. Since ORC can release oxygen

gradually over a long period of time, the addition of ORC would seem a suitable method of preventing H_2S production in wastewater systems.

The purpose of this study is to evaluate the practicability of using ORC to prevent the generation of H_2S under anaerobic conditions in the simulation set-up of a vertical section of Nomikawa River.

2 Experimental

2.1 Simulation set-up

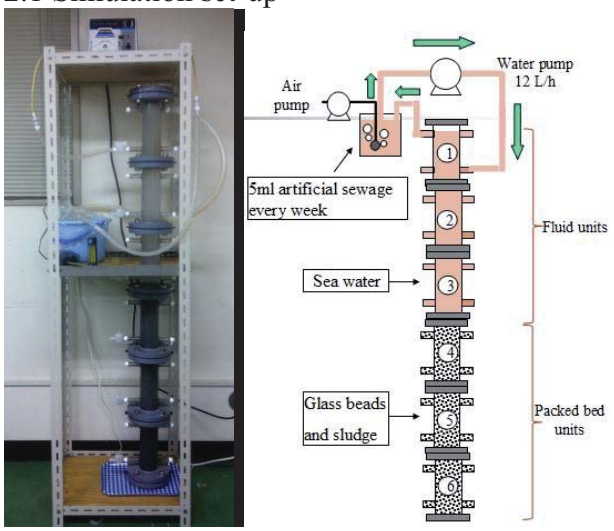

Fig.2 Simulation set-up

The set-up was started on June 6th, 2011.

The set-up was divided into 6 parts. From part 1 to Part 3 are fluid units. And from part 4 to part 6 are packed bed units. The sea water in the set-up simulates the environment of Nomikawa River. And 5ml artificial sewage is added into the set-up every week to simulate the pollution poured into Nomikawa River.

2.2 Formation of Hydrogen Sulfide (H_2S)

Hydrogen sulfide (H_2S) occurs naturally through the anaerobic decay of organic matter and is recognized by its characteristic rotten egg odor.

$$SO_4^{2-} + \text{Organic matter} \xrightarrow[\text{no dissolved oxygen}]{\text{SRB (sulfate-reducing bacteria)}} H_2S + CO_2$$

SRB (sulfate-reducing bacteria) can chemically change natural sulfates (SO_4^{2-}) in water to hydrogen sulfide (H_2S).

2.3 Effect of pH on H_2S equilibrium

It is shown in Fig.3 that at a pH of 7.0, 50% of the dissolved sulfides are present as H_2S and at a pH of 6.0, 90% of the dissolved sulfides are present as H_2S. Less than 3% of the dissolved sulfides would form gaseous H_2S at a pH above 8.5. The distinction between the types of sulfide ions is important since only H_2S can escape from the solution and create odors and corrosion problems.

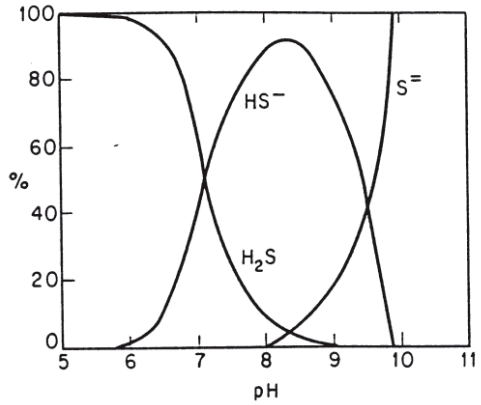

Fig.3 Solubility equilibrium of H_2S[11]

2.4 Experimental principle

MgO_2 can be reacted with water to release oxygen slowly and produce magnesium hydroxide ($Mg(OH)_2$). Produced $Mg(OH)_2$ can also be reacted with H_2S to produce $MgSO_4$.

$$2MgO_2(s)+2H_2O \rightarrow 2Mg(OH)_2(s)+O_2(g) \quad ①$$

$$O_2(g)+2H_2S(g) \rightarrow 2S(s)+2H_2O \quad ②$$

$$MgO_2(s)+H_2S(g) \rightarrow Mg(OH)_2(s)+S(s) \quad ①+②=③$$

$$Mg(OH)_2 + x\,H_2S \rightarrow Mg(OH)_2.(H_2S)x$$

$$\rightarrow Mg(HS)_2 + 2O_2 \rightarrow MgSO_4 \quad ④$$

pH value will increase as the amount of H_2S decrease. If there are enough MgO_2, the generation of H_2S can be inhibited.

2.5 Experimental material

Glucose(min.98.0%),KH_2PO_4(min.99.5%),$NaHCO_3$(min.99.0%), from Kanto Chemical Co.,Inc.; Polypeptone and $Na_2S \cdot 5H_2O$(min.99.99%)from Wake Pure Chemical Industries, Ltd. ORC(Magnesium peroxide complex(MgO_2 24-28%)) from Sigma-Aldrich Co. Ltd.

2.6 Analysis method

	H_2S (Hydrogen sulfide) (WAK-S pack Test)	SO_4^{2-} (Sulfate) (DPR-SO4 Pack Test)	DO (Dissolved Oxygen) (AZ-DO-30 Pack Test)
Measuring Range	0.05 to 0.80 ppm	10 to 100 ppm	2.0 to 11.0 ppm
Sampling Time	3 minutes	3 minutes	2 minutes
Color change	Colorless to Blue	Colorless to Whitish	Colorless to Cyan
Reaction Principle	Methylene blue method	Barium chloride turbidimetry	Indigo carmine method

The concentration of H_2S, SO_4^{2-}, and DO(Dissolved Oxygen) can be measured by Digital Pack Test DPM-MT. " Pack Test" is the most simplified water quality test. The color will be changed after the reaction time.

3 Results and discussion

3.1 pH, the concentration of H_2S, SO_4^{2-}, DO of each reactor

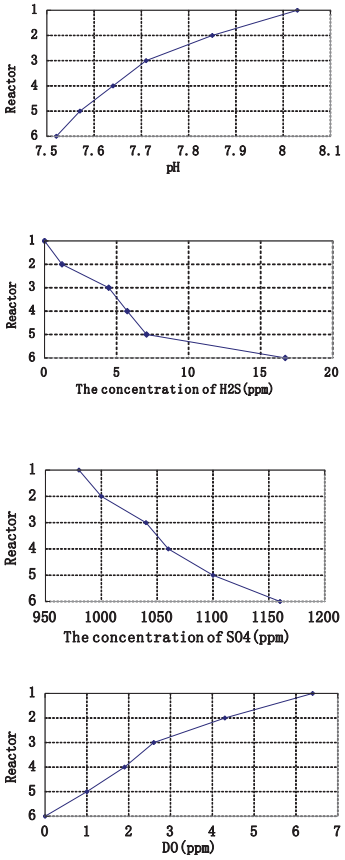

Fig.4 pH, the concentration of H_2S,SO_4^{2-},DO in each reactor

The simulation set-up was started after 4 months, pH, the concentration of H_2S, SO_4^{2-}, DO in each reactor were stabilized. The concentration of H_2S and SO_4^{2-} increased along with the depths increased. pH and DO decreased along with the depths increased.(Fig.4)

3.2 The effect of different mol ratio of H_2S:MgO_2

The solution taken from reactor 4 was divided into 4 portions. The same concentration of Na_2S was as a reference. ORC was added into each beaker on the different mol ratio of H_2S:MgO_2 including 1:1,1:2,1:3,1:4 and Na_2S:MgO_2=1:1 as a reference. pH increased in each beaker. The concentration of H_2S all decrease to nearly 0ppm after 24 hours in each beaker(Fig.5). When the mol ratio of H_2S: MgO_2 is 1:2, the removal rate is highest.

When the mol ratio of H_2S:MgO_2 is equal to 1:4, the amount of MgO_2 is too much to prevent the rate of the reaction.

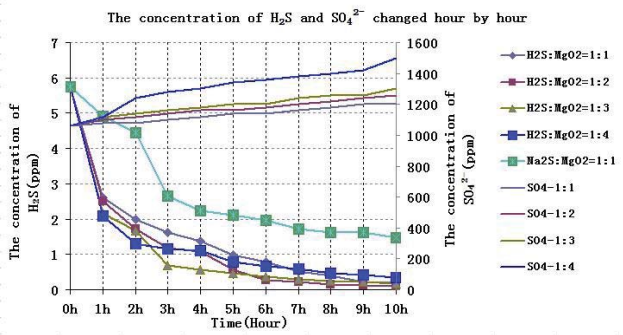

Fig.5 H_2S and SO_4^{2-} concentration changed hour by hour on the condition of different mol ratio of H_2S:MgO_2

3.3 ORC added into the simulation set-up

ORC was added into the set-up on the condition of the mol ratio of H_2S: MgO_2 is 1:1.

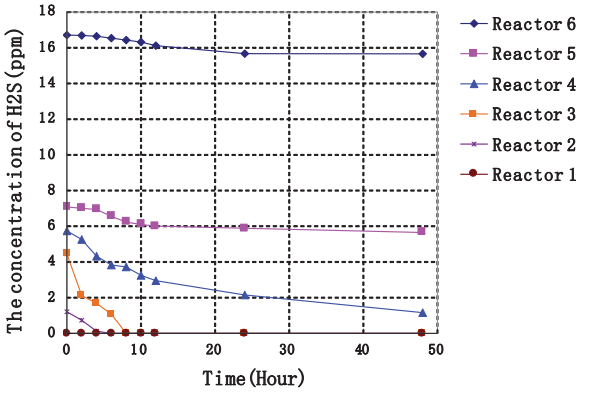

Fig.6 The concentration of H_2S changed in each reactor

After 6 hours, the concentration of H_2S in reactor 2 decreased to 0ppm.After 8 hours, the concentration of H_2S in reactor 3 decreased to 0ppm.After 48 hours, the concentration of H_2S in reactor 4 decreased to 1.16ppm.After 48 hours, the concentration of H_2S in reactor 5 decreased to 5.56ppm. After 48 hours, the concentration of H_2S in reactor 6 decreased to 15.66ppm.

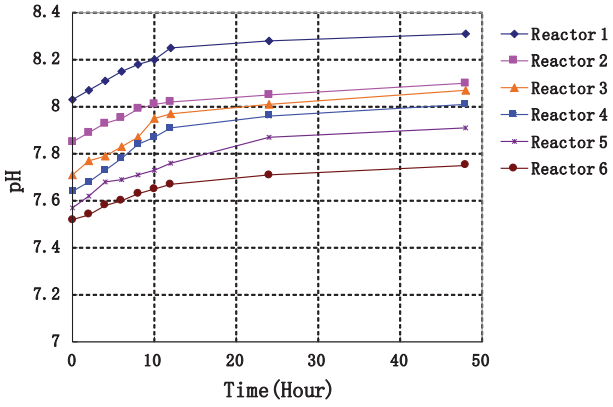

Fig.7 pH changed in each reactor

pH of each reactor increased to around 7.75-8.3 as the time passed.

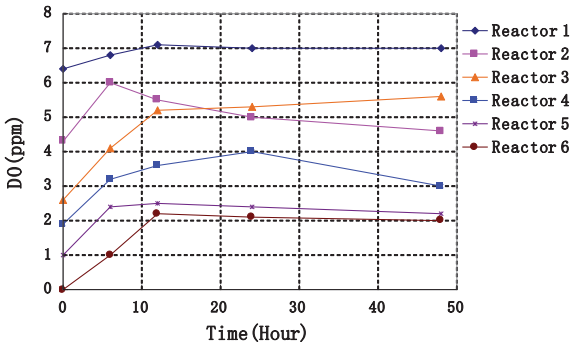

Fig.8 DO changed in each reactor

DO of each reactor increased at the beginning and at the same time O_2 was consumed by H_2S. And then Do decreased in reactor 4-6, because O_2 release rate is less than consumption rate.

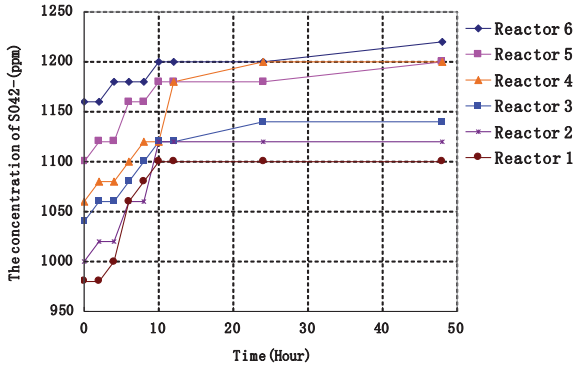

Fig.9 The concentration of SO_4^{2-} changed in each reactor

The concentration of SO_4^{2-} of reactor 1 to reactor 4 increased at the beginning and then stabilized. The concentration of SO_4^{2-} of reactor 5 and reactor 6 increased as $MgSO_4$ produced.

4 The cost of ORC for Nomikawa River

Based on the result of the previous experiment, The cost of ORC for removing H_2S from Nomikawa River was calculated on the condition of the mol ratio of H_2S: MgO_2 is 1:1.The depth and concentration of H_2S under each bridge are on the following table according to the investigation results of Nomikawa River[12].

According to the investigation results, the concentration of H_2S will increase after heavy rain, and then decreased because O_2 produced by photosynthesis in the river. In one year, the concentration of H_2S increased for four times, so ORC will be added into Nomikawa River four times one year.

Table 1 The Cost of ORC for Nomikawa River

Bridge	Sanya-bashi				Onari-bashi	
Month(H_2S odor detected)	5	8	10	1	5	10
Depth(m)	2.1				1.48	
The average depth(m)	1.79					
The concentration of H_2S(ppm)	6	6	1	2	5	2
The average concentration of H_2S(ppm)	3.67					
The length between two bridges(m)	730					

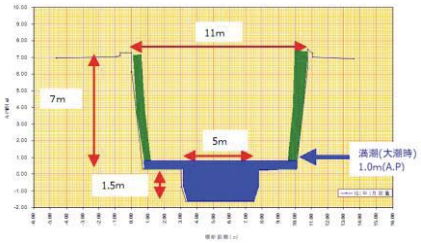

Fig.10 The vertical section of Nomikawa River

Volume between two bridges（m^3）	7.4×10^3
ORC（JPY/g）from Sigma-Aldrich Co. Ltd	13.4
ORC needed for two days (g)	1.7×10^5
The cost of ORC (JPY/one time)	2.2×10^6
The cost of ORC (JPY/one month)	3.5×10^7
The cost of ORC (JPY/one year)	1.4×10^8

If the price of ORC is lower, this method can be used in the future. ORC could be used as a common method to improve the effect of aeration treatment in a part of Nomikawa River.

5 Conclusions

The simulation set-up was successfully simulating Nomikawa River. After 4 months, the concentration of H_2S, SO_4^{2-}were stabilized. The effect of H_2S removal influenced by different concentrations of ORC was discussed. When the mol ratio of H_2S: MgO_2 is 1:2, the removal rate is highest.

ORC could effectively remove H_2S from simulation set-up of Nomikawa River.

The cost of removing H_2S from Nomikawa River was calculated. If ORC will be added into Nomikawa River for 4 times in one year, the cost of ORC is 1.4×10^8 JPY/year. ORC could be used as a common method to improve the effect of aeration treatment in a part of Nomikawa River.

References

[1] Grossman, E.L., 2001. Microbial sulfur cycling in terrestrial subsurface environments. In: Fredrickson, J.K., Fletcher, M. (Eds.),Subsurface Microbiology and Biogeochemistry. John Wiley & Sons, Inc., London, pp. 219–248.

[2] Tomar, M., Abdullah, T., 1994. Evaluation of chemicals to control the generation of malodorous hydrogen-sulfide in waste-water. Water Res. 28, 2545–2552.

[3] Jones, D.A., 1996. Principles and Prevention of Corrosion. Prentice Hall, NJ, USA.

[4] Davidova, I., Hicks, M.S., Fedorak, P.M., SuXita, J.M., 2001. The influence of nitrate on microbial process in oil industry production waters. J. Ind. Microbiol. Biotech. 27, 80–86.

[5] Dague R. R. (1972) Fundamentals of odour control. J.Wat. Pollut. Control Fed.44, 583-594.

[6] Fraser J. A. L. and Sims A. F. E. (1984) Hydrogen peroxide in municipal, landfill and industrial effluent treatment Effluent Wat. Treat. J., pp. 184-188.

[7] Henry J. G. (1980) Odour control: an operator's guide. J. Wat. Pollut. Control Fed. 52, 2523-2537.

[8] Waltrip G.D. and Synder E.G.(1985) Elimination of odour at six major waste water treatment plants. J. Wat. Pollut. Control Fed. 57, 1027-1032.

[9] Metcalf and Eddy Inc. (1991) Waste Water Engineering: Collection and Pumping of Waste water, 3rd edn. McGraw-Hill, New York.

[10]Marc W Beutel, Alex J Horne. A review of the effects of hypolimnetic oxygenation on lake and reservoir water quality. *Journal of Lake and Reservoir Management*, 1999, 15(4):285-297.

[11]Peter Churchill，David Elmer. Hydrogen sulfide odor control in wastewater collection systems. Newer Journal, May 1999(33) NO1,57-63.

[12] Investigation results of Nomikawa River. 2010

Study on effective communications in capacity assessment of technical cooperation in environmental management sector

Student Number: 10M51580 Name: Kazutoshi MACHIDA Supervisor: Naoya ABE

環境管理分野の技術協力のキャパシティ・アセスメントにおける有効なコミュニケーションに関する研究

町田　和俊

本論文では、開発途上国の環境管理分野の有効な能力評価(CA)手法の提案を目指し、技術協力の現場に精通する開発コンサルタントに対するアンケート調査を実施し、国際協力機構（JICA）とコンサルタントの有効な連携や能力評価チェックリストの改善のための分析を行った。また、ベトナムの廃棄物管理を題材として参加型ワークショップを開催し、能力開発に関わる途上国側との効果的なコミュニケーションツールとして階層分析法（AHP）の有用性を検証した。

1. Introduction

In recent years, the concept of *capacity development* (CD) has been paid huge attention by donor agencies in order to ensure sustainability of the impact of international development projects. In order to realize CD in practice, its assessment (capacity assessment, CA) is crucial for donor agencies such as the Japan International Cooperation Agency (JICA). Definition of CA by JICA includes not only the "process of *diagnosing* the current state of the developing countries' capabilities for handling issues (capacity)" but also "*sharing* results" with concerned parties (JICA, 2008). In this sense, CA has a role as a communication tool between developing countries and donors for encouraging a shared understanding of capacity for the sake of CD support.

However, the current practices of CA in real projects and its effectiveness as a communication tool have not been examined thoroughly. Since the Technical Cooperation (TC) projects by JICA are now increasingly implemented by Japanese development consultants through bidding, the coordination of JICA staff and consultants has become more important than ever (Fig. 1). Also, in the view of recipient countries, Fanany et al. (2011) claims that the meaning and nature of capacity building is not well understood locally and differs considerably from its generally accepted sense in the west. Thus, careful communication with counterpart (C/P) staff is an essential process for better CD support for JICA and consultants.

In this study, taking JICA's TC in environmental management sector as an example, effective communications in CA was studied with the following specific research objectives. The first

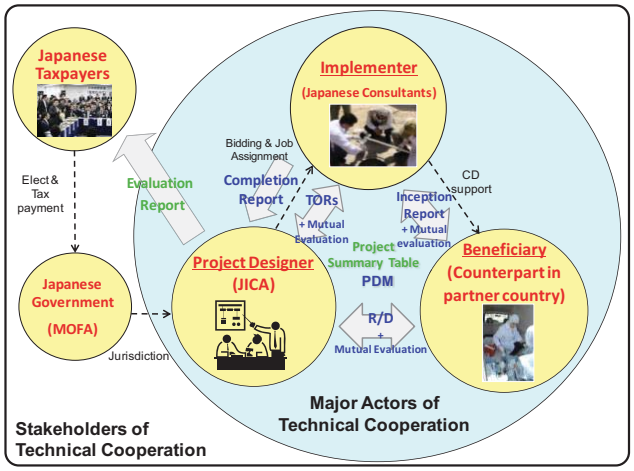

Fig. 1. Document-based communication between major actors and stakeholders of TC of Japanese ODA

is to confirm the past and current CA practices of JICA. The second is to ask consultants on existing CA checklist, which is prepared by JICA in each subsector and supposed to be a key tool for the better communication on capacity, in order to improve its practicality. The third is to seek better ways of communication between C/P staff and donor staff by verifying effectiveness of another possible tool.

2. Coordination between JICA staff and development consultants

In order to meet the objectives regarding the coordination between JICA staff and consultants, questionnaire of consultants was conducted. A sample of 40 projects was selected from past TC projects from year 2004 to 2009 managed by the Global Environment Department of JICA. Then the questionnaire sheets were sent to the managers of the sample project and there were 28 responses for the questionnaire survey to consultants (collection rate:

80%).

Main questions of the questionnaire were the means and contents of instruction on CA by JICA and the recognition of existing checklist. The checklist provided to respondents was the total of 129 CA items, which is integrated by Machida (2010) from the lists used in subsectors in environmental management sector. In the survey, items that are *not* appropriate for CA are enumerated with the reasons because capacity is very much qualitative and hard to gauge the degree of suitability of each item as included in checklist by asking what is appropriate.

2.1 Instruction of JICA to the consultants on CA

According to the survey, 9 respondents (32%) answered that they did not get any explanation or instruction about CA (Fig. 2 (a)). Furthermore, even if there are some, the instructions were limited to general one: mostly only document basis and specific CA item was rarely mentioned (Fig. 2 (b)). Yet further, the reporting style was instructed in only two projects (Fig. 2 (c)) although the sharing of CA results among stakeholders is regarded as important (JICA , 2008). Thus it is safe to say that the implementation of CA had been largely depending on the willingness of individual consultants.

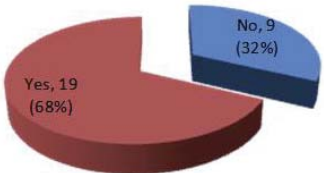

(a) Whether there was any instruction on CA (N=28)

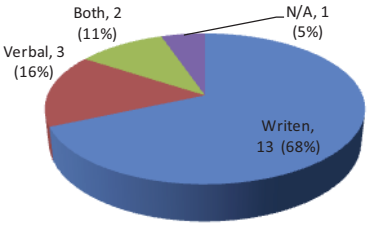

(b) Means of the instruction (Multiple Answer, N=19)

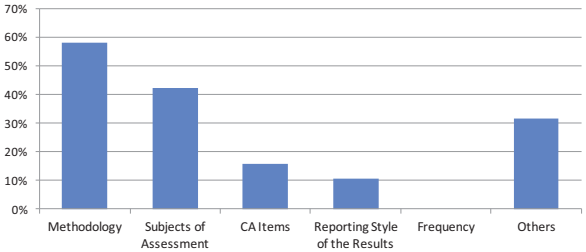

(c) Contents of the instruction (Multiple Answer, N=19)

Fig. 2. Results of questions regarding instruction on CA

2.2 The consultants' recognition of existing CA checklist

Regarding the recognition of existing CA checklist, the results of negative votes by each item are shown first. Since respondents could vote as many items as they like, there were great variances only by number of items that regarded as not appropriate. As a result, more than half (55%) of the items got negative votes at least from one respondent. Table 1 shows the items that got 4 votes or more as inappropriate. According to the list, those items that describe stakeholders who are not the direct C/P tends to be regarded as inappropriate.

The frequency of reasons of inappropriateness as CA item is shown in Fig. 3 (a). From the result, *difficult to assess* turned out to be the primary causes for being not appropriate. The follower was *irrelevant* and *other* (e.g. the item is rather a goal itself of CD project/it does not make sense individually). The detailed reasons for the difficulties of assessment are shown in Fig. 3 (b). *Technically difficult* (e.g. difficulty in definition) was the most common one and *time-consuming* followed it. The example of the description on *other* (in *difficult to assess* category) was political difficulty such as inaccessibility to data).

Table 1. Ranking of negative votes (N=28)

Rank	Type	CA Item	Negative votes	
			n	%
1	Human assets	Human resource and their capabilities in civil society organization	7	25.0
2	Human assets	Human resource and their capabilities in businesses	6	21.4
3	Social organizations	Environmental management capacity of communities	5	17.9
3	Social aspects	Implication of religion	5	17.9
3	Social aspects	Customs	5	17.9
6	Org structure /management	Aw areness of policymakers on putting solution into practice	4	14.3
6	Personnel	Performance evaluation (method, reflection to promotion)	4	14.3
6	Source of information	Literature	4	14.3
6	NGO	Activities of NGO for project formulation	4	14.3

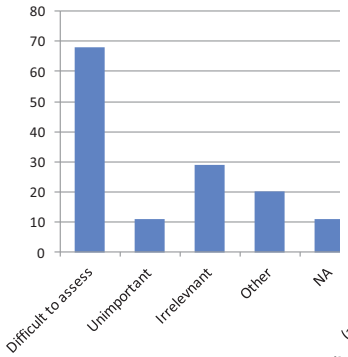

(a) General reasons

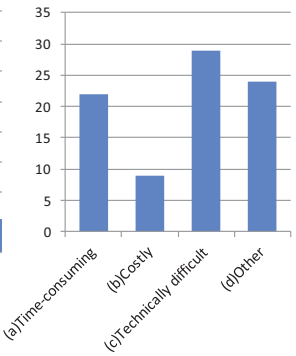

(b) Detailed reasons for difficulties of assessment

Fig. 3. Reasons of inappropriateness as CA item
(Total number of frequency by reasons for all votes, N=140, regardless of voter, Multiple answer for each votes)

The data set of negative votes by consultants was further analyzed by the Principal Component Analysis (PCA) in order to understand the similarity of each reason. PCA is a multivariate analysis method that can reduces the dimensionality of numerical multivariate data set, while retaining as much variation as present in the data set. The detailed calculation can be found in Jolliffe (2002), for example.

The proportions of components and the plots of loadings with respect to the first two components are shown in Table 2 and Fig. 4. Component 1 can be regarded as feasibility axis (whether the item can be assessed) and Component 2 can be interpreted as meaningfulness axis (irrelevance or uselessness). For those items that is technically difficult (DIFF_TECH in Fig. 4) or politically difficult (DIFF_OTHER in Fig.4), there needs to be further two investigations since they are not unimportant despite their challenges in assessment. First, their relevance to capacity should be reconsidered as they got high score in irrelevance direction. Second, if they are still relevant, elaboration of gauging would be necessary for technically difficult items. Also JICA's initiative on politically difficult items would be important as consultants are not deployed to tackle the difficulty.

Table 2. Eigen value and proportion of components (by comp.4)

Component	Eigenvalue	Proportion	Cumulative
Comp1	3.04262	0.3831	0.3831
Comp2	1.26075	0.1642	0.5473
Comp3	1.03143	0.1341	0.6814
Comp4	.839909	0.1209	0.8023

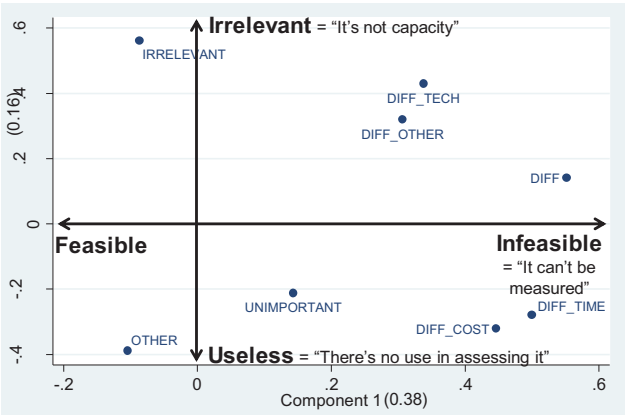

Fig. 4. The result of PCA (Component loadings)

3. Case study on communications of CD for solid waste management sector in Vietnam

In a project formulation stage, JICA (2008) suggests that CA result should be used for helping developing countries to draft a CD strategy with scenarios to an aimed future vision. Nevertheless, communication on capacity with C/P is challenging task according to the questionnaire survey to C/P conducted during the pre-field visit.

In order to gain actual recognition about CD and CA by C/P, a participatory workshop was conducted in Vietnam. The workshop was held in suburban Hanoi on 30th November and 1st December and 20 participants were gathered from various organizations related to solid waste management (SWM) in Hanoi city. The participants were divided into 4 groups and discussed an effective action plan and strategic development of necessary capacities (NCs) for future SWM.

The structure of the workshop is as follows. First is to confirm effectiveness of past and current policy of SWM. Second is to conduct scenario planning and share the preferred future vision. Third is to identify the NCs to realize a future vision (a gap from current status). Lastly, activities to develop each NCs were prioritized to develop CD strategy.

The main analytical tool used in the workshop is a decision-making support tool called Analytic Hierarchy Process (AHP). It is a simple but powerful tool developed by Thomas Saaty in 1970's for multi-criteria multiple alternatives decision problems (Tone, 1986). It constructs hierarchy that consists of goal, criteria and alternative options first. Then criterion is weighted by pair-wise comparison by a person or by a group. The data is then used for the calculation of weights for each criteria and Consistency Index (C.I.). In the participatory workshop held in Hanoi, five criteria were set by the author (effectiveness, time, budget, human resources and technology) to prioritize necessary capacities on the basis of prior discussion with Japanese and Vietnamese co-organizers. The main reason why AHP was adopted is that the development of hierarchy can assist the context of capacity and promote firm and accurate discussions regarding CD.

According to the first session, 96% of participants recognized the existing national strategy for integrated SWM is *very challenging* or *challenging* and the lack of capacity to achieve the strategy were implied. This step could be regarded as

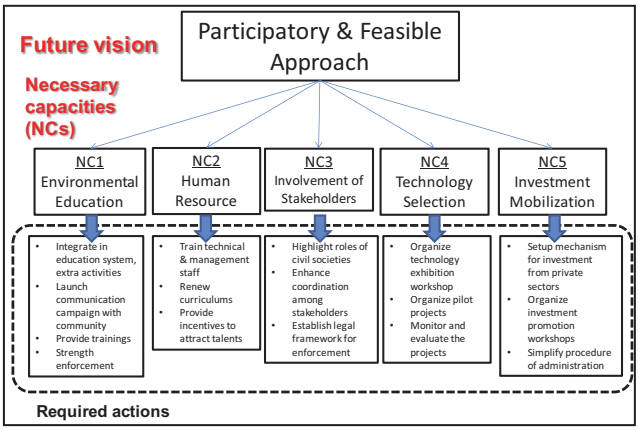

Fig. 5. Hierarchy of AHP by a group

Table 3. Result of the pair-wise comparison of NCs under each criterion by a group

	Effectiveness	Time	Budget	Human Resource	Technology
Government Budget	0.1484	0.2208	0.1831	0.3251	0.1466
Public Awareness	0.2628	0.2473	0.2249	0.2984	0.1876
Incentives	0.1187	0.0880	0.0754	0.1199	0.1561
Law & enforcement	0.2753	0.1676	0.3546	0.1505	0.3246
Human Reseource & Database System	0.1948	0.2764	0.1619	0.1061	0.1851
C.I.	0.0512	0.0424	0.0263	0.0609	0.1255

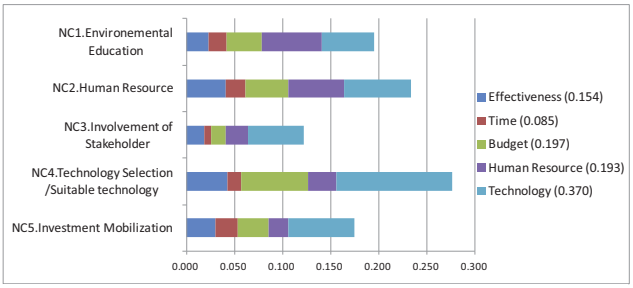

Fig. 6. Overall assessment score of five NCs by a group

self-assessment of the national capacity. On the basis of the following shared future vision in the group, weights of the five criteria and NCs with its CD activities were listed and prioritized. The example of hierarchy of AHP by a group is shown in Fig. 5. The overall assessment score by AHP and C.I. for pair-wise comparison of NCs under each criterion is shown in Table 3 and Fig. 6. The C.I. of pair-wise comparison of NCs under criterion *Technology* in the group was 0.1255, which is a little high and there is possibility on inconsistent answer. The possible reasons are as follows. First, the AHP was applied only one time and answered individually. Second, one of five preset criteria was technology (whether the technologies utilized in activities of the NC) and somewhat overlapped. This could be solved by letting participants to decide their own criteria or using advanced method of AHP, Analytic Network Process (ANP) but neither feasible options in the workshop due to logistical reason.

Although the workshop had some points to be improved, the satisfaction of participants were high (Fully satisfied: 4 and good: 16) and AHP were regarded as manageable (95%), the workshop could show one case to utilize AHP as a promoting tool on communication regarding capacity.

4. Conclusion and further studies

The following are the conclusion of this study. First, instructions on capacity assessment by JICA to consultants were confirmed to have been ad-hoc and unsystematic and thus there is room for improvement in efficiency to address CA in an integrated way in TC. Second, the criterion of whether each capacity assessment item is in the CA checklist, operational definition of capacity, converges to feasibility and meaningfulness (irrelevance and uselessness). The relatively inappropriate items and its reasons are suggested to be shared for reference, not to say to be omitted from the checklist. Third, the result of participatory workshop in Vietnam on SWM implies that the meaning of capacity by C/P staff is subject to change on the basis of preferred future visions or context. Also, it showed a case for the application of AHP to promote structured and firm discussions and continuous learning regarding capacity development, which tends to have highly sensitive meaning.

As a further study, a research on the applicability of CA items depending on the project stage is necessary for better coordination on CA by JICA staff and consultants. Second, since the visualization and dissemination of CA result is currently limited, model development of index of capacity is important. Third, the meaning of accountability should be reexamined because the progress of CD is becoming more and more immeasurable by objective manners.

References

[1] JICA, 2008. Capacity Assessment Handbook, JICA:Tokyo

[2] Fanany, I., Fanany, R., Kenny, S., 2011. The meaning of capacity building in Indonesia, Community Development Journal (2011) 46(1):89-103

[4] Machida, K., 2010. Empirical Analysis on Capacity Assessment Framework for Environmental Management Sector in Developing Countries (in Japanese), Bachelor Thesis, Tokyo Institute of Technology

[5] Jolliffe, I. T., 2002. Principal Component Analysis, 2nd ed., Springer-Verlag: New York

[6] Tone, K., 1986. *Gemu kan-kaku ishi-kettei hou* (Game-like decision-making method: Introduction to AHP), JUSE Press